TECHNISCHE UNIVERSITÄT MÜNCHEN
Lehrstuhl für Thermodynamik

# Investigation of Cryogenic Hydrogen Storage on High Surface Area Activated Carbon: Equilibrium and Dynamics

**Ricardo Gaspar Paggiaro**

Vollständiger Abdruck der von der Fakultät für Maschinenwesen der Technischen Universität München zur Erlangung des akademischen Grades eines

DOKTOR – INGENIEURS

genehmigten Dissertation.

| | |
|---|---|
| Vorsitzender: | Univ.-Prof. Dr. med., Dr.-Ing. habil. E. Wintermantel |
| Prüfer der Dissertation: | 1. Univ.-Prof. W. H. Polifke, Ph.D. (CCNY) |
| | 2. Univ.-Prof. Dr.-Ing. H. Klein |

Die Dissertation wurde am 18.08.2008 bei der Technischen Universität München eingereicht und durch die Fakultät für Maschinenwesen am 29.11.2008 angenommen.

## Abstract

This thesis investigates cryo-adsorptive systems for hydrogen storage for mobile applications. By means of macroscopic and microscopic balance models, an extensive analysis is carried out, including among others the investigation of the thermal effects during high-pressure system filling, venting losses during normal operation and inactivity, time-course of system pressure and temperature and gas delivery under various operating conditions. Model results were compared with experimental data, good agreement was obtained. The analysis also includes a comparison to other storage technologies such as cryo-compressed gas and liquefaction storage. The results show that cryo-adsorptive systems have storage characteristics comparable to compressed gas systems, but at a much lower pressure. They are also energetically more efficient than liquid hydrogen systems. However, the necessity of cryotemperatures and thermal management during operation and filling might limit their application.

## Zusammenfassung

Die Arbeit untersucht kryo-adsorptive Systeme zur Wasserstoffspeicherung für mobile Anwendungen. Mittels makro- sowie mikroskopischer Modelle wird eine umfangreiche Analyse durchgeführt, die u.a. die Untersuchung der thermischen Effekte während der Beladung, die Gasverluste während Normalbetrieb und Stillstand, den zeitlichen Verlauf des Systemdruckes und der Temperatur und die Gasabgabemenge unter verschiedenen Betriebsbedingungen umfasst. Der Vergleich der Ergebnisse mit experimentellen Daten zeigt eine gute Übereinstimmung. Die Analyse beinhaltet auch einen Vergleich mit weiteren Speichertechnologien wie Kryo-Gasverdichtung und Verflüssigung. Die Ergebnisse zeigen dass kryo-adsorptive Systeme eine ähnliche Speicherdichte haben wie Gasverdichtung, aber bei einem viel niedrigeren Druck. Sie sind auch energieeffizienter als Flüssigspeichersysteme. Jedoch führt die Notwendigkeit von Kryotemperaturen sowie Energiemanagement während des Betriebes und der Beladung zu Komplizitäten in der Anwendung.

## Acknowledgements

This thesis has been done at the Lehrstuhl für Thermodynamik of the Technische Universität München. It would not have been possible without the help, support and contribution of many people, to whom I would like to express my gratitude now that it has come to an end.

First of all, I would like to thank my supervisor Prof. Wolfgang Polifke Ph.D. for giving me the opportunity to do this project, for his support throughout all these years, and for his skillful management and advice that kept me on track during this thesis but at the same time allowed me to explore science in my own way and according to my own interests. I also would like to thank Prof. Dr.-Ing. Harald Klein for agreeing to co-examinate this thesis and Prof. Dr. med. Dr.-Ing. habil. Erich Wintermantel for chairing the defense.

Furthermore, I am greatly indebted to Prof. Pierre Bénard Ph.D. of the Institut de Recherche sur L'Hydrogène of the Université du Québec à Trois-Rivières for his co-operation in this project and for the countless discussions from which I benefited a lot. He has been a reliable source of encouragement and advice, and even on a distance helped me keeping at doing this. I appreciate his financial support and his nice hospitality during my stays in Canada and his visits to Germany.

I'm also very grateful to Dr. Walter Schütz and Florian Michl from FutureCarbon GmbH (Bayreuth, Germany) for the administration and execution of the experimental part of this joint project. It was a pleasure to work with you. I also thank GM-Opel Deutschland for financing FutureCarbon and for providing me the experimental data, and I gratefully acknowledge the financial support provided by the Bayerisches Ministerium für Wirtschaft, Verkehr und Technologie and the Loschge-Studienstiftung.

I thank all colleagues for the nice atmosphere at the institut, and specially Dr. Frank Kiesewetter for his help on working out tricky numerical solutions and Dr. Marco Auer and Dr. Jan Kopitz for the nice and adventurous activities not related to science.

Last but not least, a special thanks goes to my partner Iratxe, who had to make a lot of sacrifices during the course of this thesis but was always on my side. And finally, an unmeasureable amount of thanks goes to my parents who did their best to provide me with a good education and always support me whatever path I choose.

Munich, July of 2008

Ricardo Paggiaro

# Contents

# 1 INTRODUCTION

The potential of hydrogen as an energy carrier has been known for approximately two centuries [27]. Hydrogen exhibits the highest heating value per weight of all chemical fuels. Its conversion to heat or power is simple and clean. When combusted with oxygen or converted into electricity in a fuel cell, hydrogen generates besides energy only water, which can return to nature, where it originally came from. No pollutants or greenhouse gases are emitted in these processes. However, hydrogen use as a fuel is still very limited.

Nowadays, 80% of the huge amount of energy consumed in the whole world are based on fossil fuels (coal, oil and gas) [92]. Reserves of these fuels consist of solar energy naturally stored over millions of years. Mankind exploits these energy sources to produce electricity, heat and power. One of the major consumers is the transportation sector.

The transportation sector is 97% dependent on petroleum (oil) and is responsible for most of past and expected future growth of world oil demand [27]. This increasing consumption has placed considerable strain on oil reserves. Moreover, concerns regarding emissions of greenhouse gases, finite sources of fossil fuels and environmental quality have led to an acceleration of efforts to facilitate the development and utilisation of technologies based on alternate sources. It is argued that for the transportation sector, hydrogen offers the most promising long-term alternative as a fuel [1] [4] [80] [84]. The use of hydrogen could diversify the transportation sector concerning primary energy sources since it can be produced, unlike petroleum, from many sources.

Under normal conditions of pressure and temperature, hydrogen is a gas. And due to its low molecular weight, its density is very low (0.08 g/liter). It follows that large volumes are necessary to store only a small amount of hydrogen, which is very inadequate, specially for mobile applications such as hydrogen-

powered vehicles due to restrictive vehicular volume constrains. Thus, one of the most technically challenging aspect of enabling hydrogen-powered vehicles is the onboard hydrogen storage.

Onboard hydrogen storage requires a method to reduce the volume occupied by a certain mass of the gas. In fact, not only the volume must be minimum, but also the weight of the system must be such that it does not adversely affect the design, performance and utility of the vehicle. Further key system requirements include appropriate thermodynamics and energetic efficiency, enough hydrogen supply to enable reasonable driving ranges, short refueling times, capacity to operate and meet power supply demand under dynamic load, long cycle lifetime and safety.

There are various methods and possibilities for storing hydrogen. Current technologies being analysed involve gas compression ($CH_2$), liquefaction ($LH_2$), adsorption on high surface area carbon materials ($AH_2$) and metallic and chemical hydrides [4] [30] [80] [84] [92]. Gas compression and liquefaction belong to the conventional storage methods widely used for gas storage, whereas adsorption and hydrides are novel storage concepts, also known as solid-state storage, in which the tank is filled with a suitable material that can store large amounts of hydrogen under certain conditions of pressure and temperature. Figure 1.1 gives a qualitative assessment of these hydrogen storage technologies in terms of present development status. While some of these methods have already moved beyond the laboratory stage into prototypes or are already commercially available, adsorption systems are still in the basic research. So far, research on this field has been mostly concerned with the search of a suitable adsorbent and improvement of its storage capacity [14] [22] [23] [68]. However, this has been done predicated on the assumption that an adsorbent with high specific volume and adsorption affinitiy will increase storage capacity and therefore improve system performance. Although this is true from a materials science point of view, the engineering of the entire adsorption system have to be carefully analysed before such a system can be built. Too high specific volumes might adversely affect system dynamics and too high adsorption affinity will lead to a large amount of residual adsorbed gas at the depletion pressure and therefore to reduced gas delivery.

Thus, an analysis of the entire operation cycle (adsorption-desorption cycle) under various dynamic conditions is necessary in order to assess the utility of an adsorbent for onboard hydrogen storage.

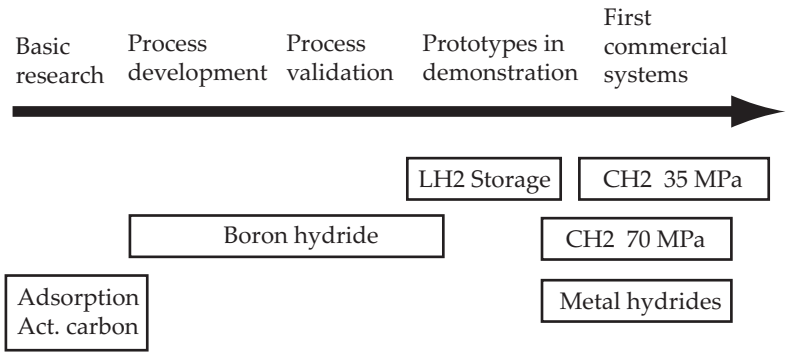


**Figure 1.1:** Status of hydrogen storage technologies [4].

The present study aims to provide new insights into the mechanisms of hydrogen storage and extraction in adsorptive storage devices. With that, system concepts and operation strategies can be devised. The analysis systematically investigates the inhibitory effects to which an adsorption system is subject during charge and discharge and suggests thereby several design concepts in order to minimise their effects and to make the operation of such a system possible. The feasibility of such concepts gives information about the viability of adsorptive storage systems for real technical solutions. The analysis is carried out using numerical models, but is also supported by experimental measurements. The models developed here can also be used in the initial phases of system design and development of any adsorptive system or process in order to evaluate different geometries and system concepts, visualise charge and discharge processes and assist system optimisation.

This introductory chapter continues with a brief discussion on the hydrogen storage methods mentioned above and balance their advantages and disadvantages. The discussion considers that 5 kg of hydrogen (equivalent to 19 liters or 5 gallons of gasoline) are necessary for a general-purpose vehicle since it provides a driving range between 320 and 640 km depending on the vehicle concept [3]. The chapter concludes with a description of the objectives and the chapters of this thesis.

## 1.1 Hydrogen storage methods

Hydrogen storage systems are often characterised in terms of gravimetric and volumetric storage capacities. Gravimetric capacity is mostly given in weight percent (wt%), which consists of the mass of hydrogen the system is able to store compared to the total system mass, including all its components, in percent. Volumetric storage capacity is the mass of hydrogen divided by the total system volume. Concerning solid-state storage, weight percent on a material basis (mat.wt%) can also be found. In this case, the mass of hydrogen is compared only to the mass of material in which it is being stored, not including vessel or components. This is done in order to compare material capacities and because laboratory stage systems do not really correspond to final technical solutions so that only the fundamental system part is considered.

### 1.1.1 Compressed gas storage system

Hydrogen can be stored in gaseous form compressed in tanks. A typical storage pressure is around 350 bar at room temperature. Under these conditions, hydrogen gas has a density of 23.4 g/l. A storage of 5 kg would require a volume of 214 liters only for the gas, not including the vessel, components and mounting devices. Compressed at 700 bar, its density is 39.3 g/l and the required volume would be 127 liters, which is still much larger than a conventional gasoline tank (50-60 liters). Thus, it is difficult to package a $CH_2$ system in a vehicle without compromising its utility. And, if the tank is designed to occupy the volume of a conventional gasoline tank, vehicle driving range is strongly reduced.

Due to the nature of hydrogen, its compression is much more energy intensive than other gas fuels, such a methane. Compressing hydrogen from 1 bar to 350 bar requires about 8-10% of the energy content of the fuel in terms of its high heating value [18]. Compressing it to 700 bar requires about 11-13% of the energy content. The small difference between both compression works is due to the fact that the work depends on the natural logarithms of the pressure ratio.

Filling times of compressed gas systems are not a problem; however, due to the temperature increase during rapid filling, the process must be monitored. In order to obtain temperatures around room temperature within the tank after rapid filling, supply gas cooling in the filling station is required if the tank is not equipped with a heat exchanger. Since no heat supply is required during discharge, discharge rates are not limited.

Storage of hydrogen as a compressed gas is a mature technology. 700 bar tanks are already certified [67]. These tanks use new lightweight materials such as carbon-fiber reinforced materials. Several hydrogen-powered vehicle prototypes utilise this technology for fuel storage [80].

### 1.1.2 Liquid hydrogen storage system

At atmospheric pressure, the saturation temperature of hydrogen is -253°C. Liquid hydrogen density is 70.8 g/l so that 71 liters are necessary to store 5 kg of liquid, a considerably smaller volume than with gas compression. However, the system has to be maintained at -253 °C for hydrogen to be in the liquid state. This requires superinsulation in order to reduce heat leakage and, consequently, boil-off of hydrogen. Superinsulation is very demanding in terms of vacuum inside the insulation space, and it is very expensive.

Heat leakage is the unavoidable heat flow by thermal conduction through the components and mounting devices and thermal radiation and convection through the insulation and external area of the vessel. This heat causes liquid evaporation and, consequently, pressure build up in the vessel so that gas must be vented to relieve pressure. The heat leakage losses are proportional to the ratio surface/volume. It follows that smaller systems for mobile applications have higher heat leakage losses. Heat leakages of 2-3 W are typical for small tanks [70], resulting in a boil-off of about 4-5% per day due to liquid evaporation. In this case, all hydrogen would be vented within 20-25 days of inactivity.

Besides hydrogen losses, further big drawbacks of liquid storage are the energy intensive liquefaction process [18], which can consume at least 35% of

the energy content of the hydrogen, and the necessity of highly centralised liquefaction plants (the bigger the liquefaction plant, the lower is the energy consumption of the process per kg of hydrogen). This obligatorily results in a complex distribution system.

The main directives for research and development on liquid hydrogen storage are on the optimisation of the insulation system and reducing the weight and cost of the tank. High-pressure cryogenic insulated tanks are also been explored. These tanks have the capacity to operate at low temperature (as low as liquid hydrogen temperature) and high pressure (up to 250-300 bar) and can be filled with either liquid hydrogen or compressed gas at any temperature. This hybrid concept significantly minimises or, under certain conditions, even eliminates evaporation losses when filled with liquid hydrogen due to its high pressure capacity and also offers sufficient storage capacity when operated with cold compressed gas. Moreover, if cryogenic hydrogen is not available due to limitations in the hydrogen infrastructure, the vessel can also be fueled with compressed gas at room temperature.

Filling $LH_2$ tanks is not a major challenge; however, the connecting and transfer lines must be cooled to $LH_2$ temperature and venting lines must be provided to capture boil-off gas. In May 1999, the world's first public filling station for liquid hydrogen was taken into service at Munich airport, in Germany. It operates fully automatically. The system delivers about 120 liters of $LH_2$ in a minute and a half. The BMW Hydrogen 7 [12] is a limited production hydrogen vehicle built by the german automobile manufacturer BMW which stores hydrogen in the liquid state. At roughly 17 hours of inactivity, the tank vents hydrogen to avoid pressure build-up. Over 10-12 days, it completely loses the content of the tank.

### 1.1.3 Hydride storage system

Hydride storage refers to the storage of hydrogen in metal hydrides and in chemical storage materials. Hydrides are chemical compounds formed when hydrogen gas reacts with these materials. A large number of hydrides have been investigated [68], and it was shown that hydrogen can be stored re-

versibly in some materials. Reversibility means that hydrogen can be released from the material by raising its temperature. Low-temperature hydrides (LTH), requiring temperatures about 70-100°C, such as LaNi and FeTi have high volumetric hydrogen storage densities (higher than the liquid hydrogen density). In order to store 5 kg of hydrogen, a volume of about 50 liters is necessary. However, their gravimetric storage is very low because about 300 kg of material is required for that (1-3 mat.wt%). Higher gravimetric capacities and volumetric storage densities can be obtained by using high-temperature hydrides (HTH), such as $MgH_2$ and $MgNiH_2$. These materials release hydrogen at temperatures around 300-350°C. In order to store 5 kg of hydrogen around 100 kg of material (4-7 mat.wt%) and 40 liters are necessary. These metrics are significantly better than that of low-temperature hydrides.

All hydrides release large amounts of energy during its formation, i.e., when hydrogen is stored into the material. The same amount of energy is required in order to release the hydrogen stored. Low-temperature and high-temperature hydrides have a heat of absorption of about 12-15 MJ/kg $H_2$ and 25-35 MJ/kg $H_2$, respectively. This makes rapid filling of a storage unit extremely difficult because high energy removal rates are required. For instance, if a hydride unit with a storage capacity of 5 kg of $H_2$ is to be refueled in 5 minutes, a heat removal rate of 250 kW is required (hydride heat of absorption of 15 MJ/kg). If this is waste heat, the impact on the overall efficiency of the system is high. During driving, the heat of absorption has to be supplied to the system in order for hydrogen to be released. However, the energy is to be supplied over longer periods of time and might be obtained from the waste heat of the engine or fuel cell.

Because of their compactness, metal hydride storage systems are proposed for mobile applications. However, the magnitude of the heat of absorption of such systems probably hinders its application. Moreover, such systems are heavy. Prototype vehicles have already been operated using low-temperature hydrides [60]. Liquid coolant from an external source is circulated through the storage system during refueling in order to remove the energy released by the absorption process. During vehicle operation, the storage system is warmed by waste heat from the engine or fuel cell. Hence, at least from a vehicle oper-

| Adsorbent form | - | Powder | | | Pellet | | |
|---|---|---|---|---|---|---|---|
| Adsorbent density | [kg/liter] | 0.3 | | | 0.7 | | |
| Storage pressure | [bar] | 35 | 50 | 100 | 35 | 50 | 100 |
| Gravimetric capacity | [mat.wt%] | 6.9 | 7.6 | 9.4 | 4.1 | 4.4 | 4.8 |
| Volumetric density | [g $H_2$/liter] | 20.7 | 23.0 | 28.2 | 29.0 | 30.7 | 34.0 |
| Material weight* | [kg] | 72 | 65 | 52 | 121 | 114 | 103 |
| Material volume* | [liter] | 240 | 218 | 177 | 172 | 163 | 147 |

*: For storage of 5 kg of hydrogen.

**Table 1.1:** Storage properties of superactivated carbon AX-21™ [14] at a temperature of 77 K for several pressures.

ation point-of-view, the application of hydrides for hydrogen storage is feasible.

### 1.1.4 Adsorptive storage system

In the case of adsorbing storage systems, the hydrogen molecules are bound on the surface of the adsorbing material only by physical adsorption forces, there is no chemical reaction as in the case of hydrides. Therefore, adsorbent materials are generally porous materials because they offer high surface area in the pores for adsorption.

The most promising and investigated materials for hydrogen adsorption are porous carbon adsorbents, such as activated carbon and carbon nanotubes. Studies have shown that high surface area carbons (> 2000 $m^2/g$) may store 5-10 mat.wt% of hydrogen. However, these storage capacities are only observed at low temperatures (77-180 K) due to the weak interaction between hydrogen molecules and the material. At room temperature, their storage capacity drops to about 0.5-1 mat.wt%.

Table 1.1 shows the storage properties of superactivated carbon AX-21™ [14] for several pressures at 77 K. In the form of powder and at a storage pressure of 50 bar, the volumetric storage density is the same as that of compressed gas at 350 bar and room temperature, but the pressure is much lower. The table also shows that the use of adsorbent powder leads to relatively large volumes (low

storage density) due to the low bulk density of the adsorbent. The latter can be increased if the adsorbent is optimised by densification. In this process, adsorbent powder is compressed to form pellets. Although this step decreases the gravimetric storage of the material, the volumetric storage increases [16]. Using pellets at 50 bar, the volumetric storage density considerably exceeds that of $CH_2$ at 350 bar but does not reach that of $CH_2$ at 700 bar.

Sorption processes are accompanied by thermal effects, adsorption being exothermic and desorption endothermic. However, desorption heats of about 3.5 MJ/kg $H_2$ for activated carbon are relatively low compared to that of hydrides, thus leading to a storage system with less energy intensity. Under normal use, $AH_2$ systems are expected to operate within the temperature range of 77 K to 130 K, so that the total energy to be expended during filling consists of the energy used for hydrogen compression to the storage pressure, storage system cooling down (from 130 to 77 K) and adsorption energy removal. This totalises about 8-10 MJ/kg $H_2$ (or 6-8% of the energy content of the hydrogen). These values does not include any losses in the cooling system.

Adsorptive storage systems, as $LH_2$ systems, operate at cryogenic temperatures and so are subject to heat leakage losses. Adsorption systems, however, have a much higher heat capacity than $LH_2$ systems, in which heat leakages lead almost exclusively to liquid evaporation. Hence, losses of $AH_2$ systems occur at a much lower rate. In this thesis, it will be shown that one month of inactivity of a $AH_2$ leads to approximately 35-40% of the initial hydrogen stored mass if the tank is initially full.

## 1.2 Comparison of current hydrogen storage methods

In order to demonstrate viable technologies, the US Department of Energy (DOE) has proposed a set of design targets and goals based on achieving a driving range of 500 km with a hydrogen-powered vehicle as well as consumer expectations and needs, which are based on conventional combustion engine vehicles using gasoline. Table 1.2 shows some of these targets. As typical in the development of new technologies, the targets become increasingly demand-

| Storage parameter | 2005 | 2010 | 2015 |
|---|---|---|---|
| Gravimetric capacity<br><br>(Specific energy) | 0.045 kg $H_2$/kg<br>4.5 wt%<br>(1.5 kWh/kg) | 0.060 kg $H_2$/kg<br>6.0 wt%<br>(2.0 kWh/kg) | 0.090 kg $H_2$/kg<br>9.0 wt%<br>(3.0 kWh/kg) |
| **System weight*:** | **111 kg** | **83 kg** | **56 kg** |
| Volumetric capacity<br>(Energy energy) | 0.036 kg $H_2$/L<br>(1.2 kWh/L) | 0.045 kg $H_2$/L<br>(1.5 kWh/L) | 0.081 kg $H_2$/L<br>(2.7 kWh/L) |
| **System volume*:** | **139 L** | **111 L** | **62 L** |
| Refueling rate | 0.5 kg $H_2$/min | 1.5 kg $H_2$/min | 2.0 kg $H_2$/min |
| **Refueling time*:** | **10 min** | **3.3 min** | **2.5 min** |

**Table 1.2:** DOE technical targets for onboard hydrogen storage systems. (*: for storage of 5 kg of hydrogen.)

ing in the course of time. Technologies that meet these targets are promising candidates for real technical solutions.

Table 1.3 summarises the main characteristics of the storage systems regarding system weight and volume, energy intensity, kinetics, fuel losses and safety as discussed in the previous sections. Figure 1.2 shows graphically the current status of the various hydrogen storage technologies discussed above in terms of gravimetric and volumetric capacities. The DOE targets are also shown. The next paragraphs compare the systems based on figure 1.2 and table 1.3, however not always referring to it. The systems are compared to the DOE targets as well.

$AH_2$ and $CH_2$ storage systems present similar characteristics in terms of system weight and volume. Regarding operating conditions, $AH_2$ systems require, on the one hand, cryogenic temperatures; $CH_2$ systems, on the other hand, very high pressures. Although both systems seem to have the potential to meet the 2010 gravimetric targets, it is not likely that they will ever meet the volumetric targets. The density of compressed hydrogen at 700 bar and room temperature alone is already lower than the 2010 volumetric target. The situation with $AH_2$ systems is not much different, since they yield similar volumetric capacities as $CH_2$ systems. A research field in adsorption aims to increase the storage capacity of adsorbents using dopants [15]. However, such a big im-

| Parameter | Unit | $CH_2$ | $CH_2$ | $LH_2$ | $AH_2$ | $AH_2$ | LTH | HTH |
|---|---|---|---|---|---|---|---|---|
| Operating pressure | [bar] | 350 | 700 | 1 | 50 | 50 | 1-10 | 1-5 |
| Operating temperature | [K] | 300 | 300 | 20 | 80 | 80 | <373 | >573 |
| Syst. gravimet. storage | [wt%] | 6.7 | 6.0 | 7.5 | 5.0 | 3.5 | 1.7 | 5.4 |
| Syst. volumet. storage | [g $H_2$/L] | 20 | 30 | 35 | 20 | 25 | 55 | 52 |
| System weight | [kg] | 75 | 83 | 67 | 100 | 140 | 300 | 92 |
| System volume | [liter] | 242 | 167 | 140 | 250 | 200 | 80 | 95 |
| Charge energy | [MJ/kg $H_2$] | 10 | 12 | 40-70 | 8-10 | 9-11 | 10-12 | 25-35 |
| Discharge energy | [MJ/kg $H_2$] | 0 | 0 | 0.45 | 3.5-4 | 3.5-4 | 10-12 | 25-35 |
| Time for 80% $H_2$ losses | [days] | NA | NA | 10 | >50 | >50 | NA | NA |
| Kinetics | + (good) | + + + | + + + | + | - | - | - - | - - - |
| Safety | - (bad) | - - | - - - | - | - | - | - | - - |

**Table 1.3:** Summary table of current hydrogen storage system characteristics [29] [30] [58] [84]. These values are estimates and may vary for different system configurations.

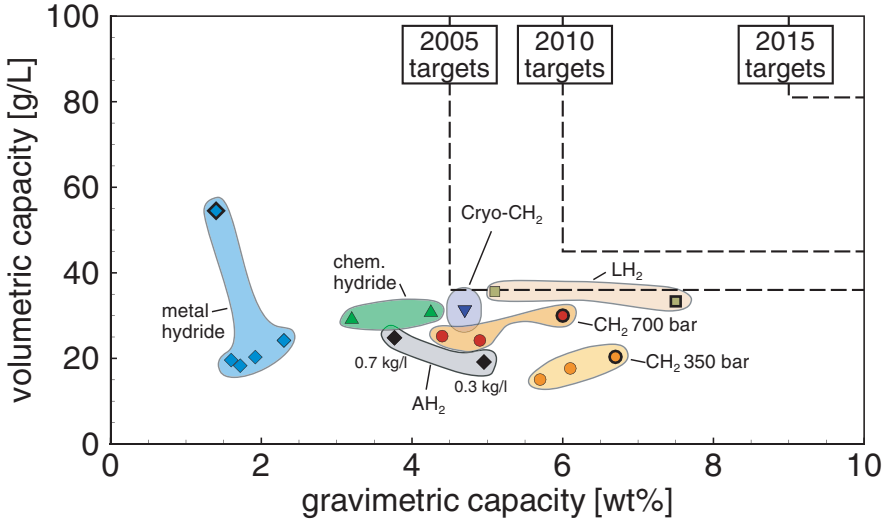


**Figure 1.2:** Status of hydrogen storage technologies [29] [30] [58] and DOE targets [29]. The symbols with bold outline correspond to state-of-the-art technology (table) [58]. These values are estimates and may vary for different system configurations.

provement so as to meet the target is not likely.

The energy intensity of both $AH_2$ and $CH_2$ storage systems are comparable.

$CH_2$ expends energy on compression, $AH_2$ mainly on cooling. $CH_2$ systems do not require thermal management during discharge. $AH_2$ systems, however, require energy removal during fueling due to adsorption thermal effects and energy addition for hydrogen desorption during discharge. In practical systems, waste heat from the fuel cell or combustion engine for hydrogen discharge should be utilised in order to increase system efficiency. However, thermal management might limit system kinetics. Hence, from an operational point-of-view, $CH_2$ systems seem to be more convenient.

Higher volumetric capacities can be achieved with $LH_2$ and hydride systems. Both systems have potential to meet the 2010 targets, but it is not likely that they achieve the 2015 targets. Liquid hydrogen density is alone lower than the 2015 volumetric target. Hydrides offer higher volumetric capacities ( > 0.1 kg $H_2$/liter on a material basis) and could, theoretically, meet the 2015 volumetric targets. However, the material weight hinders the system from achieving the gravimetric targets.

In terms of storage capacities, $LH_2$ and hydride systems are superior to $CH_2$ and $AH_2$ systems. However, $LH_2$ and hydrides are very energy intensive. $LH_2$ systems require energy for hydrogen liquefaction, but not for system operation. Hydrides require energy addition and removal during operation, i.e., charge and discharge. Rapid filling (3 min) require heat removal rates higher than 500 kW so that powerful cooling systems with high energy expenses are necessary. During discharge, the necessity of energy addition might limit system kinetics. A further issue regarding $LH_2$ system is heat leakage losses, which can lead to a complete loss of the stored hydrogen in 10-15 days of inactivity.

The comparison indicates mainly two issues. Comparatively energy efficient systems ($CH_2$ and $AH_2$) yield lower volumetric capacities. Hence, in order for these systems to fit the volumetric constrains of a vehicle, driving range reductions of about 50% are to be expected. Higher volumetric capacities are obtained with $LH_2$ and hydrides systems. However, these systems are very energy intensive. It follows that better energetic efficiency is obtained at the cost of driving range and longer driving range at the cost of energy efficiency. Since higher energy expenses mean higher costs and shorter driving ranges only an inconvenience, relative energy efficient systems seem to be the most satisfac-

tory near term technology. From an operational point-of-view, $CH_2$ systems are more convenient. However, it is too early to dismiss adsorption systems because these still have many unanswered research and development questions. The present study aims to contribute to a better understanding of these systems.

## 1.3 Objectives of this thesis

Within the scope of this study, adsorptive systems for hydrogen storage are investigated. A systematic analysis of these systems is carried out, including the search for the best operating conditions, thermal management, dynamic behaviour, filling times and charge and discharge rates. The detailed description and knowledge of these factors are fundamental for design, optimisation and viability analysis of such systems.

In an adsorption storage system, the tank is filled with an adsorbent material, whose interaction with the gas molecules results in a better packaging of the gas molecules compared with the bulk gas phase under the same conditions. It follows that same storage densities are obtained at much lower pressures. However, the operation of an adsorption system is not as simple as that of a gas compression system. Besides the fact that, at least for the case of hydrogen, viable storage densities for mobile applications are only achieved at cryogenic temperatures, the system is subject to several other inhibitory effects, which determine the time required for charging a cryo-adsorptive system and ultimately limit the maximum hydrogen (or power) output.

Both storage (adsorption) and extraction (desorption) are accompanied by intrinsic thermal effects; adsorption being exothermic and desorption endothermic. These facts, together with the sensitivity to temperature of the storage capacity of the adsorbent, can lead to undesirable effects during operation. During filling under conditions in which the heat of adsorption is not efficiently dissipated, the system heats up. This results in reduced storage capacity due to temperature increase. In a discharge process without energy supply for desorption, the system temperature drops and the adsorbent is able

to retain larger amounts of gas. It follows that the residual amount of hydrogen at the depletion pressure increases and only a small amount of gas can be extracted from the system. Hence, thermal management of an adsorptive storage device is more than just providing optimal insulation for maximum long-term storage.

Furthermore, adsorption systems deal with porous materials. This may increase mass and heat transfer resistances within the storage device and, consequently, limit charge and discharge rates and influence its dynamic behaviour under real conditions.

The main objective of this study is to investigate the influence of these inhibitory effects on the dynamic behaviour of a cryo-adsorptive storage device for hydrogen. In order to be able to perform the analysis, a numerical model of an adsorption storage system will be developed and used to study the system. Modeling, particularly in the initial phases of system design and development, is of key importance because it allows the evaluation of different geometry and system concepts, process visualisation – giving detailed information of the conditions within the system –, analysis of the interaction between processes occurring simultaneously within the system, reduction of the number of lengthy experiments and others. The analysis presented here is also supported by experimental measurements.

The present text is divided as follows. In Chapter 2, basic concepts of adsorption are introduced, which will be used throughout the following chapters. Thereunder, the Gibbs approach for the description of adsorption systems is presented. Chapter 3 addresses the formalism to completely describe an adsorption system thermodynamically. Solution thermodynamics is applied, since it gives relatively simple thermodynamic functions with which energy balances can be easily performed. These functions are valid at any condition of pressure and temperature, even at high pressures, where other theories, such as the surface thermodynamics, fail. In chapter 4, the modeling of adsorption isotherms is presented. Adsorption isotherms are curves that describe the storage capacity of the adsorbent and are the most fundamental information of any adsorption system or process. The model, based on Ono-Kondo lattice theory, is parametrised by means of experimental data over wide

ranges of pressure and temperature. In chapter 5, the thermodynamic functions obtained in chapter 3 are applied to the modelled isotherms of chapter 4 in order to quantify these functions for the gas-adsorbent pair in question. The subject of chapter 6 is the set up of mass and energy balances for the investigation of the dynamic behaviour of an adsorption system during long processes by means of a lumped model (macroscopic balances). The investigation is enriched by also considering other storage technologies under the same conditions of operation. The goal of this chapter is to study the overall changes of extensive quantities of the storage systems without a detailed description of what is happening within them. Such as detailed description is addressed in chapter 7, where general equations of change are adapted for adsorption systems. Since the structure of the adsorbent is very complex and its description is an almost impossible task, the equations of change contain effective transport coefficients with parameters which have to be determined by means of experiments. Chapter 8 introduces these experiments and shows the functionality of the model. An analysis of different filling strategies and cooling concepts is carried out with the model in chapter 9. The conclusions are summarised in chapter 10.

# 2 BASICS OF ADSORPTION

The objective of this chapter is to introduce basic concepts of adsorption, which will be used throughout the text. First, a basic discussion on the interaction forces that cause adsorption of a gas on a surface is given. A detailed theory for this topic can be found in the book by Steele [76]. After that, the Gibbs approach for the description of adsorption systems is presented. This approach treats the adsorbed molecules as a single entity, to which the classical thermodynamic concepts can be applied. Many thermodynamics textbooks use this approach and the ones by Ruthven [65], by Young and Crowell [88] and by Suzuki [77] are suggested for further reading. The chapter ends with the introduction of a widely used porous adsorbent, the activated carbon, which is used in this work as storage medium for hydrogen.

## 2.1 Adsorption

When a gas is brought in contact with a solid surface, the concentration of molecules close to the surface is found to be higher than that in the free gas phase, regardless of the nature of the gas and surface [88]. This is called adsorption.

Forces exist between molecules and their origin lies in the electromagnetic interactions of nuclei and electrons [76]. Adsorption is a consequence of these interactions because the atoms at the surface of a solid (the adsorbent) create a field force which attracts the molecules of the gas (adsorbate). The forces of attraction may be of two main kinds: physical and/or chemical [35]. Chemical adsorption, or chemisorption, involves transfer of electrons between the adsorbent and the adsorbate [35] and will not be considered in this thesis. This thesis deals only with physical adsorption.

The forces involved in physical adsorption include both van der Waals forces, which are intermolecular forces of attraction and become repulsive when atoms come close enough to allow interpenetration of the electron clouds, and electrostatic interactions comprising polarization, dipole and quadrupole interactions [65]. Van der Waals forces are always present, while the further contributions are only significant for certain pairs of gas and solid. In any case, the interaction of an isolated gas molecule with a surface is given by the summation of all individual interactions of each atom of the gas molecule with each atom of the solid structure [35]. This interaction energy can be described with a potential energy function $U(x, y, z)$, where $x$, $y$ and $z$ are the cartesian coordinates of the molecule. Being the $(x, y)$-plane the surface plane, while the $z$-axis is normal to the surface, the general form of $U(z)$ at a given position $(x, y)$ is shown schematically in figure 2.1. The force in $z$-direction is equal to $dU(z)/dz$, where positive values are attractive forces. This force is zero at the minimum of the potential curve, so that the distance $r_0$ corresponds to the equilibrium position of the adsorbed molecule with respect to the surface. The surface attracts the molecule for distances larger than $r_0$ and repels it for distances lower than $r_0$. Generally, $r_0$ is approximately equal to the diameter of the gas molecule [35]. The value of $r_0$ and the minimum of the potential curve may be strongly dependent on the position $(x, y)$ but the general shape of the curve remain unaltered.

The dependence of $U$ on $x$ and $y$ at a given $z$ may exhibit various characteristics depending on the molecular structure of the solid [64]. Figure 2.2 shows qualitative examples for a homogeneous surface, a periodic homogeneous surface and a random heterogeneous surface. The difference $\Delta U^0$ between the energy of a minimum in the three-dimensional function $U(x, y, z)$ and the average energy of molecules in the equilibrium bulk gas phase is the energy of adsorption [64] for that minimum, i.e., it is the energy released by the molecule during adsorption at that minimum. The negative of it, the energy of desorption, is the energy which must be supplied in order to remove the molecule from the solid surface and return it to the gas phase. These minima are usually called adsorption sites. If the energy of the adsorbed molecules considerably exceeds the oscillations in $U$, the potential barrier identified as $\Delta V^0$, they will be able to move freely in the $(x, y)$-plane jumping from one ad-

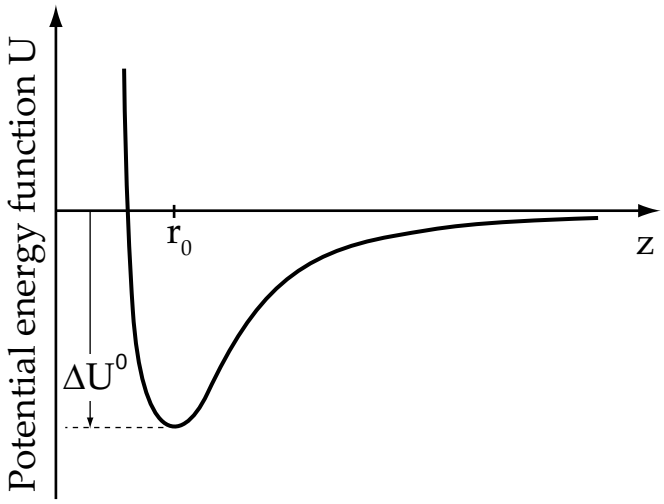


**Figure 2.1:** Potential energy of an isolated molecule with respect to a surface as a function of normal distance $z$ of the molecule from the surface.

sorption site to another, but their motion in the $z$-direction is still restricted as long as they don't acquire enough energy to overcome the energy of adsorption and return to the gas phase. Adsorption in which the molecules retain two translational degrees of freedom is classified as mobile adsorption [64]. On the other hand, if $\Delta V^0$ considerably exceeds the energy of adsorbed molecules, lateral translation is hindered and the molecules are effectively trapped on the adsorption sites. This is called localized adsorption [64]. These concepts are important in order to choose the appropriate theoretical approach to describe processes involving adsorption, as it will be discussed in the next sections.

## 2.2 Adsorption and the Gibbs model

As already mentioned in previous section, a consequence of adsorption is a region near the solid surface in which the local density of the gas is different from that in the adjoining bulk phase.

Figure 2.3a illustrates an adsorption system composed of two macroscopic

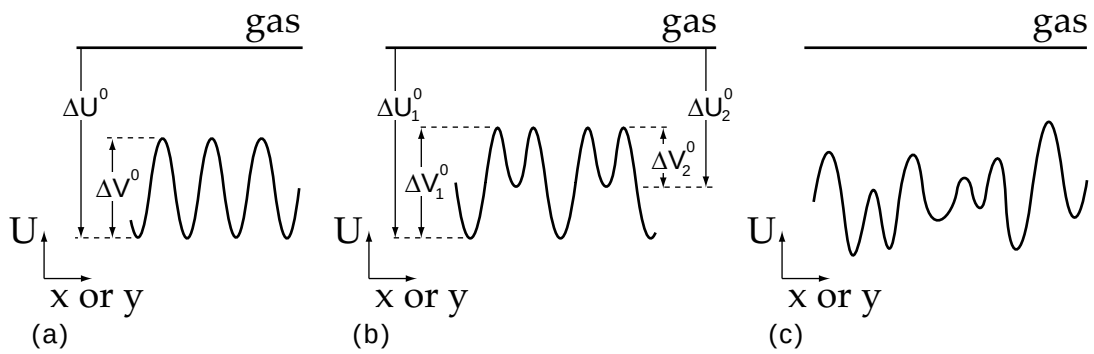


**Figure 2.2:** Variation of the potential energy $U$ across the surface of an adsorbing solid (oscillating curve): (a) homogeneous surface, (b) homogeneous periodic surface and (c) random heterogeneous surface. The average energy level of gas molecules is represented by the straight line. $\Delta U^0$ is the energy of adsorption; $\Delta V^0$ is the potential barrier between adsorption sites.

phases: a gas and a solid phase. Figure 2.3b shows the density profile of the gas at the gas-solid interface. Within the solid, the density $\rho^g$ is zero. Close to the surface the density is not uniform and varies with the distance $z$ from the surface until it reaches a certain distance $D$. At distances larger than $D$, the density is uniform and equal to the bulk gas density $\rho^g$ at same pressure and temperature. $D$ represents the thickness of the interfacial layer and it may extend to several diameters of the adsorbate molecules from the surface [73].

The absolute amount adsorbed $n^a$, which is the amount of gas within the interfacial layer, is obtained from

$$n^a = \int_{V^a} \rho(\vec{\mathbf{r}})\, dV = \int_0^D \rho(z)\, A\, dz, \tag{2.1}$$

where $V^a$ is the volume of the interfacial layer, $\vec{\mathbf{r}}$ is the position vector and $A$ is the surface area of the solid in contact with the gas. The amount adsorbed obviously depends on the thickness $D$. However, $D$ cannot be unequivocally defined because it is not possible to calculate or measure it with today's technology. Moreover, the density profile is also unknown and an experimental method to measure $n^a$ directly does not exist [53]. Thus, $n^a$ is unfortunately an unknown quantity.

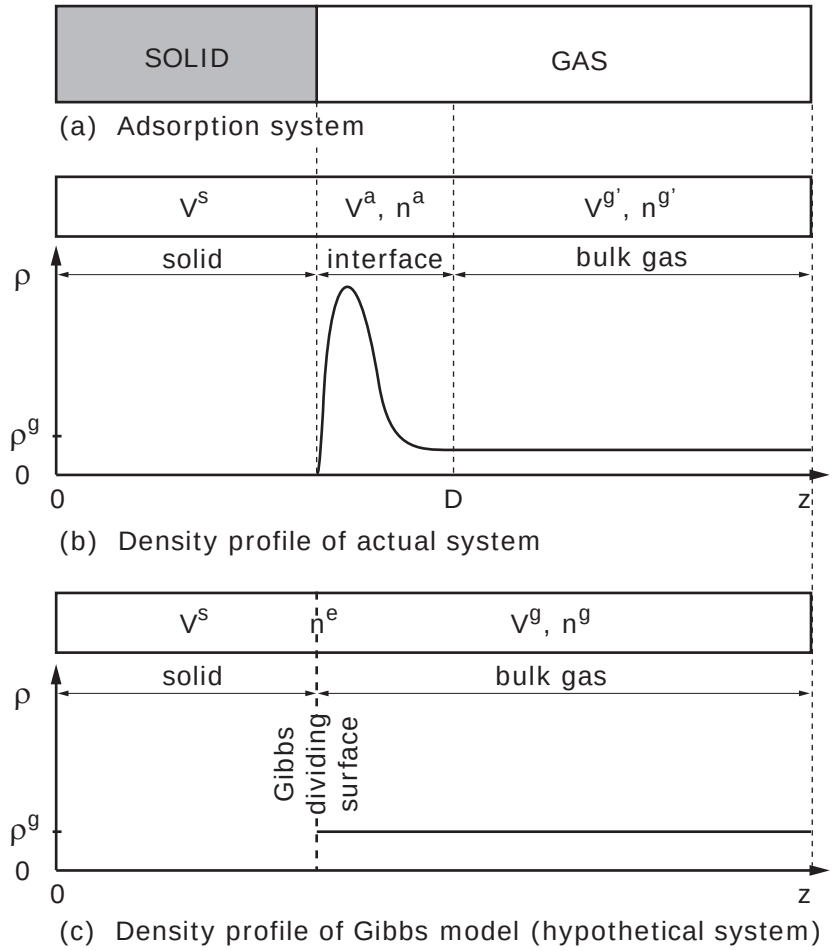


**Figure 2.3:** Schematic representation of the density profile $\rho$ of a gas as a function of height $z$ normal to the phase boundary in a two-phase system (a). The actual profile is shown in (b) whereas the profile according to the Gibbs Model is shown in (c).

In order to circumvent this problem, J. W. Gibbs proposed an elegant model to describe the adsorbed phase without the need to know its size, structure and density profile. Following Gibbs [33], a mathematical surface in the system is to be imagined, called the dividing surface, which gives a precise separation of both gas and solid phases. The surface also divides the whole volume $V$ occupied by the system into two volumes $V^g$ for the gas phase and $V^s$ for the solid phase. Although, from the purely mathematical point of view, the location of the dividing surface is rather arbitrary, for the case of gas-solid interfaces its natural and most convenient location is at the surface of the solid. Still follow-

ing Gibbs, now a hypothetical system is to be imagined composed of the same solid and gas phases, which are, however, both strictly homogeneous right up to the dividing surface. Thus, the gas phase in the volume $V^g$ has a homogeneous density $\rho^g$ right up to the dividing surface. Figure 2.3c illustrates the Gibbs Model, in which the dividing surface is located exactly at the surface of the solid. Comparing the total amount of gas $n$ in the actual system with that in the hypothetical system, it can be seen that the difference can be expressed as

$$n^e \;=\; n^a - \rho^g V^a \;=\; n - \rho^g V^g\,, \tag{2.2}$$

where $n^e$ may be considered as the contribution to the total amount of gas in the actual system due to adsorption. Gibbs called it the surface excess amount and proposed it to be located at the dividing surface in the hypothetical system. The quantity $n^e$ gives the amount of gas adsorbed in excess of the bulk gas which would normally occupy the gas volume at the same pressure and temperature without any adsorption effects. As long as $V^g$ is determined, the quantity $n^e$ can be obtained because $n$ and $\rho^g$ are experimentally measurable quantities.

The idea behind his model is a mathematical transformation in terms of operationally accessible functions because defining surface excess quantities relative to a reference system of homogeneous bulk phases eliminates the thickness problematic in equation 2.1 [36]. Applying his transformation given by equation 2.2 to the volume $V^a$ of figure 2.3a and using equation 2.1 and knowing that $\rho(z)$ for $z > D$ is equal to $\rho^g$ and that $V^a = \int_0^D A\,dz$

$$\begin{aligned} n^e = n^a - \rho^g V^a \;&=\; \int_0^D \rho(z)\,A\,dz - \rho^g \int_0^D A\,dz \\ &=\; \int_0^D \left(\rho(z) - \rho^g\right) A\,dz \\ &=\; \int_0^\infty \left(\rho(z) - \rho^g\right) A\,dz. \end{aligned}$$

As can be seen, the upper integration limit can be set to be infinity since the integrand is zero for $z > D$. Mathematically seen, the adsorbed phase of the Gibbs model is a surface and it does not have a volume [36]. The justification

of placing the dividing surface at the surface of the solid becomes now evident: it yields zero surface excess for the solid [57].

The Gibbs excess concept can be easily extended to adsorption of gas mixtures. In this case the surface excess amount of $i$th component $n_i^e$ is given according to equation 2.2 by

$$n_i^e = n_i - V^g \rho^g y_i \,, \tag{2.3}$$

where $n_i$ is the total amount of component $i$ in the system, $y_i$ its mol fraction in the bulk phase and $\rho^g$ the molar density of the bulk gas mixture. $n_i^e$ is a measurable quantity.

In most of the cases, solid adsorbents used in adsorption processes are of porous nature, since they offer large specific surface area for providing large adsorption capacity [77]. In this case, adsorption occurs inside the adsorbent in macropores, mesopores and micropores. That doesn't hinder the application of the Gibbs excess concept because the dividing surface can be chosen to be a complex three-dimensional structure defined by the internal solid/gas interface of the porous material. The volume $V^g$, called void volume or dead space of the system, includes now not only the volume in the adsorption system external to the porous adsorbent, but also the pore volume of the adsorbent. The only difficulty here is to measure $V^g$. If a non-adsorbing gas existed, the determination of the void volume of a system would be straightforward by the relation $V^g = n/\rho^g$ since the surface excess for the gas would be zero. However, such a gas doesn't exist but helium at low pressure and room temperature is usually considered in good approximation to be a non-adsorbing gas [53] [54] [72] [73].

## 2.3 Adsorption isotherms

The excess amount adsorbed depends on the equilibrium pressure $P$, the temperature $T$, and also on the nature of the gas components and of the solid:

$$n_i^e = f\big(P,\, T,\, \text{gas mixture},\, \text{solid}\big) \,. \tag{2.4}$$

There are many different techniques for the measurement of $n_i^e$ and two of the most frequently used methods are the gravimetric method and the volumetric method. The article by Sircar [73] and references therein give a detailed discussion about the different techniques. For pure gas adsorption on a given solid, the system maintained at a fixed temperature, equation 2.4 simplifies to

$$n_i^e = f(P)_{T,\,\text{gas},\,\text{solid}} \cdot \tag{2.5}$$

Equation 2.5 is the expression of the excess adsorption isotherm, i.e., the relationship between the excess amount adsorbed and the pressure, for a given gas adsorbed on a given solid at a given temperature [35].

A porous adsorbent possesses a finite number of adsorption sites, almost all of which are located within its pores. It follows that there is a maximum number of molecules that can be adsorbed at high pressures. Consequently, the absolute adsorbed amount $n^a$ initially increases with increasing pressure and asymptotically approximates a maximum value. The density of the gas, in contrast, increases monotonically and indefinitely at supercritical conditions. Thus, the excess adsorbed amount $n^e$, according to its definition given by equation 2.2, must have a maximum at the pressure at which the increasing rate of $n^a$ is equal to the increasing rate of $\rho^g V^a$. A further increase in pressure causes a decrease of $n^e$ and it can even become negative.

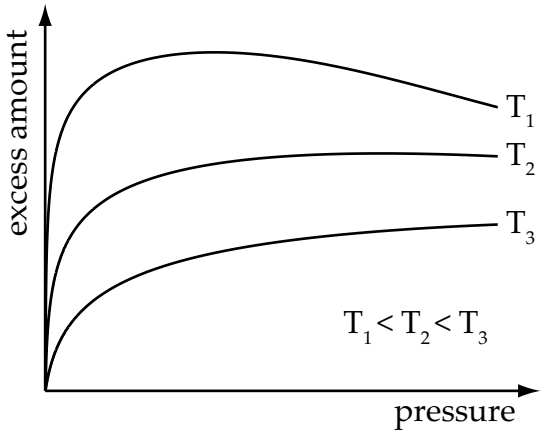


**Figure 2.4:** Excess adsorption isotherms of a pure gas on a microporous adsorbent for supercritical conditions at three different temperatures.

Figure 2.4 shows qualitatively adsorption isotherms of a pure gas on a microporous adsorbent for supercritical conditions. As it can be seen, $n^e$ is not mono-

tonic and this is an important aspect to be considered in describing thermodynamically adsorption systems in the next chapter.

## 2.4 Activated carbon

Activated carbon is a highly microporous adsorbent and so offers extremely high surface area for adsorption. It is normally made by thermal decomposition of carbonaceous material followed by activation with steam or carbon dioxide at elevated temperatures [65]. The activation process involves essentially the removal of tarry carbonization products formed during the pyrolysis, thereby opening the pores.

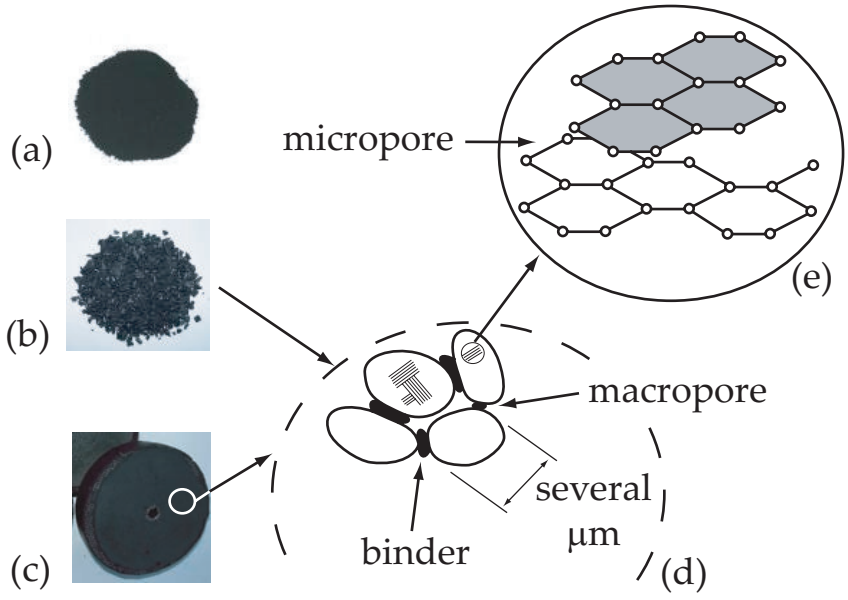


**Figure 2.5:** Forms of activated carbon used for adsorption: (a)-powder, (b)-granules and (c)-pellets. (d)-Schematic representation of the structure of activated carbon pellets or granules. (e)-Turbostratic configuration of graphitic layers.

The structure of activated carbon consists of elementary microcrystallites of graphite. The microcrystallites are stacked together in random orientation and it is the spaces between the crystals which form the micropores [77].

Activated carbon for adsorption is mainly found in two forms: powder form and granular or pelletized form. Activated carbon powder consists of very small grains with diameters going down to 20 $\mu$m, whereas granules or pellets are essentially powder shaped into larger particles using binders [77]. Figures 2.5a-c show the forms of activated carbon discussed here and figure 2.5d shows a schematic representation of the structure of pellets or granules. The macropore volume in pellets and granules is formed by the spaces between the microparticles. Thus, activated carbon has a bimodal (sometimes trimodal) pore size distribution, as shown qualitatively in figure 2.6. The macropore network is desirable since it provides paths for the transport of molecules to the interior through diffusion, improving the kinetics of the adsorption process. On the other hand, the micropore volume is also important, since most of adsorption occurs in the micropores due to their high interaction with the adsorbate molecules. This suggests that a good adsorbent must have a combination of two pore ranges: the micropore range for adsorption and the macropore range for transport.

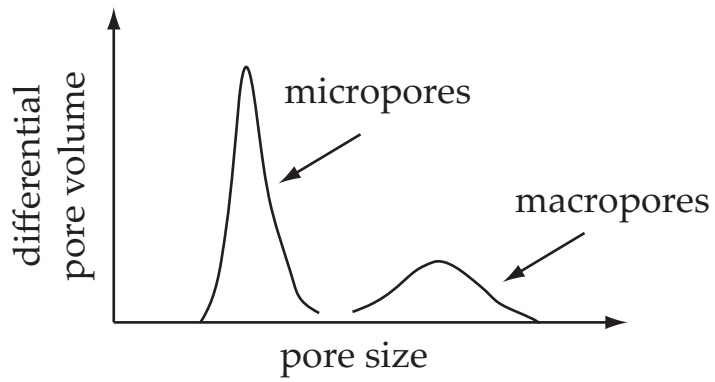


**Figure 2.6:** Qualitative curve for the pore size distribution of activated carbon.

The pore network as well as the microporous structure of activated carbon is very complex so that its description is very complicated. Thus, for studies of adsorption on it, the pores are idealized as to be a slit made of two parallel planes of graphite [45], as shown in figure 2.5e. This allows relatively simple lattice models to be built, as it will be shown in section 4.1.

# 3 THERMODYNAMICS OF ADSORPTION

This chapter is dedicated to summarizing the thermodynamic formalism to describe an adsorption system. It is based on the Gibbs model presented in the last chapter together with the concepts of solution thermodynamics, with the distinction that the solvent is a solid adsorbent. Solution thermodynamics is applied instead of the widely used surface thermodynamics because it offers some advantages concerning adsorption in porous materials. Surface thermodynamics uses variables such as surface area and spreading pressure [88], which are, at least for porous materials, practically impossible to be calculated or measured due to its geometric complexity [53]. Solution thermodynamics, in contrast, offers the possibility to describe the system thermodynamically by means of variables with obvious physical significance while avoiding the undefined variables of surface thermodynamics. Moreover, the latter offers relatively simple thermodynamic functions with which mass and energy balances for adsorption system can be easily performed.

The theoretical development is mainly based on the publications by Myers [53] and by Myers and Monson [54] as well as the ones by Sircar [72] [73].

## 3.1 Surface contribution to thermodynamic quantities

According to the Gibbs model and in much the same way as explained in the previous chapter for the case of the total amount of gas (section 2.2), the contribution due to adsorption to any extensive property is obtained by the difference between that extensive property of the system and that of the hypothetical system of homogeneous phases. In other words, any extensive thermodynamic property of the system can be seen as the sum of three contributions: that due to the solid adsorbent, that due to the gas phase and that due to

the adsorbed phase. Stated mathematically with $Z$ representing any extensive property

$$Z = Z^s + Z^g + Z^e. \tag{3.1}$$

The solid phase contribution $Z^s$ in equation 3.1 is determined from independent measurements of the solid adsorbent in its standard state (clean from any adsorbate). The gas phase contribution $Z^g$ is obtained from

$$Z^g = V^g \rho^g z^g. \tag{3.2}$$

where $z^g$ is the appropriate intensive property. The intensive properties $z^g$ are determined from independent measurements on the bulk gas as well. Specifically, from equation 3.2

$$n_i^g = V^g \rho^g y_i, \tag{3.3}$$
$$U^g = V^g \rho^g u^g, \tag{3.4}$$
$$S^g = V^g \rho^g s^g, \tag{3.5}$$
$$V^g = V^g \rho^g v^g = V^g. \tag{3.6}$$

$Z^e$ is the adsorbed phase contribution, the functions for which will be developed in the next sections. From equation 3.1, for the adsorbed phase

$$n_i^e = n_i - n_i^g, \tag{3.7}$$
$$U^e = U - U^g - U^s, \tag{3.8}$$
$$H^e = H - H^g - H^s, \tag{3.9}$$
$$S^e = S - S^g - S^s, \tag{3.10}$$
$$G^e = G - G^g - G^s, \tag{3.11}$$
$$V^e = V - V^g - V^s = 0. \tag{3.12}$$

which emphasizes that the adsorbed phase is a mathematical plane of zero volume, $V^e = 0$. In equation 3.3-3.12, $U$ stands for internal energy, $H$ for enthalpy, $S$ for entropy, $G$ for Gibbs free energy and $v^g$ for specific volume.

## 3.2 Fundamental relation for energy

In the thermodynamic discussion of bulk phases the fundamental differential equation that summarizes the first and second law of thermodynamics for a system may be written as [75]

$$dU = T\,dS - P\,dV + \sum_{i=1}^{C} \mu_i\,dn_i . \tag{3.13}$$

The intensive variables of the system are the temperature $T$, the pressure $P$ and the chemical potential of each gas component $\mu_i$. The extensive variables are the internal energy $U$, the entropy $S$, the volume $V$ and the total amount of each gas component $n_i$. The summation is over the $C$ gas components.

Equation 3.13 written for bulk solutions can be extended to adsorption by adding a term for the solid adsorbent, which in a sense can be viewed as a solvent [54]. It becomes then

$$dU = T\,dS - P\,dV + \sum_{i=1}^{C} \mu_i\,dn_i + \mu^s\,dm^s , \tag{3.14}$$

where $\mu^s$ is the chemical potential of the solid adsorbent (intensive variable) and $m^s$ its mass (extensive variable). The volume $V$ is in this case the volume of the solid adsorbent, which includes both skeletal and pore volume. It could, if necessary, also include the space in the adsorption apparatus external to the porous material where bulk gas phase is found. If the structure of the adsorbent is assumed to be uniform, its external surface area and consequently its adsorption capacity are directly proportional to its mass, equation 3.14 for the energy has the property of being a homogeneous first-order function of the extensive variables. That is, if all extensive parameters of the system are multiplied by a constant $\lambda$, the energy is multiplied by the same constant

$$U(\lambda\,S,\,\lambda\,V,\,\lambda\,n_1,\,...,\,\lambda\,n_C,\,\lambda\,m^s) = \lambda\,U(S,\,V,\,n_1,\,...,\,n_C,\,m^s) . \tag{3.15}$$

It follows from equation 3.15 and Euler's theorem (section A.1) for homogeneous functions that

$$U = TS - PV + \sum_{i=1}^{C} \mu_i n_i + \mu^s m^s . \tag{3.16}$$

Placing the Gibbs dividing surface at the external surface of the adsorbent as explained in Section 2.2, we can write the fundamental relations for both the homogeneous phases. For the adsorbent in its pure standard state at the equilibrium pressure and temperature

$$dU^s = T\,dS^s - P\,dV^s + \mu^s_{st}\,dm^s, \tag{3.17}$$

$$U^s = TS^s - PV^s + \mu^s_{st} m^s, \tag{3.18}$$

where $\mu^s_{st}$ is the chemical potential of the adsorbent in its pure standard state (clean from any adsorbate). For the gas phase

$$dU^g = T\,dS^g - P\,dV^g + \sum_{i=1}^{C} \mu_i\,dn^g_i, \tag{3.19}$$

$$U^g = TS^g - PV^g + \sum_{i=1}^{C} \mu_i n^g_i. \tag{3.20}$$

According to equation 3.8, given the equilibrium values of pressure and temperature, the energy function of the adsorbed phase is obtained by subtracting from the total energy of the system the energy of the pure adsorbent and the energy of the bulk gas mixture. So, for the integral functions, subtracting equations 3.20 and 3.18 from equation 3.16 and using equations 3.7-3.12

$$U^e = TS^e + \sum_{i=1}^{C} \mu_i n^e_i + \Phi\, m^s, \tag{3.21}$$

where

$$\Phi = \mu^s - \mu^s_{st} \tag{3.22}$$

is called the surface potential [53]. It is defined as the chemical potential of the solid adsorbent relative to its pure standard state. Section 3.6 will show how to calculate the surface potential. The same can be done for the differentials

$$dU^e = T\,dS^e + \sum_{i=1}^{C} \mu_i\,dn^e_i + \Phi\,dm^s. \tag{3.23}$$

Adsorption processes deal with systems such as a packed column or sample cell containing a fixed mass of adsorbent [54] so that the $\Phi\,dm^s$ in equation 3.23 vanishes. Adsorption systems are open to the $C$ adsorbates but

closed with respect to the solid adsorbent. As a result, it is more useful to convert all extensive variables to mass extensive variables, that is, extensive variables per unit mass of adsorbent. Rewriting equation 3.21 and 3.23 for a system containing a constant mass of adsorbent and using mass extensive variables

$$U^e = TS^e + \sum_{i=1}^{C} \mu_i n_i^e + \Phi, \tag{3.24}$$

$$dU^e = T\,dS^e + \sum_{i=1}^{C} \mu_i\, dn_i^e, \tag{3.25}$$

which are the integral and differential equations governing the adsorbed phase. The surface potential term in the integral equation does not appear explicitly in the differential equation.

Note that there has been no distinction between the chemical potential of the adsorbed phase $\mu_i^e$ and the chemical potential in the gas phase $\mu_i^g$. The equality $\mu_i = \mu_i^g = \mu_i^e$ has been used, which is the condition of equilibrium between the adsorbed phase and the bulk gas phase [65]. A difference in chemical potential provides a "potential" for matter flow and in this case the system would not be in equilibrium.

## 3.3 Legendre transformations

The thermodynamic potentials enthalpy $H$, Helmholtz free energy $F$ and Gibbs free energy are obtained by applying the Legendre transformations to the fundamental equation for energy [21]. They are

$$H = U + PV, \tag{3.26}$$

$$F = U - TS, \tag{3.27}$$

$$G = F + PV = H - TS. \tag{3.28}$$

From equations 3.24 and 3.26-3.28, these potentials for the adsorbed phase are

$$U^e = TS^e + \sum_{i=1}^{C} \mu_i n_i^e + \Phi,$$

$$H^e = U^e = TS^e + \sum_{i=1}^{C} \mu_i n_i^e + \Phi, \tag{3.29}$$

$$F^e = \sum_{i=1}^{C} \mu_i n_i^e + \Phi, \tag{3.30}$$

$$G^e = F^e = \sum_{i=1}^{C} \mu_i n_i^e + \Phi. \tag{3.31}$$

The enthalpy is equal to the internal energy because the volume of the adsorbed phase is zero. The Helmholtz and Gibbs free energies are equal for the same reason. Deriving equations 3.29-3.31 and using equation 3.25 it follows that

$$dU^e = T\,dS^e + \sum_{i=1}^{C} \mu_i\,dn_i^e,$$

$$dH^e = dU^e = T\,dS^e + \sum_{i=1}^{C} \mu_i\,dn_i^e, \tag{3.32}$$

$$dF^e = -S^e\,dT + \sum_{i=1}^{C} \mu_i\,dn_i^e, \tag{3.33}$$

$$dG^e = dF^e = -S^e\,dT + \sum_{i=1}^{C} \mu_i\,dn_i^e. \tag{3.34}$$

Note that the potentials introduced here are mass extensive variables.

## 3.4 Integral thermodynamic functions of the adsorbed phase

An important property for energy balances is the enthalpy. The enthalpy of the adsorbed phase, as given by equation 3.29, contains the property entropy, which is obtained from equation 3.34

$$S^e = \left[\frac{\partial G^e}{\partial T}\right]_{n_i^e}. \tag{3.35}$$

However, the use of $n_i^e$ as an independent variable at high pressure fails because pressure is a multivalued function of $n_i^e$ as shown in section 2.3. There

is, nevertheless, a possibility to derive thermodynamic functions for the adsorbed phase which are smooth and well-defined under all conditions and this is the objective of this section. These integral functions have pressure, temperature and molar fractions ($P$, $T$ , $y_i$) as natural independent variables, which is an important feature since they are experimentally controllable variables. The integral functions are defined relative to the perfect-gas reference state at the same temperature and reference pressure $P^o$

$$\Delta G^e = G^e - \sum_{i=1}^{C} n_i^e \mu_i^o , \tag{3.36}$$

$$\Delta H^e = H^e - \sum_{i=1}^{C} n_i^e h_i^o , \tag{3.37}$$

$$\Delta S^e = S^e - \sum_{i=1}^{C} n_i^e s_i^o . \tag{3.38}$$

The quantities $\mu_i^o$, $h_i^o$ and $s_i^o$ refer to the molar values in the perfect-gas reference state at the same temperature and reference pressure $P^o$.

Differentiating equation 3.31, solving for $\Phi$ and substituting equation 3.34 for $dG^e$ gives

$$\begin{aligned} d\Phi &= dG^e - \sum \mu_i \, dn_i^e - \sum n_i^e \, d\mu_i , \\ d\Phi &= -S^e \, dT - \sum_{i=1}^{C} n_i^e \, d\mu_i . \end{aligned} \tag{3.39}$$

Taking the differential changes in equation 3.39 to be changes with respect to temperature at constant pressure and amount of components (which implies at constant molar fractions)

$$\left[\frac{\partial \Phi}{\partial T}\right]_{P,y_i} = -S^e - \sum_{i=1}^{C} n_i^e \left[\frac{\partial \mu_i}{\partial T}\right]_{P,y_i,y_j} . \tag{3.40}$$

Using the quotient rule for derivatives in Calculus it follows that

$$-T^2 \left[\frac{\partial}{\partial T}\left(\frac{\Phi}{T}\right)\right]_{P,y_i} = \Phi - T \left[\frac{\partial \Phi}{\partial T}\right]_{P,y_i} . \tag{3.41}$$

Substituting equation 3.40 and equation 3.31 solved for $\Phi$ into equation 3.41 gives

$$\begin{aligned}
-T^2\left[\frac{\partial}{\partial T}\left(\frac{\Phi}{T}\right)\right]_{P,y_i} &= G^e - \sum_{i=1}^{C}\mu_i n_i^e - T\left(-S^e - \sum_{i=1}^{C} n_i^e\left[\frac{\partial \mu_i}{\partial T}\right]_{P,y_i,y_j}\right), \\
-T^2\left[\frac{\partial}{\partial T}\left(\frac{\Phi}{T}\right)\right]_{P,y_i} &= \overbrace{G^e + TS^e}^{H^e} - \sum_{i=1}^{C} n_i^e\left(\mu_i - T\left[\frac{\partial \mu_i}{\partial T}\right]_{P,y_i,y_j}\right), \\
-T^2\left[\frac{\partial}{\partial T}\left(\frac{\Phi}{T}\right)\right]_{P,y_i} &= H^e - \sum_{i=1}^{C} n_i^e\left(-T^2\left[\frac{\partial}{\partial T}\left(\frac{\mu_i}{T}\right)\right]_{P,y_i,y_j}\right). \qquad (3.42)
\end{aligned}$$

The set of Maxwell Relations for multicomponent systems provides the following equality of derivatives, and using the definition of partial molar entropy for gas mixtures[1] follows:

$$\left[\frac{\partial \mu_i}{\partial T}\right]_{P,n_i^g,n_j^g} = \left[\frac{\partial \mu_i}{\partial T}\right]_{P,y_i,y_j} = -\left[\frac{\partial S^g}{\partial n_i^g}\right]_{P,T,n_j^g} = -\bar{s}_i^g . \qquad (3.43)$$

With this result and using the definition of chemical potential (partial molar Gibbs free energy), the term in parentheses at the right-hand side of equation 3.42 can be written as

$$-T^2\left[\frac{\partial}{\partial T}\left(\frac{\mu_i}{T}\right)\right]_{P,y_i,y_j} = \mu_i - T\left[\frac{\partial \mu_i}{\partial T}\right]_{P,y_i,y_j} = \bar{g}_i^g + T\bar{s}_i^g = \bar{h}_i^g .$$

Substituting it into equation 3.42 and rearranging

$$H^e = \sum_{i=1}^{C} n_i^e \bar{h}_i^g - T^2\left[\frac{\partial}{\partial T}\left(\frac{\Phi}{T}\right)\right]_{P,y_i} . \qquad (3.44)$$

The independent variables of equation are pressure, temperature and molar fractions. From equation 3.28 it follows that

$$G^e = H^e - TS^e . \qquad (3.45)$$

[1] Partial molar properties for component $i$ in a mixture are defined as: $\bar{x}_i = \left[\frac{\partial X}{\partial n_i}\right]_{P,T,n_j}$, where $X$ is an extensive property.

Substituting equation 3.31 and equation 3.44 into equation 3.45 and solving for $S^e$ gives

$$\begin{aligned}\sum_{i=1}^{C}\mu_i n_i^e + \Phi &= \sum_{i=1}^{C} n_i^e \bar{h}_i^g - T^2\left[\frac{\partial}{\partial T}\left(\frac{\Phi}{T}\right)\right]_{P,y_i} - TS^e,\\ S^e &= -\sum_{i=1}^{C} n_i^e\left(\frac{\mu_i - \bar{h}_i^g}{T}\right) - \left[\frac{\partial\Phi}{\partial T}\right]_{P,y_i}. \end{aligned} \tag{3.46}$$

Noting that

$$\frac{\mu_i - \bar{h}_i^g}{T} = \frac{\bar{g}_i^g - \bar{h}_i^g}{T} = \frac{-T\bar{s}_i^g}{T} = -\bar{s}_i^g,$$

equation 3.46 becomes

$$S^e = \sum_{i=1}^{C} n_i^e \bar{s}_i^g - \left[\frac{\partial\Phi}{\partial T}\right]_{P,y_i}. \tag{3.47}$$

Now, substituting equation 3.31 for $G^e$, 3.44 for $H^e$ and 3.47 for $S^e$ into equations 3.36-3.38, the thermodynamic functions for the adsorbed phase become

$$\Delta G^e = \sum_{i=1}^{C} n_i^e(\mu_i - \mu_i^o) + \Phi, \tag{3.48}$$

$$\Delta H^e = \sum_{i=1}^{C} n_i^e(\bar{h}_i^g - h_i^o) - T^2\left[\frac{\partial}{\partial T}\left(\frac{\Phi}{T}\right)\right]_{P,y_i}, \tag{3.49}$$

$$\Delta S^e = \sum_{i=1}^{C} n_i^e(\bar{s}_i^g - s_i^o) - \left[\frac{\partial\Phi}{\partial T}\right]_{P,y_i}. \tag{3.50}$$

## 3.5 Immersion functions

The thermodynamic functions for the adsorbed phase 3.48-3.50 obtained in the previous section show that adsorption may be decomposed into a two-step process:

1. isothermal compression of $n_i^e$ moles of each gas from its perfect-gas reference state at reference pressure $P^0$ to the equilibrium pressure $P$ (given by the first terms on the right-hand side of equations 3.48-3.50) and

2. isothermal, isobaric adsorption immersion of clean adsorbent in the compressed gas ($\Phi$ and its derivatives).

Step 1 depends only on the properties of the bulk gas and the contributions are given by

$$\Delta G^{\text{comp}} = \sum_{i=1}^{C} n_i^e(\mu_i - \mu_i^o) = \sum_{i=1}^{C} n_i^e \left( g_i^R + RT \ln \frac{P y_i}{P^0} \right), \tag{3.51}$$

$$\Delta H^{\text{comp}} = \sum_{i=1}^{C} n_i^e(\bar{h}_i^g - h_i^o) = \sum_{i=1}^{C} n_i^e h_i^R, \tag{3.52}$$

$$\Delta S^{\text{comp}} = \sum_{i=1}^{C} n_i^e(\bar{s}_i^g - s_i^o) = \sum_{i=1}^{C} n_i^e \left( s_i^R - R \ln \frac{P y_i}{P^0} \right). \tag{3.53}$$

The compression terms for the bulk gas are obtained from partial pressures ($P y_i$) and from residual functions ($g_i^R$, $h_i^R$, $s_i^R$) which vanish for a perfect gas [75].

Step 2, immersion of the clean adsorbent, is a physical property of the porous material which deserves to be isolated from the compression step. The immersion function are related to the surface potential by

$$\Delta G^{\text{imm}} = \Phi, \tag{3.54}$$

$$\Delta H^{\text{imm}} = -T^2 \left[ \frac{\partial}{\partial T} \left( \frac{\Phi}{T} \right) \right]_{P,y_i} = \left[ \frac{\partial \left( \frac{\Phi}{T} \right)}{\partial \left( \frac{1}{T} \right)} \right]_{P,y_i}, \tag{3.55}$$

$$\Delta S^{\text{imm}} = -\left[ \frac{\partial \Phi}{\partial T} \right]_{P,y_i}. \tag{3.56}$$

Normally the immersion functions are all negative because adsorption is a spontaneous and exothermic process.

## 3.6 Surface potential

The surface potential has been defined in equation 3.22 as the chemical potential of the adsorbent relative to its pure standard state. However, the most

convenient way to calculate it is using equation 3.39

$$d\Phi = -S^e\,dT - \sum_{i=1}^{C} n_i^e\,d\mu_i\,.$$

At constant temperature and replacing chemical potential by fugacity, this equation reduces to

$$[d\Phi]_T = -R\,T\sum_{i=1}^{C} n_i^e\left[d\ln f_i\right]_T\,, \tag{3.57}$$

where $f_i$ is the fugacity of component $i$ and $R$ is the universal gas constant.

At zero pressure no adsorption occurs, so $\mu^s = \mu^s_{st}$ and the surface potential is zero. Integrating equation 3.57 from the unadsorbed state at zero pressure to the equilibrium pressure $P$

$$\begin{aligned}\int_0^P d\Phi &= -R\,T\sum_{i=1}^{C}\int_0^P n_i^e\,d\ln f_i \ \text{(at constant temperature)}\,,\\ \Phi &= -R\,T\sum_{i=1}^{C}\int_0^P \frac{n_i^e}{f_i}\,df_i \ \text{(at constant temperature)}\,.\end{aligned} \tag{3.58}$$

If measurements of adsorption isotherms are available, the surface potential can be obtained by equation 3.58. $\Phi$ represents the Gibbs free energy change associated with isothermal, isobaric immersion of the clean adsorbent in the bulk fluid (compare equations 3.48 and 3.54). Hence, its absolute value $|\Phi|$ represents the minimum isothermal work required to regenerate the adsorbent [55].

## 3.7 Molar integral functions of the adsorbed phase

The integral functions obtained in section 3.4 are extensive variables per unit mass of adsorbent. They can be converted to molar variables (per unit mol of adsorbate) by dividing each function by the total amount adsorbed $n^e = \sum n_i^e$

$$\Delta g^e = \frac{\Delta G^e}{n^e}\,, \tag{3.59}$$

$$\Delta h^e = \frac{\Delta H^e}{n^e}, \tag{3.60}$$

$$\Delta s^e = \frac{\Delta S^e}{n^e}. \tag{3.61}$$

Equations 3.59-3.61 are defined per mol of adsorbate.

## 3.8 Enthalpy balances

The Gibbs model and solution thermodynamics give the thermodynamic properties of the entire system as the sum over the gas, adsorbed and solid phases. The enthalpy, the most important thermodynamic property for energy balances, is given according to equation 3.1 as

$$H = H^s + H^g + H^e. \tag{3.62}$$

The gas phase contribution $H^g$ can be easily obtained from gas property tables or calculated by means of ideal gas heat capacity curves $c_p^o$ and residual properties (superscript $^R$) [86]

$$H^g = \sum_{i=1}^{C} n_i^g h_i^g = \sum_{i=1}^{C} \left[ n_i^g \left( h_{i,\text{ref}}^o + \int_{T^o}^{T} c_{p_i}^o dT + h_i^R \right) \right]. \tag{3.63}$$

where $T^o$ is the reference temperature and $h_{ref}^o$ is the enthalpy at $T^o$.

The adsorbed phase contribution is obtained according to equation 3.37 which states that the enthalpy of the adsorbed phase is a sum of ideal gas contributions and the integral function given by equation 3.49

$$H^e = \sum_{i=1}^{C} \left[ n_i^e \left( h_{i,\text{ref}}^o + \int_{T^o}^{T} c_{p_i}^o dT \right) \right] + \Delta H^e. \tag{3.64}$$

The solid contribution refers to its properties in its standard clean state at equilibrium temperature and pressure as discussed in section 3.2. This is not an assumption that the solid adsorbent is inert. The changes in the solid properties caused by adsorption are included in the thermodynamic functions for

the adsorbed phase. The enthalpy of the solid adsorbent is given by [86]

$$H^s = H^{s^*}_{\text{ref}} + \int_{T^o}^{T} c_p^{s^*}\, dT + P\, V^s. \tag{3.65}$$

where the asterisk refers to properties of the adsorbent per unit mass in vacuo. The enthalpy $H^{s^*}$ is, in vacuo, equal to the internal energy $U^{s^*}$. If the solid adsorbent is assumed to be incompressible, then $U^{s^*} = U^s$ and the internal energy $U^s$ is a function of temperature only.

# 4 Modeling of Adsorption Isotherms

The design of adsorption based processes and systems requires the characterisation of the behaviour of the adsorption isotherms over a wide range of pressures and temperatures. Moreover, as depicted in the previous chapter, the thermodynamic analysis of an adsorption system from the equilibrium adsorption data using solution thermodynamics requires the calculation of several derivatives of the adsorption isotherms and functions of them, which are only accurate if a very large number of measurements are available. Modeling is in this case a very useful tool because predicting the adsorption isotherms can reduce the number of experiments. Once a suitable model is available, only a small number of experiments are required to parametrise it and then it can be used for design optimisation and studies of dynamic behaviour of the adsorption system.

The literature provides a variety of adsorption models and equations. The most basic approach, the Langmuir theory, describes monolayer adsorption on an ideal surface, completely neglecting interactions between adsorbate-adsorbate molecules. Practical porous adsorbents, due to their complex pore and surface structure, rarely conform to such a simple description so that many semi-empirical approaches have been proposed, for example the Toth equation, the Freundlich equation or the Dubinin-Radushkevich equation (a extensive list of these equations is presented in the books by Do [28] and by Ruthven [65]). In many studies, these equations have been used with success in describing equilibrium adsorption data. However, these approaches fail for a wide variety of gases at high pressures above the critical conditions because they can only be applied over a small temperature range and because they were designed for absolute adsorption isotherms or low-pressure regime.

For the case of adsorption in microporous adsorbents, the most widely used model has been the Dubinin-Radushkevich model and its variants [35]. They

propose the equation

$$a/a_0 = \exp\left[-\left(\frac{R\,T\ln(P/P_s)}{E_D}\right)^2\right] \tag{4.1}$$

where $a$ is the amount adsorbed, $a_0$ is the maximum amount adsorbed (corresponding to filling the entire volume of pores), $P_s$ is the saturation pressure and $E_D$ is a characteristic energy of adsorption. For supercritical adsorption, $P_s$ has no physical interpretation and becomes a purely empirical parameter. Further, the Dubinin-Radushkevich equation does not reduce to the Henry's law[2] as $P$ goes to zero. At the origin ($P = 0$), the slope of the equation is zero, and thus incorrect. This characteristic makes the model unsuitable for calculating the surface potential [78].

A suitable model must have a set of parameters with clear physical interpretation in terms of the thermodynamic properties of the gas-solid system and, for the case of high-pressure excess adsorption isotherms, it must be able to exhibit the maximum of the isotherms. In this work, the Ono-Kondo lattice theory has been used for describing the excess adsorption isotherms due to its excellent capability of representing high-pressure, pure gas adsorption data. This model has already been used with success for adsorption of gaseous adsorbates on activated carbon [5], methane on activated carbon [13] and hydrogen on activated carbon [14]. The next section presents the Ono-Kondo equations adapted for adsorption on microporous adsorbents with slit pores proposed by Aranovich and Donohue [5]. The detailed theory and model development can be found in the books by Ono and Kondo [59] and Rowlinson and Widom [63].

## 4.1 The Ono-Kondo approach

In a lattice model, the fluid system is assumed to be composed of layers of lattice cells that contain fluid molecules and vacancies. In each cell, at most one molecule can be located. For the case of adsorption on activated carbon,

[2]The Henry's law states that the amount adsorbed increases linearly with pressure when the pressure is very low. That is, $n^a = K\,P$, where K is the Henry constant.

the microporous structure of the adsorbent is often described as a slit pore made of two parallel planes of graphite spaced apart by a few molecular diameters [45]. The planes are usually considered large enough to neglect finite-size effects. Thus, the lattice used in the model is formed of layers of hexagonal planes separated by a distance of one adsorbate molecule. The slit pore width is divided into $N$ layers. Figure 4.1 shows a schematic representation of the lattice located between two graphite planes. In the figure, the lattice is composed of 3 layers of cells.

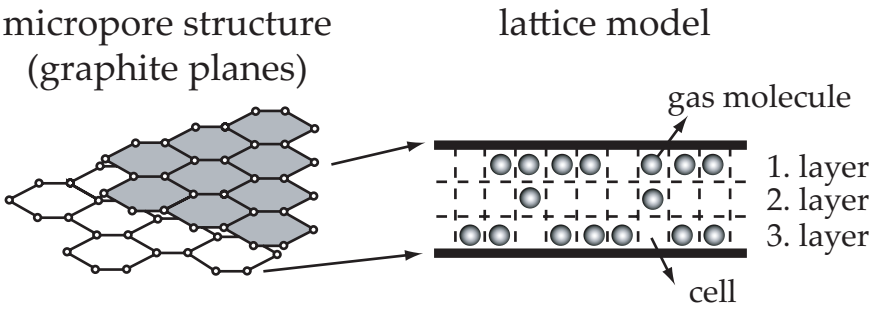


**Figure 4.1:** Schematic representation of the activated carbon microporous structure, described as a slit pore made of two parallel planes of graphite) as well as the lattice model.

Molecular interactions are assumed to exist only between the nearest neighboring molecules and, following Bénard and Chahine [14], monolayer adsorption is assumed, i.e. the effect of the attractive forces between the adsorbent surface and the adsorbate molecules is only felt on the layer nearest to the surface.

The Ono-Kondo equations are a set of coupled self-consistent nonlinear equations that describes the density profile of successive layers of adsorbed molecules in terms of site fraction (fraction of sites or cells in a layer occupied by fluid molecules relative to the total number of cells in that layer). The site fraction $x_i$ on the $i$th layer is related to the molar density $\rho_i$ on the $i$th layer by

the expression

$$x_i = \frac{\rho_i}{\rho_{\mathrm{mc}}} \tag{4.2}$$

where $\rho_{\mathrm{mc}}$ is the molar density at maximum capacity, i.e. the density corresponding to a completely filled layer. The Ono-Kondo equations are expressed as

$$\ln\left(\frac{x_i\,(1-x_b)}{x_b\,(1-x_i)}\right) + z_0\frac{E}{kT}\,(x_i + x_b) + z_2\frac{E}{kT}\,(x_{i+1} - 2x_i + x_{i-1}) = 0\,, \tag{4.3}$$

with the following boundary conditions

$$\ln\left(\frac{x_1\,(1-x_b)}{x_b\,(1-x_1)}\right) + \frac{E}{kT}\,(z_1\,x_1 + z_2\,x_2 - z_0\,x_b) + \frac{E_a}{kT} = 0 \tag{4.4}$$

and

$$x_1 = x_N\,. \tag{4.5}$$

In equations 4.3-4.5, the parameter $E$ is the interaction energy of adsorbate-adsorbate molecules, the parameter $E_a$ is the interaction energy between the adsorbent surface and adsorbate molecules at the surface (interaction with only one pore wall) and $z_0$, $z_1$ and $z_2$ are the coordination number of the lattice. For a hexagonal lattice: $z_1 = 6$, $z_2 = 1$ and $z_0 = z_1 + 2z_2 = 8$. The site fraction $x_b$ is, according to equation 4.2, the bulk molar density divided by the density at maximum capacity. Equation 4.3 describes the density distribution in the slit. Equation 4.4 represents the boundary condition for $i = 1$, where the adsorbate molecules interact with one adsorbent surface, and equation 4.5 comes out of the assumption that the slit pore is composed of two identical parallel graphite planes, i.e., the attraction of one adsorbent surface on layer 1 is the same as the one of the other adsorbent surface on layer $N$.

The excess adsorbed amount, following the concepts presented in section 2.2, is given by

$$n^e = C\sum_{i=1}^{N}(x_i - x_b)\,. \tag{4.6}$$

The prefactor $C$ in equation 4.6 takes into account the density of the active pores of the adsorbent and other structural properties of the adsorbent. A second possibility for defining the excess adsorbed amount is given by

$$n^e = A \sum_{i=1}^{N} x_i - V^g \rho^g \,. \tag{4.7}$$

In equation 4.7, the void volume $V^g$ of the adsorbent explicitly appears as a parameter in the equation and may be treated as a fitting parameter.

## 4.2 The adsorption model and the fit

The adsorption model consists of the Ono-Kondo equations 4.2-4.5 and equation 4.6 or 4.7 for the excess adsorbed amount. The fit procedure explained in this section considers the case in which equation 4.7 is used. However, the same procedure can be carried out if equation 4.6 is used. Thus, the model contains the parameters $N$, $E$, $E_a$, $\rho_{\mathrm{mc}}$ and $V^g$ and the prefactor A. The prefactor is, initially, assumed to be described as a general function of temperature. This function contains $m$ parameters: $A_1$, $A_2$, ..., $A_m$. Accordingly, the set of model parameters becomes: $N$, $E$, $E_a$, $\rho_{\mathrm{mc}}$, $V^g$, $A_1$, $A_2$, ..., $A_m$.

The number of layers $N$ was set to 3, since the pore-volume distribution of the activated carbon used in the experiments determined using density functional theory showed a sharp peak around 12.5 Å with a half-width of about 1 Å and the diameter of $H_2$ molecule is about 2.9 Å [14]. The molar density at maximum capacity $\rho_{\mathrm{mc}}$ may be estimated in various ways. Arri [7] used the saturated liquid density at a defined condition and Hocker, Aranovich and Donohue [6] [37] suggested a theoretical value from close-packed molecules. It has been seen, however, that application of these estimates does not produce optimum fits of the Ono-Kondo model isotherms applied for wide range of temperatures for hydrogen on activated carbon. This has also been observed for other gases, such as nitrogen, and carbon dioxide on activated carbon [32]. Hence, $\rho_{\mathrm{mc}}$ is, like all remaining parameters, treated as a fitting parameter.

In order to best fit the model to experimental data, a fitting error function has to be minimised. This error function $\Psi$ is, in this case, a combination of two

parts: excess adsorbed amount errors and isotherm virial coefficient errors. Mathematically, it is defined as

$$\Psi = \sum_i \sum_j \frac{\left( [n^e]_{i,j}^{\text{exp}} - [n^e]_{i,j}^{\text{mod}} \right)^2}{\left( [n^e]_{i,j}^{\text{exp}} \right)^2} + \sum_i \frac{\left( [B_{AS}]_i^{\text{exp}} - [B_{AS}]_i^{\text{mod}} \right)^2}{\left( [B_{AS}]_i^{\text{exp}} \right)^2} \tag{4.8}$$

in which the index $i$ corresponds to temperature points $T_i$ (adsorption isotherm $i$) and the index $j$ to pressure points. $[n^e]_{i,j}^{\text{exp}}$ and $[n^e]_{i,j}^{\text{mod}}$ are the experimental and model excess adsorbed amount of point $(i, j)$, respectively, and $[B_{AS}]_i^{\text{exp}}$ and $[B_{AS}]_i^{\text{mod}}$ are the second virial coefficient for the $i$th experimental and modelled isotherms (A more detailed explanation of these coefficients is given in section 4.4).

The fit method employed was the one proposed by Nelder and Mead [56], called Nelder-Mead method, simplex method or downhill simplex method. It is a numerical method for minimising an objective function (here, the error function) in a many-dimensional space. This method is implemented in the commercial software MatLab, where the fit was performed, as the function *fminsearch*.

Like all general purpose multidimensional optimisation algorithms, Nelder-Mead occasionally gets stuck in a local minimum that might be far away from the best possible fit. This happens because an objective function with many parameters may have many local minima. Thus, the choice of the initial guess is of crucial importance to successfully find the global minimum. The next section depicts the procedure for estimating an initial guess near the global minimum as well as the definition of an explicit equation for the prefactor.

### 4.2.1 Initial guess and prefactor equation

In order to determine an appropriate initial guess for the fit, error maps were created by systematically varying some parameters. This procedure also made it possible to find an explicit equation for the prefactor. Basically, it consisted of varying the parameters $E$, $E_a$, $\rho_{\text{mc}}$ and $V_g$ within reasonable ranges by a

constant variation step. With each possible combination between the parameter values, the following steps were carried out to calculate the error of the combination:

(a). Using $E$, $E_a$ and $\rho_{\mathrm{mc}}$, solve the Ono-Kondo equations 4.2-4.5 at each experimental point. The bulk gas density is calculated at the same pressure and temperature as the experimental point.

(b). Using $V^g$, the solutions calculated in (a) and equation 4.7, find the prefactor value that best fits each isotherm independently. The error function was defined as in equation 4.8.

(c). Calculate the total error for the combination by summing the errors of all isotherms obtained in (b).

The combination with the lowest error was considered to be the most suitable initial guess for the parameters $E$, $E_a$, $\rho_{\mathrm{mc}}$ and $V_g$ for the final fit. Regarding the equation for the prefactor, step (b) gives the prefactor values at several temperatures. With these data, an equation for the prefactor could be determined. The form of the equation was, *a priori*, not defined and it was tried to use as few parameters as possible.

## 4.3 Experimental adsorption measurements of hydrogen on activated carbon and fit results

Measurements of adsorption of hydrogen on activated carbon were carried out at the Hydrogen Research Institute[3] (IRH) of the University of Quebec - Trois-Rivieres, Canada. The adsorption isotherms were obtained using a standard volumetric approach (see Sircar [73] and references therein for more information on this measurement procedure).

The adsorbent used in the experiments was the superactivated carbon AX-21™ with a specific surface area of 2800 $m^2/g$ and a bulk density

[3] http://irh.uqtr.ca

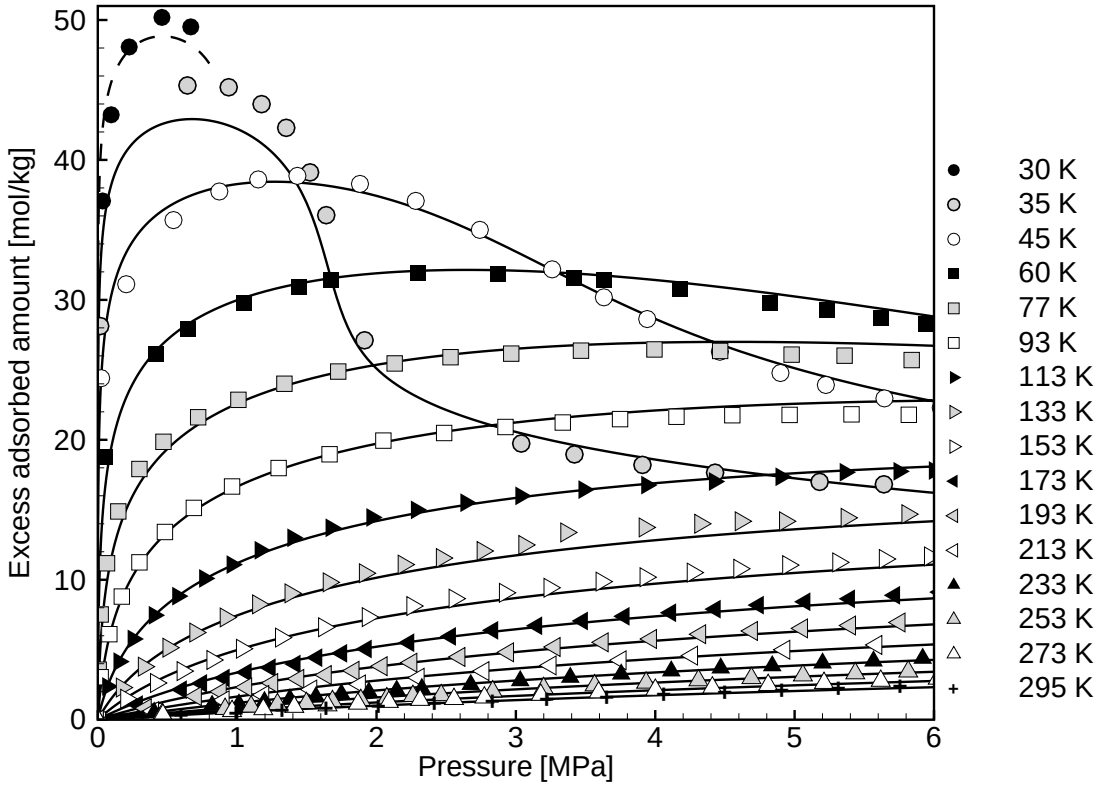


**Figure 4.2:** Excess adsorption isotherms of hydrogen on superactivated carbon AX-21™ from 30 K to 295 K and from 0 MPa to 6 MPa. The points represent the experimental data, the continuous lines represent the isotherms predicted by the parametrisation shown at table 4.1. The dashed line is not predicted by the model.

of 0.3 g/cm$^3$. The adsorbate used was 99.99% pure hydrogen. Adsorption isotherms were measured from 273 K to 93 K by 20 K intervals. Measurements were also made at 77 K, 60 K, 45 K, 35 K, 30 K and ambient temperature. The set of adsorption isotherms from 77 K to 295 K has been first published by Bénard and Chahine [14]. The isotherms below 77 K were measured at a later time and the modeling of the whole temperature range going from 35 K to 295 K was carried out in this work. The fit yielded the model parametrisation shown in Table 4.1. The fit used equation 4.6 for describing the excess adsorption isotherms. The prefactor could be fitted to the simple function:

$$C(T) = C_1 \left(1 - e^{-C_2/T}\right). \tag{4.9}$$

A further model parametrisation obtained in this work, but using equation 4.7 for describing the excess adsorption isotherms, has been published by Bénard *et al.* [15]. Figure 4.2 depicts the excess adsorption isotherms, represented by the points, and the modeled isotherms, represented by the continuous lines.

| Parameter | Unit | Value |
|---|---|---|
| $E$ | kJ/mol | 0.4145 |
| $E_a$ | kJ/mol | -3.7741 |
| $\rho_{\mathrm{mc}}$ | mol/l | 49.426 |
| $C_1$ | mol/kg | 25.71 |
| $C_2$ | K | 125.68 |

**Table 4.1:** Adsorption model parametrisation.

At low temperatures, the maximum of the isotherms can be clearly seen. This feature is characteristic of excess adsorption isotherms, as explained in section 2.3. The model successfully reproduces the maxima of the isotherms. The isotherm at 30 K stops at 0.8 MPa because condensation occurs. The isotherms are fully reversible and present no hysteresis. The pressure corresponding to the maximum increases with temperature. The excess isotherms intersect, so that on each isotherm curve there exists a pressure at which a differential increase in temperature doesn't change the excess amount, i.e., the derivative of the excess amount with respect to temperature is equal to zero. The isotherms also show that hydrogen adsorbed densities for storage applications can only be achieved at low temperatures. At ambient temperature, only small quantities of hydrogen can be adsorbed due to its weak interaction with carbon [8].

## 4.4 Gas-surface virial expansion

The adsorption second virial coefficient was used as a part of the error function 4.8. This section shows how it is determined.

The gas-surface virial expansion theory [24] [76] expresses the excess adsorption isotherm as

$$n^e = B_{AS}\left(\frac{P}{RT}\right) + C_{AAS}\left(\frac{P}{RT}\right)^2 + D_{AAAS}\left(\frac{P}{RT}\right)^3 + \ldots \tag{4.10}$$

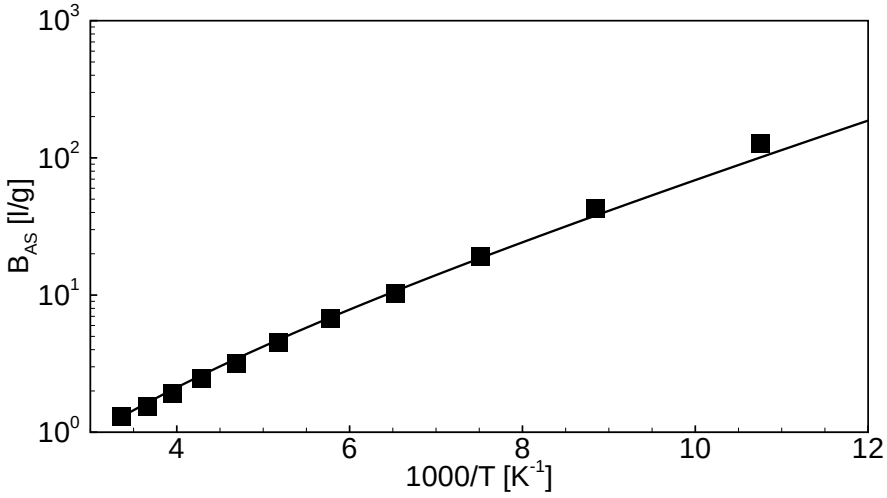


**Figure 4.3:** Variation of gas-solid virial coefficient with temperature of experimental (points) and model isotherms (line).

where the coefficients of $\left(\frac{P}{RT}\right)^n$ are called the gas-surface virial coefficients. In order to compute them, it is necessary to have explicit expressions for $U_s(\mathbf{r})$, the interaction potential of a molecule with the solid surface and for $U(\mathbf{r}_i, \mathbf{r}_j)$, the pairwise interaction of gas molecules with each other. The coefficient $B_{AS}$ can also be obtained experimentally from isotherms. For that, plots of excess volume $V_{ex} \equiv n^e RT/P$ versus $P$ are necessary. Equation 4.10 shows that

$$\lim_{P \to 0} V_{ex} = B_{AS} \tag{4.11}$$

The coefficient $B_{AS}$ was calculated for each experimental isotherm between 77 K and 298 K and the results are shown in figure 4.3. The isotherms below 77 K were not included because they are very steep at low pressure region and there are not enough experimental points in this region for an accurate calculation. The line in figure 4.3 represents the variation of $B_{AS}$ with temperature obtained with the model. Good agreement with the experimental points can be seen.

## 4.5 Adsorbent densification

The adsorption capacity of a porous adsorbent depends on many factors and its surface area plays an important role [66]. Activated carbon in powder form presents very high surface area per unit mass of material, however, due to its low bulk density, a relatively low storage density is achieved because the surface area per unit volume is low. The process of densification (compressing powder into pellets - see section 2.4) increases the adsorbent bulk density in order to increase the adsorption capacity per unit volume. Although this process might also decrease the surface area per unit mass, higher volumetric storage densities are achieved due to the higher bulk density of the adsorbent.

Bénard and Chahine [14] compared the excess adsorption isotherm at 77 K obtained with activated carbon powder AX-21™ (section 4.3) with the one obtained with pelletized AX-21™. The comparison showed a constant ratio (equal to 1.47) between the excess adsorbed amounts for the whole pressure range investigated (see figure 4.4a). The difference in the adsorption properties is fully accounted for by the changes in the specific surface area caused by densification [14], suggesting that the Ono-Kondo parametrisation for activated carbon powder obtained in section 4.3 can be applied to pelletized carbon once the model prefactor $C_1$ is corrected by the ratio of the specific surface areas. Thus, whenever pellets are used in the calculations in the next chapters, the model prefactor is corrected by a factor of 1.47 in order to account for the densification. This method is applied since the characterisation of the adsorption isotherms of densified AX-21™ over a wide range of temperature is not available. Table 4.2 shows the physical properties of both powder and pellet AX-21™ (according to Bénard and Chahine [14]).

The gravimetric excess storage capacity of pellets is lower than that of powder (figure 4.4a). However, its volumetric excess storage capacity (figure 4.4b) is higher since the density increase ratio due to densification (0.7/0.3 = 2.33 - see table 4.2) is higher than the specific area decrease ratio (1.47). This results in a volumetric excess storage increase of approximatelly 60% (2.33/1.47 = 1.59). But, since densification also decreases the bulk gas volume within the adsorbent, the absolute volumetric storage increase is around 20%, as it will be dis-

cussed in chapters 8 and 9.

| Property | Unit | Powder | Pellet |
|---|---|---|---|
| Bulk density | $g/cm^3$ | 0.3 | 0.7 |
| Surface area per unit mass | $m^2/g$ | 2800 | 2000 |
| Surface area per unit volume | $m^2/cm^3$ | 840 | 1400 |

**Table 4.2:** Physical properties of superactivated carbon AX-21™ in powder and pelletized form.

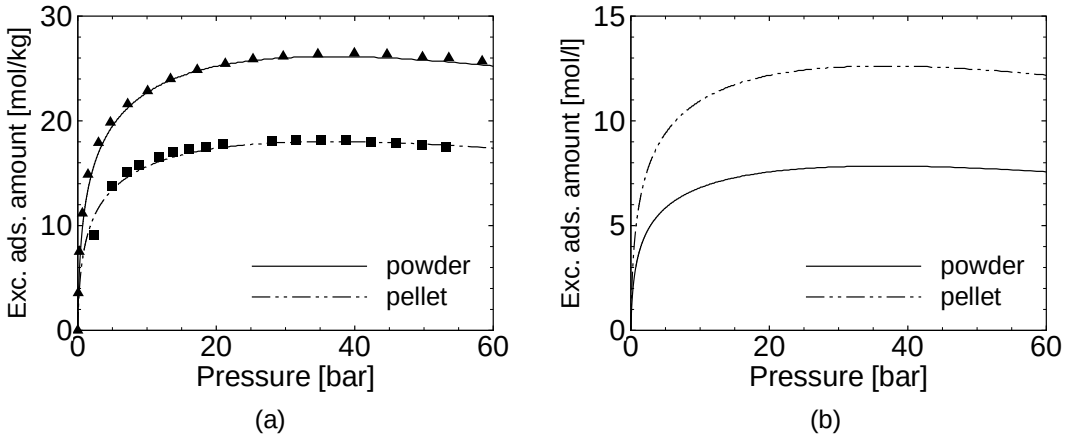


**Figure 4.4:** Excess adsorption isotherms at 77 K of superactivated carbon AX-21™ in powder and pelletized form on a gravimetric (a) and volumetric (b) base. In (a), the powder curve is obtained by the model presented in section 4.3 whereas the pellet curve is obtained by scaling the powder curve according to their specific surface area ratio. The points represent experimental data. The volumetric isotherms in (b) are obtained by multiplying the gravimetric isotherms by the respective adsorbent bulk density given in table 4.2.

## 4.6 Conditions for adsorptive storage

The performance of hydrogen adsorption systems must be carefully analyzed in order to define the operating conditions. The absolute storage capacity of

such systems undergoes a dramatic decrease with increasing temperature. At room temperature, the absolute storage capacity per unit volume can be even lower than that of a bulk gas storage because the adsorbed amount doesn't compensate the loss of volume caused by the presence of the adsorbent. Multiplying equation 2.2 by the bulk density of the adsorbent $\rho^s$, the hydrogen storage density $\rho_{H_2}$ for adsorption storage systems may be written as

$$\rho_{H_2} = \rho^s n^e + \varepsilon \rho^g , \tag{4.12}$$

$$\varepsilon = 1 - \frac{\rho^s}{\rho^s_{esk}} , \tag{4.13}$$

where $\varepsilon$ is the adsorbent porosity and $\rho^s_{esk}$ is the adsorbent skeleton density ($\rho^s_{esk} = 2.3$ g/cm$^3$ for graphite).

Figure 4.5 compares the hydrogen storage density of an adsorption system filled with pellets with that of a compressed gas system ($\rho_{H_2} = \rho^g$) for various temperatures as a function of pressure. As can be seen, the advantages of adsorption are pronounced only at low temperatures. At room temperature, the systems exhibit almost no storage difference. At 77 K, for instance, the advan-

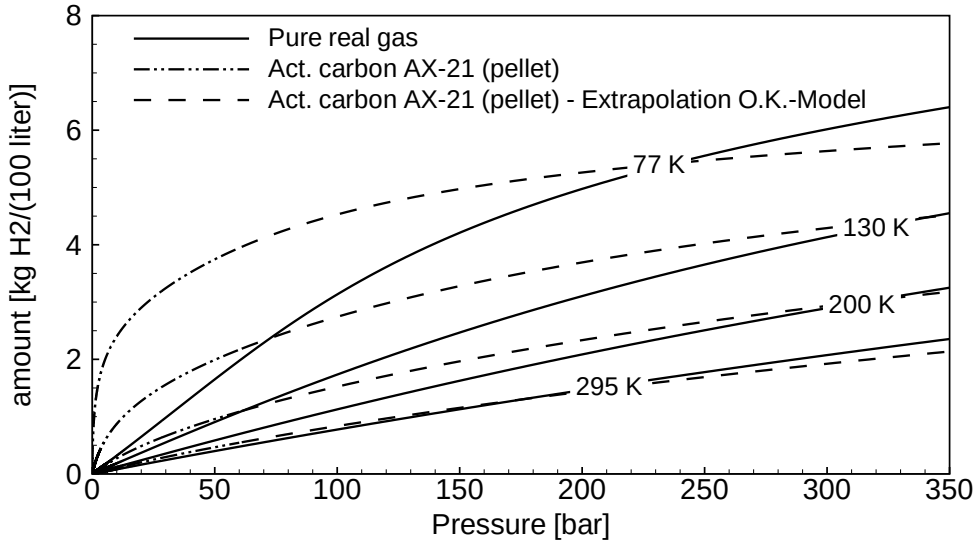


**Figure 4.5:** Hydrogen storage capacity as a function of pressure for various temperatures. Comparison between adsorptive (on AX-21 pellets) and compressed gas storage.

tage of using adsorption is clearly seen. At low pressures, its storage capacity increases much steeper with pressure than that of a compressed gas system. At 30 bar and 77 K, activated carbon AX-21 in pelletized form has a hydrogen storage density 3.23 higher than just compressed gas (4.41 at 20 bar and 7.5 at 10 bar). However, compressed gas storage systems are more likely to operate at room temperature and very high pressures so that the major advantage of adsorption systems over compressed gas systems is the considerable storage pressure reduction. This directly translates to a safer system. Though, temperature reduction alone doesn't improve the effectiveness of adsorption systems because that may decrease its net storage capacity. Normally, adsorption vessels are to work within two limits of pressure: the depletion pressure $P_{\mathrm{d}}$ and the storage pressure $P_{\mathrm{st}}$. Under isothermal conditions, the quantity of gas that can be released from the vessel is the difference between the total stored quantity at $P_{\mathrm{st}}$ and $T$ and that at $P_{\mathrm{d}}$ and $T$. This quantity is called delivery and can be mathematically expressed as

$$D = m^s \left( n\left(P_{\mathrm{st}}, T\right) - n\left(P_{\mathrm{d}}, T\right)\right), \tag{4.14}$$

where $n$ is the absolute stored amount and is given by equation 2.3. Figure 4.6 shows the delivery of a unit amount of mass of a pellet-like adsorbent as a function of temperature for four values of storage pressure: 10, 20, 30 and 40 bar. The depletion pressure is set to 1 bar. The solid lines show the total delivery $D$, which is the sum of the delivery from excess adsorption (dot-dashed lines) and that from the bulk gas in the void volume (dashed lines). The latter monotonically increases with decreasing temperature because the gas density is inversely proportional to temperature. The excess delivery, in contrast, initially increases with decreasing temperature, reaches a maximum and then starts to decrease. These curves show maxima lying within 80 K and 100 K, depending on the storage pressure. The presence of maxima on the excess delivery curves is mainly due to two factors: saturation behaviour of the isotherms at low temperatures and high pressures and steep increase of the isotherms at low temperatures and low pressures. In addition, it can also be seen that the higher the storage pressure, the lower is the improvement of the excess delivery. The total delivery curves have a similar behaviour, except to the fact that the bulk gas delivery moves the maxima of the curves towards lower temperatures. Based on these curves, it is clearly seen that the optimum storage

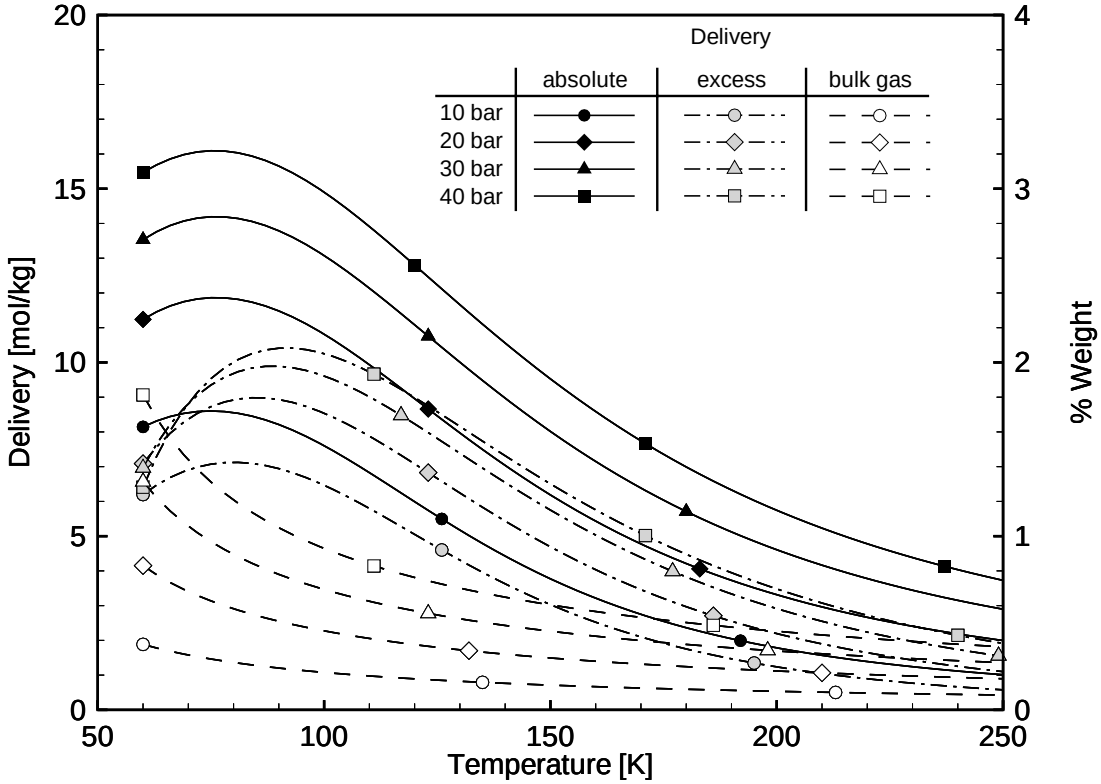


**Figure 4.6:** Absolute, excess and bulk gas delivery of a AX-21™ pellet as a function of temperature for various pressures.

temperature should lie within 80 K and 100 K.

From the above discussion, it is evident that improving the storage capacity of the adsorbent in isolation doesn't necessarily lead to higher delivery because a considerable amount of gas might still be retained in the system at the depletion pressure. Thus, an analysis of the entire adsorption-desorption cycle is required in order to assess the utility of an adsorbent for storage [45].

# 5 Thermodynamics of Adsorption Applied to Hydrogen on Activated Carbon

In chapter 3, the thermodynamic functions for description of gas adsorption in porous materials were presented in terms of solution thermodynamics and, in chapter 4, a model based on the lattice gas theory was employed for the prediction of adsorption equilibria of hydrogen on activated carbon. This chapter addresses the application of the solution thermodynamic functions to the predicted isotherms in order to quantitatively evaluate the thermodynamic functions needed for the description of an adsorption system. Specifically, the text will concentrate on enthalpy related functions, which are required for energy balances of an adsorption system. The other functions, such as the ones related to entropy required for calculation of lost work and efficiency, will not be considered but can be obtained in much the same way.

The adsorption model presented in chapter 4 doesn't consist of an analytical equation but rather a system of nonlinear equations that has to be solved at each point of interest. Thus, the integrations and derivations carried out in this chapter have to be done with numerical techniques [83].

Besides information about adsorption equilibria, the description also requires the bulk properties of the gas. These can be determined from independent PVT measurements and have no relation with adsorption itself. For hydrogen, the properties were calculated with very accurate equations proposed by Younglove [89].

## 5.1 Surface potential

The most convenient route for calculating the excess functions is through the surface potential by integrating the isotherms according to equation 3.58. The surface potential at several temperatures is shown in figure 5.1. The surface

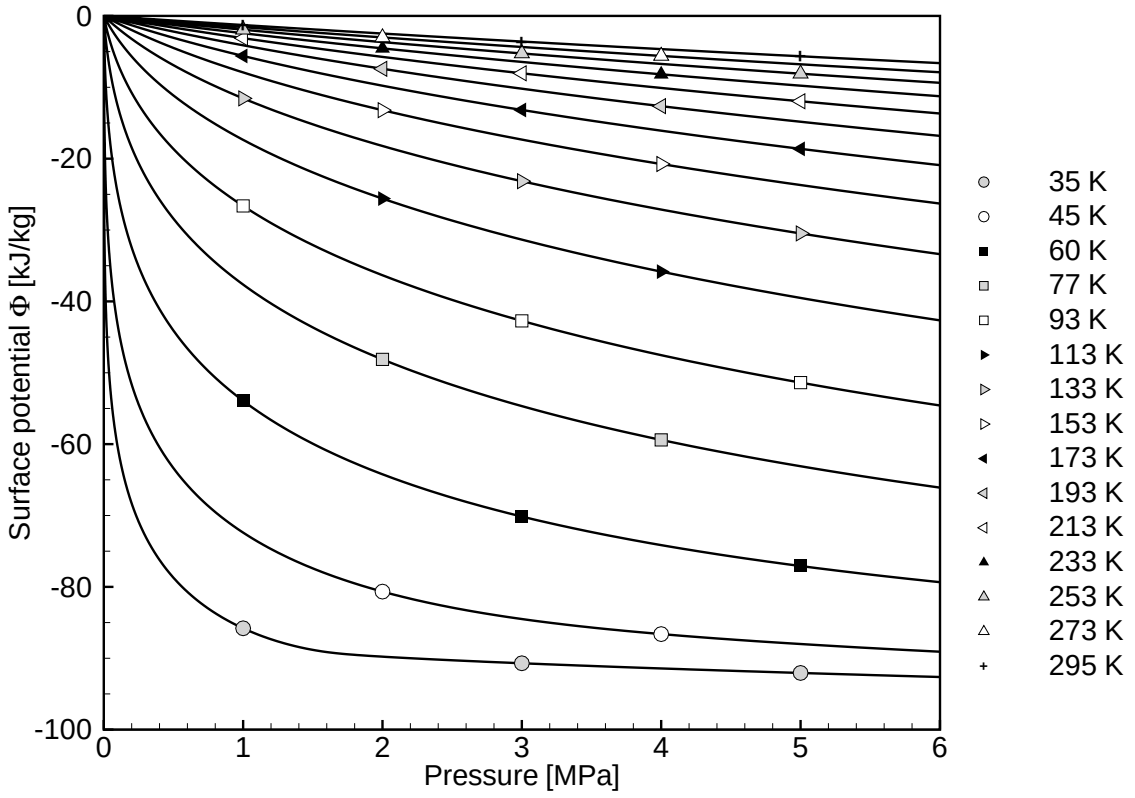


**Figure 5.1:** Surface potential for adsorption of hydrogen on activated carbon at several temperatures.

potential is negative in sign because adsorption is a spontaneous process. Physically, the surface potential is the free energy of formation of an adsorption system [55]. It is worth to remember that all extensive properties are defined per unit mass of adsorbent.

## 5.2 Enthalpy of immersion and integral enthalpy

The immersion functions are the terms related to adsorption in the integral functions for the adsorbed phase. They are simply related to the surface potential by the equations 3.54-3.56. The integral functions (equations 3.48-3.50) have, in addition, terms related to bulk gas compression. Specifically, the enthalpy of immersion and the integral enthalpy of the adsorbed phase differs only by the quantity $n^e h^R$ in the case of one-component gas. This term vanishes for an ideal gas.

The enthalpy of immersion and the integral enthalpy are shown in figure 5.2 and 5.3, respectively. Due to the moderate conditions of pressure and low temperatures used for adsorption storage, the ideal gas assumption cannot be accepted and the two functions differ. Again, they are defined per unit mass of adsorbent.

The physical significance of these functions can be better understood by considering the formation of an adsorption system. This can be conceptually achieved by contacting $n$ moles of gas at pressure $P$ and temperature $T$ with a unit amount of clean adsorbent in an evacuated and thermostated chamber fitted with a frictionless piston, as illustrated in figure 5.4. This chamber is connected to a gas reservoir at $P$ and $T$ through a valve, which is initially closed. When the valve is opened, gas comes into contact with the adsorbent and adsorption occurs. The piston position can be adjusted so that the bulk gas phase is always found at pressure $P$.

A mass balance gives that

$$n^g_{\text{initial}} = \left(n^g + n^e\right)_{\text{final}}. \tag{5.1}$$

The initial and final enthalpy of the entire system can be, according to section 3.8, expressed as

$$H_{\text{initial}} = n^g_{\text{initial}} h^g + H^{s^*}, \tag{5.2}$$

$$H_{\text{final}} = n^g_{\text{final}} h^g + H^{s^*} + P\,V^s + n^e_{\text{final}} h^o + \Delta H^e, \tag{5.3}$$

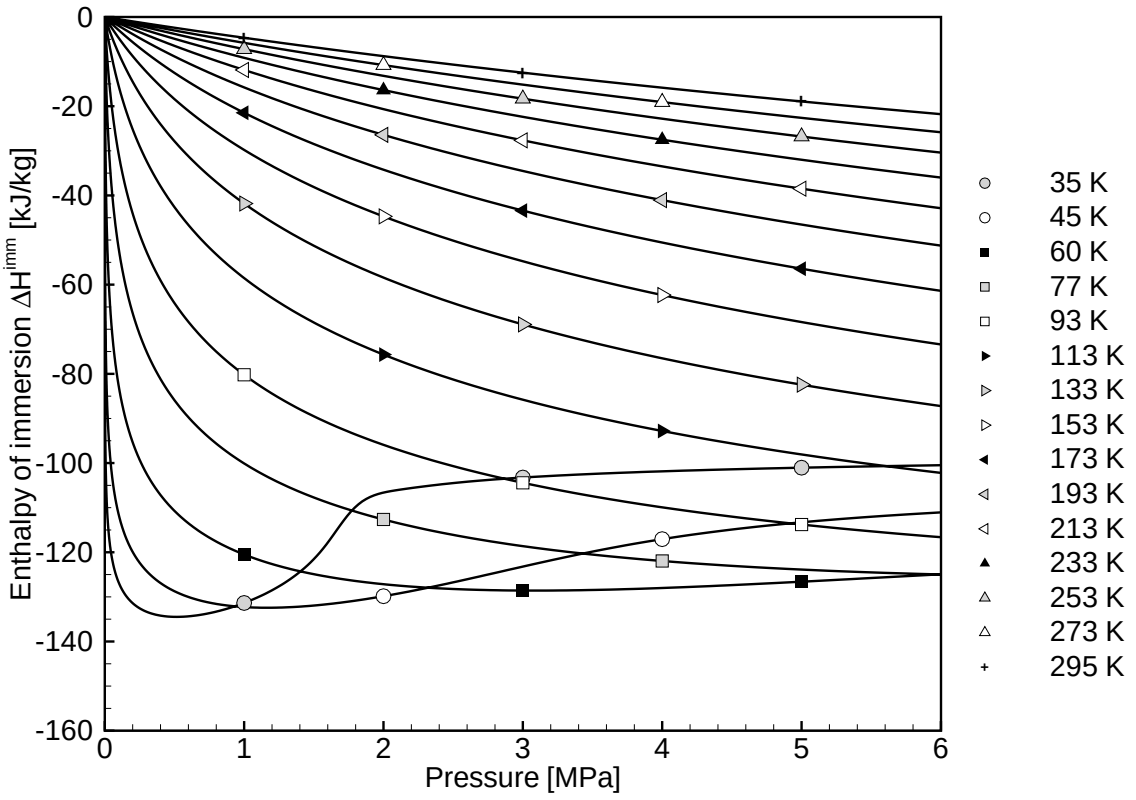


**Figure 5.2:** Enthalpy of immersion for adsorption of hydrogen on activated carbon at several temperatures.

so that the change in enthalpy $\Delta H$ for the formation of the adsorption system is

$$\Delta H = H_{\text{final}} - H_{\text{initial}} = \Delta H^{e} - n^{e} h^{R} + P\,V^{s} = \Delta H^{\text{imm}} + P\,V^{s}\,. \tag{5.4}$$

For the case of low pressure, the term $PV^s$ may be ignored and the residual gas enthalpy is approximately zero so that the integral functions $\Delta H^e$ and $\Delta H^{imm}$ are the isothermal enthalpy of formation of the adsorption system.

Applying the first law of Thermodynamics [21] to this system, it can be shown that the net amount of energy $Q$ to be removed from the system during the formation of the adsorption system in order to keep temperature constant can be expressed as

$$Q = \Delta H^{e} - n^{e} h^{R} = \Delta H^{\text{imm}} = \Delta H - P\,V^{s}\,. \tag{5.5}$$

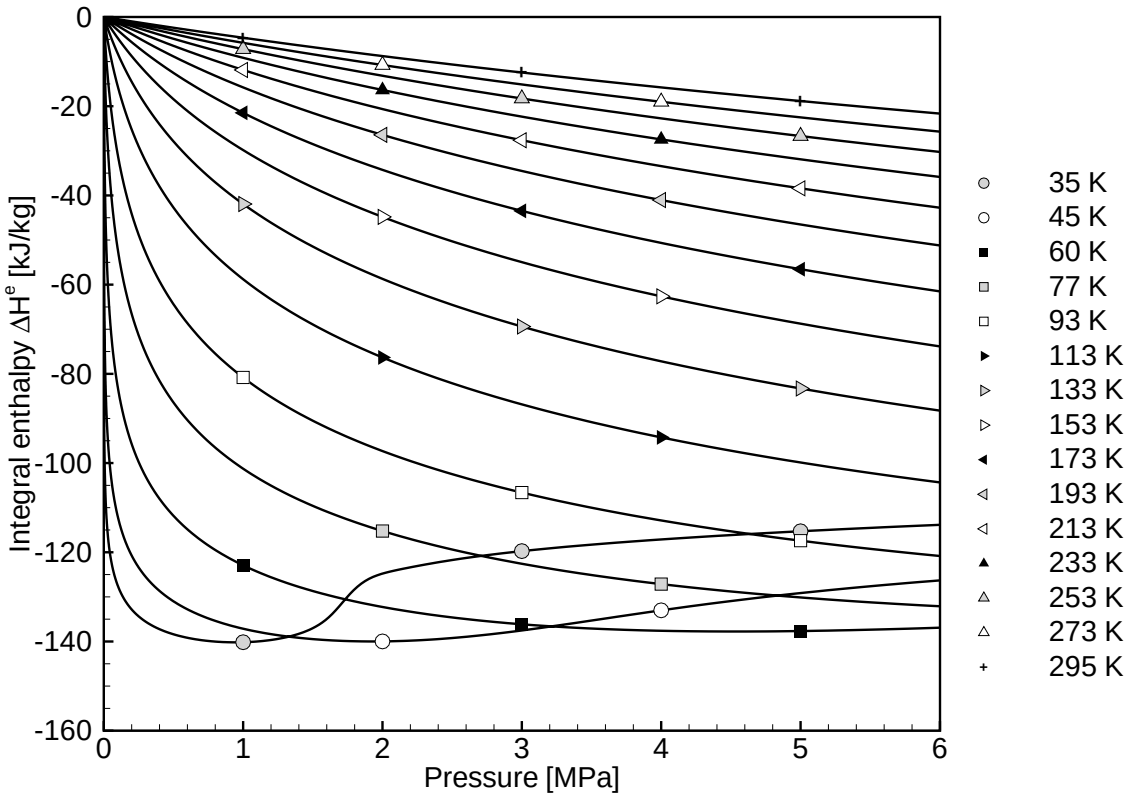


**Figure 5.3:** Integral enthalpy of the adsorbed phase for adsorption of hydrogen on activated carbon at several temperatures.

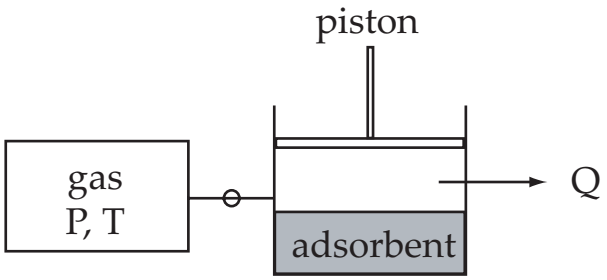


**Figure 5.4:** Schematic diagram of the process of formation of an adsorption system.

Equation 5.5 shows that the integral functions can be measured experimentally by calorimetry. Generally, the term $PV^s$ is negligible compared to $\Delta H$.

## 5.3 Enthalpy of the adsorbed phase

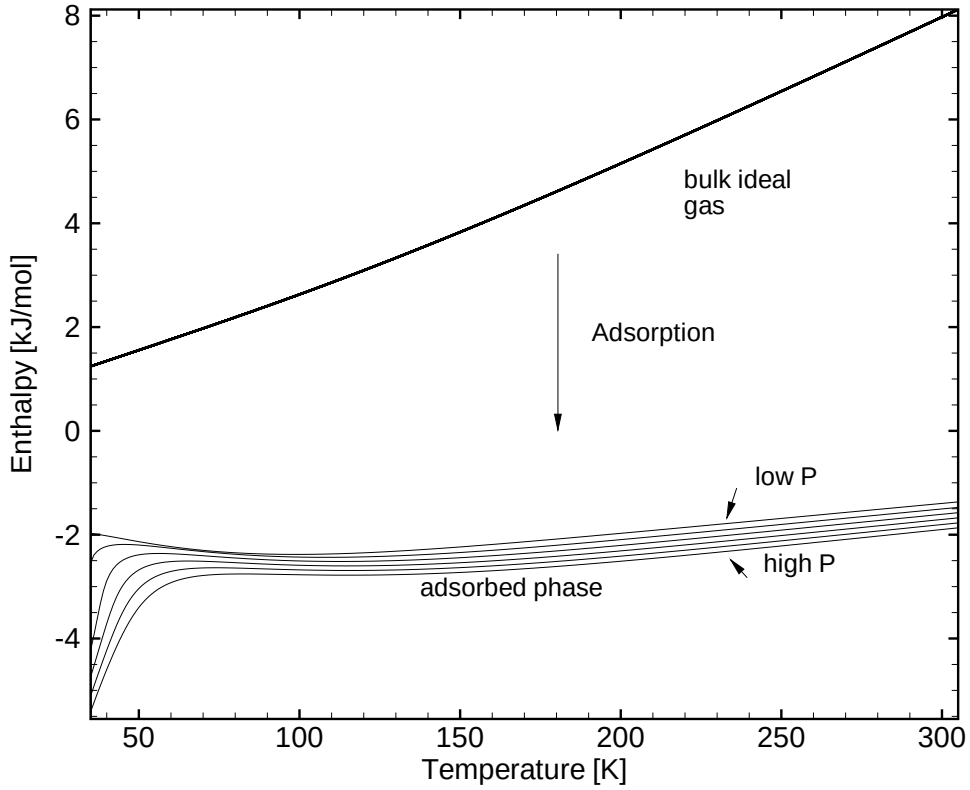


**Figure 5.5:** Molar integral enthalpy of the adsorbed phase for adsorption of hydrogen on activated carbon at several isobarics. The bulk gas enthalpy is also shown for comparison.

The enthalpy is one of the most important thermodynamic property for drawing energy balances. The enthalpy of the adsorbed phase is given by equation 3.64, which, using equation 3.63 and the molar integral enthalpy (equation 3.60), can be written as

$$h^e = h^o + \Delta h^e. \tag{5.6}$$

Real gas effects are included in the term $\Delta h^e$ in equation 5.6. The enthalpy of the adsorbed phase $h^e$ as well as the bulk ideal gas enthalpy $h^o$ are plotted in figure 5.5 at isobarics. The figure shows the reduction of the enthalpy of the molecules due to adsorption. At low temperatures and high pressures, $h^e$

decreases rapidly as the temperature decreases. This effect is caused by the maximum of the isotherms.

# 6 THERMODYNAMIC ANALYSIS OF ADSORPTION VESSELS FOR HYDROGEN STORAGE

In the literature, adsorption vessels have been proposed for the storage of fuel gases such as methane or hydrogen [16] [52]. In such a system, for example, gas is released from the vessel in order to supply a fuel cell, a combustion engine or any other energy conversion device. The removal of gas from the vessel is accompanied by a temperature decrease due to enthalpy loss with the flow discharging. In addition, due to the endothermic nature of desorption, temperature is further decreased. The capability of the vessel to maintain full supply will be dictated by the conditions of pressure and temperature inside it, which are, among other factors, dependent on the working conditions to which the vessel is submitted. Therefore, the investigation of the dynamic behaviour of adsorption vessels is of key importance for a smooth operation of such systems and this is the purpose of the present chapter. The investigation will be carried out by means of a zero-dimensional unsteady model (lumped model) that is obtained by writing down a set of equations called the "macroscropic balances", which describe how extensive quantities – such as mass, energy, momentum, ... – in the system change because of the introduction and removal of these quantities via the entering and leaving streams, and because of various other inputs to the system from the surroundings. No attempt is made for understanding all the details of the system (this subject will be treated in the later chapters). In studying an engineering system, it is a good idea to start with this macroscopic description in order to make a global assessment of the problem; in some cases it is only this overall view that is needed. For instance, lumped models are commonly used to investigate the slow depressurization due to mass release of high-pressure vessels

employed in processing industries [87] [91]. Concerning hydrogen storage, Aceves *et al.* [3] also used a lumped model to investigate low pressure liquid hydrogen vessels and high pressure insulated vessels. The latter has been proposed by the authors as an alternative to low pressure liquid hydrogen vessels. High pressure insulated vessels have the capacity to operate at low temperature (as low as liquid hydrogen temperature) and high pressure (up to 248 bar; 3600 psi) and can be filled with either liquid hydrogen or compressed gas at any temperature. This hybrid concept significantly minimises evaporation losses when filled with liquid hydrogen due to high pressure capacity and also offers sufficient storage capacity when operated with cold compressed gas. Moreover, if cryogenic hydrogen is not available due to limitations in the hydrogen infrastructure, the vessel can also be fueled with compressed gas at room temperature.

In this chapter, three types of hydrogen storage will be considered: adsorption ($AH_2$), compression ($CH_2$) and liquefaction ($LH_2$). Besides the development of lumped models for vessels for each type of hydrogen storage, it also presents a thermodynamic analysis of each vessel's behaviour during operation, dormancy and filling. Different insulation levels are considered as well. $CH_2$ and $LH_2$ vessels have been extensively analysed by Aceves *et al.* [3]. Their results are in some degree reproduced here and compared with an $AH_2$ vessel.

## 6.1 Thermodynamic models

The general equations for the conservation of mass and energy for a control volume can be expressed, respectively, as [86]

$$\frac{dm_{CV}}{dt} - \sum_i \dot{m}_i = 0, \tag{6.1}$$

$$\frac{dE_{CV}}{dt} - \sum_i \dot{m}_i \left( h + \frac{\vec{V}^2}{2} + gZ \right)_i - \dot{Q}_{CV} + \dot{W}_{CV} = 0. \tag{6.2}$$

In equation 6.1, $m_{CV}$ denotes the instantaneous mass inside the control volume and $\dot{m}$ is the instantaneous rate of mass flow entering or leaving the con-

trol volume (positive value = entering, negative value = leaving). The summation accounts for the possibility of several flow streams entering or leaving the control volume. In equation 6.2, $E_{CV}$ denotes the instantaneous total energy (internal energy $U_{CV}$ + kinetic energy + potential energy) inside the control volume, the term in the summation accounts for the rate of energy (enthalpy + kinetic energy + potential energy) flowing in or out the control volume as a result of mass flow and $\dot{Q}_{CV}$ and $\dot{W}_{CV}$ account for the rate of heat transfer and of mechanical work into the control volume, respectively.

The lumped models are obtained by applying equations 6.1-6.2 to a control volume representing the vessel in question. Thereby, the following assumptions are used:

(a) Kinetic and potential energies are negligible.

(b) The state of the mass within the control volume may change with time, but at any instant of time the state is uniform throughout the entire control volume (or over several identifiable regions that make up the entire control volume).

(c) No mechanical work is done.

(d) No conversion between para and ortho phases of hydrogen. As pointed out by Aceves [3], this assumption is a conservative one and corresponds to the investigation of the worst case since the conversion tends to minimise vessel heating due to heat leakage. This is because vessels are likely to be charged with hydrogen in phase equilibrium, which, at cryogenic temperatures, has a high concentration of para-hydrogen. This concentration decreases with increasing temperature, but, since the conversion from para-hydrogen to ortho-hydrogen is endothermic, it tends to keep the vessel cold and goes against vessel heating. Moreover, the natural conversion rate is of the order of several days [49], so that the concentration of each phase inside the vessel remains fairly constant because hydrogen does not stay long enough in the vessel for significant conversion to occur.

With these assumptions, equation 6.2 reduces to

$$\frac{dU_{CV}}{dt} - \sum_i \dot{m}_i h_i - \dot{Q}_{CV} = 0. \tag{6.3}$$

The following subsections discuss how the several terms in equations 6.1 and 6.3 are defined for each vessel as well as the approach used to solve the differential equations.

### 6.1.1 Adsorption vessel

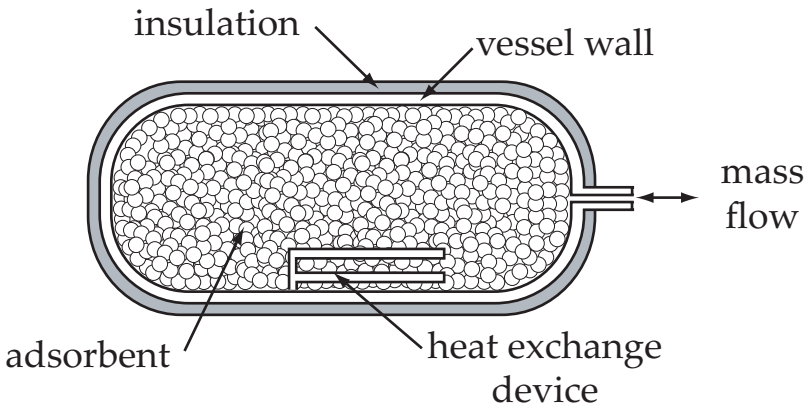


**Figure 6.1:** Typical cryogenic adsorption-based vessel.

Figure 6.1 depicts a typical low-temperature adsorption vessel. The vessel is completely filled with adsorbent material and is insulated to minimize heat transfer with the environment. The purpose of the heat exchange device is to cool or heat the system, depending on what is necessary at the moment. The control volume is defined such that everything within the insulation except the heat exchange device is inside it. Thus, the control surface is defined by the vessel wall external surface and surrounds the heat exchange device. The vessel opening crosses the control surface. Heat transfer to or from the heat exchange device is described as heat flow across the control surface.

The instantaneous mass within the control volume can be written, using equation 2.3, as

$$(m_{CV})_{AH_2} = m^s \left(n^e + V^g \rho^g\right) + m^s + m^w \tag{6.4}$$

where $n^e$ and $V^g$ are given per unit mass of adsorbent and $m^w$ is the vessel wall mass. The instantaneous energy within the control volume can be written, using equations 3.12, 3.26, 3.62, 3.63, 3.64 and 3.65, as

$$(U_{CV})_{AH_2} = m^s \left(V^g \rho^g u^g + n^e h^o + \Delta H^e\right) + m^s u^s + m^w u^w. \tag{6.5}$$

The heat transfer rate, $\dot{Q}_{CV}$, consists of three terms:

(1) Heat transfer through insulation: Since the diameter of the vessel is much bigger than the insulation thickness $d_{ins}$, curvature effects may be neglected [39] and the insulation layer may be seen as a plane plate. Thus, this contribution can be expressed by means of the Fourier's Law of conduction as [39]

$$\dot{Q}_{insulation} = k_{ins} A_{ins} \frac{T_\infty - T}{d_{ins}}. \tag{6.6}$$

where $k_{ins}$ is the insulation thermal conductivity, $A_{ins}$ is the internal surface area and $T_\infty$ is the temperature of the external fluid. Convection on the insulation surface is assumed to be negligible in comparison to insulation resistance and is not considered.

(2) Heat transfer through accessories: This contribution takes into account heat transfer through accessories, connecting lines, vessel support, etc. It is expressed by means of a effective heat transfer coefficient as

$$\dot{Q}_{accessories} = (\alpha A)_{accessories} (T_\infty - T)\,. \tag{6.7}$$

The term $(\alpha A)_{accessories}$ is set to $\frac{1}{220}\frac{W}{K}$, so that $\dot{Q}_{accessories}$ is equal to 1 $W$ when the vessel temperature and the external temperature are 80 $K$ and 300 $K$, respectively. One Watt is a typical value in the case of cryogenic vessels [31] [70].

(3) Heat transfer through the heat exchange device: This contribution may be positive (device heats the vessel), negative (device cools the vessel) or zero. In the analysis, the heat exchange device is used as a component to provide or remove energy from the system so that some constraint, such as to keep system temperature constant, is satisfied. Hence, it is assumed

that the device is always able to satisfy the heat transfer requirements for the process in question and its behaviour is not a function of temperature differences and/or thermal resistances.

### 6.1.2 Compressed gas vessel

The geometric representation of the $CH_2$ vessel and the $LH_2$ vessel in the next subsection is similar to the $AH_2$ vessel shown in figure 6.1, except that the vessel is not filled with adsorbent material. The instantaneous mass and energy within the control volume are, respectively,

$$(m_{CV})_{CH_2} = V\rho^g + m^w \tag{6.8}$$

$$(U_{CV})_{CH_2} = V\rho^g u^g + m^w u^w \tag{6.9}$$

where $V$ is the internal volume of the vessel. The heat transfer rate, $\dot{Q}_{CV}$, is defined as in section 6.1.1 for the $AH_2$ vessel, wheres the heat exchange device is always turned off.

### 6.1.3 Liquefaction vessel

The $LH_2$ vessel always contains hydrogen in two phases: liquid and gaseous. It is assumed that both phases are at saturated conditions. The instantaneous mass and energy within the control volume are, respectively,

$$(m_{CV})_{LH_2} = m_{H_2} + m^w, \tag{6.10}$$

$$(U_{CV})_{LH_2} = m_{H_2} u_{H_2} + m^w u^w, \tag{6.11}$$

where $m_{H_2}$ and $u_{H_2}$ are given by the sum of the liquid and the gaseous contributions as

$$m_{H_2} = m^l + m^g, \tag{6.12}$$

$$u_{H_2} = x u^g + (1-x)\, u^l. \tag{6.13}$$

The property quality, $x$, is obtained from

$$x = \frac{\frac{V}{m_{H_2}} - v^l}{v^g - v^l}, \tag{6.14}$$

where $V$ is the internal volume of the vessel. $v$ is the specific volume. The heat transfer rate, $\dot{Q}_{CV}$, is defined as in section 6.1.1 for the $AH_2$ vessel. Unless otherwise noted, gaseous hydrogen is preferred to be extracted from the vessel. Liquid hydrogen is only extracted when the mass of gas available is not enough to fulfill the demand.

When all liquid hydrogen has been evaporated, the $LH_2$ vessel becomes a $CH_2$ vessel and the equations presented in the previous section are used to calculate the control volume properties from this point on.

## 6.2 Solution

The system of differential equations to be solved consists of equations 6.1 and 6.3. Since the analytical solution of the system is very complicated, it is solved numerically by a iterative time step method [61]. For that, it is considered that the control volume undergoes a process going from state 1 at time $t$ to state 2 at time $t + \Delta t$. Integrating the equations over time from $t$ to $t + \Delta t$ gives, respectively,

$$(m_{t+\Delta t} - m_t)_{CV} - \sum_i \left[ \int_t^{t+\Delta t} \dot{m}_i \, dt \right] = 0, \tag{6.15}$$

$$(U_{t+\Delta t} - U_t)_{CV} - \sum_i \left[ \int_t^{t+\Delta t} \dot{m}_i h_i \, dt \right] - \sum_i \left[ \int_t^{t+\Delta t} \dot{Q}_{CV} \, dt \right] = 0, \tag{6.16}$$

where $m_t$, $U_t$, $m_{t+\Delta t}$ and $U_{t+\Delta t}$ are the mass and energy within the control volume at states $t$ and $t + \Delta t$, respectively. Depending on the process, the integral terms may depend on the instantaneous vessel conditions so that they cannot be, *a priori*, calculated. However, by choosing $\Delta t$ so that the variation of the integral terms during the time period of $t$ to $t + \Delta t$ is linear-like, the integrals

can be accurately evaluated as

$$\int_t^{t+\Delta t} \Phi dt \cong \frac{\Phi(t)+\Phi(t+\Delta t)}{2}\Delta t = \overline{\Phi}\Delta t, \tag{6.17}$$

where $\overline{\Phi}$ represents the average value of $\Phi$ between $t$ and $t+\Delta t$. Equation 6.17 corresponds to the Crank-Nicholson implicit scheme [61], since it assumes a linear variation of the integral term over the time step. Inserting equation 6.17 into equations 6.15-6.16, they become

$$(m_{t+\Delta t} - m_t)_{CV} - \Delta t \sum_i \overline{\dot{m}_i} = 0, \tag{6.18}$$

$$(U_{t+\Delta t} - U_t)_{CV} - \Delta t \sum_i \overline{\dot{m}_i h_i} - \Delta t \overline{\dot{Q}_{CV}} = 0. \tag{6.19}$$

Equations 6.18-6.19 are solved for each vessel, together with the mass and energy terms described in sections 6.1.1-6.1.3, iteratively for the whole time period of interest with a computer program, which also includes functions for calculating the properties of hydrogen, vessel materials as well as activated carbon. Real-gas hydrogen properties are obtained from equations by Younglove [89] and temperature dependent material properties are obtained from the extensive data compilation by Touloukian and Ho [79].

As can be seen in equations 6.15-6.16, if the integrands are not a function of the state within the control volume (i.e., are not a function of pressure and temperature within the control volume), it is possible to correlate the initial and final states directly without having to solve the equations numerically. This may be the case, for instance, when analyzing a filling process where the vessel is fed with a gas at always the same state and no outflow exists (an outflow may exist, however, the state of the gas crossing the control surface must be the same over time). In this case, the equations become

$$(m_{\text{final}} - m_{\text{initial}})_{CV} - \sum_i \Delta m_i = 0, \tag{6.20}$$

$$(U_{\text{final}} - U_{\text{initial}})_{CV} - \sum_i \Delta m_i h_i - Q_{CV} = 0, \tag{6.21}$$

where $\Delta m_i$ is the total mass entering (or leaving) the control volume at the $i$th flow stream during the process and $h_i$ is the specific enthalpy of this mass. $Q_{CV}$ is the liquid energy transferred to or from the control volume.

### 6.2.1 Vessel characteristics

The analysis considers three types of vessels and a total of five configurations – two types are equipped with two different insulation levels. The configurations are described as follows:

(1). An $AH_2$ vessel with multilayer vacuum superinsulation (MLVSI) and 35 bar maximum operating pressure.

(2). An $AH_2$ vessel with microsphere insulation and 35 bar maximum operating pressure.

(3). An insulated high-pressure vessel with MLVSI and 248 bar maximum operating pressure.

(4). An insulated high-pressure vessel with microsphere insulation and 248 bar maximum operating pressure.

(5). A low-pressure $LH_2$ vessel with MLSVI and 5 bar maximum operating pressure.

The vessels are designed to store 5 kg of hydrogen and their properties are listed in table 6.1. The vessels can either be filled with liquid hydrogen or compressed gas. Properties of vessels (3)-(5) are taken from the publication by Aceves *et al.* [3], which are calculated from data given by James *et al.* [40]. The adsorbent for the $AH_2$ vessels is pellets with a bulk density of 700 kg/m$^3$. The same insulation properties are used as by Aceves *et al.* [3]. He obtained them from Bunger and Owren [19], who list ranges of measured conductivity. The highest conductivity values are selected, thus considering the worst case, and are assumed to be constant.

Table 6.1 shows that the liquid hydrogen vessel provides the smallest and lightest system for storage, followed by insulated high-pressure vessels. The adsorption storage vessel, within the scope of this analysis, is the heaviest system, mainly due to the adsorbent mass, and occupies a much larger volume. However, when compared with room temperature compressed gas systems, an adsorption vessel is both lighter and smaller [31].

| Property | Unit | $AH_2$ vessel | High-pressure vessel | low-pressure $LH_2$ vessel |
|---|---|---|---|---|
| Storage capacity | kg | 5 | 5 | 5 |
| Internal volume | liter | 158 | 95 | 85 |
| Mass contained within insulation | kg | 130 | 20 | 9 |
| Mass of aluminum within insulation | kg | 14 | 10 | 9 |
| Mass of carbon fiber within insulation | kg | 6 | 10 | 0 |
| Mass of activated carbon in the vessel | kg | 110 | - | - |
| Void volume | liter/kg | 0.98 | - | - |
| Adsorption isotherms factor* | - | 0.68 | - | - |
| Design pressure | bar | 35 | 248 | 5 |
| Insulation thermal conductivity | W/(m K) | MLVSI**: 0.0001; Microsphere: 0.0004 | | |
| Insulation thickness | cm | 2 | 2 | 2 |
| Internal surface area | $m^2$ | 1.6 | 1.1 | 1 |
| Heat transfer through accessories | W | T < 80 K: 1; T ≥ 80 K: 1/220*(T-$T_\infty$) | | |
| Ambient temperature $T_\infty$ | K | 300 | 300 | 300 |

*= See section 4.5.
**= Multilayer vacuum superinsulation.

**Table 6.1:** Properties of the vessels considered in the analysis.

## 6.3 Results and discussion

This section analyses several aspects of the performance of hydrogen storage vessels such as hydrogen losses and pressure and temperature conditions inside the vessels during dormancy, normal operation and filling. For adsorption vessels, a circulation circuit is proposed for filling and discharging hydrogen therefrom.

### 6.3.1 Filling

Many hydrogen filling stations in operation or planned worldwide dispense either liquid hydrogen and/or compressed hydrogen at 350 or 700 bar at room temperature [1]. Some of them also dispense compressed hydrogen at cryogenic temperatures, which is obtained from liquid hydrogen via evaporation

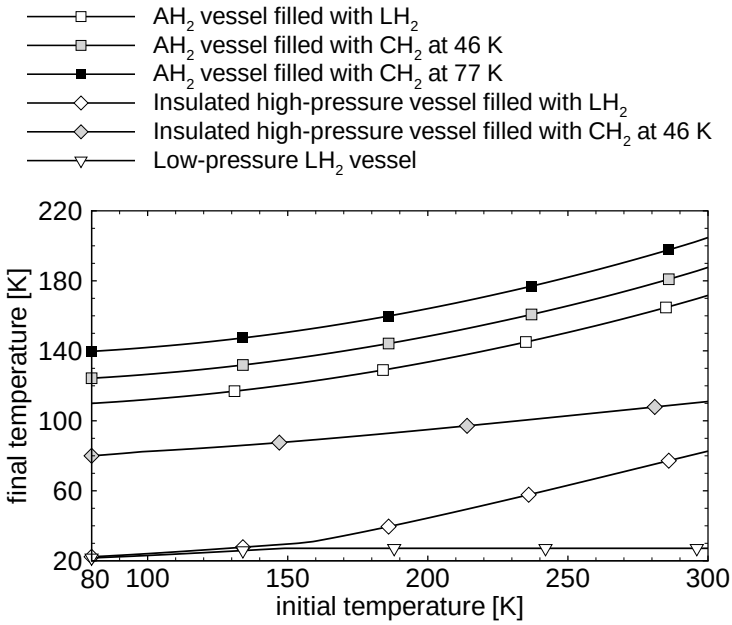


(a)

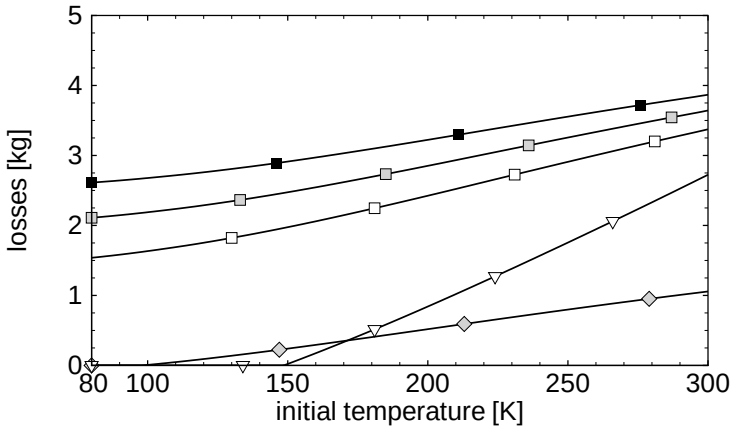


(b)

**Figure 6.2:** Final vessel temperature (a) and total hydrogen losses (b) after filling as a function of the initial empty vessel temperature for all vessels in the analysis.

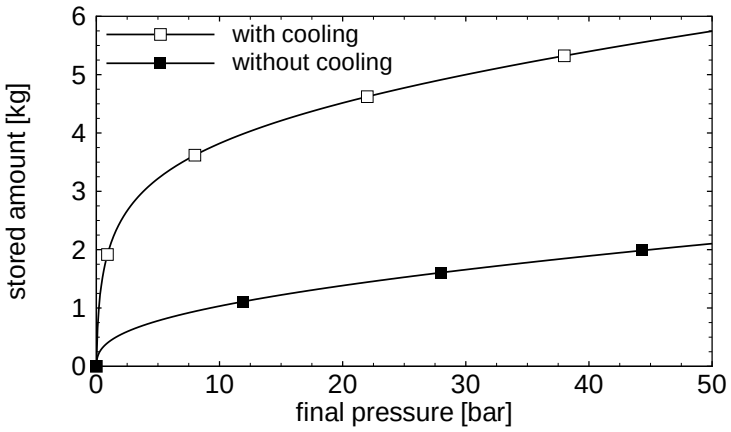


(a)

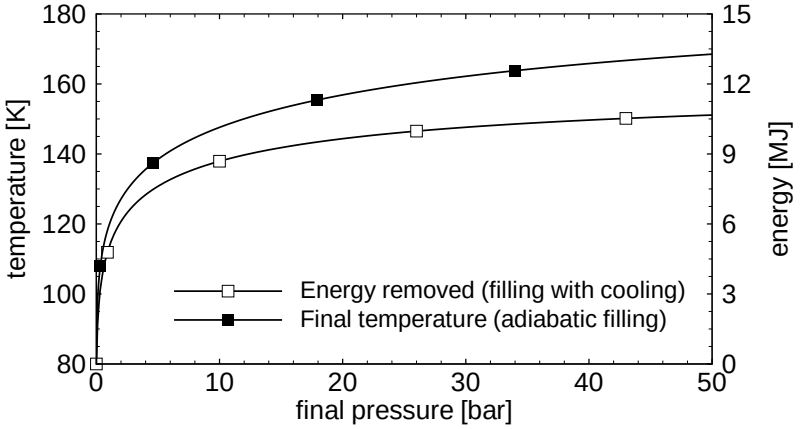


(b)

**Figure 6.3:** Adsorption vessel storage amount (a) as a function of the storage pressure for adiabatic filling (without cooling) and cooled filling (cooling keeps vessel at 80 K) starting with an empty vessel. Part (b) shows the final vessel temperature for adiabatic filling and the energy removed from the vessel in order to maintain it at 80 K for cooled filling.

and compression [4]. In this analysis, it is assumed that hydrogen is available for filling at three states: saturated liquid at 21 K, compressed gas at 44 K and 248 bar and compressed gas at 80 K and 35 bar.

The filling process consists of feeding 5 kg of hydrogen into the vessel. It is considered to be fast enough so that the thermal interaction between vessel and ambient can be neglected. The $LH_2$ vessel is filled with saturated liquid hydrogen at 21K. The insulated high-pressure vessel is filled with either gaseous hydrogen at 44 K and 250 bar or liquid hydrogen. Filling the vessel with gas at 44 K results in a final filling temperature of 80 K if the initial temperature of the empty vessel is 80 K. This is the operation condition proposed by Aceves [3]. The $AH_2$ vessel can be either filled with liquid hydrogen or compressed gas at 35 bar and 44 K or 80 K. Unless otherwise stated, the vessel is initially empty and cooled down to 80 K.

Figure 6.2 shows the final vessel temperature and hydrogen losses of the filling process as a function of the initial vessel temperature. Hydrogen losses result from the warm vessel, which warms up or vaporizes the hydrogen increasing its pressure, so that gas must be released in order not to exceed the maximum operating pressure of the vessel. Warm hoses and connecting lines are not included. Starting with a vessel at 80 K, figure 6.2 shows that only the adsorption vessel has hydrogen losses no matter with what it is filled. As the initial vessel temperature increases, the final temperature of all vessels increases. For initial temperatures higher than 100 K, the insulated high-pressure vessel filled with compressed gas loses hydrogen. The low-pressure $LH_2$ vessel loses hydrogen for temperatures higher than 150 K. Starting with a vessel at ambient temperature (300 K) results in a loss of 1 kg of hydrogen for the high-pressure vessel, 2.7 kg for the low-pressure $LH_2$ vessel and 3.4 kg, 3.6 kg and 3.8 kg for the $AH_2$ vessel, respectively. The insulated high-pressure vessel filled with liquid hydrogen does not lose any hydrogen even if the initial temperature is 300 K (at this condition, the safe valve is at the imminence of opening). Except for the adsorption vessel, where the final temperature is at some cases higher than the initial temperature due to adsorption thermal effects, the filling process cools down the vessels substantially. The final temperature of the $LH_2$ vessel remains at 27 K for a wide range of initial temperatures because

this is the equilibrium pressure corresponding to a vapor pressure of 5 bar. The $AH_2$ vessel shows a bad performance even when it is filled with liquid hydrogen. This is mainly due to adsorption heat generation and it evidences that the filling of an adsorption vessel must be accompanied by simultaneous cooling.

A comparison between adiabatic filling and filling with liquid nitrogen cooling of the $AH_2$ vessel is shown in figure 6.3. The cooling system keeps the vessel at 80 K. Figure 6.3a shows the total amount stored as a function of storage pressure (in figure 6.3 it is assumed that the vessel stands pressures higher than 35 bar). Without cooling, the storage capacity is strongly reduced due to temperature increase caused by adsorption. At 30 bar, the cooled vessel stores three times more mass than the adiabatic vessel. The stored amount increases steeply at low pressures because the isotherms at low temperatures and pressures are very steep. At higher pressures, adsorption isotherms are saturated and the stored amount increases less steeply with pressure, the increase being mainly due to gas density increase in the bulk gas volume. Figure 6.3b shows the adiabatic filling final temperature and the energy removed from the vessel in order to keep temperature constant for the case of cooling during filling. 30 bar final pressure shows a temperature increase of 85 K with adiabatic conditions, whereas, with cooling, it requires the removal of 10.1 MJ from the vessel. This is equivalent to the vaporization heat of about 63 liters of liquid nitrogen.

Figure 6.4 shows the contributions of each part to the total energy amount to be removed from the vessel during filling of the empty $AH_2$ vessel for different initial temperatures. The storage pressure is set to 30 bar and the vessel is filled with gaseous hydrogen at 80 K. At 80 K, the initial and final vessel temperatures are the same, so that heat capacity contributions of vessel wall and activated carbon are zero and the energy amount consists merely of two parts: adsorption thermal effects and gas-phase flow work[4] (adsorption and gas areas in the figure, respectively). As the initial temperature increases, both vessel wall and activated carbon must be cooled down as well and their con-

[4]Flow work is referred to the work done on a certain mass as it enters a control volume or the work done by a certain mass as it leaves a control volume. Various other terms are encountered in the literature such as flow energy, work of introduction and work of expulsion. The flow work is equal to $\dot{m}\frac{p}{\rho}$ [3] [86].

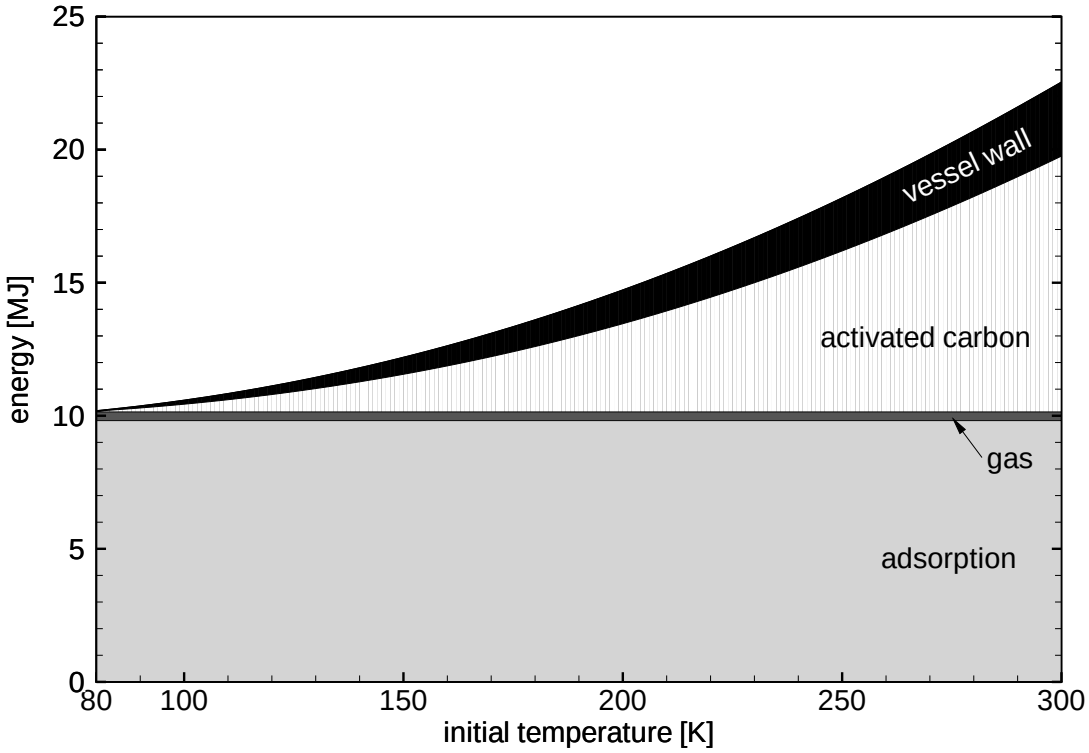


**Figure 6.4:** Contribution of each part to the total energy to be removed from the adsorption vessel during filling of the empty vessel to a final pressure of 30 bar as a function of the initial vessel temperature. The final temperature is always 80 K and the vessel is filled with hydrogen at 80 K.

tributions increase. Starting the filling with the vessel at ambient temperature requires removal of 22.5 MJ, which corresponds to about 140 liters of liquid nitrogen. The adsorption energy remains constant over the whole temperature range because the vessel is initially empty and the final condition is always the same no matter which is the initial temperature. The flow work contribution remains constant as well because hydrogen is introduced into the system always at the same state.

Table 6.2 shows the cooling performance of some other filling processes, in which the adsorption vessel goes from the initial to the final states given. The quantity of $LN_2$ required to cool down the vessel is also given. The top table

Adsorption vessel - Filling with $H_2$ at 30 bar and 80 K

| Description | Unit | Filling 1 | Filling 2 | Filling 3 | Filling 4 |
|---|---|---|---|---|---|
| Vessel initial state | - | 0 bar, 80 K | 1 bar, 80 K | 1 bar, 180 K | 0 bar, 300 K |
| Vessel final state | - | 30 bar, 80 K | 30 bar, 80 K | 30 bar, 80 K | 30 bar, 80 K |
| $H_2$ addition[1] | [kg] | 5.0 | 3.0 | 4.9 | 5.0 |
| Energy removal[2] | [MJ] | 10.1 | 5.3 | 13.5 | 22.5 |
| %Q solid parts[3] | [%] | 0.0 | 0.0 | 25.7 | 55.0 |
| $LN_2$ equiv.[4] | [l/kg $H_2$] | 12.6 | 11.0 | 17.0 | 28.0 |

Adsorption vessel - Filling with $H_2$ at 30 bar and 300 K

| Description | Unit | Filling 1 | Filling 2 | Filling 3 | Filling 4 |
|---|---|---|---|---|---|
| Vessel initial state | - | 0 bar, 80 K | 1 bar, 80 K | 1 bar, 180 K | 0 bar, 300 K |
| Vessel final state | - | 30 bar, 80 K | 30 bar, 80 K | 30 bar, 80 K | 30 bar, 80 K |
| $H_2$ addition[1] | [kg] | 5.0 | 3.0 | 4.9 | 5.0 |
| Energy removal[2] | [MJ] | 25.1 | 14.3 | 28.2 | 37.5 |
| %Q solid parts[3] | [%] | 0.0 | 0.0 | 12.3 | 33.1 |
| $LN_2$ equiv.[4] | [l/kg $H_2$] | 31.2 | 29.6 | 35.6 | 46.6 |

[1] Quantity of hydrogen to be added to the system in order to go from the initial to the final state.
[2] Quantity of energy to be removed from the system through the cooling system during filling.
[3] Percentage of the total energy ([2]) required to cool down solid parts (i.e., adsorbent and vessel wall).
[4] Liters of liquid nitrogen per kilo added hydrogen required to cool down the system if a $LN_2$ cooling system is used. It is assumed that all vaporization heat is used for cooling.

**Table 6.2:** Cooling performance for filling an adsorption vessel from several vessel initial states.

shows filling processes with compressed and pre-cooled hydrogen, whereas the bottom table shows filling processes with compressed hydrogen at room temperature. In the latter case, the entering gas has to be cooled in the vessel during filling. As it can be seen, high amounts of energy have to be removed from the vessel, leading to big quantities of $LN_2$ consumption, so that, in order to achieve these cooling performances over short times, powerful cooling systems with high energy expenses have to be utilized.

When cooling the vessel with liquid nitrogen such as discussed above, adsorbent poor thermal conductivities can considerably limit the process [10] [40]

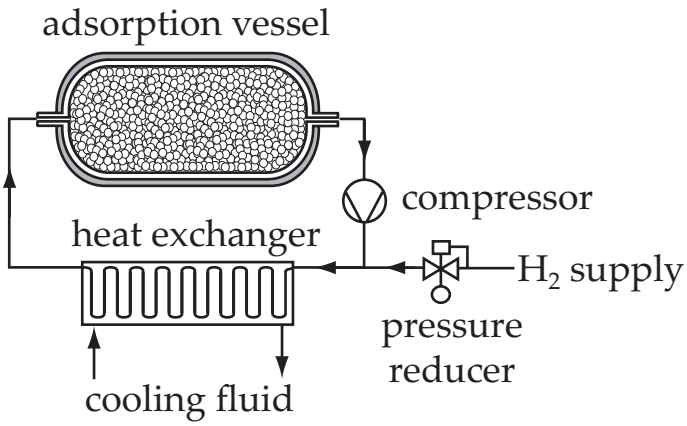


**Figure 6.5:** Recirculation circuit for cooling the adsorption vessel during filling [69].

and thus causing relatively long filling times. A further possibility to cool down the vessel is to remove energy from the system through heat advection using hydrogen as energy carrier [69]. In this method, the vessel is integrated in a circulation circuit as shown in figure 6.5. The circuit comprises a device to move the hydrogen contained in it, such as a compressor, as well as a heat exchanger to cool it down. Hydrogen condensation in the heat exchanger is not excluded. When cold hydrogen enters the $AH_2$ vessel, the adsorbent and vessel wall are cooled down and, simultaneously, hydrogen is adsorbed, releasing energy. The adsorption energy as well as heat capacity energies are then transported out of the vessel by the hydrogen leaving the vessel and removed from the recirculation system through the cooling fluid in the heat exchanger. Since during the process the vessel temperature decreases and hydrogen is stored in it, mainly due to adsorption, additional hydrogen has to be supplied to the circuit in order to maintain the pressure at the required level, which is controlled by adjusting the pressure reducer that connects the circuit to the hydrogen supply. The final vessel temperature can be adjusted by controlling the heat exchanger performance through the mass flows of both hydrogen and cooling fluid as well as by choosing different cooling fluid temperatures.

Mass and heat transfer in the adsorbent plays an important role when cooling the vessel through recirculation, but these effects are not considered by the lumped model. However, the model is very useful for investigating how much

mass is necessary to recirculate in order to achieve a certain vessel temperature. Figures 6.6, 6.7 and 6.8 show the final vessel temperature as well as the stored mass as a function of storage pressure and recirculated mass for the cases in which the heat exchanger liquefies the hydrogen flowing through it or cools it down to 44 K or 77 K, respectively. The recirculated mass is given by the numbers on the lines, whereas they represent the total mass in percent pushed by the compressor relative to the vessel storage capacity at the corresponding storage pressure and 77 K (this quantity is given by the bold lines in figures 6.6b-6.8b). The storage pressure in this case is the pressure at which the system is being operated. The vessel, and consequently the circuit, is initially empty and the compressor starts to work only after an adiabatic filling of the system to the storage pressure. It must be mentioned that these simulations do not consider mass and energy accumulations in connecting lines and heat exchanger. The curve for 0% recirculation corresponds to adiabatic filling up to the storage pressure in question. Allowing the compressor to recirculate some fluid, warm hydrogen leaves the vessel and is cooled down or liquefied in the heat exchanger in order to enter the vessel again. At the same time, hydrogen from supply is introduced in the recirculation system in order to compensate the stored mass in the vessel. The final vessel temperature and stored mass according to the recirculated mass are given by the other curves in figures 6.6-6.8. For 30 bar storage pressure (the filled circles in figures 6.6b-6.8b), it is necessary to recirculate about 73% of mass or 3.65 kg in order to bring the vessel to 80 K again for the case in which hydrogen is liquefied in the heat exchanger (figure 6.6). If hydrogen is only cooled down to 44 K (figure 6.7) or 77 K (figure 6.8), 176%, or 8.8 kg, or 750%, or 37.5 kg, have to be recirculated, respectively. The high amount for the last case is due to the small enthalpy difference between vessel inlet and outlet flows. As shown by equation 6.3, the rate of change of energy inside the vessel is given as

$$\frac{dU_{\text{vessel}}}{dt} = \dot{m}_{\text{in}} h^g_{\text{in}} - \dot{m}_{\text{out}} h^g_{\text{out}}. \tag{6.22}$$

Since $\dot{m}_{\text{in}}$ and $\dot{m}_{\text{out}}$, vessel inlet and outlet mass flows, respectively, are of comparable magnitude, the rate of cooling is dictated by the enthalpy difference $h^g_{\text{in}} - h^g_{\text{out}}$, which goes to zero when the vessel temperature approaches the temperature at which hydrogen leaves the heat exchanger. Thus, for this sys-

tem to be efficient, either the heat exchanger has to have a good cooling capacity, i.e. it has to cool down the gas to temperatures much lower than the desired final vessel temperature or extremely high amounts of mass must be recirculated in the circuit.

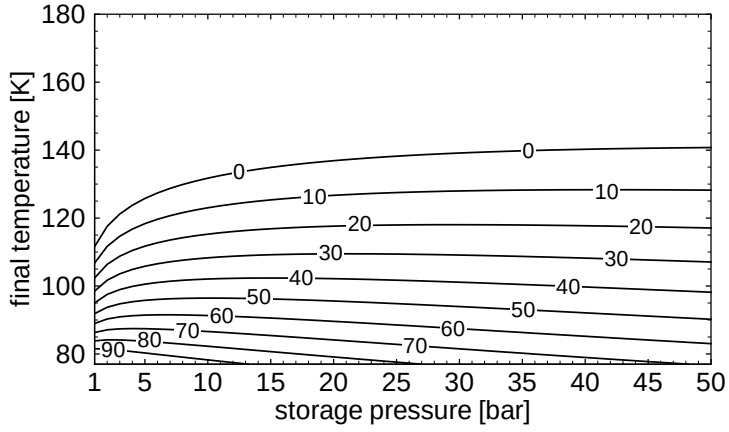


(a)

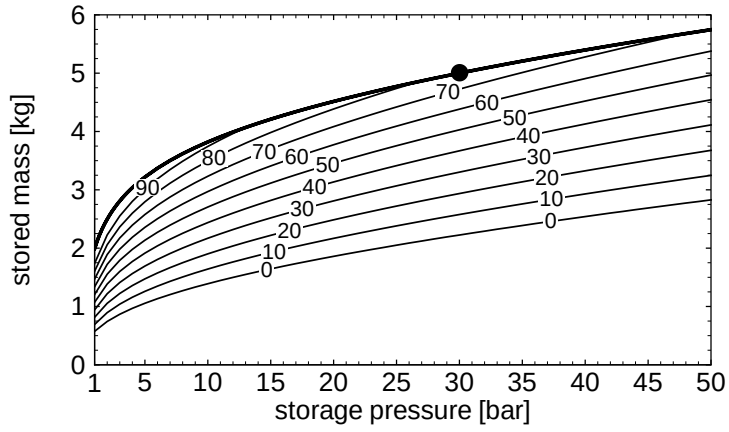


(b)

**Figure 6.6:** Final vessel temperature (a) and stored mass (b) as a function of storage pressure for the case in which the recirculation system heat exchanger (figure 6.5) liquefies the hydrogen flowing through it. The numbers represent the total recirculated mass in percent relative to the vessel storage capacity at the corresponding storage pressure and 80 K, given by the bold line.

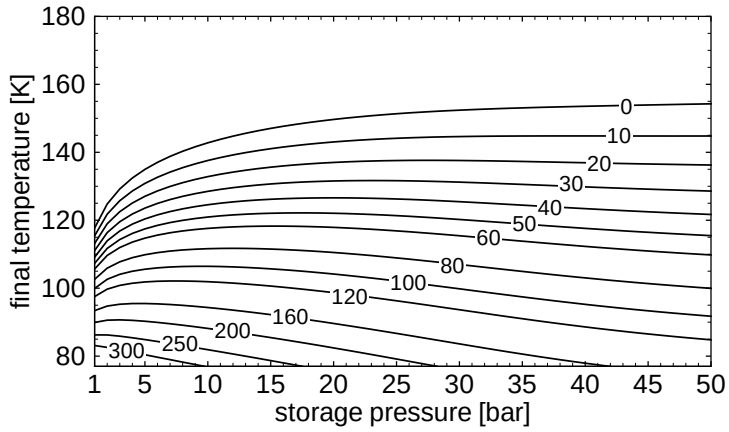


(a)

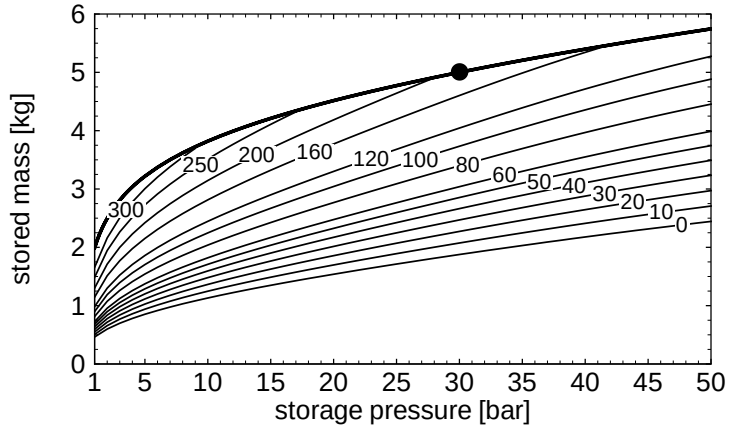


(b)

**Figure 6.7:** Final vessel temperature (a) and stored mass (b) as a function of storage pressure for the case in which the recirculation system heat exchanger (figure 6.5) cools down the hydrogen flowing through it to 46 K. The numbers represent the total recirculated mass in percent relative to the vessel storage capacity at the corresponding storage pressure and 80 K, given by the bold line.

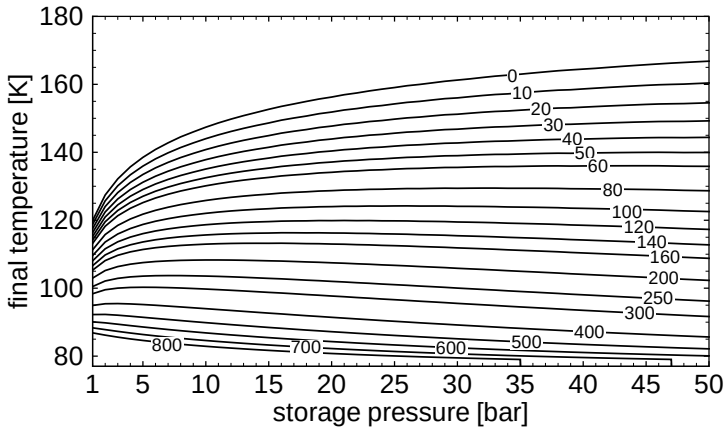


(a)

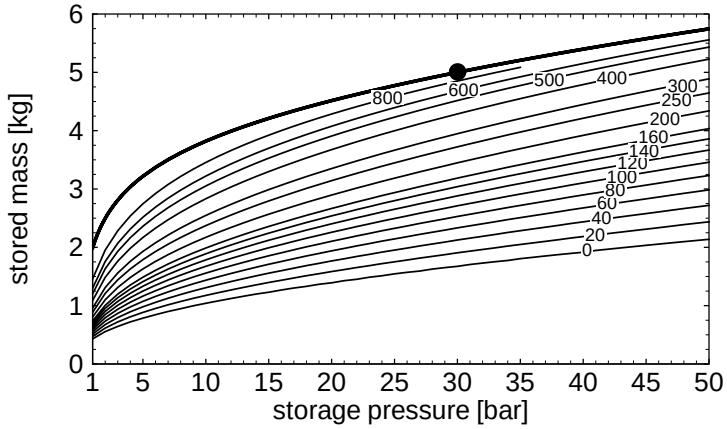


(b)

**Figure 6.8:** Final vessel temperature (a) and stored mass (b) as a function of storage pressure for the case in which the recirculation system heat exchanger (figure 6.5) cools down the hydrogen flowing through it to 77 K. The numbers represent the total recirculated mass in percent relative to the vessel storage capacity at the corresponding storage pressure and 80 K, given by the bold line.

### 6.3.2 Dormancy

The time period between putting a cryogenic vessel into an idle or inactive mode and the start of the venting process is usually called dormancy [2] [70]. Venting gas is necessary in order to reduce pressure build up in the vessel due to heat transfer with the environment. Figure 6.9a show cumulative hydrogen venting losses as a function of the number of days that the vessels remain idle. The vessels are initially full (5 kg of hydrogen) and at 21 K (low-pressure $LH_2$ vessel and insulated high-pressure vessel filled with $LH_2$) and 80 K ($AH_2$ vessel and insulated high-pressure vessel filled with $CH_2$). These conditions are unfavourable since inactivity occurs immediately after full filling.

The low-pressure $LH_2$ vessel starts losing hydrogen after two days. This is the time needed for the pressure to rise from 1 bar to 5 bar due to evaporation. Once venting has started, cumulative losses increase quickly and practically all hydrogen is lost after 15 days. The $AH_2$ vessel and the high-pressure vessel with $CH_2$, both with MLVSI insulation, start losing hydrogen after 1 and 0.5 day, respectively. Their dormancy time is very short because they are filled to nearly the maximum pressure. However, they lose hydrogen much slower than the low-pressure $LH_2$ vessel. During the first 30 days, hydrogen losses are comparable for both vessels. For the case with microsphere insulation, both vessels lose hydrogen right after dormancy begins. However, their losses after 4 days are lower than the low-pressure $LH_2$ vessel losses. After 10 days, the $AH_2$ vessel losses increase faster since adsorptive storage capacity considerably decreases as a consequence of temperature increase. The high-pressure vessel with $LH_2$ has the longest dormancy times: 5 days with microsphere insulation and 13 days with MLVSI insulation. This is because the pressure has to increase from 1 bar to 248 bar for venting to start.

Figure 6.10a show the temperature inside the vessels as a function of days of inactivity. During venting, $LH_2$ vessel temperature remains at 27.1 K (saturation temperature at 5 bar). After all liquid is evaporated, vessel temperature increases quickly. $AH_2$ vessel temperatures increase not as quick as high-pressure vessel temperatures filled with $CH_2$ due to adsorbent thermal mass and desorption energy effects. However, no appreciable advantage is seen on

hydrogen losses because a small temperature increase liberates substantial amounts of adsorbed gas leading to high pressure increase inside the vessel.

Figures 6.9b and 6.10b show hydrogen losses and vessel temperatures for the case in which the vessels are initially half full (2.5 kg of hydrogen), a more reasonable initial condition. Although not true for the $LH_2$ vessel, there is a substantial increase in dormancy times. MLVSI insulated $AH_2$ and high-pressure $CH_2$ vessels have in this case dormancy times longer than 2 weeks because pressure has to increase considerably before any hydrogen needs to be vented. The insulated high-pressure vessel filled with $LH_2$ has even a dormancy time longer than 1 month (curve not shown on the graph). Vessel temperatures show a qualitative similar behaviour compared to the first case.

When all vessels reach ambient temperature, they are able to keep the following masses of hydrogen: 0.034 kg ($LH_2$ vessel), 0.55 kg ($AH_2$ vessel) and 1.6 kg (high-pressure vessel).

### 6.3.3 Discharge / Dynamic operation

The discharge and dynamic operation of the storage vessels are analysed for the case in which they provide hydrogen to run a vehicle. Storage of 5 kg of hydrogen provides a range of about 320 km in a car with an energy efficiency equivalent to a conventional gasoline car (17 km/liter of gasoline) [3]. Considering a fuel cell vehicle, 5 kg of hydrogen would provide a range of about 640 km. Although the results presented here are based on the requirements of an equivalent 17 km/liter conventional car, they can also be used for a fuel cell vehicle if the driving distance is doubled, i.e., a 10-km/day curve for a conventional car corresponds to a 20-km/day curve for a fuel cell vehicle. Moreover, a certain daily driving distance can be achieved by several ways, for example, by a long slow trip or by several short trips. However, little difference is obtained for these different driving conditions so that only the results for driving distances distributed over the whole day are presented. Concerning the initial conditions of the vessels, unless otherwise stated, they always contain 5 kg of hydrogen at 21 K (when filled with $LH_2$) or 80 K (when filled with $CH_2$ or for the $AH_2$ vessel).

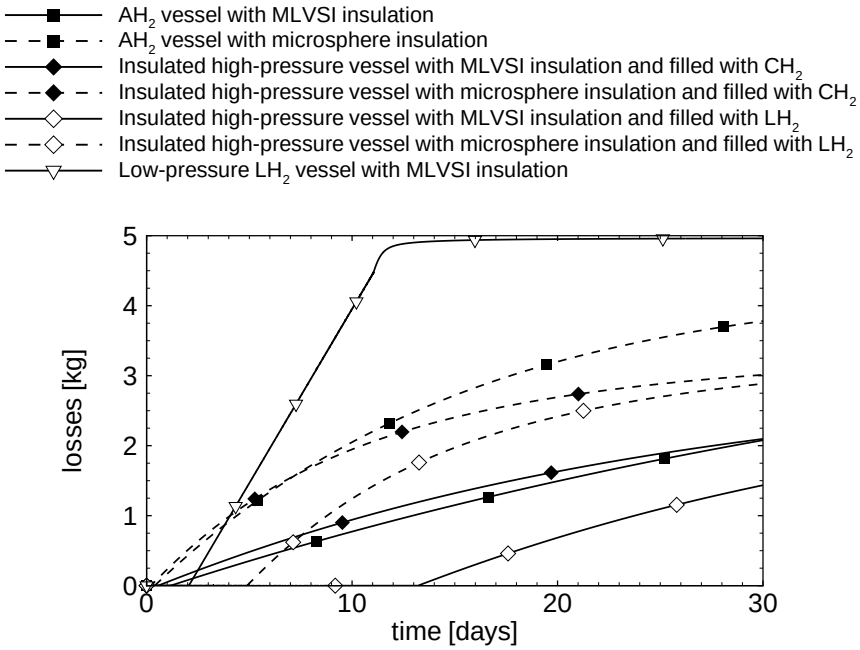


(a)

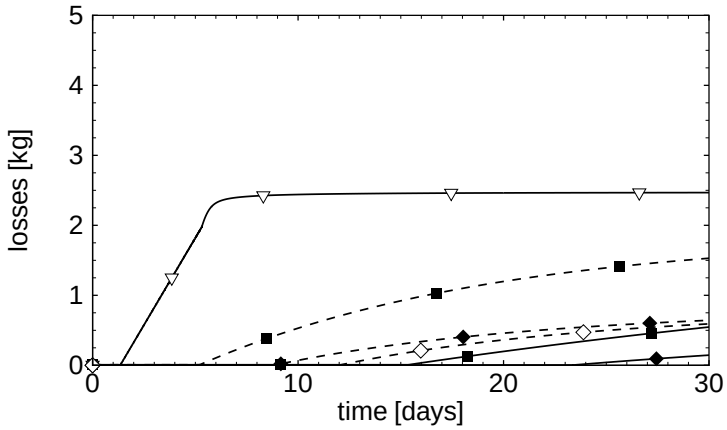


(b)

**Figure 6.9:** Cumulative losses as a function of the number of days that the vessels remain inactive: (a) for the case the vessels are initially full (5 kg of hydrogen) and (b) for the case the vessels are initially half-full (2.5 kg of hydrogen). The initial temperature is 21 K for vessel filled with $LH_2$ and 80 K for the others (see figure 6.10).

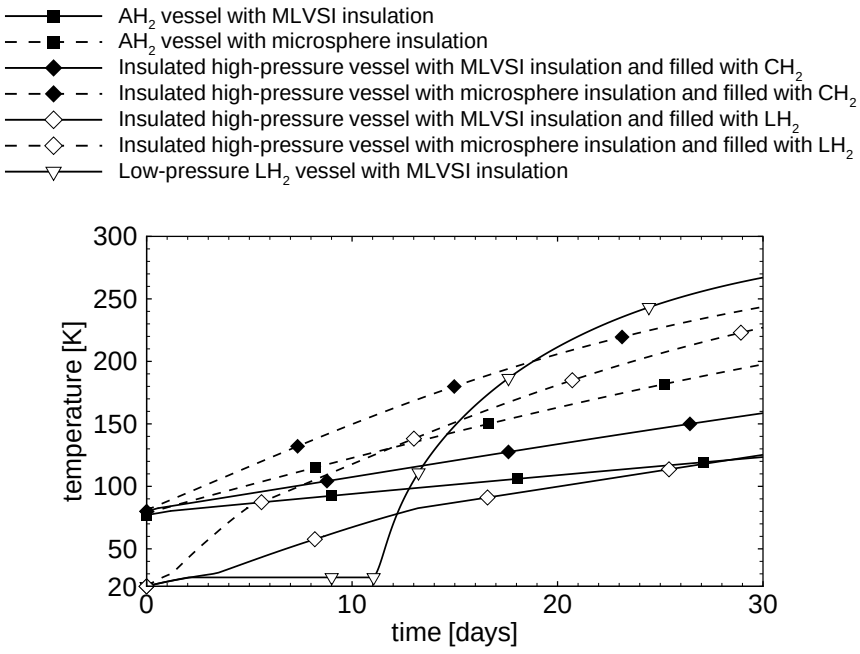


(a)

(b)

**Figure 6.10:** Vessel temperature as a function of the number of days that the vessels remain inactive: (a) for the case the vessels are initially full (5 kg of hydrogen) and (b) for the case the vessels are initially half-full (2.5 kg of hydrogen).

Figures 6.11-6.17 show pressure and temperature inside the vessels as a function of the day of operation since the vessel was filled for different daily driving distances for all configurations. Specifically, figures 6.11 and 6.12 show the $AH_2$ vessel results with MLVSI and microsphere insulation, respectively. It can be seen that pressure and temperature are strongly dependent of daily driving distance. For low daily driving distances, temperature continuously increases and pressure rapidly achieves the maximum pressure of 35 bar. At this point, the vessel starts venting hydrogen in order to avoid further pressure increase. For high daily driving distances, pressure as well as temperature decrease continuously and no hydrogen is lost. For the case of MLVSI insulation, final vessel temperature is from 20 km/day on lower by more than 20 K relative to the initial vessel temperature, thus causing high amounts of residual gas in the vessel once the depletion pressure is reached. Vessel temperature reduction is caused not only by the flow work but mainly also by the endothermic effects of desorption.

Figure 6.18 shows both excess adsorbed and bulk gas amounts for both types of insulation. For the case of MLVSI insulation, it is clear that for high daily driving distances, hydrogen is mainly provided by the bulk gas portion; the adsorbed portion remains practically constant and only supplies a small amount of hydrogen. Though for the case of microsphere insulation the hydrogen amount provided by the adsorbed portion is higher, the final residual gas is still high and can be more than half of the initially stored amount.

Figures 6.13 and 6.14 show pressure and temperature inside the high-pressure vessel with MLVSI and microsphere insulation, respectively, filled with compressed gas. Although pressure behaves qualitatively similar to results of the $AH_2$ vessel, temperature behaviour is quite different, at least for high daily driving distances. In this case, and considering MLVSI insulation, while $AH_2$ vessel temperature decreases always steeper with time (because more desorption occurs as pressure gradually reduces and the saturation region of the isotherms is left behind), $CH_2$ vessel temperature decreases always slower and at the end it even increases (this behaviour is mainly caused by the variation of the flow work as pressure and density inside the vessel varies). A comparison of figures 6.13b and 6.14b also shows that temperature dependence on daily

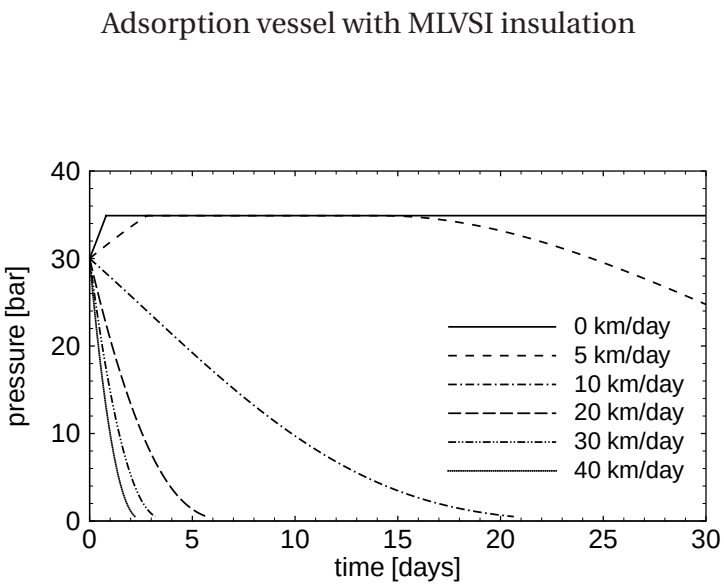


(a)

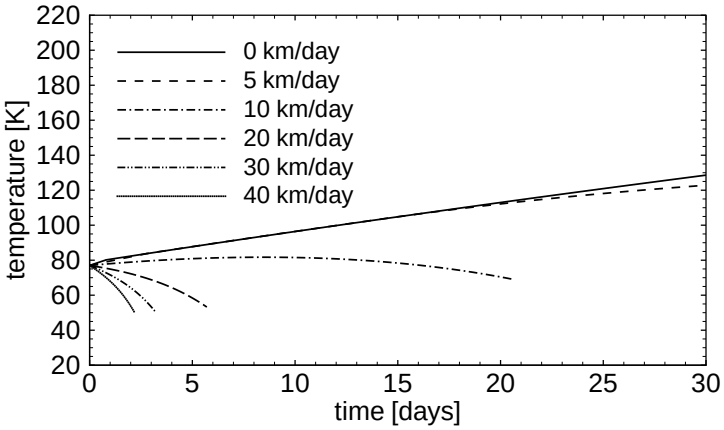


(b)

**Figure 6.11:** Pressure (a) and temperature (b) inside a MLVSI insulated adsorption-based vessel as a function of time since the vessel was filled, for several daily driving distances. Initially, the vessel contains 5 kg of hydrogen at 80 K.

Adsorption vessel with microsphere insulation

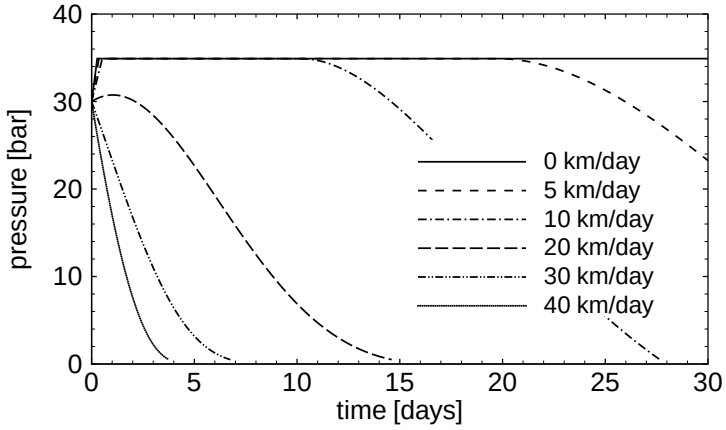


(a)

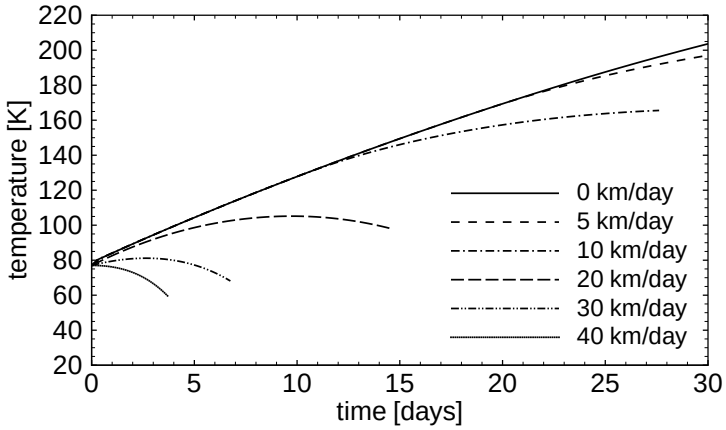


(b)

**Figure 6.12:** Pressure (a) and temperature (b) inside a microsphere insulated adsorption-based vessel as a function of time since the vessel was filled, for several daily driving distances. Initially, the vessel contains 5 kg of hydrogen at 80 K.

Insulated high-pressure vessel with MLVSI insulation and filled with compressed gas

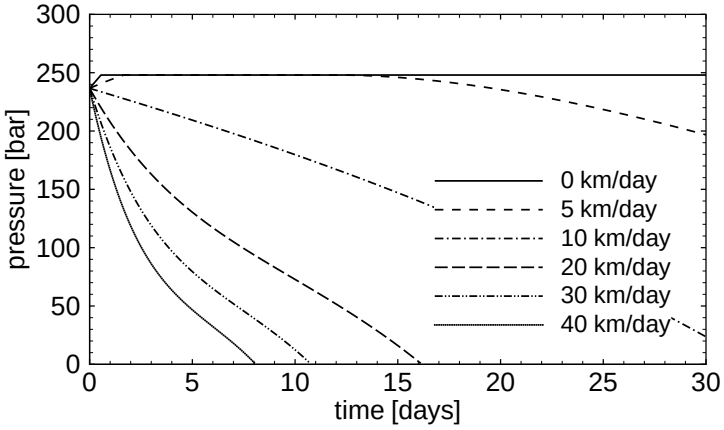


(a)

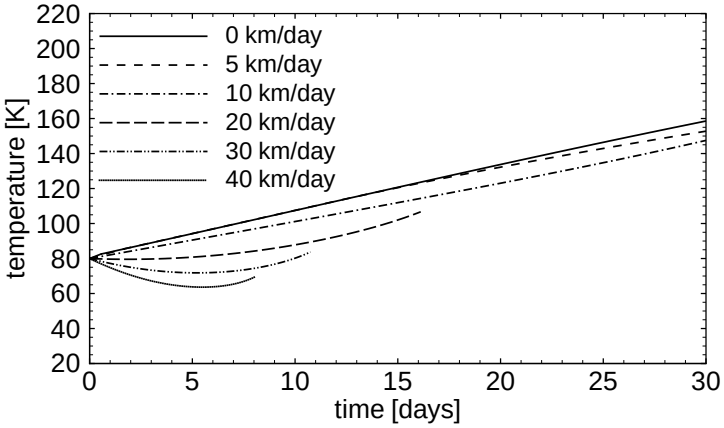


(b)

**Figure 6.13:** Pressure (a) and temperature (b) inside a MLVSI insulated high-pressure vessel as a function of time since the vessel was filled, for several daily driving distances. Initially, the vessel contains 5 kg of hydrogen at 80 K.

Insulated high-pressure vessel with microsphere insulation and filled with compressed gas

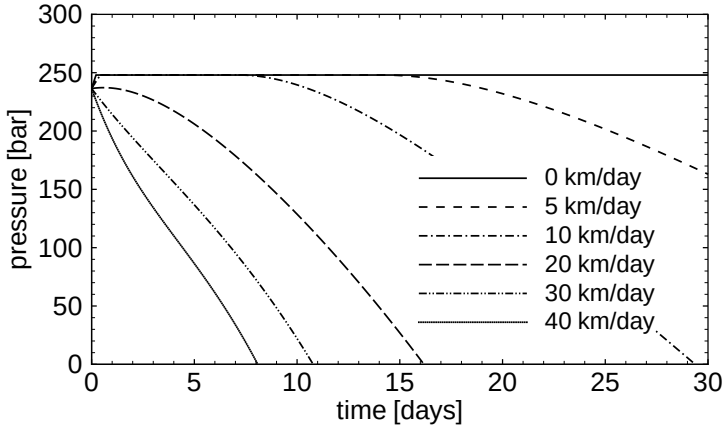


(a)

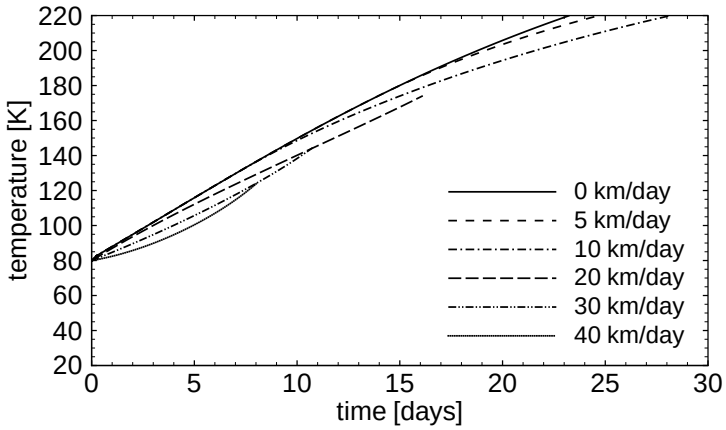


(b)

**Figure 6.14:** Pressure (a) and temperature (b) inside a microsphere insulated high-pressure vessel as a function of time since the vessel was filled, for several daily driving distances. Initially, the vessel contains 5 kg of hydrogen at 80 K.

Insulated high-pressure vessel with MLVSI insulation and filled with liquid hydrogen

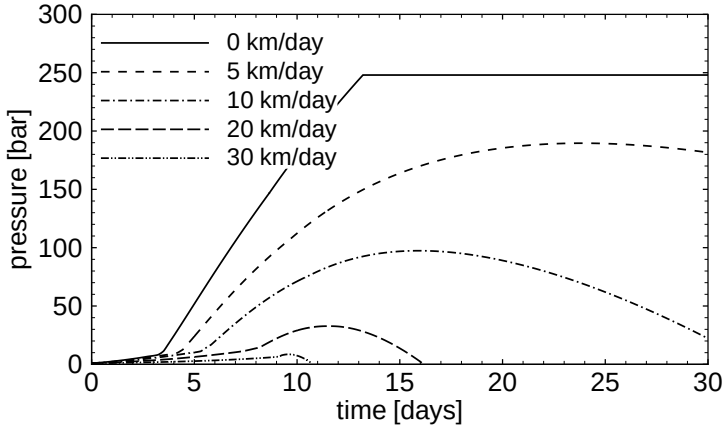


(a)

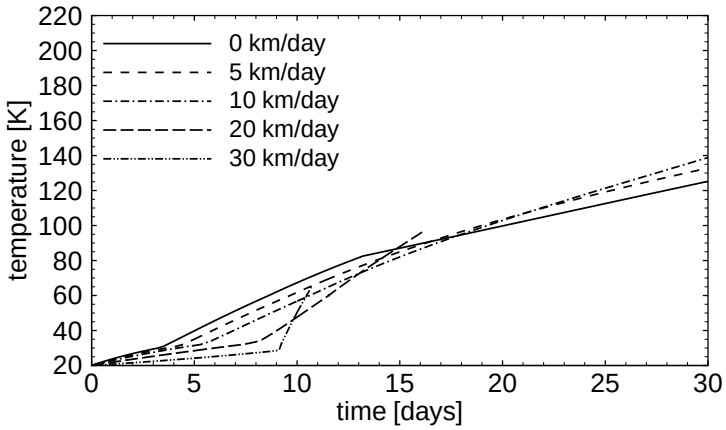


(b)

**Figure 6.15:** Pressure (a) and temperature (b) inside a MLVSI insulated high-pressure vessel as a function of time since the vessel was filled, for several daily driving distances. Initially, the vessel contains 5 kg of liquid hydrogen at 21 K.

Insulated high-pressure vessel with microsphere insulation and filled with liquid hydrogen

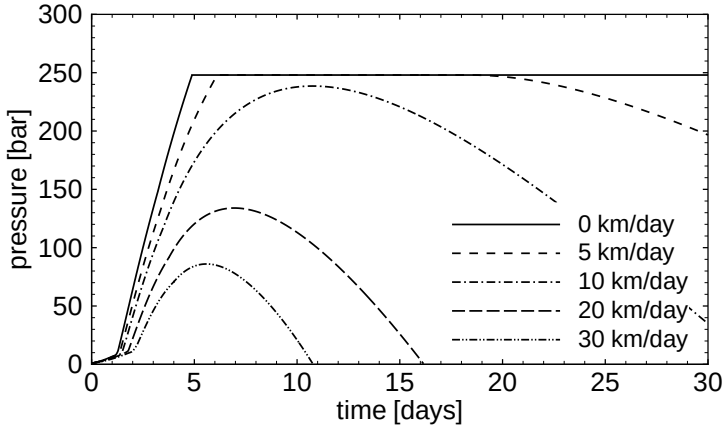


(a)

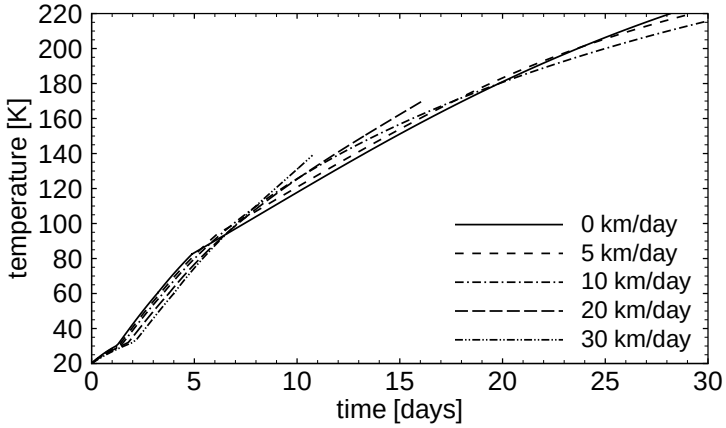


(b)

**Figure 6.16:** Pressure (a) and temperature (b) inside a microsphere insulated high-pressure vessel as a function of time since the vessel was filled, for several daily driving distances. Initially, the vessel contains 5 kg of liquid hydrogen at 21 K.

Low-pressure liquid hydrogen vessel with MLVSI insulation

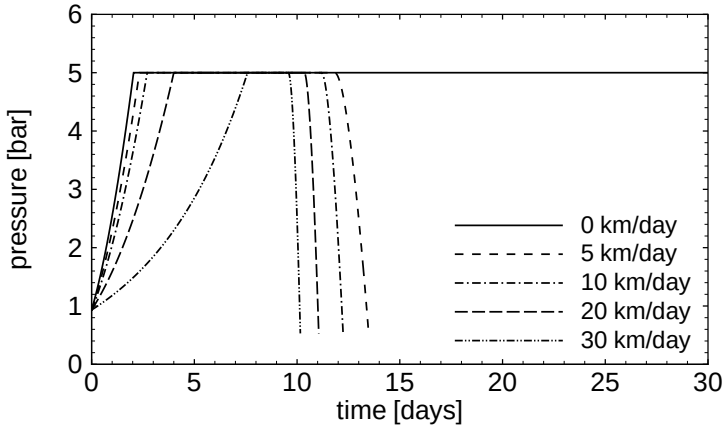


(a)

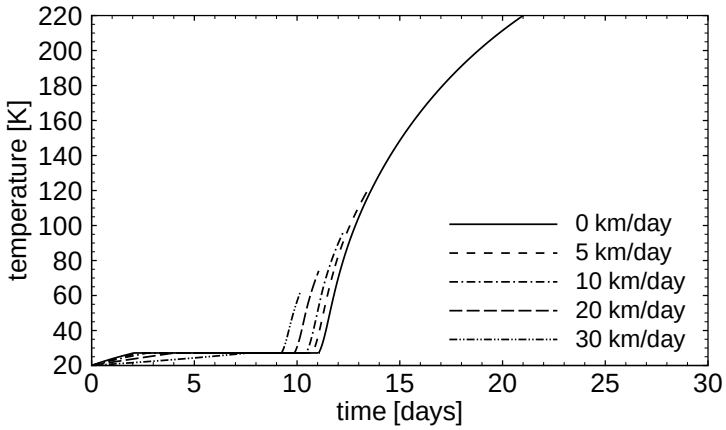


(b)

**Figure 6.17:** Pressure (a) and temperature (b) inside a MLVSI insulated low-pressure vessel as a function of time since the vessel was filled, for several daily driving distances. Initially, the vessel contains 5 kg of liquid hydrogen at 21 K.

Adsorption vessel

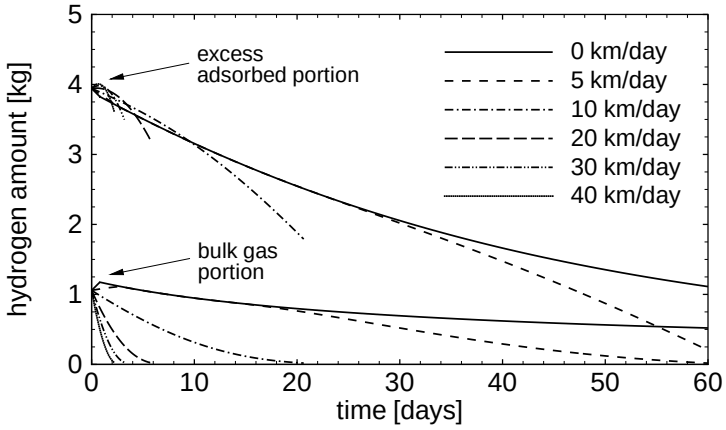


(a) MLVSI insulation

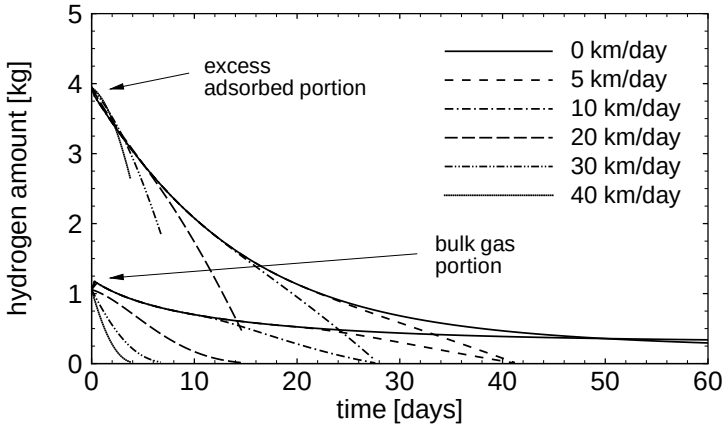


(b) Microsphere insulation

**Figure 6.18:** Excess adsorbed and bulk gas amounts inside an adsorption-based vessel for two types of insulation as a function of time since the vessel was filled, for several daily driving distances. Initially, the vessel contains 5 kg at 80 K.

driving distance is reduced as insulation performance worst.

Concerning vessels filled with liquid hydrogen, figures 6.15 and 6.16 show pressure and temperature inside the high-pressure vessel with MLVSI and microsphere insulation, respectively, and figure 6.17 shows the results for the low-pressure vessel. For the last vessel, both pressure and temperature increase until the pressure reaches the maximum pressure of 5 bar and hydrogen venting starts. The temperature remains at 27.1 K, the saturation temperature corresponding to 5 bar, until all liquid hydrogen inside the vessel evaporates. At this point, heat transfer from the environment results in a sudden increase in temperature since the heat capacity of the vessel and the remaining hydrogen is very low. In these calculations, only gaseous hydrogen is extracted from the vessel and it is possible to see a dependence of the initial pressure and temperature increase on the daily driving distance. If liquid hydrogen, however, had also been extracted this dependence would be very weak and all curves would behave similarly to 0 km/day curve due to the fact that the flow work is very low because of the high density with which hydrogen is extracted, thus resulting on little cooling [5]. The curves for the high-pressure vessel shows that the pressure reaches the maximum pressure of 250 bar only for very low daily driving distances, and that only for the case of microsphere insulation, so that the configuration barely loses hydrogen. The pressure inside the vessel typically increases due to heating and starts to decrease after some time because hydrogen is being extracted from the vessel. Comparing 6.15b and 6.16b, it can be seen that temperature is more sensitive to different driving distances when the insulation performance is better.

Section 6.3.2 discussed the dormancy behaviour of the vessels and showed cumulative hydrogen losses due to inactivity. However, losses also occur for low daily driving distances, which are recognizable when the pressure inside the vessels remains constant at the vessel's maximum operating pressure in figures 6.11-6.17. Starting with a full vessel (5 kg of hydrogen), figure 6.19a shows the cumulative hydrogen losses during operation as a function of daily driving distance for all vessels. The figure shows that the low-pressure $LH_2$ vessel

[5] The german car company BMW, whose hydrogen storage research is focused on liquid hydrogen, heats the vessel in order always to have gaseous hydrogen available since the technology by now doesn't allow a precise injection of liquid hydrogen into the combustion engine [85].

losses hydrogen for all daily driving distances shown in the figure. The high-pressure vessel filled with liquid hydrogen, on the other hand, losses hydrogen only for very short daily driving distances. Even the worst case of microsphere insulation, this vessel does not lose any hydrogen for driving distances of 10 km/day or more. The same vessel filled with compressed hydrogen gas also has only losses for low daily driving distances. The microsphere insulated vessel does not lose any hydrogen when driven 17 km/day or more. Insulated pressure vessels, due to their high pressure capacity, keep about 32% of their original load when the daily driving distance goes to zero. Adsorption vessels, on the other hand, keep only about 10% due to their lower pressure capacity and strongly reduced adsorption storage capacity at high temperatures. However, as the daily driving distance increases, $AH_2$ vessel hydrogen losses reduce more rapidly than high-pressure vessel losses so that, for some daily driving distances, $AH_2$ vessels do not lose any hydrogen while high-pressure vessels with $CH_2$ still have losses.

Figure 6.19b shows the number of days as a function of daily driving distance that the vehicle can operate with a full vessel before the pressure inside it achieves the depletion pressure, point at which no further hydrogen delivery from the vessel is possible. In the figure, the filled area gives the region of possible operating times according to the daily driving distance and the initial amount of hydrogen stored, being the upward limiting hyperbola the maximum operating time possible, i.e., the operating time for a vessel with no losses. Since the high-pressure vessel loses hydrogen only for very short daily driving distances (compare figure 6.19a) and it has a very small amount of residual gas, only the worst case (microsphere insulated high-pressure vessel filled with $CH_2$) is shown. The curves for the other configurations lie between this curve and the maximum operating time hyperbola. The curve for the high-pressure vessel shows that its operating time is reduced for driving distances of 15 km/day or less due to hydrogen losses. For higher driving distances, all hydrogen is used to run the vehicle and the curve coincides with the hyperbola. The curve for the low-pressure $LH_2$ vessel is more likely to be a line than a hyperbola. The reason for that is the substantial increase of hydrogen losses as the daily driving distance decreases, thus drastically reducing the operating time. For high daily driving distances, the operating time

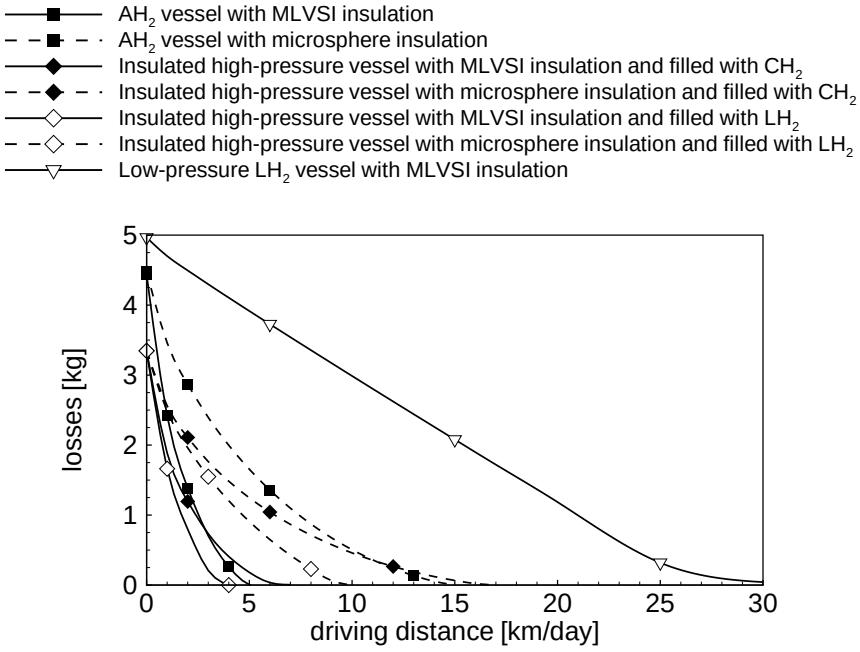


(a) Cumulative hydrogen losses

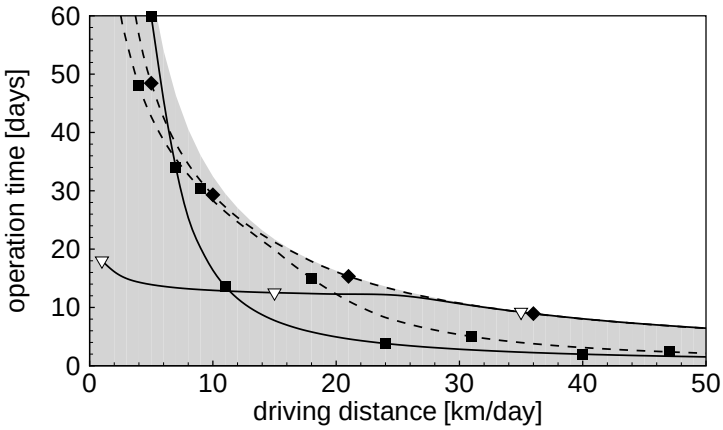


(b) Days of operation

**Figure 6.19:** Cumulative hydrogen losses (a) and number of days of vehicle operation (b) as a function of daily driving distance for all vessels in the analysis. Initially, all vessels store 5 kg of hydrogen.

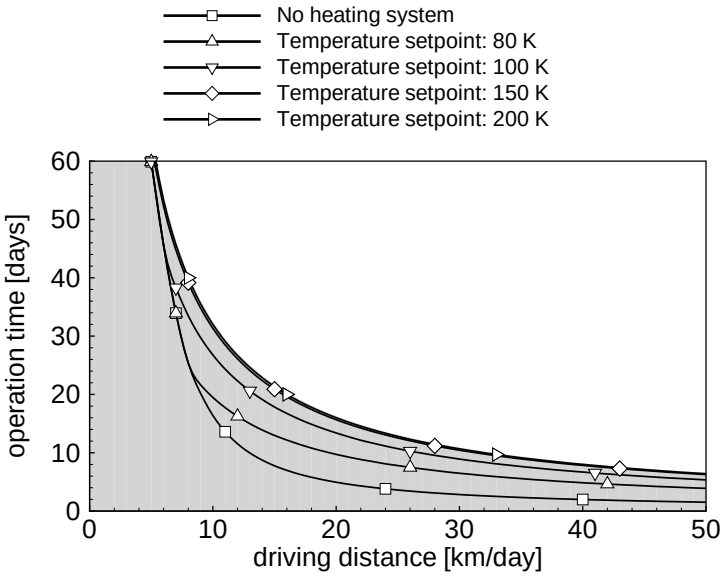


(a) MLVSI insulation

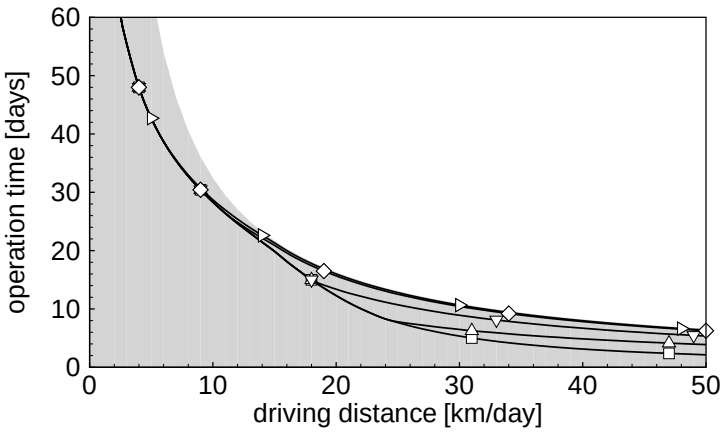


(b) Microsphere insulation

**Figure 6.20:** Number of days of vehicle operation for an adsorption-based vessel equipped with a heating device as a function of daily driving distance. Two types of insulation and several minimum final vessel temperatures are considered.

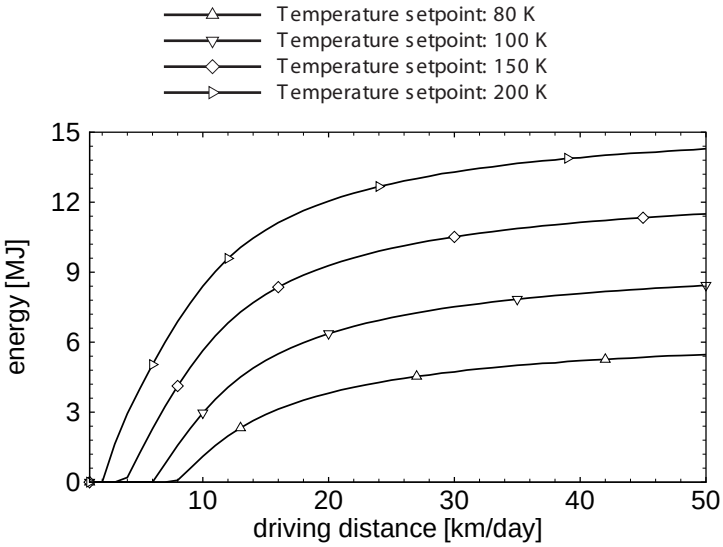


(a) MLVSI insulation

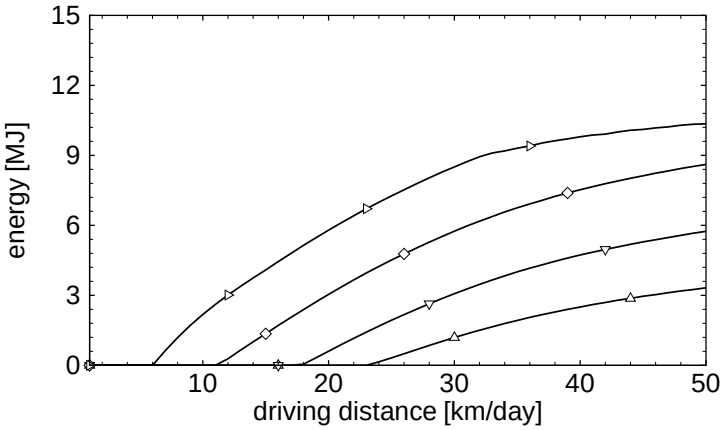


(b) Microsphere insulation

**Figure 6.21:** Total energy amount to be added into an adsorption-based vessel equipped with a heating device as a function of daily driving distance in order to achieve a certain minimum final vessel temperature.

coincides with the maximum. However, it must be noted that gaseous hydrogen is preferably extracted from the vessel and that liquid hydrogen is only extracted to complement the demand not covered by the gas. This requires extraction of a fluid with quality between 0.4 and 1.0 depending on the daily driving distance, which might be a difficult task. The curves for the adsorption vessels with MLVSI and microsphere insulation cross each other at about 7 km/day. For lower daily driving distances, the MLVSI insulated $AH_2$ vessel has longer operating times because it vents less hydrogen than the microsphere insulated vessel due to better insulation. However, for higher daily driving distances, the microsphere insulated vessel has longer operating times because the worse insulation leads to higher heat transfer from the environment, which provides more energy for desorption. Between 10 and 15 km/day, the microsphere insulated vessel offers almost the maximum operating time. At about 11 and 20 km/day, the curves cross the low-pressure $LH_2$ vessel curve and show much shorter operating times than the maximum. The reason for that is not hydrogen losses but high amounts of residual gas inside the vessel due to the temperature decrease caused mainly by endothermic effects of desorption.

The residual gas of an adsorption vessel can be minimized if energy is introduced in the system in order to further desorption. To illustrate these effects, the analysis considers a heating system that turns itself on if the pressure inside the vessel is approaching the depletion pressure and the temperature is still below an adjustable final temperature setpoint. For example, if the vessel has to provide hydrogen for high daily driving distances, its temperature decreases with time as shown in figure 6.11. When the pressure is approaching the depletion pressure, the heating system comes into operation and introduces energy into the vessel in order to avoid that the pressure further reduces and the vessel does not fulfill the hydrogen demand. The heating system provides energy as long as the vessel temperature is below the final temperature setpoint. Otherwise, it turns itself off. Figure 6.20 shows the operation time of the $AH_2$ vessel equipped with a heating system for different temperature setpoints and for both insulation levels. Figures 6.20 show the operation time for both MLVSI and micro insulated $AH_2$ vessels equipped with a heating system as a function of daily driving distances. Curves for different temperature

setpoints are shown. It can be seen that the higher the temperature setpoint, the longer are the operating times. But, it must be noted that increasing the temperature setpoint from 150 K to 200 K barely improves the system performance because the former already offers almost the maximum operating time. Comparing 6.20a and 6.20b it is also possible to see that the heating system of the microsphere insulated $AH_2$ vessel comes into operation only for higher daily driving distances because the worse insulation undertakes some heating (the heating system comes into operation at the point at which the corresponding curve separates from the curve without heating system). Figure 6.21 shows the total amount of energy introduced into the vessel through the heating system as a function of the daily driving distance. For the case of high daily driving distances and high temperature setpoints (150 K, 200 K), in which nearly all of the adsorbed gas is released, the amount of energy practically reaches the energy amount necessary to cool down and fill the vessel when the initial temperature of the empty vessel is the temperature setpoint, as shown by figure 6.4.

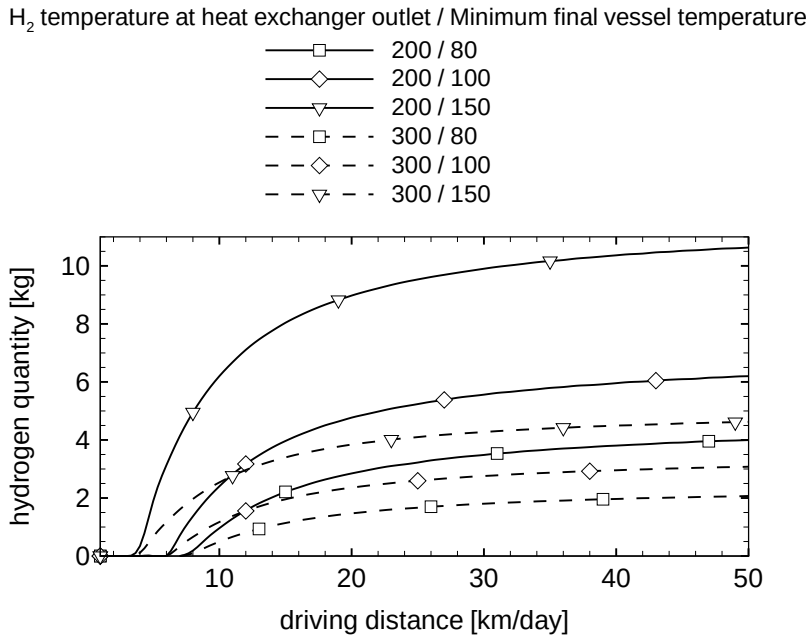


**Figure 6.22:** Total recirculated mass as a function of daily driving distance when using a recirculation system to heat a MLVSI insulated adsorption vessel.

Energy addition in adsorption vessels can also be carried out by a recirculation circuit such as the one presented in section 6.3.1 for energy removal during filling. In this case, hydrogen is extracted from the vessel, heated in at least one heat exchanger and introduced back into the vessel [69]. The heat exchanger might simply allow heat transfer between the recirculating hydrogen and the environment or, in a more sophisticated system, couple the vessel circuit with the energy converter device cooling circuit (fuel cell cooling system or internal combustion engine cooling system, for example), thus increasing the energy performance of the whole system. Using the same strategy such as the one used for heating the vessel with a heating device, figures 6.22 shows the total mass recirculated in the circuit in order to obtain at least 80 K, 100 K and 150 K as the final vessel temperature. Thereby it is considered that the circuit heat exchanger is able to heat the hydrogen mass flow to 200 K and 300 K. In the case of 300 K, it can be seen that the recirculated quantity is always lower than the initially stored mass (5 kg) for the three temperatures considered, while for 200 K the recirculated quantity is more than two times the initial hydrogen mass if the vessel is to be heated to 150 K.

## 6.4 Energy consumption

The choice of a storage system should not be limited to the vessel characteristics alone. The analysis of the whole process from hydrogen production, transport, storage, delivery is needed for the decision which storage type has a better energetic efficiency and is more suitable for a determined application. Several analyses are available [17] [18] [34], in which different configurations are compared against each other. Particularly, Bossel *et al.* [18] have studied the energy consumption of several hydrogen delivery paths, from hydrogen production by electrolysis till delivery to the consumer. Their results, in which the energy consumption of each step is given relative to the high heating value (HHV) of $H_2$, are presented in table 6.3, where the three possible supply pathways are:

A : produced by electrolysis, compressed to 20 MPa and distributed by road

to filling stations or consumers, stored at 10 MPa, then compressed to 40 MPa for rapid transfer to vehicles at 35 MPa.

B : produced by electrolysis, liquefied and distributed by road to filling stations or consumers, then transferred to vehicles.

C : produced by electrolysis on-site at filling stations or consumers, stored at 10 Mpa, then compressed to 40 MPa for rapid transfer to vehicles at 35 MPa.

| | Energy cost in HHV of $H_2$ | Factor | Path A gas | Path B liquid | Path C onsite |
|---|---|---|---|---|---|
| **Production of $H_2$** | | | | | |
| Electrolysis | 43% | 1.43 | 1.43 | 1.43 | |
| Onsite production | 65% | 1.65 | | | 1.65 |
| **Packaging** | | | | | |
| Compression 20 MPa | 8% | 1.08 | 1.08 | | |
| Liquefaction | 40% | 1.40 | | 1.40 | |
| **Distribution** | | | | | |
| Road, 20 MPa $H_2$, 100 km | 6% | 1.06 | 1.06 | | |
| Road, $LH_2$, 100 km | 1% | 1.01 | | 1.01 | |
| **Storage** | | | | | |
| $LH_2$, 10 days | guess: 5% | 1.05 | | 1.05 | |
| **Transfer** | | | | | |
| 10 MPa to 40 MPa | 3% | 1.03 | 1.03 | | 1.03 |
| **Delivered to User** | | | | | |
| Energy Input/HHV of $H_2$ | | | 1.69 | 2.12 | 1.69 |

**Table 6.3:** Energy consumption for different hydrogen delivery paths. From Bossel *et al.* [18].

Table 6.3 reveals that considerable amounts of energy are lost between the electrical source energy and the hydrogen energy delivered to the consumer, where the electrical energy input exceeds the HHV of $H_2$ by a factor of at least 1.69. Paths A and C deal with compressed gaseous hydrogen and are comparable on energy consumption. On path C, electrolysis consumes more energy because the facility is smaller, thus decreasing its efficiency. On path B, liquid

hydrogen is considered. Hydrogen liquefaction is a highly energy consuming process [17]. Small liquefaction plants (10 kg/h) need about 100 MJ/kg, while large plants (1000 kg/h) or more capacity consume about 40 MJ of electrical energy for each kg liquefied hydrogen (about 40% of the higher heating value of hydrogen). Although the specific energy input decreases with plant size, a minimum of about 40 MJ per kg of hydrogen always remains. Thus, better efficiencies are only achieved with highly centralized liquefaction facilities. This would require a hydrogen distribution system in order to serve other locations and, since further energy is necessary for that, it makes the process less efficient. On this path, electrical energy input exceeds the HHV of $H_2$ by a factor of at least 2.12.

Adsorption-based systems require gaseous hydrogen at moderate pressures of about 35 bar. The pressure at the outlet of commercially available electrolyzers ranges between 10 and 30 bar [82], so that small amounts of energy are necessary for posterior compression. Adsorption-based systems also require a cooling facility, much probable a $LN_2$ cooling facility. The power consumption to liquefy nitrogen is about 0.4 kWh/kg [46]. Considering onsite hydrogen production and a $LN_2$ cooling system, the energy consumption of the filling processes given in table 6.2 is shown in table 6.4.

Although lower than the energy consumption of path B - liquefaction path, factor 2.12 -, the electrical energy input of adsorption-based systems exceeds the HHV energy of the delivered hydrogen in average by a factor of 1.93. If, in addition, a recirculation system is used for faster filling (see chapter 9), compressor energy consumption must be added, thus increasing energy consumption. Compressor energy consumption might probably be 0.02% of HHV of $H_2$ per kg of gas recirculated. Due to high input energy consumption, it is unlikely that any of these scenarios might become attractive.

Adsorption vessel - Filling with $H_2$ at 300 K

| Description | Unit | Filling 1 | Filling 2 | Filling 3 | Filling 4 |
|---|---|---|---|---|---|
| Vessel initial state | - | 0 bar, 80 K | 1 bar, 80 K | 1 bar, 180 K | 0 bar, 300 K |
| Vessel final state | - | 30 bar, 80 K | 30 bar, 80 K | 30 bar, 80 K | 30 bar, 80 K |
| **Production of $H_2$** | | | | | |
| Onsite production | [% HHV of $H_2$] | 65% | 65% | 65% | 65% |
| **Compression** | | | | | |
| Compression | [% HHV of $H_2$] | 0.5% | 0.5% | 0.5% | 0.5% |
| **Cooling** | | | | | |
| $LN_2$ quantity | [l/kg $H_2$] | 31.2 | 29.6 | 35.6 | 46.6 |
| $LN_2$ liquefaction | [% HHV of $H_2$] | 26% | 24% | 29% | 38% |
| **Delivered to User** | | | | | |
| Energy Input | [% HHV of $H_2$]<br>(Factor) | ≈ 91%<br>(1.91) | ≈ 89 %<br>(1.89) | ≈ 94%<br>(1.94) | ≈ 103%<br>(2.03) |

**Table 6.4:** Input energy consumption for filling an adsorption vessel from several vessel initial states.

# 7 CONSERVATION EQUATIONS IN ADSORPTION SYSTEMS

The foremost information for understanding an adsorption system is the adsorption equilibrium, as discussed in preceding chapters. However, to properly design and investigate an adsorption system, additional information concerning adsorption kinetics is needed. The reason for this is simply that most practical adsorbents used in adsorption processes and systems are porous and the overall adsorption rate is controlled by the ability of adsorbate molecules to diffuse into its interior through the porous network pathways due to the fact that the intrinsic adsorption rate at the surface is usually much faster than the diffusion rate [47]. Moreover, because adsorption is accompanied by the release of energy, adsorption kinetics is also influenced by the heat dissipation properties of these materials.

In an adsorption system, mass transport occurs over a wide range of length scales [90], as illustrated in figure 7.1. At the largest scale (figure 7.1a), hydrodynamic effects within interparticle volume influence flow patterns and mass transfer between bulk fluid and porous particles or pellets. In the adsorbent (particle or pellet - figure 7.1b), mass transport in its pores may occur by several different mechanisms depending on many factors, such as pore size, pressure and temperature conditions and others. In macropores, where the diffusing molecule escapes from the adsorbent surface field, gas-phase diffusion occurs via bulk diffusion (figure 7.1c) or Knudsen diffusion (figure 7.1d), depending on the relative magnitude of the mean free path of molecules, $\lambda$, and the mean pore size, $\overline{r}_p$, as it will be discussed in the next sections. In micropores, such as the intracrystalline pores of activated carbon (see section 2.4), the diffusing molecule never escapes from the force field of the adsorbent and mass transport occurs by an activated process involving jumps between adsorption sites. Such a process is often called surface diffusion (figure 7.1e) or,

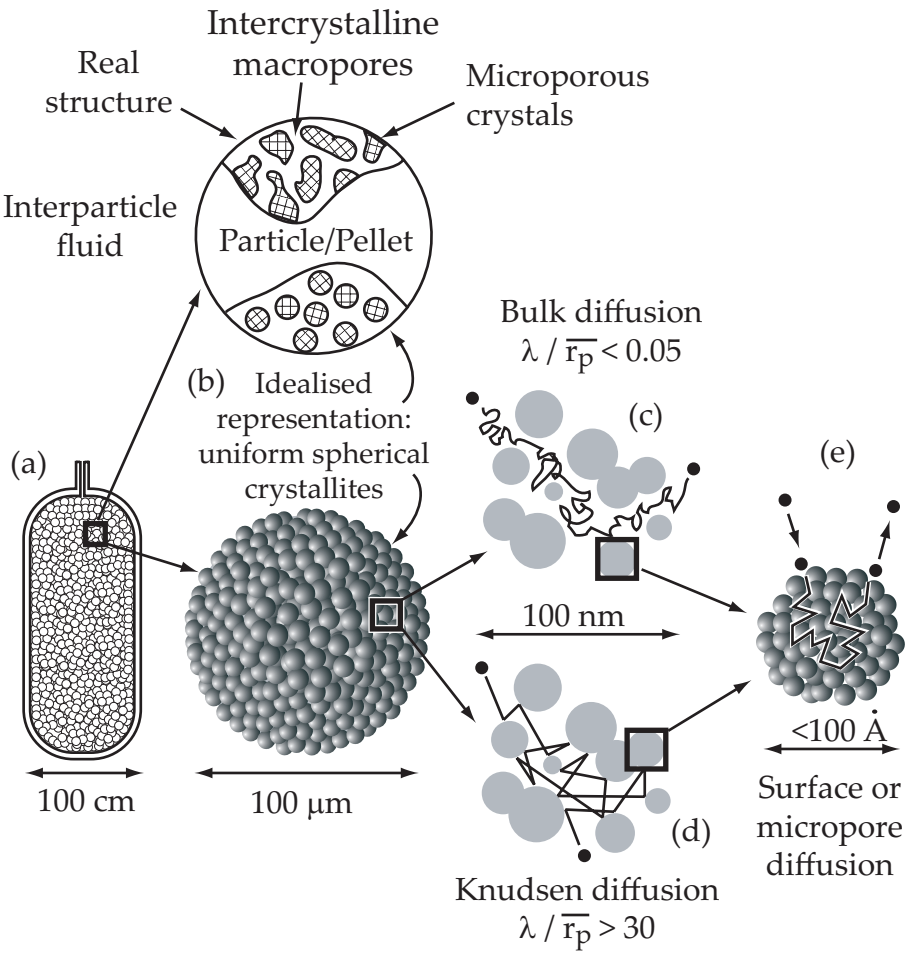


**Figure 7.1:** Different length scales over which mass transport occurs in an adsorption system [90]: Hydrodynamic flow driven by local pressure gradients at device length scales (a), intraparticle mass transport (b) involving bulk (c) or Knudsen (d) gas phase diffusion driven by local concentration gradients. Surface diffusion (e) occurring over atomic length scales as adsorbed molecules move on the microporous surface. (b) also shows the idealised porous structure of an adsorbent pellet or particle.

more generally, micropore diffusion. Surface diffusion also occurs along the pore walls of macropores, thus contributing as an additional transport path.

In chapter 6, an adsorption system was analysed by means of a lumped model, with which no attempt is made to describe all the details of the system and

only an overall view of average conditions is obtained. In this chapter, the system will be analysed at the microscopic level. For that, a set of equations is written down, called the "equations of change" or "conservation equations", which describe how mass, momentum and energy change within a small region in the system. The aim here is to get information about pressure, temperature, velocity profiles, among others, within the system. This more detailed information permits a better understanding of what is happening inside the vessel.

The chapter starts by presenting the equations of change used in this work. Since these equations are extensively analyzed in related literature and their derivation and analysis is not subject of this work, they will just be written down with a explanation of their various terms. For detailed information and derivation, the reader is referenced to the books by Bird [11], Kaviany [42] and Do [28].

Subsequently, mass transport equations are presented to describe gas diffusion in porous media. These equations are then used to describe essential terms in the conservation equations. Different transport mechanisms, as exemplified above, are considered. Several books and publications address this subject and the theory presented here is mainly based on the books by Ruthven [65], Suzuki [77], Do [28], Cunningham and Williams [25] and Mason and Malinauskas [44].

## 7.1 Conservation equations

The conservation equations are equations of balance for particular extensive properties obtained by taking account of the different ways these properties can be changed. These extensive properties are: mass, momentum and energy.

This section presents the conservation equations for fluid flow in porous media with adsorption effects. They include as a special case the conservation equations for pure fluid flow, which are obtained by setting some coefficients

and properties to zero. This is an important feature when investigating adsorption systems with bulk gas volume because the structure of the equations is the same and the coupling of fluid flow and porous media domains is straightforward.

The equations presented here use the superficial velocity in porous media regions, which is related to the physical velocity by

$$\vec{v}_{\text{superficial}} = \varepsilon_{\text{void}} \vec{v}_{\text{physical}}, \tag{7.1}$$

where $\varepsilon_{\text{void}}$ is the total porosity of the medium. The superficial velocity (denominated by $\vec{v}$ in the following text) is commonly used when dealing with porous media since porous resistance coefficients of well-established empirical correlations are usually based on superficial velocity.

### 7.1.1 The equation of continuity

The equation of continuity describes the time rate of change of the fluid density at a fixed point in space. Using vector notation, it can be written as

$$\underbrace{\frac{\partial}{\partial t}\left(\varepsilon_{void}\rho^{g} + \rho^{s} n^{e}\right)}_{\substack{\text{rate of increase of mass} \\ \text{per unit volume}}} = \underbrace{-\nabla \cdot \vec{J}}_{\substack{\text{net rate of mass addition} \\ \text{per unit volume by} \\ \text{convection}}} . \tag{7.2}$$

where $\vec{J}$ stands for the mass flux ($\vec{J} = \rho \vec{v}$). In a pure fluid flow domain: $\varepsilon_{void} = 1$ and $\rho^{s} = 0$.

Equation 7.2 assumes local thermodynamic equilibrium between bulk gas and adsorbed phase, since the intrinsic adsorption rate is much faster than the diffusion rate [47].

### 7.1.2 The equation of motion

The equation of motion describes the time rate of change of momentum at a fixed point in space. It is a vectorial equation and can be expressed as

$$\underbrace{\frac{\partial}{\partial t}\rho^g \vec{v}}_{\substack{\text{rate of increase of}\\ \text{momentum per unit}\\ \text{volume}}} = \underbrace{-\left[\nabla \cdot \rho^g \vec{v}\vec{v}\right]}_{\substack{\text{rate of momentum}\\ \text{addition by convection}\\ \text{per unit volume}}} \underbrace{-\nabla P - [\nabla \cdot \tau]}_{\substack{\text{rate of momentum}\\ \text{addition by molecular}\\ \text{transport per unit}\\ \text{volume}}} \underbrace{+\vec{F}}_{\substack{\text{external}\\ \text{force on}\\ \text{fluid per}\\ \text{unit}\\ \text{volume}}} . \tag{7.3}$$

where $\tau$ is the stress tensor. There is no term related to the adsorbed phase on the left side of the equation 7.3 because the adsorbed phase is assumed to be stationary and the momentum loss due to adsorption is neglected.

In a pure fluid flow domain: $\vec{F} = 0$ (gravity is not considered). In a microporous medium domain, such as activated carbon, $\vec{F}$ includes the porous medium resistance forces and its absolute value is a very large number. Due to this reason, all other terms in equation 7.3 (with exception of $\nabla P$, which is the driving force) are negligible compared to $\vec{F}$ and equation 7.3 reduces to

$$\nabla P \cong \vec{F}. \tag{7.4}$$

Equation 7.4 has essentially the form of well-established empirical correlations for describing flow in porous media: pressure gradients as a function of mass fluxes or gas velocities — $\nabla P = \vec{F}$ =f($\vec{J}$) or $\nabla P = \vec{F}$ =f($\vec{v}$) — or vice-versa. As shown by Sereno and Rodrigues [71], such a steady-state momentum equation can be safely used for describing adsorption processes such as the pressurization/blowdown of adsorption systems. However, the general momentum equation 7.3 is used since it allows easily coupling to pure fluid flow domains. Transport equations of the form of equation 7.4, to be presented in the next sections, are just used to define $\vec{F}$.

### 7.1.3 The energy equation

This equation of change describes the energy conservation at a fixed point in space and is given by

$$\underbrace{\frac{\partial}{\partial t}\left(\varepsilon_{void}\rho^g u^g + \rho^s H^e + U^s\right)}_{\text{rate of increase of energy per unit volume}} = \underbrace{-\left[\nabla \cdot u\vec{J}\right]}_{\substack{\text{rate of energy addition} \\ \text{per unit volume by} \\ \text{convective transport}}} \underbrace{+\left[\nabla \cdot k_{\text{eff}}\nabla T\right]}_{\substack{\text{rate of energy} \\ \text{addition per unit} \\ \text{volume by heat} \\ \text{conduction}}} \underbrace{-\left[\nabla \cdot P\vec{v}\right]}_{\substack{\text{rate of work done on} \\ \text{fluid per unit volume} \\ \text{by pressure forces}}} \underbrace{-\left[\nabla \cdot (\tau \cdot \vec{v})\right]}_{\substack{\text{rate of work done on} \\ \text{fluid per unit volume} \\ \text{by viscous forces}}} \underbrace{+\left[\vec{F} \cdot \vec{v}\right]}_{\substack{\text{rate of work} \\ \text{done on fluid} \\ \text{per unit volume} \\ \text{by external} \\ \text{forces}}} . \qquad (7.5)$$

where $k_{\text{eff}}$ is the effective thermal conductivity. In equation 7.5, local thermal equilibrium between phases is assumed [42][6]. The term related to work by viscous forces may be neglected because it is only important for systems with very large velocity gradients. The terms on the left side of equation 7.5 are described according to chapter 3 (specially sections 3.1 and 3.62). In a pure fluid flow domain, $\varepsilon_{void}$ is equal to one and $\rho^s$ and $U^s$ are both equal to zero.

The energy equation for pure heat conduction regions, such as the vessel wall,

[6] For local thermal equilibrium between the solid and the fluid to be valid, length and time scale criteria must be satisfied. The time scale $t$ must satisfy

$$\frac{\varepsilon(\rho c)^f l^2}{t}\left(\frac{1}{k^s}+\frac{1}{k^f}\right) \ll 1 \quad \text{and} \quad \frac{(1-\varepsilon)(\rho c)^s l^2}{t}\left(\frac{1}{k^s}+\frac{1}{k^f}\right) \ll 1.$$

The lenght scale must satisfy

$$\frac{\varepsilon k^f l}{AL^2}\left(\frac{1}{k^s}+\frac{1}{k^f}\right) \ll 1 \quad \text{and} \quad \frac{(1-\varepsilon)k^s l}{AL^2}\left(\frac{1}{k^s}+\frac{1}{k^f}\right) \ll 1.$$

Since for the system in consideration here the length scale $l$ is in the order of $\approx 100\ \dot{A}$ ($l$ is the mean pore size) and the specific surface area $A$ in the order of $\approx 3000\ m^2/g$, the criteria are easily satisfied.

is

$$\underbrace{\frac{\partial}{\partial t}U^w}_{\substack{\text{rate of increase of energy} \\ \text{per unit volume}}} = \underbrace{\left[\nabla \cdot k^w \nabla T\right]}_{\substack{\text{rate of energy} \\ \text{addition per unit} \\ \text{volume by heat} \\ \text{conduction}}}. \tag{7.6}$$

## 7.2 Special case: pellets

As noted in section 2.4, pellets consist of small microporous crystals compressed into larger forms, thus showing a bi-disperse porous structure. Due to this reason, several different types of diffusion mechanisms may occur within its pores and sometimes two or three of them may even compete or cooperate. The relative importance of them depends on the ratio of their diffusional time constants which varies widely depending on many factors, such as pressure and temperature.

In studying diffusion, the diffusion flux is often described by means of the diffusion coefficient defined by Fick's first law [39] taking pressure gradients as the driving force [28] [77]

$$J_x = -D_{\text{eff}} \frac{M}{RT} \frac{\partial P}{\partial x}, \tag{7.7}$$

where $D_{\text{eff}}$ is the effective diffusion coefficient. Transport equations engage in defining this coefficient. The following two subsections present the transport equations used in macropores and micropores.

### 7.2.1 Diffusion in macropores

Macropores act as a path for the adsorbate molecules to reach the interior of the adsorbent. Two distinct mechanisms of transport may be identified: Knudsen diffusion and bulk diffusion (which, under a pressure gradient, becomes a viscous flow). In addition, surface diffusion may also occur on the walls of the macropores. However, since the mobility of adsorbed molecules

is much smaller than that of bulk gas molecules [65], surface flow contribution is not expected to be significant in macropores. Thus, only gas phase diffusion is assumed in macropores.

The Knudsen number $Kn$ is a dimensionless number defined as the ratio of the molecular mean free path to a representative physical length scale, here, the pore size. It is useful for determining whether statistical mechanics or the continuum mechanics formulation of fluid dynamics should be used to describe a process. When $Kn \gg 1$, the continuum assumption of fluid mechanics is no longer a good approximation and the theoretical analysis is undertaken using the kinetic theory of gases. For a one component system under this condition, a pressure gradient (a gradient of concentration of molecules) causes a net flux of molecules towards the region of lower concentration due to the chaotic motion of the molecules. In this flow, which is known as Knudsen diffusion or Knudsen flow, the probability of collisions between gas molecules is negligible compared to that of gas molecules and pore wall, so that the main diffusional resistance for the advancing molecules is the latter collisions. The Knudsen flux $J_K$ is given by [28]

$$J_{K_x} = -\underbrace{\frac{4}{3}K_0\sqrt{\frac{8RT}{\pi M}}}_{D_K}\frac{M}{RT}\frac{\partial P}{\partial x}, \tag{7.8}$$

where $D_K$ is the Knudsen diffusion coefficient and $K_0$ is a structural parameter to characterize the porous medium or pore. For a straight cylindrical pore of radius $r$, this parameter is $K_0 = r/2$.

In the opposite condition, namely when $Kn \ll 1$, the continuum mechanics is again applicable and this mechanism may be analyzed using fluid mechanics. Under a pressure gradient, gas transport may be viewed as a laminar viscous flow in the pore volume, the fluid layer on the pore wall being stationary against it. This flow can be described by the well-known Hagen-Poiseuille equation [11], obtained from the Navier-Stokes equation [11]. The viscous flux

$J_V$ is given by [28]

$$J_{V_x} = -\rho^g \frac{B_0}{\mu^g}\frac{\partial P}{\partial x} = -\underbrace{B_0 \frac{P}{\mu^g}}_{D_V}\frac{M}{RT}\frac{\partial P}{\partial x}, \tag{7.9}$$

where $D_V$ is the "diffusion coefficient" for viscous flow and $B_0$ is likewise a structural parameter to characterize the porous medium or pore. For a straight cylindrical pore of radius $r$, this parameter is $B_0 = r^2/8$.

It is evident that there must be an intermediate region, in which the permeating gas maintains some of the features of a bulk fluid (making the theoretical analysis amenable to fluid mechanical interpretation) and some of the features of an assembly of independent molecules (making the kinetic theory of gases appropriate as well). This phenomenon is called slip flow. It is called so because the fluid on the pore wall has a certain velocity with respect to it, in contrast to a viscous flow, where the relative velocity is zero. In a viscous flow, the molecules colliding with the wall are diffusely reflected and so have lost, on the average, the component of their momentum along the direction of the flow of gas produced by the pressure gradient. These molecules tend to decrease the average velocity of the molecules surrounding the pore wall and this damping effect continues until the velocity of the fluid layer on the wall reaches the same velocity as the wall. In a slip flow, however, not all rebounded molecules from the pore wall collide with adjacent gas molecules, so that the damping effect is not as strong as in a viscous flow and the fluid layer on the wall maintains a certain velocity with respect to the wall. In the literature, many semiempirical descriptions have been proposed to characterize slip flow [25], however, in this work the results obtained by a very popular gas diffusion model, the dusty gas model, are used to characterize it.

The dusty gas model, described in detail in the book by Mason and Malinauskas [44], is so called because it treats the porous medium as consisting of uniformly distributed, giant molecules held stationary in space, like dust in a gas. Transport equations for the gas through the porous media are derived by applying the kinetic theory of gases to this “mixture” of free gas and fixed solid molecules. A force balance for single-gas permeation yields an expression for the flux of the advancing molecules, which, in a sense, explains the

semi-empirical correlation proposed by Knudsen to correlate his experimental data covering a wide range of pressure. It takes the form

$$J_x = -\left(D_V + D_K \frac{1+2c_K P}{1+2.47 c_K P}\right)\frac{M}{RT}\frac{\partial P}{\partial x}, \tag{7.10}$$

where

$$c_K = \sqrt{\frac{8}{\pi}}\frac{r}{\mu\overline{v}} \quad \text{and } \overline{v} = \sqrt{\frac{8RT}{\pi M}}. \tag{7.11}$$

The first term in the parenthesis of equation 7.10 accounts for the viscous flow (equation 7.9). The second term is the Knudsen flow (equation 7.8) multiplied by a term which is equal to one when the pressure is zero and approximately equal to 2/2.47 (=0.81) for very high pressures. Thus, the dusty gas model explains the slip flow as a combination of viscous and Knudsen flows. As it can be seen in equation 7.9, the viscous flow goes to zero as the pressure goes to zero so that the Knudsen term dominates at low pressures, whereas, at high pressures, the viscous term dominates. At intermediate pressures, the two mechanisms control the transport. Mason [44] shows that experimental measurements over wide range of pressures are well described by the combination of viscous plus Knudsen components.

Using equation 7.10 for describing diffusion in porous media requires the porous medium structural parameters $K_0$ and $B_0$, which are generally unknown. They can be determined if the porous structure of the solid is known, however, the porous structure of a real adsorbent is so complex that these parameters are often obtained experimentally by fitting the model to experimental data. Several works in related literature concentrate on describing the porous structure of solids. Burganos *et al.* [20], for instance, used randomly oriented capillary structures whereas Malek *et al.* [43] used capillaries with obstacles on its internal surface. More realistic results are obtained when the structure of ramdonly packed and overlapped spheres or cylinders is used to describe the details of a porous medium, as shown in figure 7.2 from the publication by Zalc *et al.* [90].

Monte-Carlo simulations are carried out to determine the gas diffusion coefficients in such structures and the results are often given by means of a tortu-

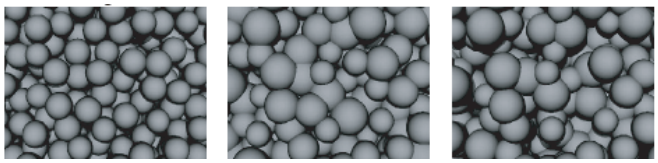

**Figure 7.2:** Examples of model complex porous structures constructed with sphere packing in the publication by Zalc *et al.* [90]. The pictures show structures with different porosities.

osity factor $\tau$, which is defined as

$$\tau_{\text{ma}} = \varepsilon_{\text{ma}} \frac{D_{\text{cap}}}{D_{\text{eff}}}, \tag{7.12}$$

where $\varepsilon_{\text{ma}}$ is the macroporosity of the structure and $D_{\text{ma}}$ is the diffusion coefficient in an equivalent capillary of radius $\overline{r}_p$, the mean pore size of the structure.

The tortuosity relates the diffusion coefficient in a porous media to that in a capillary, which can be accurately estimated. Thus, the knowledge of the tortuosity of a porous media allows one to estimate gas diffusion coefficients in its porous structure. The tortuosity accounts for two effects: random orientation of the pores, which gives a longer diffusion path and reduced driving force gradients in the direction of flow, and the variation in the pore size or diameter, since the extra resistance in narrow parts is not balanced by the reduced resistance in wide parts. The results from Zalc *et al.* [90] for the tortuosity of porous structures such as the one shown in figure 7.2 is shown in figure 7.3 as a function of the void fraction (macroporosity). Experimental tortuosities generally fall within the range 2-6.

Comparing equation 7.10 written for a porous medium and for a capillary (subscript $_{cap}$) and using equations 7.8, 7.9 and 7.12, it can be shown that the structural parameters $K_0^{'}$ and $B_0^{'}$ of the porous medium are given by

$$K_0^{'} = \frac{\varepsilon_{\text{ma}}}{\tau_{\text{ma}}} K_{0\text{cap}} = \frac{\varepsilon_{\text{ma}}}{\tau_{\text{ma}}} \frac{\overline{r}_p}{2}, \tag{7.13}$$

$$B_0^{'} = \frac{\varepsilon_{\text{ma}}}{\tau_{\text{ma}}} B_{0\text{cap}} = \frac{\varepsilon_{\text{ma}}}{\tau_{\text{ma}}} \frac{\overline{r}_p^{\,2}}{8}. \tag{7.14}$$

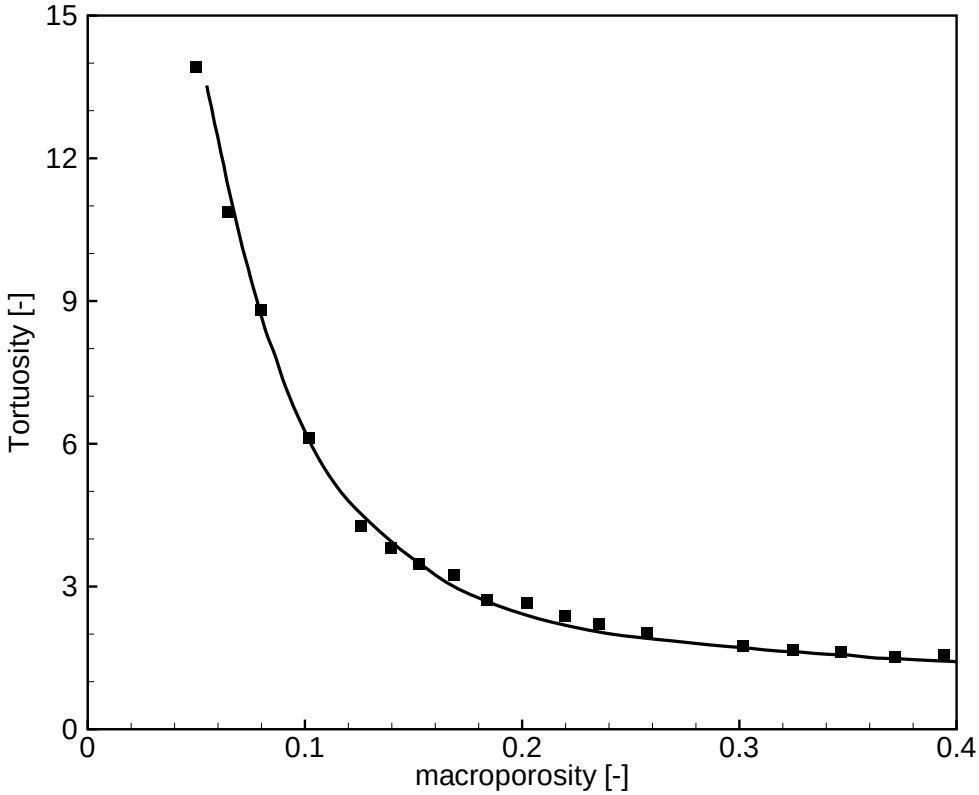


**Figure 7.3:** Macrovoid tortuosity as a function of macroporosity for porous structures constructed with sphere packing as shown in figure 7.2. From the publication by Zalc *et al.* [90].

Thus, the total flux $J_{\mathrm{ma}}$ in the macropores is given by equation 7.10, whereas the terms $D_K$ and $D_V$ are given by equations 7.8 and 7.9, respectively, and the structural parameters are given by equations 7.13 and 7.14. Joining all these equations, it gives that

$$J_{\mathrm{ma}_x} = \frac{\varepsilon_{\mathrm{ma}}}{\tau_{\mathrm{ma}}} \left( \frac{\overline{r}_p^2}{8} \frac{P}{\mu^g} + \frac{2\overline{r}_p}{3} \sqrt{\frac{8RT}{\pi M}} \cdot \frac{1+2c_K P}{1+2.47c_K P} \right) \frac{M}{RT} \frac{\partial P}{\partial x}. \tag{7.15}$$

The pore size distribution of the activated carbon used in this work has not been explicitly determined. Therefore, the mean pore radius $\overline{r}_p$ in equation 7.15 is used as a fitting parameter in order to reproduce experimental data presented in the next chapters.

### 7.2.2 Diffusion in micropores

Diffusion in micropores is analogous to surface diffusion, in which the diffusing molecules never scape from the force field of the adsorbent and mass transport occurs by an activated process involving jumps between adsorption sites (compare section 2.1). The existence of a net flux in the micropore is thus a probabilistic phenomenon that depends on the existence of a concentration gradient of hopping molecules.

The literature offers some models for the estimation of micropore diffusitivies. However, the application of these models requires the knowledge of parameters of the adsorbed molecule - pore wall interaction, the determination of which is almost impossible [25]. But these models do show that the micropore diffusivity $D_S$ may be given by [25] [77]

$$D_S = D_S^* \exp\left(\frac{-E_s}{RT}\right), \tag{7.16}$$

where $D_S^*$ is the diffusivity at infinite temperature and $E_S$ is the activation energy of hopping, i.e., the energy barrier between two consecutive adsorption sites. The net flux in the micropores can then be defined in terms of a Fick's-type law with adsorbed concentration gradients as the driving force as [25] [77]

$$J_{\mathrm{mi}_x} = \frac{\varepsilon_{\mathrm{mi}}}{\tau_{\mathrm{mi}}} D_S \rho^s M \frac{\partial n^a}{\partial x} = \frac{\varepsilon_{\mathrm{mi}}}{\tau_{\mathrm{mi}}} D_S \rho^s M \frac{\partial n^a}{\partial P}\frac{\partial P}{\partial x}, \tag{7.17}$$

where $\varepsilon_{\mathrm{mi}}$ is the microporosity and $\tau_{\mathrm{mi}}$ is the micropore tortuosity.

Because of the lack of suitable and theoretical models for calculating $D_S$, attempts have been made to obtain an "universal" empirical relationship for estimating it. Using extensive data given in the literature and his own results, Sladek *et al.* [74] proposed the following relation:

$$D_S = 1.6 \cdot 10^{-6} \exp\left(\frac{-E_s}{mRT}\right), \tag{7.18}$$

$$E_s = 0.45|\overline{\Delta h^e}|. \tag{7.19}$$

where $m$ depends on the type of sorbent-sorbate bond and is equal to one for the case of hydrogen on carbon and $|\overline{\Delta h^e}|$ stands for the average isosteric heat. In equation 7.18, $D_S$ is given in $[m^2/s]$.

### 7.2.3 Total diffusional flux

The total diffusional flux in the adsorbent is obtained by adding the diffusional flux in both macropores (section 7.2.1) and micropores (section 7.2.2) as

$$\vec{J} = \vec{J}_{\mathrm{ma}} + \vec{J}_{\mathrm{mi}}\,. \tag{7.20}$$

Inserting equations 7.15 and 7.17 into equation 7.20, one obtains

$$J_x = \left[\frac{\varepsilon_{\mathrm{ma}}}{\tau_{\mathrm{ma}}}\left(\frac{\overline{r}_p^2}{8}\frac{P}{\mu^g} + \frac{2\overline{r}_p}{3}\sqrt{\frac{8RT}{\pi M}}\cdot\frac{1+2c_K P}{1+2.47c_K P}\right)\frac{M}{RT} + \frac{\varepsilon_{\mathrm{mi}}}{\tau_{\mathrm{mi}}}D_S\rho^s M\frac{\partial n^a}{\partial P}\right]\frac{\partial P}{\partial x}\,. \tag{7.21}$$

Writing the vectorial form of equation 7.22, solving for the pressure gradient and using the relation $\vec{J} = \rho^g\,\vec{v}$, it follows that

$$\nabla P = \frac{\rho^g}{\left[\frac{\varepsilon_{\mathrm{ma}}}{\tau_{\mathrm{ma}}}\left(\frac{\overline{r}_p^2}{8}\frac{P}{\mu^g} + \frac{2\overline{r}_p}{3}\sqrt{\frac{8RT}{\pi M}}\cdot\frac{1+2c_K P}{1+2.47c_K P}\right)\frac{M}{RT} + \frac{\varepsilon_{\mathrm{mi}}}{\tau_{\mathrm{mi}}}D_S\rho^s M\frac{\partial n^a}{\partial P}\right]}\vec{v}\,. \tag{7.22}$$

Equation 7.22, which corresponds to equation 7.4 relating pressure gradients to resistance forces per unit volume in porous media, can be used to describe $\vec{F}$ in pellets. Comparing equations 7.4 and 7.22, it follows that

$$\vec{F}_{\mathrm{pellet}} = \frac{\rho^g}{\left[\frac{\varepsilon_{\mathrm{ma}}}{\tau_{\mathrm{ma}}}\left(\frac{\overline{r}_p^2}{8}\frac{P}{\mu^g} + \frac{2\overline{r}_p}{3}\sqrt{\frac{8RT}{\pi M}}\cdot\frac{1+2c_K P}{1+2.47c_K P}\right)\frac{M}{RT} + \frac{\varepsilon_{\mathrm{mi}}}{\tau_{\mathrm{mi}}}D_S\rho^s M\frac{\partial n^a}{\partial P}\right]}\vec{v}\,. \tag{7.23}$$

## 7.3 Special case: adsorption bed

The adsorption bed to be investigated in this work is formed by filling a volume with powdered activated carbon, the powder particles are assumed to be spherical. Considering, for instance, the filling of an adsorption system composed of such an adsorption bed, there is an initial time period during which the filling is controlled by hydrodynamics of flow through the packed bed (in

the interparticle volume). Due to the increase of the interparticle pressure, diffusion of gas molecules into the particles through the pores (intraparticle diffusion) starts because of pressure gradients along the radius. Depending on factors such as the size of the particles and the magnitude of the diffusion coefficient, intraparticle diffusion may, or not, limit the filling rate. Mota *et al.* [50] has shown that the consideration of intraparticle diffusion is only important if

$$\frac{D_{\text{eff}}}{R_p^2} < 0.1\,, \tag{7.24}$$

where $D_{\text{eff}}$ is the intraparticle diffusion coefficient and $R_p$ is the particle radius. If equation 7.24 is not satisfied, then the particle response to changes in the interparticle volume is very fast and pressure distribution along radius reaches homogeneity quickly. The reason for that is that either the diffusion is quick enough or the particle is small enough.

Intraparticle diffusion may be described in the same way as done for diffusion in pellets in section 7.2, so that the diffusion coefficient is expected to be of order of $10^{-8} - 10^{-6}$ m$^2$/s, which is in agreement with results of dynamic molecular simulations [9]. As it will be discussed in the next chapters, the mean particle radius considered in this work is about 100 $\mu$m, so that, in this work,

$$\frac{D_{\text{eff}}}{R_p^2} \geq 1\,. \tag{7.25}$$

Thus, intraparticle resistances can be safely neglected because the particles are sufficiently small and homogeneous pressure (but time varying) may be assumed within the particles, which is equal to the interparticle pressure. Thus, adsorption bed dynamics is controlled by the hydrodynamics of the flow through it. This process may be described the same way as diffusion in pellets, however, with different resistance forces in the momentum equation.

Many theoretical approaches for studying pressure drops through packed beds can be found in the literature [11] and a well-known and widely used correlation due to its wide range of validity is the Ergun's equation, which regards the packed bed as a bundle of tangled tubes of weird cross section. The vectorial form of Ergun's equation, using the superficial velocity, can be expressed

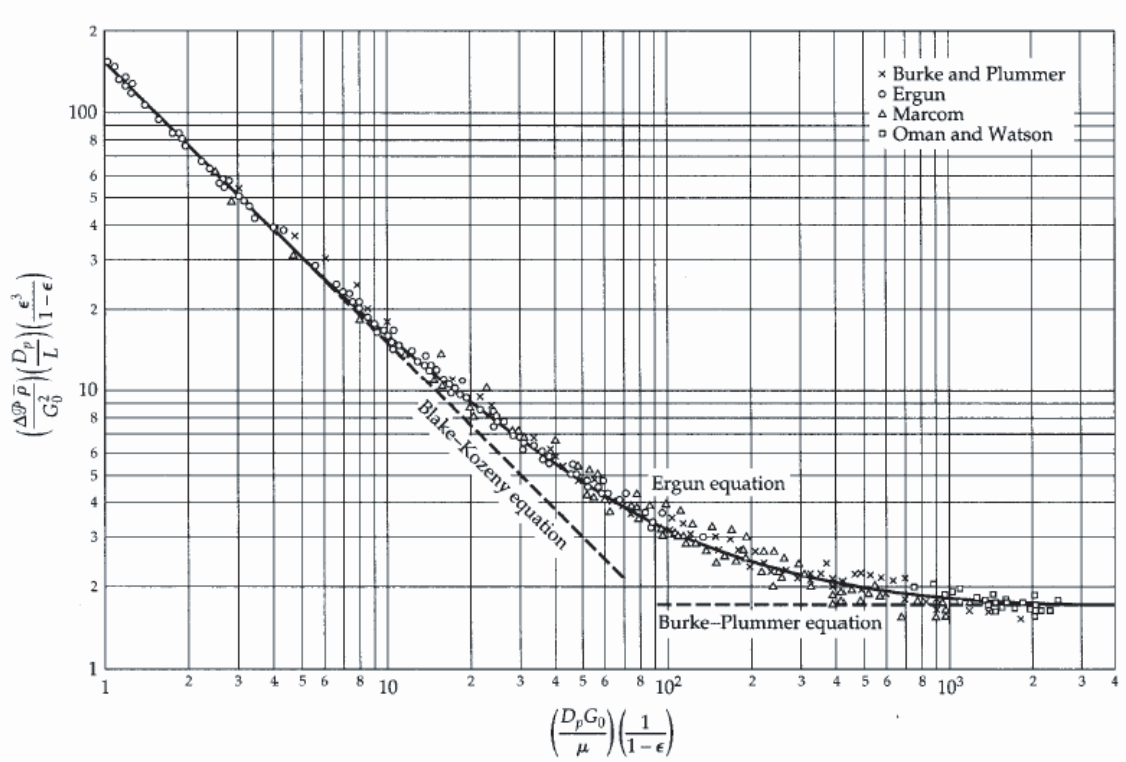


**Figure 7.4:** The Ergun Equation for flow in packed beds and the two related asymptotes. From the book by Bird [11].

as [11]

$$\nabla P = \underbrace{150\frac{\mu^g}{D_p^2}\left(\frac{(1-\varepsilon_b)^2}{\varepsilon_b^3}\right)\vec{v}}_{\text{viscous losses}} + \underbrace{1.75\frac{\rho^g}{D_p}\left(\frac{1-\varepsilon_b}{\varepsilon_b^3}\right)|\vec{v}|\,\vec{v}}_{\text{inertial losses}}, \tag{7.26}$$

where $\varepsilon_b$ is the bed porosity and $D_p$ is the equivalent spherical particle diameter, which is defined by

$$D_p = 6\frac{\text{Volume of the particle}}{\text{Surface area of the particle}}. \tag{7.27}$$

It must be noted that, for undensed beds, $D_p$ is the real particle diameter, whereas, for densed beds, the flow is governed by the width of channels between particles and an effective particle diameter relative to it has to be used [26]. Equation 7.26 is shown in figure 7.4 along with the Blake-Kozeny and Burke-Plummer equations, which represents the asymptotes of Ergun's

equation, and experimental data. Ergun's equation has been applied with success to gas flow through packed beds [11].

Comparing equations 7.4 and 7.26, it follows that the flow resistance forces in packed beds can be expressed as

$$\vec{F}_{\text{bed}} = 150\frac{\mu^g}{D_p^2}\left(\frac{(1-\varepsilon_b)^2}{\varepsilon_b^3}\right)\vec{v} + 1.75\frac{\rho^g}{D_p}\left(\frac{1-\varepsilon_b}{\varepsilon_b^3}\right)|\vec{v}|\,\vec{v}\,. \tag{7.28}$$

As to heat transfer, it appears to be realistic to consider it only at bed scale, i.e., to assume an uniform temperature (but time varying) within the particles and to assume local thermal equilibrium between interparticle fluid and particles. Temperature gradients exist only between different particles. Uniform temperature is based upon the fact that the Lewis number[7] of the particles is sufficiently large (approx. $\geq 10$, pointing to a much faster thermal diffusivity compared to mass diffusivity) and that the Fourier number[8] of the particles is much larger than one, even for small times. Concerning the local thermal equilibrium, it can be justified by the fact that the thermal time constant[9] of the particles is much lower than one, meaning that the particles response to changes in the interparticle volume is very fast and the time required to reach thermal equilibrium approaches zero.

[7]The Lewis number is a dimensionless number defined as the ratio of thermal diffusivity to mass diffusivity:

$$Le = \frac{\alpha}{D} = \frac{\frac{k^s}{\rho c_p}}{D}.$$

[8]The Fourier number is a dimensionless time defined as the ratio of the heat conduction rate to the rate of thermal energy storage:

$$Fo = \frac{\alpha\, t}{L^2} = \frac{\frac{k^s}{\rho c_p}\, t}{L^2}.$$

[9]The thermal time constant is defined as:

$$\tau_{th} = \frac{1}{Fo\,Bi}, \text{ where } Bi = \frac{h\,L}{k^s} \text{ is the Biot number}.$$

The lower $\tau_{th}$, the faster is the response of a solid to changes in its thermal environment (the shorter is the time to reach thermal equilibrium). The particle-to-fluid heat transfer coefficient $h$ can be estimated from Nusselt correlations [81] ($Nu = \frac{hL}{k^f} = 2 + 1.1 Pr^{1/3} Re^{0.6}$) and the value obtained for this case for quiescent fluid is about 250 W/(m$^2$ K).

## 7.4 Effective thermal conductivity

Heat conduction through fully saturated matrices, i.e., a fluid occupying the pores of a solid, depends on the porous structure as well as on the thermal conductivity of each phase. One of the most difficult aspects of the analysis of heat conduction through a porous medium is the structural modeling because the representative elementary volumes are three-dimensional and have complicated structures. Since the thermal conductivity of the solid is generally larger than that of the fluid, the manner in which the solid is interconnected influences the conduction significantly. Even when dealing with non-consolidated particles (packed beds), the contact between the particles plays a significant role.

For the analysis of the macroscopic heat conduction through packed beds, effective properties, such as the effective thermal conductivity $k_{\text{eff}}$, are used. Several models and strategies are available for the calculation of $k_{\text{eff}}$. One possibility is to consider the packed bed to be a periodic arrangement of particles, and the effective thermal conductivity is obtained by a series-parallel arrangement of different modes of heat conduction [62], such as conduction through the particles, heat transfer through particle contacts, conduction through the stagnant fluid near the contact surface and others. Another possibility is to apply the technique of volume averaging [42] and introduce the structure of the bed through a function that has to be determined empirically. Hadley [42] used the volume averaging approach and experimental data to arrive at a generalized correlation. He suggests that the effective thermal conductivity $k^0_{\text{eff}}$ of a quiescent bed may be calculated by

$$\frac{k^0_{\text{eff}}}{k^f} = (1-\alpha_0)\,\frac{\epsilon f_0 + \frac{k^s}{k^f}\left(1-\epsilon f_0\right)}{1-\epsilon\left(1-f_0\right)+\frac{k^s}{k^f}\epsilon\left(1-f_0\right)} + \\ +\alpha_0\,\frac{2\left(\frac{k^s}{k^f}\right)^2(1-\epsilon)+(1+2\epsilon)\,\frac{k^s}{k^f}}{(2+\epsilon)\,\frac{k^s}{k^f}+1-\epsilon}, \tag{7.29}$$

where

$$f_0 \;=\; 0.8+0.1\epsilon\,, \tag{7.30}$$

$$\log \alpha_0 = -4.898\epsilon, \text{ for } 0 \leq \epsilon \leq 0.0827, \tag{7.31}$$

$$\log \alpha_0 = -0.405 - 3.154\,(\epsilon - 0.0827), \text{ for } 0.0827 < \epsilon \leq 0.298, \tag{7.32}$$

$$\log \alpha_0 = -1.084 - 6.778\,(\epsilon - 0.298), \text{ for } 0.298 < \epsilon \leq 0.580. \tag{7.33}$$

In equation 7.29, $k^s$ is the thermal conductivity of a particle (activated carbon thermal conductivity), $k^f$ is the fluid thermal conductivity and $\epsilon$ is the interparticle porosity. Figure 7.5 shows the prediction of several models, inclusive that of Hadley, against experimental data. The four predictions are in agreement.

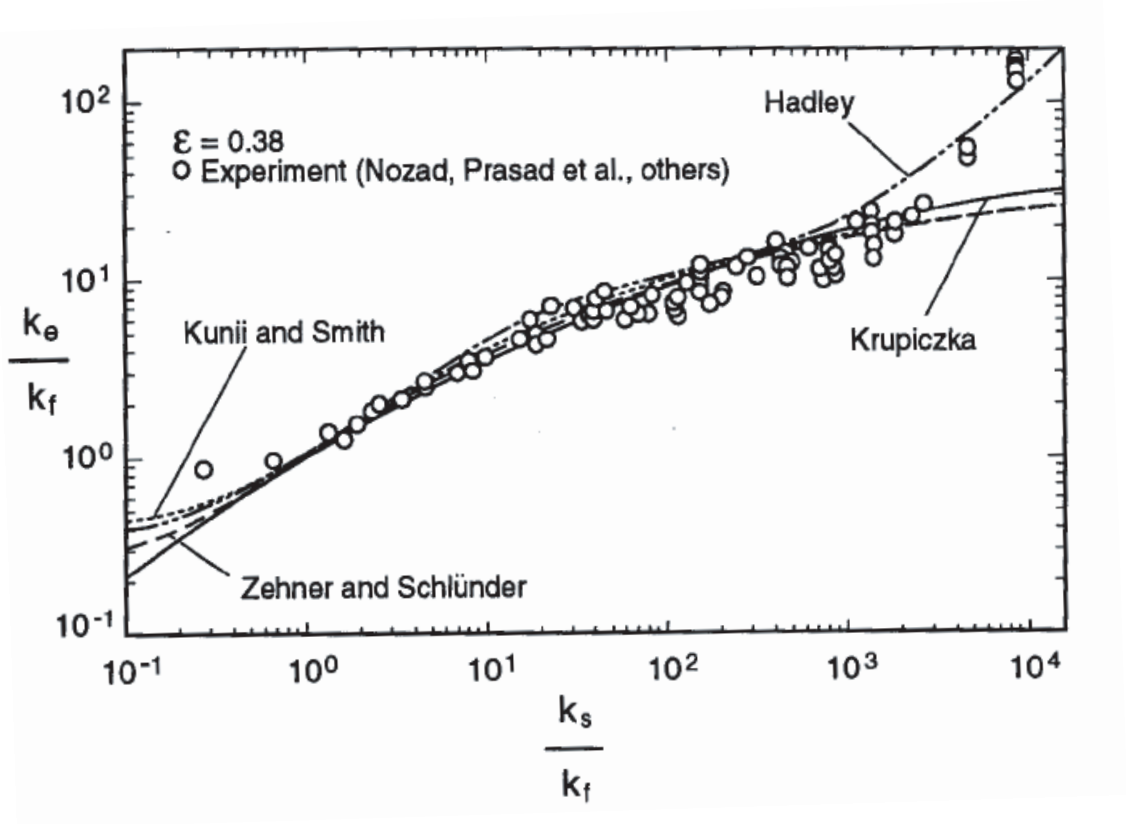


**Figure 7.5:** Effective thermal conductivity of beds of spherical particles predicted by various analyses, including Hadley's model given by equation 7.29. Figure from Kaviany [42].

When the fluid phase flows through the packed bed, the effective thermal conductivity has to be corrected to account for this effect. Wakao and Kaguei [81]

suggests the correlation

$$\frac{k_{\text{eff}}}{k^f} = \frac{k^0_{\text{eff}}}{k^f} + 0.5\,(Pr)\,(Re)\,, \tag{7.34}$$

which is also used in this work. The effective thermal conductivity of both pellet and adsorption bed is calculated with equations 7.29 and 7.34. For adsorption beds, the interparticle porosity of equation 7.29 is set to be the bed porosity, whereas, for pellets, it is set to zero, due to consolidation. (Hadley's model has been chosen because his model is still valid for $\epsilon = 0$).

The thermal conductivity of activated carbon is required as an input for calculating effective thermal conductivities, but there is almost no information available. Biloe *et al.* [10] has measured about 7.3 W/(m K) at room temperature and, according to activated carbon manufactures, it seems to be around one tenth to one thousandth of that of graphite depending on the manufacturing process. Thus, in the calculations to be presented in the next chapters, thermal conductivity of activated carbon is considered to be a fraction of that of graphite, the factor $f_{k^s}$ being used as a fitting parameter to experimental data, i. e.,

$$k^s = \frac{k^{\text{graphite}}}{f_{k^s}}\,, \tag{7.35}$$

where $k^{\text{graphite}}$ is the graphite thermal conductivity.

# 8 Experimental Measurements and Simulations

In the previous chapter, a set of equations has been introduced that describe mass, momentum and energy transport within the different domains of an adsorption vessel system. In this chapter, these equations are used to simulate the behaviour of an adsorption vessel. The latter has been built as test rig for experimental purposes by our project partner FutureCarbon GmbH (located in Bayreuth, Germany), with financial support from GM-Opel Deutschland.

This chapter starts by presenting the vessel geometry and concept as well as the experimental set-up. Capable to accommodate between 10 to 20 kg of adsorbent, depending on the adsorbent type used, the vessel abandons the laboratory scale typical for material characterisation (in the order of milligrams of adsorbent) and gets close to the dimensions of a real system solution (in the order of 100 kg of adsorbent).

Subsequently, a mathematical model of the vessel is developed to describe its dynamic behaviour. Thereby, several geometrical simplifications and assumptions are made in order to obtain an easy-to-handle model without essential loss of details and accuracy.

At the end, the applicability of the model is evaluated by comparing simulation results with dynamic experimental measurements. The results show good agreement between experiments and simulations, thus, allowing the model to be used for investigations of dynamical questions, e.g. loading and unloading strategies and system related occurrences during dynamical processes. This is the goal of the next chapter.

In addition, the comparison of simulations and experiments also includes results obtained with a lumped model such as the one presented in chapter 6.

The lumped model assumes homogeneous distribution of the system properties and completely neglects transport processes and resistances within the system. It is, thus, much simpler than the model to be presented in this chapter. However, in some cases, lumped model results are sufficient to analyse a system. Here, the comparison of both models aims to evaluate the influence of the lumped model assumptions on the results.

## 8.1 Experimental set-up

This subsection presents the test rig and the adsorption vessel [48] built by our project partner FutureCarbon with financial support from GM-Opel Deutschland.

### 8.1.1 Adsorption vessel

Basically, the adsorption vessel consists of three different parts, each one with a specific function. These parts are:

(1) hydrogen storage,

(2) thermal management (cooling and heating) and

(3) insulation.

Hydrogen storage is achieved by the adsorbent contained in several pressure tubes, as shown in figure 8.1a. Altogether, seven tubes are used and they are switched and arranged in parallel. Geometrically, the tubes are completely separated from each other, but they share the same vessel inlet/outlet opening. The utilization of several pressure tubes increases the geometrical flexibility because they can be arranged and grouped in several different ways and other external forms of the adsorption vessel rather than the cylindrical may be obtained. Two adsorbents were used in the experiments: powered activated carbon and pelletized activated carbon (pellet external diameter equal

to the internal tube diameter).Thermocouples were introduced axially into the tubes. In order to be able to introduce the thermocouples through the pellets, they had an axial hole at the centre. In regions where no thermocouple guidance was necessary, there was an eccentrical hole parallel to the pellet axis in order to facilitate gas flow along the pressure tube. The pellets were stacked to completely fill the pressure tubes. The pressure tubes are about one meter long and their internal diameter is about 80 mm.

The pressure tubes are located inside a vessel that can be filled with liquid nitrogen ($LN_2$) to cool down the vessel, as shown in figure 8.1b. The $LN_2$ vessel is as well filled up with cooper wool in order to achieve a better thermal distribution along the tubes, smooth $LN_2$ boiling effects and physically connect the pressure tubes and the $LN_2$ vessel wall, on the outer surface of which a heating mat is located, through which energy is supplied to the system.

The outer vessel layer is the insulation, which consists of several layers of microporous insulation material in an evacuated volume (see 8.1b). The insulation properties are good enough to ensure adiabatic conditions during the course of the experiments.

### 8.1.2 Test rig

Figure 8.2 shows the experimental setup. Four thermocouples are distributed throughout the adsorption vessel, each one at a different pressure tube. One thermocouple is located at the top, two in the middle and one at the bottom. A further thermocouple measures the temperature of the gas entering the vessel and another one is located at the outlet of the gas reservoir. Two pressure transmitters measure the pressure at the vessel inlet and at the gas reservoir outlet, respectively. A mass flow controller is used to control the quantity of gas going from the gas reservoir into the adsorption vessel. The total amount of gas introduced in the vessel was measured simultaneously by the mass flow controller and by the pressure decrease at the gas reservoir. The gas entering the vessel can be pre-cooled by letting it flow through a $LN_2$ bath. All the data were collected at the interface of a microcomputer.

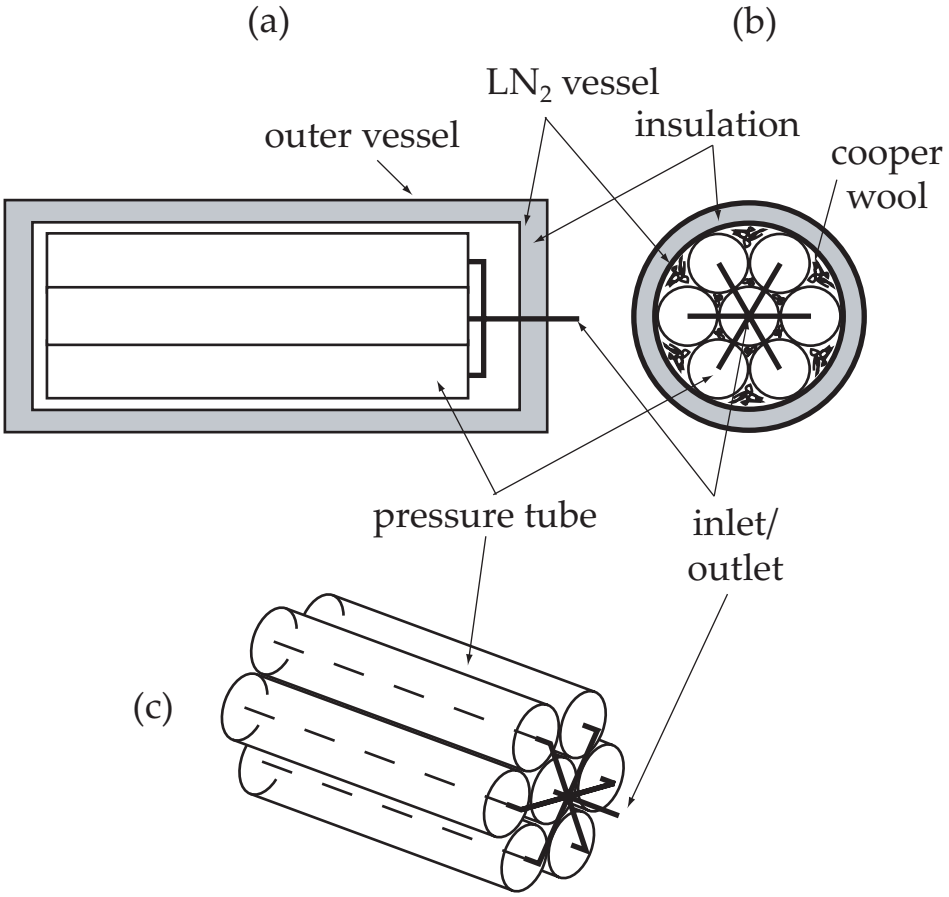


**Figure 8.1:** Adsorption vessel: the different parts and components can be seen. (a) View along the axis. (b) Axial cross-section view. (c) Pressure tubes arrangement inside the $LN_2$ vessel.

## 8.2 Adsorption vessel model

A model is defined as a selected simplified version of the real system that satisfactorily reproduces the behaviour of the latter relevant to the problem at hand. This section presents the conceptual model (set of selected simplifying assumptions that describe the system composition and the processes of transport that take place in it, the mechanism that govern them and the relevant medium properties) used to represent the real adsorption vessel.

In the modelling process, one of the first steps is to define the system boundary, which, in this case, is defined as the external surface of the $LN_2$ vessel wall,

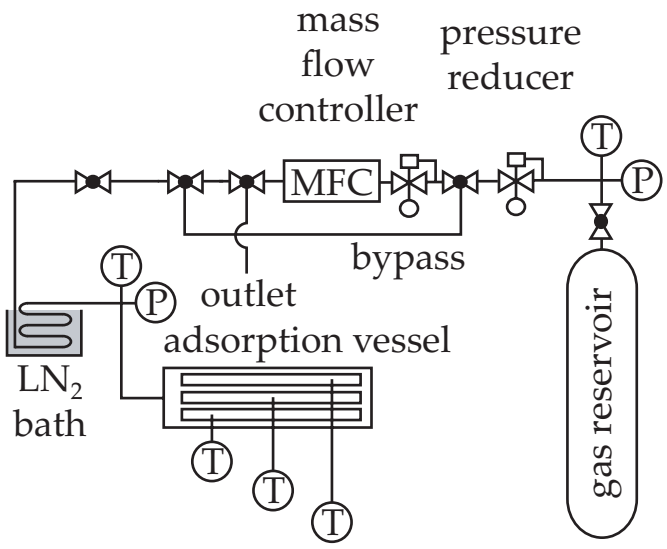


**Figure 8.2:** Test rig to investigate the dynamic behaviour of the adsorption vessel [48].

or the internal surface of the insulation layer. For the sake of convenience, the system in consideration may be divided in different domains, in each of which other medium properties exist or in which the transport processes (mass transfer, heat transfer and so on) may be described mathematically differently. The domains are then connected to each other through appropriate balance equations at the domain borders. The domains are, in the adsorption vessel, for example, the tube walls, the adsorbent, bulk gas volumes, the $LN_2$ vessel wall and its interior volume.

Having defined the system domains and their governing equations, the next step is to choose a method to solve the system of equations, that, due to its complexity, is in the majority of cases a numerical method. In this work, the finite element method is used to solve the model equations. In this method, the calculation domain is divided into many elements and in each element basis functions are applied to approximately describe the solution in the element region. For 3D systems this may lead to a high number of elements, thus requiring computers with very fast CPUs for processing and high amount of physical memory for storing. Moreover, in order to simulate a process which extends over a real-time period of, for example, one day, very long CPU-running time of weeks or months may be expected. Therefore, it is advanta-

geous to look for symmetries in the system and to simplify as much as possible its geometry in order to reduce the number of elements and to obtain a more handable model. Thereby care must be taken not to oversimplify the problem from the point of view of details and accuracy. The next section addresses the model geometry and its simplifications as well as the association of the conservation equations presented in chapter 7 to the respective domains.

### 8.2.1 Model geometry and governing equations

In the adsorption vessel, there are seven pressure tubes, which interact thermally with the interior of the $LN_2$ vessel by heat transfer. If this interaction as well as the conditions governing heat flux on the outer tube wall at a determined position are equal for each tube, they will have identical dynamic behaviours. This is clearly true when the $LN_2$ vessel is filled with liquid nitrogen because the outer surface of the tube walls is in contact with the fluid with a well defined temperature. When there is no liquid nitrogen inside the vessel, the requirement for this to be true is that there is a good temperature homogenisation in the $LN_2$ vessel interior over a cross-section perpendicular to the vessel axis. A axial homogenisation is not essentially necessary, only a radial homogenisation suffices. Since there is a big quantity of cooper wool inside the $LN_2$ vessel that contributes to this homogenisation, cross-section homogeneous conditions in the $LN_2$ vessel at a position along its axis seems to be reasonable and this is assumed in the present study. Hence, the behaviour of the adsorption vessel can be investigated by considering only one pressure tube, since the behaviour of the others is identical. The conditions in the domains external to the pressure tubes, i.e., $LN_2$ vessel interior and wall are assumed to vary only axially; radially, they are homogeneous. Moreover, due to the fact that the pressure tube opening is located at the centre of its front face, it will show an axial-symmetric behaviour so that only a tube slice has to be considered. Thus, the geometry for the mathematical model can be reduced from a complex 3D-geometry to a simple 2D-axial-symmetric slice. The cooper wool and liquid nitrogen wall vessel are modelled as thermal masses along the tube wall axis which interact with the outer surface of the pressure tube. Figure 8.3 illustrates the model geometry and the interaction between

the pressure tube wall and the external thermal mass.

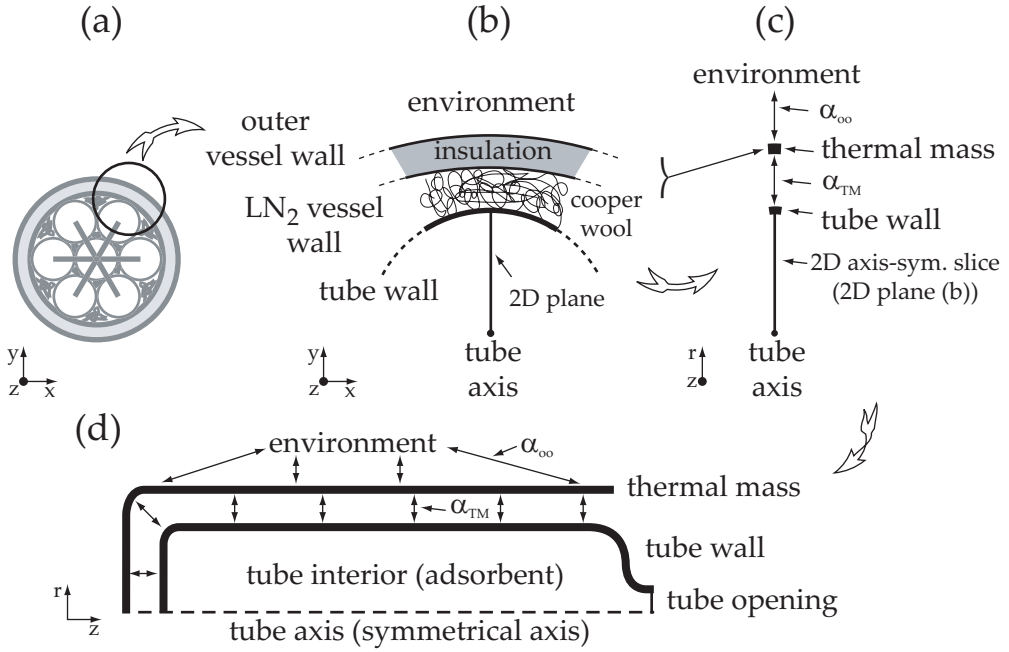


**Figure 8.3:** Steps showing the reduction of the complex 3D-geometry of the real adsorption vessel (a) to the 2D-axial-symmetric model geometry (d).

In figure 8.3a, an axial cross-section of the vessel is shown (figure 8.1) whereas figure 8.3b shows a close view depicting the several layers of the vessel. With the assumptions discussed above, the geometry of figure 8.3b can be reduced to a 2D-axial-symmetric geometry, as shown in figure 8.3c. Figure 8.3d shows a view along the symmetrical axis. In the model geometry, the tube axis is the symmetrical axis. The next subsections associate the conservation equations presented in chapter 7 to the domains and discuss their connections at the borders.

#### 8.2.1.1 Pressure tube wall

In the tube wall domain, a 2D-axial symmetric geometry as shown in figure 8.3, heat transfer is described by the heat conduction equation 7.6. The

material is stainless steel. The tube wall interacts thermally with two other domains: on the inner surface with the pressure tube interior and on the outer surface with the thermal mass or, as the case may be, with the liquid nitrogen occupying the $LN_2$ vessel.

On the inner surface, the interaction is described by the effective heat transfer coefficient $\alpha_S$ ($s$ for solid adsorbent) and the heat flux at a point on the surface is given by

$$\dot{Q}_{TW\rightarrow S} = \alpha_S \left(T^w - T\right), \tag{8.1}$$

where $T^w$ and $T$ are the tube wall and the tube interior temperatures at the domain border. The estimation of $\alpha_S$ is given in subsection 8.2.1.3.

On the outer surface, the boundary conditions differs depending on whether $LN_2$ is present or not. The outward heat flux on the outer tube wall surface is thus given by

$$\dot{Q}_{TW\rightarrow TM} = \alpha_{TM}\left(T^w - T^m\right), \text{ (if no } LN_2 \text{ present)}, \tag{8.2}$$
$$\dot{Q}_{TW\rightarrow LN_2} = \alpha_{LN_2}\left(T^w - T^{LN_2}\right), \text{ (if } LN_2 \text{ present)}, \tag{8.3}$$

where $\alpha_{TM}$ and $\alpha_{LN_2}$ are the respective effective heat transfer coefficients and $T^m$ is the thermal mass temperature. $T^{LN_2}$, the liquid nitrogen temperature, is constant and set to 77 K. Although $\alpha_{LN_2}$ is easy to be estimated from Nusselt correlations [39], this is not true for $\alpha_{TM}$ due to the cooper wool complex structure, so that the latter was used as a fitting parameter to the experiment results.

#### 8.2.1.2 Thermal mass: cooper wool and $LN_2$ vessel wall

Heat transfer in the thermal mass is, as for the tube wall described in the previous subsection, described by the heat conduction equation 7.6. The heat flux on its inner surface is given, in accordance to equations 8.2 and 8.3, as

$$\dot{Q}_{TM\rightarrow TW} = \alpha_{TM}\left(T^m - T^w\right), \text{ (if no } LN_2 \text{ present)}, \tag{8.4}$$
$$\dot{Q}_{TM\rightarrow LN_2} = \alpha_{LN_2}\left(T^m - T^{LN_2}\right), \text{ (if } LN_2 \text{ present)}. \tag{8.5}$$

On its outer surface, the thermal mass interacts with the environment through another effective heat transfer coefficient $\alpha_\infty$. The heat flux is given by

$$\dot{Q}_{TM\to\infty} = \alpha_\infty \left(T^m - T^\infty\right), \tag{8.6}$$

where $T^\infty$ is the environment temperature. $\alpha_\infty$ may be estimated by considering one-dimensional heat transfer through a series configuration of insulation, outer vessel and natural convection or set to zero for adiabatic conditions.

The total mass of the thermal mass, which is distributed equally along its length, is equal to the sum of the total mass of cooper wool and the mass of the $LN_2$ vessel wall divided by the number of pressure tubes. The thermal mass effective thermal conductivity is a mass-weighted combination of steel and cooper.

#### 8.2.1.3 Pressure tube interior

The tube may be filled with either powered activated carbon or activated carbon pellets, as shown in figure 8.4. In each configuration, bulk gas volumes are also found. In the case of bed, the whole volume, except for a small bulk gas volume at the tube opening, is occupied by the adsorbent. In the case of pellets, 43 pellets are stacked together along the tube axis. The pellets are perforated at the center to allow for gas flow through the tube. One in five pellets is not center-perforated and the gas has flow around it along the tube wall. The center holes have a diameter of 2 mm whereas the gaps between pellets are 1 mm thick.

All transport processes occurring inside the tube can be described by the same set of equations. These are the continuity equation (equation 7.2), the momentum equations (equation 7.3) and the energy equation (equation 7.5) presented in chapter 7. The differentiation between bed, pellets and gas volume is made by defining the terms according to table 8.1.

On the domain borders in contact with the tube wall and on the axis, no fluid flow is allowed and the normal component of velocity vector is zero. This may

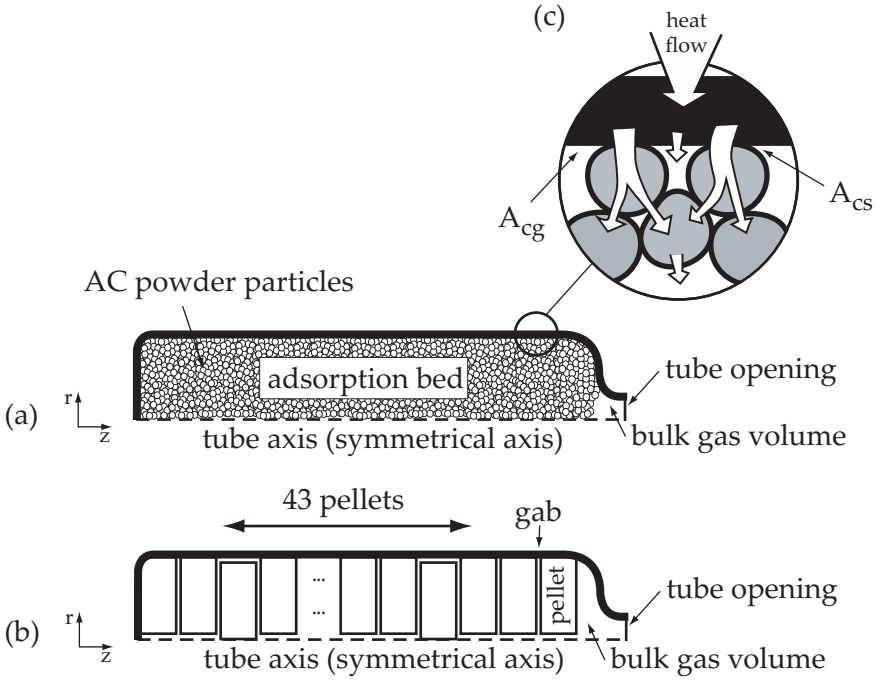


**Figure 8.4:** Pressure tube interior for the (a) adsorption bed and (b) pellets configuration. (c) shows the wall-adsorbent particles interface contact.

| Symbol | Bulk gas volume | Adsorption bed | Pellet |
|---|---|---|---|
| $\varepsilon_{\text{void}}$ | 1 | total bed porosity * | pellet porosity |
| $\rho^s$ | 0 | bed density | pellet density |
| $\vec{F}$ | 0 | $\vec{F}_{bed}$ - equation 7.28 | $\vec{F}_{pellet}$ - equation 7.23 |
| $U^s$ | 0 | adsorbent internal energy | adsorbent internal energy |
| $k_{\text{eff}}$ | $k^g$ | equation 7.34 with $\epsilon = \varepsilon_b$ | equation 7.34 with $\epsilon = 0$ |

* Total bed porosity: $\varepsilon_t = \varepsilon_b + (1-\varepsilon_b)\,\varepsilon_{prt}$, ($\varepsilon_b$ =bed porosity, $\varepsilon_{prt}$ = particle porosity).

**Table 8.1:** Definition of the terms in the conservation equations 7.2-7.6 in order to describe mass, momentum and energy balances in three different domains: bulk gas volume, adsorption bed and pellets.

be described with a slip/symmetry boundary condition such as

$$\vec{n} \cdot \vec{v} = 0\,, \tag{8.7}$$

where $\vec{n}$ is the normal vector. No wall boundary layer effects are considered because they are only significant when the bed-particle diameter ratio

is small (<10) or when detailed boundary layer studies are needed [52], which is not the case in this work. At the tube opening, mass flow boundary conditions are imposed with the respective inlet temperature.

Heat transfer from tube wall into fluid-adsorbent domains is considered to occur through wall-gas and wall-adsorbent contacts, as shown in the detailed view of figure 8.4c. The heat flux is given by

$$\begin{aligned} \dot{Q}_{TW\leftrightarrow S} &= \frac{\alpha_{cs} A_{cs} \left(T^w - T\right) + \alpha_{cg} A_{cg} \left(T^w - T\right)}{A} \\ \dot{Q}_{TW\leftrightarrow S} &= \left[\alpha_{cg} + \frac{A_{cs}}{A}\left(\alpha_{cs} - \alpha_{cg}\right)\right]\left(T^w - T\right), \end{aligned} \tag{8.8}$$

where $\alpha_{cs}$ and $\alpha_{cg}$ are the heat transfer coefficients at wall-adsorbent and wall-gas contacts, respectively, and $A_{cs}/A$ is the ratio of wall-adsorbent contact area to total area. Thus, $\alpha_S$ in equation 8.2 is given by

$$\alpha_S = \left[\alpha_{cg} + \frac{A_{cs}}{A}\left(\alpha_{cs} - \alpha_{cg}\right)\right]. \tag{8.9}$$

The wall-adsorbent contact area is calculated with the method proposed by Artz [62].

### 8.2.2 Model grid

Figure 8.5a shows the model grid for the adsorption bed case. On the right side, a section of the tube inlet can be seen, whereas, on the left side, a section of the tube bottom can be seen. The grid consists of unstructured triangular elements with a maximum element size of 2 mm. At the interface adsorption bed-bulk gas volume, smaller elements are used in order to resolve larger gradients. The adsorption bed grid consists of about 30000 quadratic elements.

Figure 8.5b shows the model grid for the pellets case. On the right side, a section of the tube inlet can be seen where pellets with eccentrical holes are located, whereas, on the left side, a section of the tube bottom can be seen where the last pellet is not centre-perforated. In the middle, a section shows a non-perforated pellet surrounded by two perforated pellets. Again, the grid

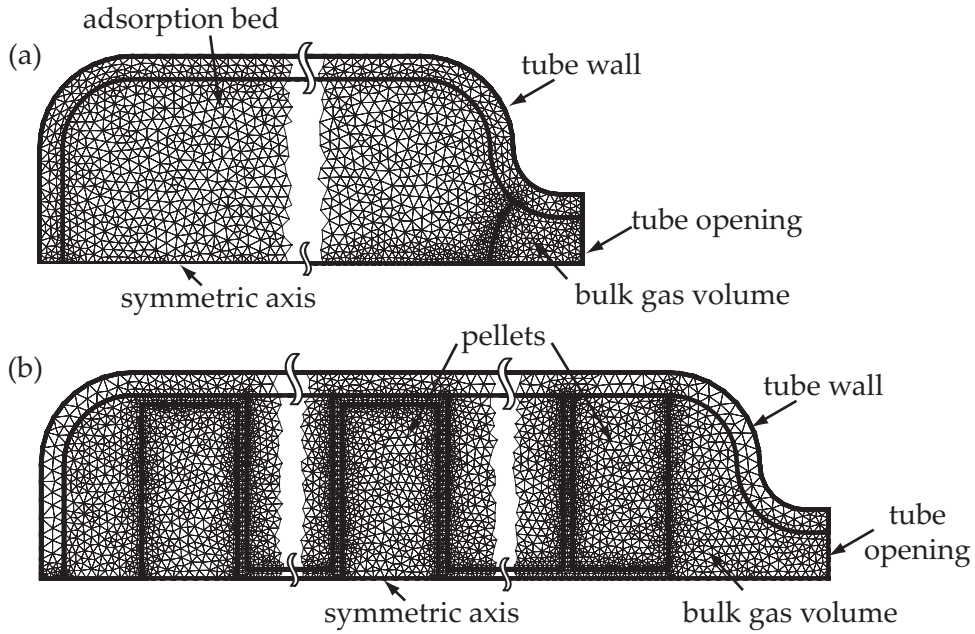


**Figure 8.5:** Finite element grids for (a) the adsorption bed model and (b) the pellets model. The grids consist of unstructured triangular elements.

consists of unstructured triangular elements with a maximum element size of 2 mm. At the interface pellet-bulk gas volume, smaller elements are used in order to resolve larger gradients. This grid consists of about 50000 quadratic elements.

### 8.2.3 Solution approach

As already said, the finite element method (FEM) has been applied to solve the partial differential equations. The model has been set up in the commercial software Comsol Multiphysics®. Here, a very basic overview of FEM is presented and the reader is referenced to FEM books such as the ones by Huebner [38] and by Kaliakin [41] for detailed information.

In general, the first step in FEM is to approximate the computational domain $\Omega$ with a union of simple geometric objects, such as triangles. The triangles form a mesh or grid and each vertex is called a node. Next, the solution

is approximated by simple functions on each triangle (polynomials or linear functions are a good choice) and it is imposed that the solutions in neighboring triangles connect to each other continuously across the edges.

For instance, if the equation

$$-\nabla \cdot (c\nabla u) + au = f \tag{8.10}$$

is to be solved, a piecewise linear approximation $u_h$ to the solution $u$ is tested for all possible functions $v$ for the same class. Testing means formally to multiply the residual of the solution $u_h$ against any function and then integrate, i.e., determine $u_h$ such that

$$\int_\Omega \left(-\nabla \cdot (c\nabla u_h) + au_h - f\right) v dx = 0 \tag{8.11}$$

for all possible $v$. Since $v$ is arbitrary, the integral in equation 8.11 is only zero when the residual (the term in parentheses) is zero, in which case $u_h$ approximates the solution. The functions $v$ are usually called *test functions*. Partial integration (Green's Formula) of equation 8.11 yields that $u_h$ should satisfy

$$\int_\Omega \left[(c\nabla u_h)\nabla v + au_h v\right] dx - \int_{\partial\Omega} \vec{n} \cdot (c\nabla u_h)\, v ds = \int_\Omega f v dx, \quad \forall v \tag{8.12}$$

where $\partial\Omega$ is the boundary of $\Omega$ and $\vec{n}$ is the outward pointing normal vector on $\partial\Omega$. The integral on $\partial\Omega$ defines the boundary conditions.

Any continuous piecewise linear $u_h$ is represented as a combination

$$u_h(x) = \sum_{i=1}^{N} U_i \phi_i(x) \tag{8.13}$$

where $\phi_i$ are some special piecewise linear basis functions, $U_i$ are scalar coefficients and $N$ is the number of nodes. The basis function $\phi_i$ is chosen such that it has the value 1 at the node $i$ and the value 0 at all other nodes and it varies linearly on the edges between the nodes (piecewise linear case). For any fixed $v$, the FEM formulation (equation 8.11) yields an algebraic equation in the unknowns $U_i$. Since $N$ unknowns ($N$ $U_i$'s) are to be determined, so $N$ different instances of $v$ are needed. The best candidates are $v = \phi_j$, $j = 1, 2, ..., N$. From that, a linear system $KU$=$F$ is obtained, where the matrix $K$ and the right

side $F$ contain integrals in terms of the test functions $\phi_i$, $\phi_j$, the coefficients defining the problem ($c$, $a$, $f$) and the boundary conditions. The solution vector $U$ contains the expansion coefficients of $u_h$, which are also the values of $u_h$ at each node $x_i$ since $u_h(x_i) = U_i$.

Although triangles and a piecewise linear approximation has been used to describe FEM, any other function may be used such as piecewise quadratic functions or even piecewise high-order polynomial functions. FEM is also not restricted to triangles, but can also be defined on quadrilateral subdomains and so on. In this work, piecewise quadratic triangles have been used to approximate the solution of all variables.

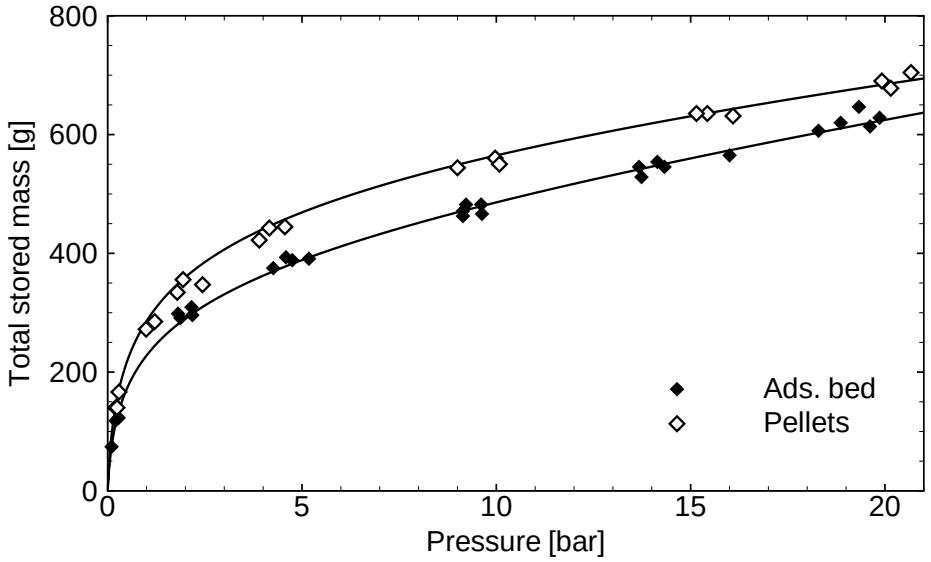


**Figure 8.6:** Adsorption vessel absolute storage capacity as a function of pressure at a constant temperature of 77 K for two configurations: filled with activated carbon powder (adsorption bed) and with pellets. The symbols represent experimental points and the lines are obtained with the model.

## 8.3 Comparison, results and discussion

This section presents some of the experiments carried out with the adsorption vessel. In total, four experiments are presented: three with the adsorption bed and one with pellets. Moreover, numerical simulations with the model described in the previous sections corresponding to the experiments are also shown. At this point, the models still have four unknowns: the mean pore radius $\overline{r}_p$ for diffusion in pellets (see section 7.2.3), the effective particle diameter $D_p$ for flow through packed beds (see section 7.3), the factor $f_{k^s}$ between the activated carbon and graphite thermal conductivities (see section 7.4) and the effective heat transfer coefficient $\alpha_{TM}$ describing the heat flux between the pressure tube and the thermal mass – cooper wool and $LN_2$ vessel wall – when no $LN_2$ is present (see section 8.2.1). These experiments are used to determine these unknowns and thus to parametrise the model. A systematic variation of these unknowns was carried out and the set that satisfactorily described the vessel behaviour in all experiments was chosen. The values are given in tables 8.2-8.3. It must be stressed that the same set of parameters was used for all simulations.

| Symbol/Parameter | Units | Value |
|---|---|---|
| $\rho^s$ (bed density) | $kg/m^3$ | 340 |
| $\varepsilon_b$ (bed porosity) | - | 0.25 |
| $\varepsilon_{void}$ (total porosity) | - | 0.8 |
| Isotherms factor | - | 0.7 |
| $D_p$ (eff. particle diameter) | $\mu m$ | 130 |
| $A_{cs}/A$ (wall-adsorbent contact) | - | 0.15 [62] |
| $\alpha_{cs}$ (wall-adsorbent h.tr.coeff.) | $W/(m^2K)$ | 2000 [10] |
| $\alpha_{cg}$ (wall-gas h.tr.coeff.) | $W/(m^2K)$ | 30 |
| $\alpha_{TM}$ (tube-thermal mass h.tr.coeff.) | $W/(m^2K)$ | 30 |
| $f_{k^s}$ (graphite-AC thermal cond. ratio) | - | 100 |

**Table 8.2:** Adsorption bed model parametrisation for simulations of the experimental vessel.

In order to run a simulation of an experimental measurement, two observed experimental quantities are used as boundary conditions in the model. These

quantities are: mass flow rate and vessel inlet gas temperature. The mass flow rate was obtained from the rate of pressure decrease in the gas reservoir (experimental set-up shown in figure 8.2). Averaged mass flow rates over time periods of some minutes were used in the boundary conditions of the model in order to avoid the strongly oscillating experimental curves. While obtaining these smooth curves, attention was paid to ensure that the same amount of gas is introduced in the vessel during the simulations as in the experiments.

In some experiments, the evacuated vessel is at first cooled with $LN_2$ to approximately 77 K and, after that, $LN_2$ is removed from the system and the vessel is then filled with hydrogen, causing a temperature increase. At some point during the filling, $LN_2$ is again introduced into the system to cool it down back to 77 K. Due to the horizontal vessel position in the experiments, pressure tubes at the bottom of the assembly are cooled before the tubes at the top. Furthermore, this cooling procedure leads to non-axial-symmetric behaviour in the tubes, which cannot be reproduced with the 2D axis-symmetric model. Nevertheless, the cooling phase of the experiments are included in the simulations as a mean to cool the system back to 77 K and to show the pressure decrease caused by it. No efforts have been made to correctly reproduce the experimental data during the introduction of $LN_2$ into the system.

Concerning the vessel initial conditions in the simulations, unless otherwise

| Symbol/Parameter | Units | Value |
|---|---|---|
| $\rho^s$ (pellet density) | $kg/m^3$ | 700 |
| $\varepsilon_{void}$ (pellet porosity) | - | 0.7 |
| Isotherms factor | - | 0.53 |
| $\overline{r}_p$ (mean pore radius) | $\dot{A}$ | 500 |
| $A_{cs}/A$ (wall-adsorbent contact) | - | 0.3 |
| $\alpha_{cs}$ (wall-adsorbent h.tr.coeff.) | $W/(m^2K)$ | 2000 [10] |
| $\alpha_{cg}$ (wall-gas h.tr.coeff.) | $W/(m^2K)$ | 30 |
| $\alpha_{TM}$ (tube-thermal mass h.tr.coeff.) | $W/(m^2K)$ | 30 |
| $f_{k^s}$ (graphite-AC thermal cond. ratio) | - | 100 |

**Table 8.3:** Pellet model parametrisation for simulations of the experimental vessel.

stated, it was set to 0.01 bar and 77 K. In the experiments, however, not all temperature curves initiate exactly at the same value (77 K) after the cooling with liquid nitrogen. Effects such as heat transfer with the environment during the removal of the liquid nitrogen may lead to local temperature changes. Moreover, at cryogenic temperatures, the uncertainties of the instruments are high so that initial temperature in the experiments may vary from measurement point to measurement point. In such cases, the qualitative behaviour of the curves was used as a criterion for the model correctness. Besides that, model geometric simplifications, differences on modelled and real properties of materials (activated carbon) as well as isotherms scaling may be sources of differences between simulations results and experiment measurements. Concerning the latter point, the scale factor has been obtained by matching both isotherms at 77 K. However, the validity for other temperatures is an assumption since it is dependent of the porous structure of the material.

In this section, little effort is made in order to explain all the details of the vessel dynamic behaviour. Such a discussion is presented in the next chapter, where simulations with well-defined boundary conditions are carried out.

### 8.3.1 Adsorption bed experiments

The adsorption bed consisted of fine-grained activated carbon with a mean-particle size of about 200 $\mu m$. In the tubes, the powder was somewhat compressed and a bed density of 340 $kg/m^3$ was obtained. Table 8.2 shows the values of all parameters used in the simulations with the adsorption bed. The table includes the unknowns obtained by fitting as well as the factor for isotherms scaling because the activated carbon used in the experiments was not as good as the one used in the measurements in Canada for the obtainment of the adsorption isotherms over wide ranges of pressure and temperature (comparison of their adsorption characteristics at 77 K showed a nearly constant ratio between the isotherms for the whole pressure range).

The absolute storage capacity of the system filled with activated carbon powder as a function of pressure at a constant temperature of 77 K is shown in figure 8.6. It can be seen that there is a good agreement between experiments

and the model curve, thus confirming the model parametrisation given by table 8.2.

#### 8.3.1.1 Experiment B1

In this experiment, the evacuated vessel was at first cooled with $LN_2$ to approximately 77 K and, after that, $LN_2$ was removed from the system. The vessel was then filled to 20 bar with a constant mass flow rate. During the filling, the hydrogen entering the vessel was pre-cooled by a $LN_2$ bath. After 30 min, the filling process stops and the vessel is let to come into equilibrium. Finally, after about 80 min, $LN_2$ is introduced into the system to cool it back to 77 K.

Figure 8.7 shows the experimental data as well as the simulated curves for this experiment. Specifically, figure 8.7-top shows the pressure and the integrated mass supplied to the system (time derivative of this curve is the mass flow rate used as boundary condition in the simulations), whereas Figure 8.7-bottom shows temperature at the top, middle and bottom positions and the vessel inlet gas temperature (boundary condition for the simulation). Concerning the pressure, good agreement can be seen between the experiment points and the simulated curve. Since the mass flow rate is slow, very low pressure gradients appear along the tube axis and this curve represents the pressure within the whole vessel. After mass supply is stopped, pressure levels in the simulation and in the experiments differ by about 2-3 bar. Among other effects, this might be due to isotherms scaling (see section 8.3.1).

As to temperature, comparison of the time-dependent behaviour of the curves shows that the model correctly reproduces the dynamic behaviour of the vessel. As stated in the beginning of the section, not all thermocouples start at the same temperature so that the absolute temperature of the experimental points and model curves differ. However, a near to constant temperature difference between these data can be seen over the whole time. At the top, temperature suddenly increases as filling starts due to adsorption effects as well as due to the fact that, at the beginning, the temperature of the entering gas is somewhat higher than the expected 77 K. After 5 minutes, the temperature decreases because cold gas is entering the vessel. At the middle and bottom

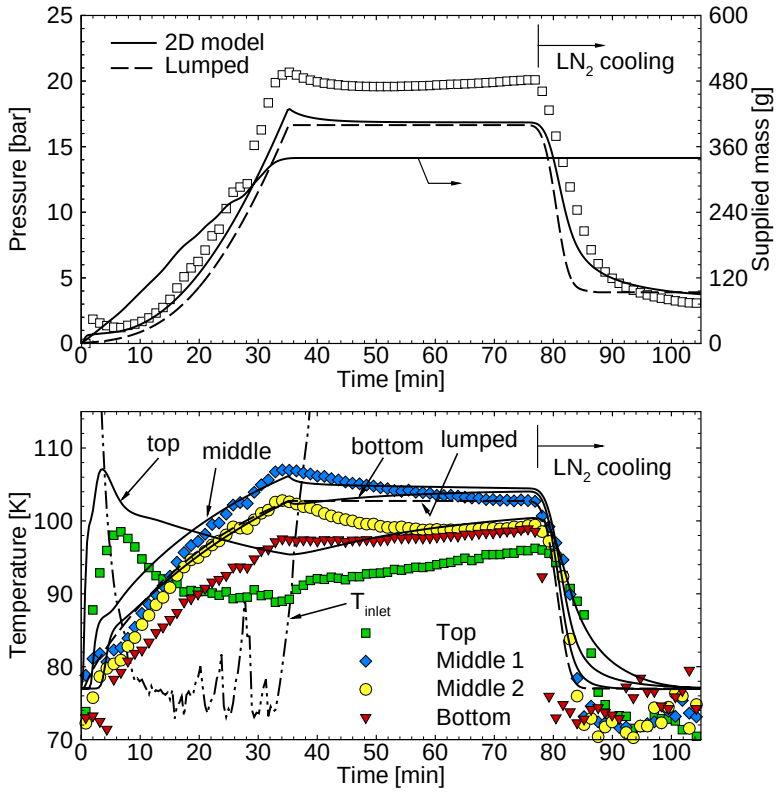


**Figure 8.7:** Experiment B1: Comparison of experimental data (symbols) and simulation results (solid lines: 2D model, dashed lines: lumped model).

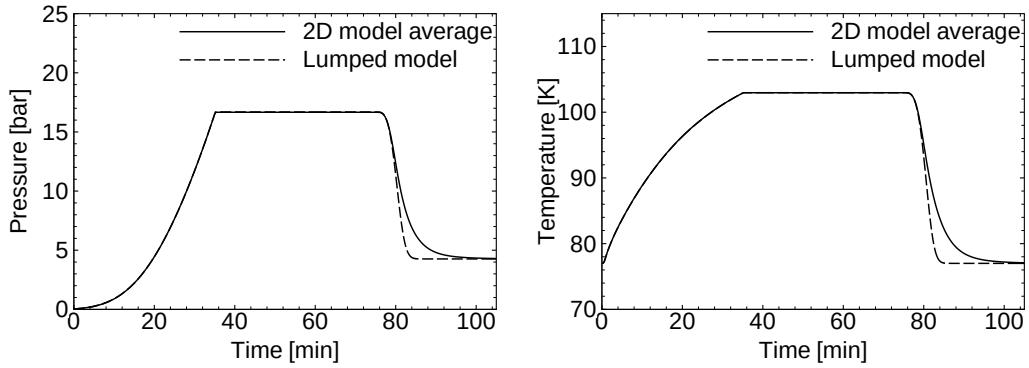


**Figure 8.8:** Experiment B1: Comparison of experimental data (symbols) and simulation results (solid lines: 2D model, dashed lines: lumped model).

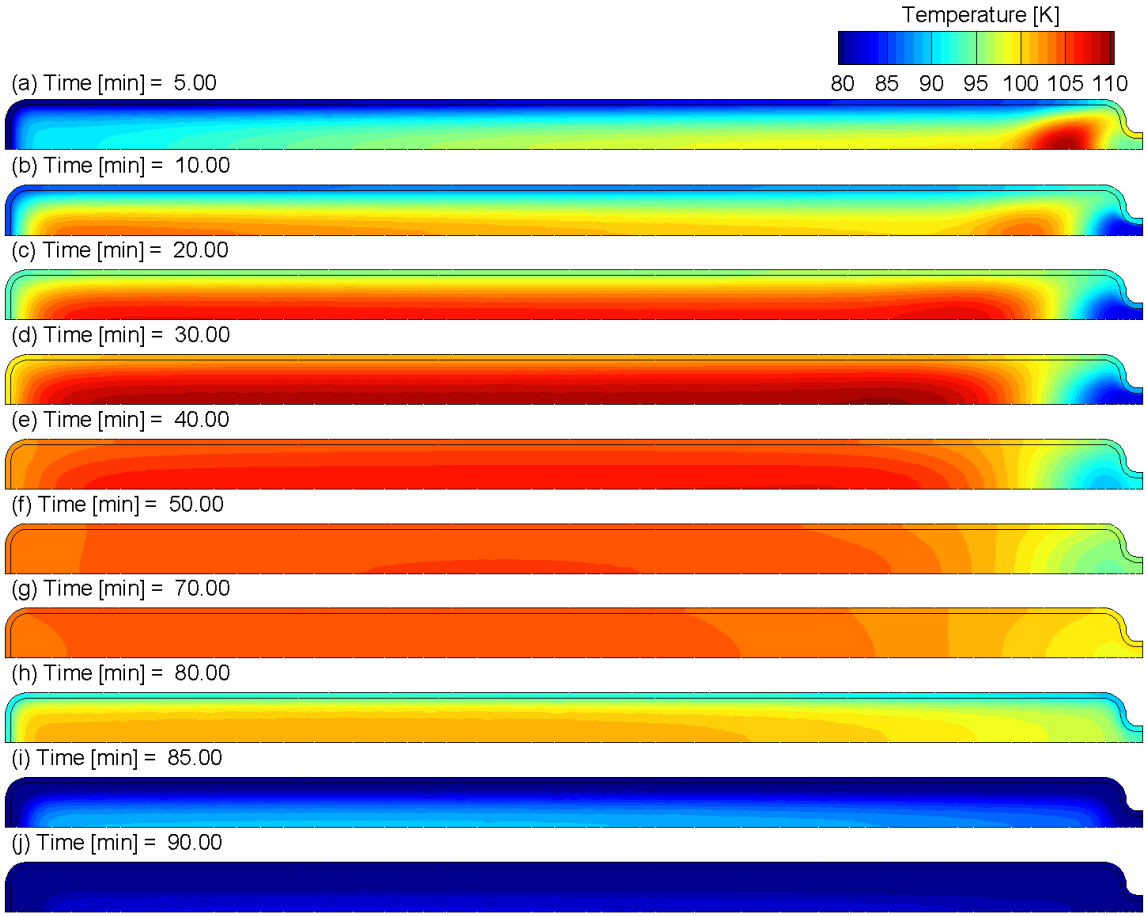


**Figure 8.9:** Experiment B1: Contour plots of temperature at various times during the simulation of filling of the vessel with pre-cooled hydrogen. The pressure tubes contain activated carbon powder.

positions, the temperature increases monotonically until the end of the filling process and stabilizes as the vessel comes into equilibrium.

Temperature contour plots at various times during the filling are shown in figure 8.9. At the very beginning (contour (a)), the region near the inlet is the warmest in the tube due to the reasons given above, but the cold gas entering afterwards cools it down. The rest of the tube has a similar behaviour: the temperature being higher at the axis and lower near the wall. Contours (e), (f) and (g) show the temperature homogenisation.

The dashed lines in figure 8.7 represent the results of a lumped model for this experiment. In addition, figure 8.8 compares the lumped model results with

mass-averaged properties obtained with the 2D-model. It can be seen that the lumped model satisfactorily reproduces the 2D-model results within its assumptions. The success of the lumped model in this case lies on one characteristic of the process, namely, that it is an adiabatic filling. Due to this reason, extensive quantities of the system can only change because of the entering gas, whose terms are identical for both models and not influenced by the lumped model assumptions. That is the reason for the excellent agreement between the models as shown in figure 8.8. Only once cooling starts a difference between the models can be seen, since the lumped model does not consider internal thermal resistances.

#### 8.3.1.2 Experiment B2

This experiment characterises a charge without inlet gas pre-cooling. Again, as in experiment B1, the vessel was cooled to $LN_2$ boiling temperature and then the $LN_2$ was removed from the system. After that, it was slowly filled with hydrogen at room temperature with a constant mass flow rate. After 100 min, $LN_2$ is introduced into the system for cooling purposes. Figure 8.10 shows the experimental data as well as the simulated curves. The time derivative of the supplied mass curve gives the mass flow rate used in the simulations. The vessel inlet gas temperature was set to 25°C.

Pressure progression is shown in figure 8.10-top. Again, good agreement can be seen between experiment and simulation. Figure 8.10-bottom shows the temperature at the four positions. The contour plots are shown in figure 8.12. As it can be seen, the entering gas strongly heats the region near the inlet (about 1/3 of the whole length), but the temperature increase in the middle and in the bottom is not as high; this increase being mainly due to compression and adsorption. Again, experiment and simulation curves start at different temperature levels. However, a near to constant temperature difference can be seen between the curves.

The dashed lines in figure 8.10 show the results of a lumped model for this experiment. Figure 8.8 compares the lumped model results with mass-averaged properties obtained with the 2D-model. As pointed out in section 8.3.1.1, the

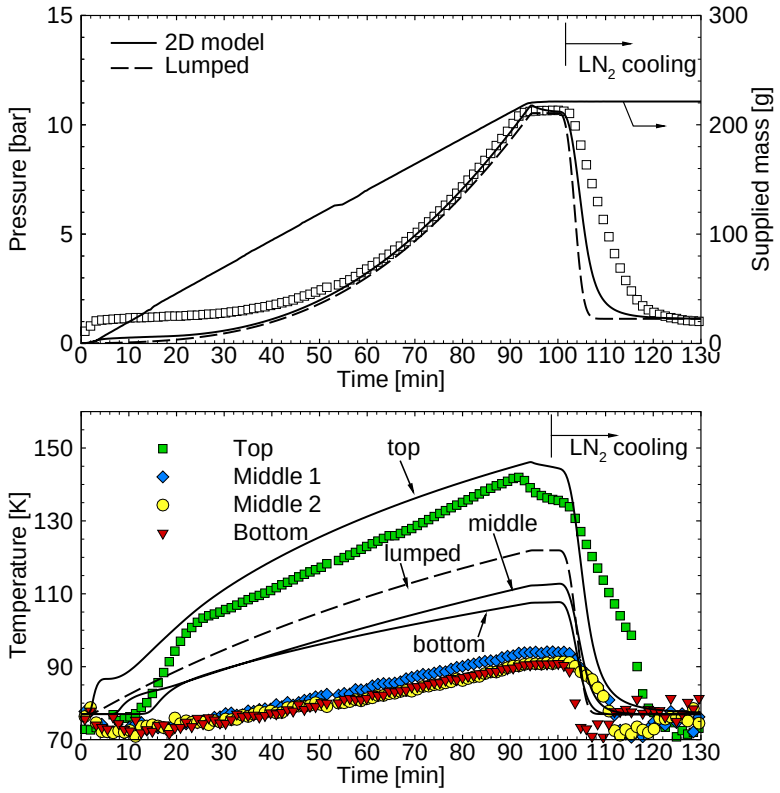


**Figure 8.10:** Experiment B2: Comparison of experimental data (symbols) and simulation results (solid lines: 2D model, dashed lines: lumped model).

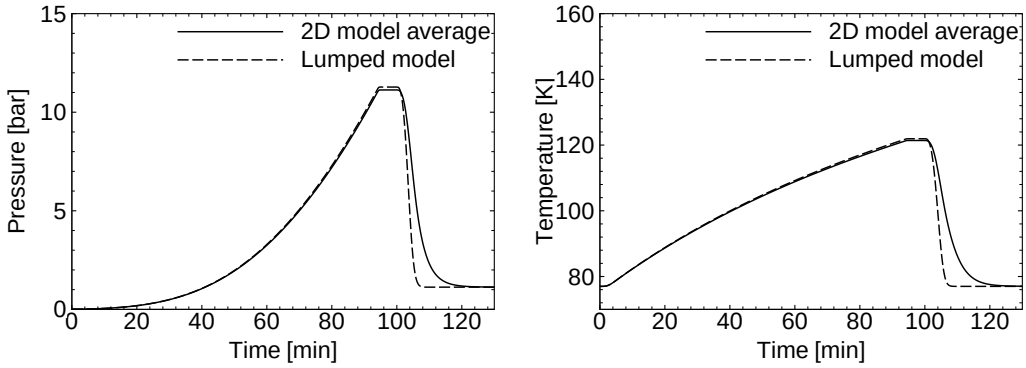


**Figure 8.11:** Experiment B1: Comparison of experimental data (symbols) and simulation results (solid lines: 2D model, dashed lines: lumped model).

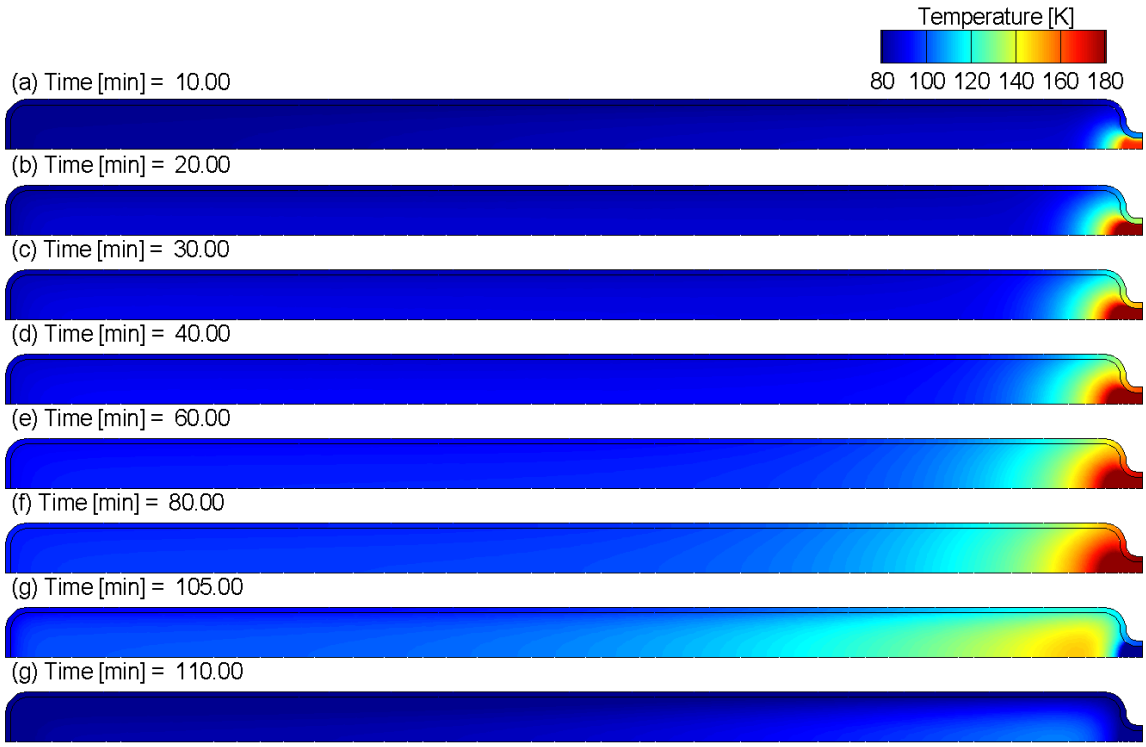


**Figure 8.12:** Experiment B2: Contour plots of temperature at various times during the simulation of filling of the vessel with hydrogen at room temperature. The pressure tubes contain activated carbon powder.

reason for the excellent agreement between the models is that the process is an adiabatic filling.

#### 8.3.1.3 Experiment B3

In this experiment, isothermal filling is demonstrated. The vessel is initially at 77 K and contains a certain mass of gas corresponding to about 0.5 bar. The filling occurs with $LN_2$ present in the system. The filling procedure is the following: introduction of some gas into the system; waiting time for tube cooling; introduction of the next portion of gas. When a pressure of about 20 bar is achieved, filling finishes and controlled discharge starts. The entering gas is pre-cooled. Unfortunately, the inlet temperature for this experiment is not available, but it could be deduced from the inlet temperature of figure 8.7 that

short gas feeds with pauses in-between may lead to an average inlet temperature of about 150 K, which is the one used in the simulation.

Figure 8.13 shows measured and simulated progression of pressure and temperatures. As gas is introduced into the system, the temperature at the top increases considerably, whereas the temperature at the middle and bottom barely changes. Pressure also increases suddenly. During the cooling phase, the top temperature decreases at an always slower rate. Pressure also decreases due to gas adsorption at the adsorbent region being cooled. During discharge, a small temperature decrease can be seen at the top. Figure 8.14 illustrates by means of contour plots one introduction of gas and the subsequently cooling.

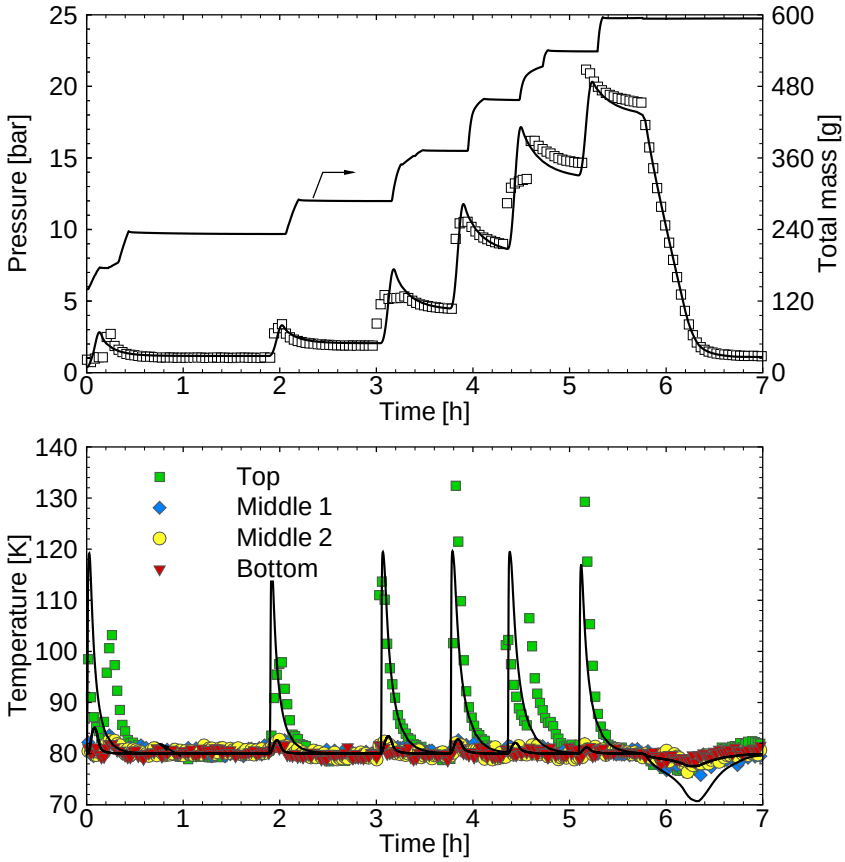


**Figure 8.13:** Experiment B3: Comparison of experimental data (symbols) and simulation results.

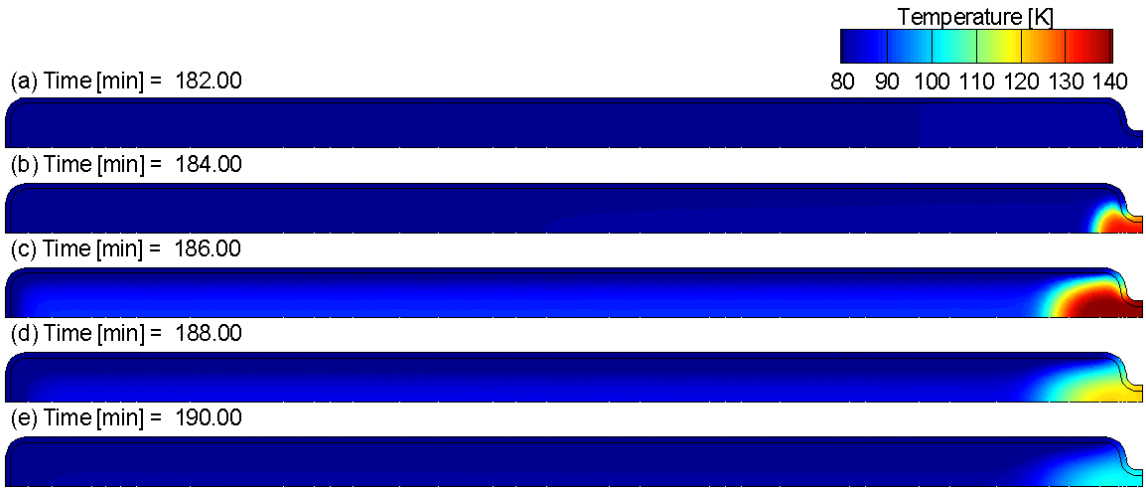


**Figure 8.14:** Experiment B3: Contour plots of temperature during a short gas feed. The vessel is filled with pre-cooled hydrogen and simultaneously cooled with liquid nitrogen. The pressure tubes contain activated carbon powder.

### 8.3.2 Pellets

Experiments with pellets were also conducted and one of them is presented in this section. The pellets were produced by compressing activated carbon powder with pressures up to 6 tons per $cm^2$ [48], the mechanical stability was guaranteed by using a binder. Table 8.3 shows the model parametrisation in the simulations with pellets. The table also includes the unknowns obtained by fitting.

The absolute storage capacity of the system filled with pellets as a function of pressure at a constant temperature of 77 K is shown in figure 8.6. It can be seen that there is a good agreement between experiments and the model curve, thus confirming the model parametrisation given by table 8.3. The figure also shows that the system configuration with pellets stores in average approximately 20% more gas than that with activated carbon powder.

#### 8.3.2.1 Experiment P1

In this experiment, the evacuated vessel was at first cooled with $LN_2$ to approximately 77 K and, after that, $LN_2$ was removed from the system. The vessel was then filled to about 11 bar. During the filling, the hydrogen entering the vessel was pre-cooled by a $LN_2$ bath. After about 50 min, $LN_2$ is introduced into the system while filling continues.

Figure 8.15 shows pressure and temperature from the experiment and the simulation together with the supplied mass and the inlet gas temperature (boundary conditions). Initially, pressure raises very slowly because most of the gas entering gets adsorbed. All three temperatures raise to about 120 K during the filling. The temperature at the top goes through a maximum at the beginning of the loading process caused by the temperature of the entering gas.

Temperature contour plots at various times are shown in figure 8.17. At the very beginning (contour (a)), somewhat warmer gas enters the vessel and raises the temperature of the region near the inlet. The temperature at the rest of the tube increases very homogeneously.

The lumped model results are shown by the dashed lines in figure 8.15 as well as compared to the mass-averaged quantities of the 2D model in figure 8.16. The discussion on the lumped model in section 8.3.1.1 also applies for this case.

## 8.4 Concluding remarks

The main objectives of this chapter have been the development, parametrisation and validation of an adsorption vessel model. By means of dynamic experimental data, the model unknowns have been parametrised and, at the same time, it has been shown that the model is capable of reproducing the dynamic behaviour of the adsorption vessel investigated. This model can now be used to investigate, optimize and visualize loading and unloading processes and this is the aim of the next chapter.

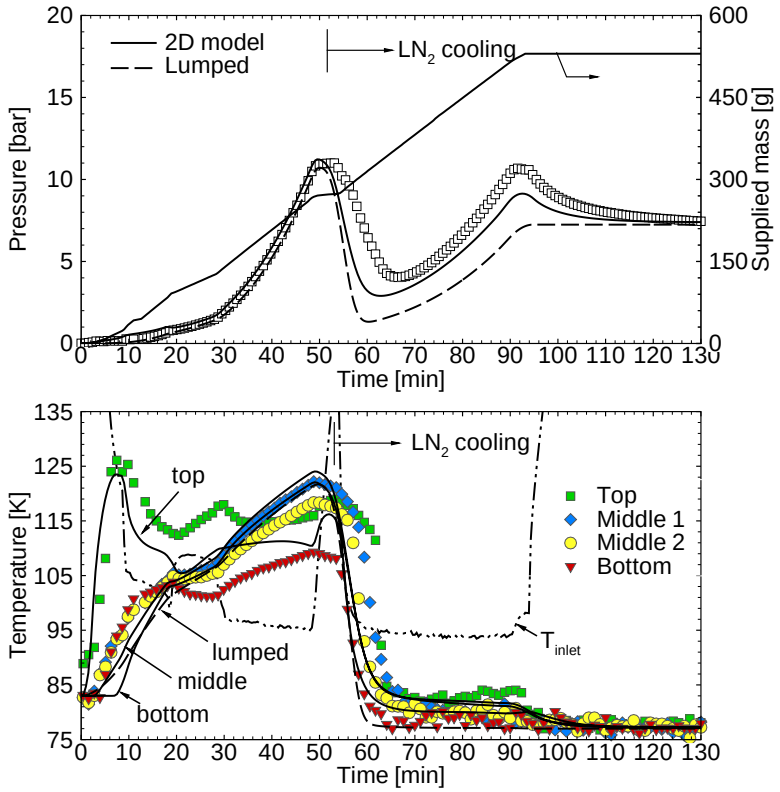


**Figure 8.15:** Experiment P1: Comparison of experimental data (symbols) and simulation results (solid lines: 2D model, dashed lines: lumped model).

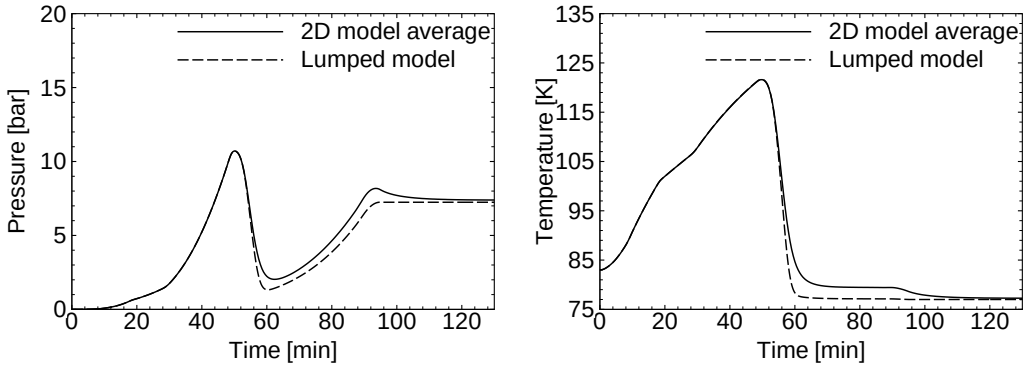


**Figure 8.16:** Experiment B1: Comparison of experimental data (symbols) and simulation results (solid lines: 2D model, dashed lines: lumped model).

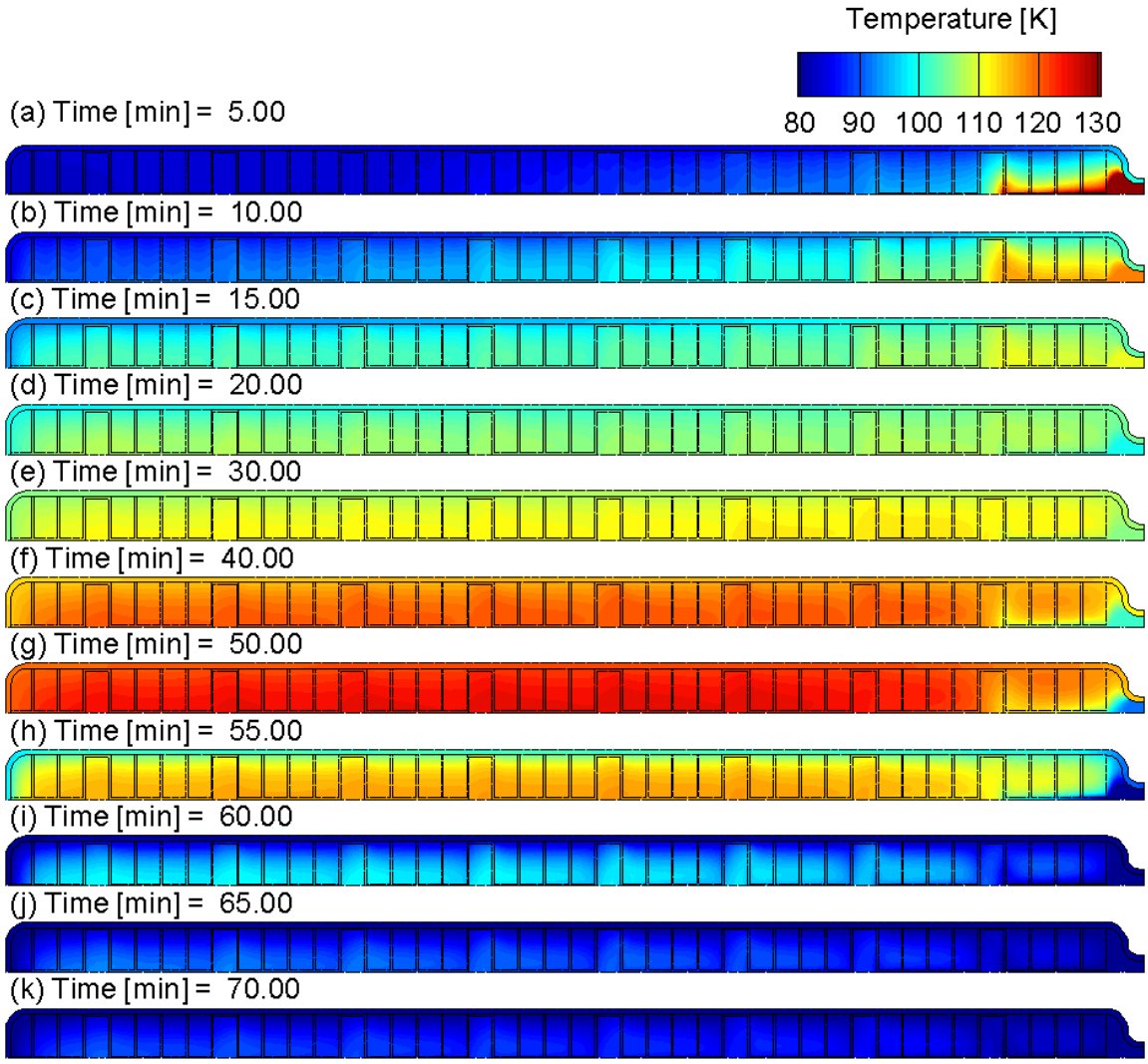


**Figure 8.17:** Experiment P1: Contour plots of temperature at various times during the simulation of filling of the vessel with pre-cooled hydrogen. The pressure tubes contain pellets.

Results obtained with a lumped model have also been presented. The lumped model has proven to be useful. However, its success lies on the characteristics of the processes investigated: relatively slow filling processes under adiabatic and/or nearly isothermal conditions. Regarding the adiabatic characteristic, the extensive quantities of the system in this case can only change due to the entering gas, whose terms are identical for both models and not influenced by the lumped model assumptions. Whereas, under isothermal conditions, the system exhibits nearly homogeneous distribution of properties, which is the main fundamental assumption for the validity of a lumped model. Thus, if a detailed distribution of the properties within the system is not required, a lumped model would suffice to analyse the system. In the next chapter, where fast processes are investigated, the lumped model turns out not to be satisfactory.

# 9 Adsorption Storage System Dynamic Behaviour

A model for simulation of an adsorption storage vessel for hydrogen has been presented in the last chapter. This model has been validated with experimental data. With the model, an extensive investigation of the processes undergone by the adsorption system can be carried out, thus contributing to a better system design.

In this chapter, filling and discharge of adsorption vessels for hydrogen will be investigated. Concerning filling processes, simultaneous cooling is required due to adsorption thermal effects. Thus, the duration of the process is mainly dictated by how efficiently the cooling procedure can remove energy from the system. The present analysis addresses two configurations – a vessel internal $LN_2$ cooling system such as the one used for the experimental adsorption vessel (section 8.1.1) and the recirculation system introduced in section 6.3.1 (figure 6.5) – and estimates the resulting filling duration. Concerning discharge processes, an extensive analysis of long discharges has been presented in chapter 6 with a lumped model. The aim in this chapter is to verify the assumption of temperature homogeneity within the vessel during long discharges, a fundamental assumption of the lumped model, thus, validating the lumped model results. Moreover, fast discharges are also investigated. Both activated carbon powder and pellets are considered.

## 9.1 Model Parametrisation

### 9.1.1 Adsorption Bed Model

In the analysis, the adsorption bed model is parametrized as given in table 9.1. To be noted is the bed optimization in terms of density and the use of high-quality activated carbon (no isotherms scaling). In addition, no external thermal mass is being considered (heat transfer coefficient is set to zero).

| Symbol/Parameter | Units | Value |
|---|---|---|
| $\rho^s$ (bed density) | $kg/m^3$ | 400 |
| $\varepsilon_b$ (bed porosity) | - | 0.2 |
| $\varepsilon_{void}$ (total porosity) | - | 0.8 |
| Isotherms factor | - | 1.0 |
| $D_p$ (eff. particle diameter) | $\mu m$ | 130 |
| $A_{cs}/A$ (wall-adsorbent contact) | - | 0.15 [62] |
| $\alpha_{cs}$ (wall-adsorbent h.tr.coeff.) | $W/(m^2K)$ | 2000 [10] |
| $\alpha_{cg}$ (wall-gas h.tr.coeff.) | $W/(m^2K)$ | 30 |
| $\alpha_{TM}$ (tube-thermal mass h.tr.coeff.) | $W/(m^2K)$ | 0 |
| $f_{k^s}$ (graphite-AC thermal cond. ratio) | - | 100 |

**Table 9.1:** Adsorption bed model parametrisation for the analysis.

| Initial state | | 0 bar, 77 K | | 0 bar, 300 K | |
|---|---|---|---|---|---|
| Final state | | 30 bar, 77 K | | 30 bar, 77 K | |
| Description | Unit | Vessel total (per kg $H_2$ added) | | Vessel total (per kg $H_2$ added) | |
| $H_2$ addition | [g] | 5000 (1000) | | 5000 (1000) | |
| Energy removal | [MJ] | 9.54 (1.9) | | 25.65 (5.1) | |
| % solid | [%] | 0 (-) | | 62.8 (-) | |
| $LN_2$ equiv. | [l ] | 59.3 (11.7) | | 159.5 (31.5) | |
| | | per kg adsorbent | per liter (adsorb. vol.) | per kg adsorbent | per liter (adsorb. vol.) |
| $H_2$ addition | [g] | 72 (7.2%wt) | 28.9 | 72 (7.2%wt) | 28.9 |

$*$: See table 6.2 for explanation of the quantities given.

**Table 9.2:** Cooling requirement for filling the adsorption vessel of table 9.1. The state of the entering gas is 30 bar and 77 K.

With this parametrisation, each pressure tube contains 2 kg of adsorbent and can store about 144 g of hydrogen (7.2%wt, considering only the adsorbent, and ≈ 2%, considering as well the tube wall), so that 35 pressure tubes are necessary in order to achieve a storage capacity of 5 kg. Concerning energy management, the removal of 9.54 MJ of energy is required for filling the vessel from the evacuated state to 30 bar at 77 K, as given in table 9.2. The values are slightly different from the ones given in table 6.2 because the adsorbent characteristics are different, leading to different ratios of bulk gas and adsorbed amounts, and because the tube configuration has more wall material.

### 9.1.2 Pellet Model

The pellets model in the analysis is parametrized as given in table 9.3.

With this parametrisation, each pressure tube of 1 m in length contains 3.4 kg of adsorbent and can store about 155 g of hydrogen (4.6%wt, considering only the adsorbent, and ≈ 1.8%wt, considering as well the tube wall), so that 32 pressure tubes are necessary in order to achieve a storage capacity of 5 kg. Concerning energy management, the removal of 10 MJ of energy is required for filling the vessel from the evacuated state to 30 bar at 77 K, as given in table 9.4. Comparing table 9.2 for the adsorption bed vessel and table 9.4 for the pellets vessel, it can be seen that the pellets configuration offers a lower gravimetric storage capacity but a slightly higher volumetric storage density. The pellets configuration requires more energy for the same amount of stored hydrogen because, on the one hand, a larger portion of gas is adsorbed and, on the other hand, there is more adsorbent material in the vessel.

## 9.2 Filling

Two filling strategies are considered in the analysis. In both strategies, the gas supply system delivers hydrogen at 77 K and at least 30 bar. The vessel is initially evacuated and already cooled down to 77 K. The desired storage conditions (final conditions) are 30 bar and a maximum temperature of 80 K. Under

these conditions, the vessel stores approximately 5 kg of $H_2$.

*Strategy I* consists of connecting the vessel to a feeding line. The pressure in the feeding line might also be higher than 30 bar in order to ensure fast and several simultaneous vessel fillings from the same line. In this case, a pressure reduction mechanism between supply and vessel must be used to avoid overpressure in the vessel. The pressure reduction mechanism can be operated so as to obtain a constant feed gas mass flow rate. In strategy I, filling with constant mass flow rates is considered. The limiting case of a very high mass flow rate characterizes the filling through a pressure difference.

| Symbol/Parameter | Units | Value |
|---|---|---|
| $\rho^s$ (bed density) | $kg/m^3$ | 700 |
| $\varepsilon_{void}$ (pellet porosity) | - | 0.7 |
| Isotherms factor | - | 0.68 |
| $\overline{r}_p$ (mean pore radius) | $\dot{A}$ | 500 |
| $A_{cs}/A$ (wall-adsorbent contact) | - | 0.3 |
| $\alpha_{cs}$ (wall-adsorbent h.tr.coeff.) | $W/(m^2K)$ | 2000 [10] |
| $\alpha_{cg}$ (wall-gas h.tr.coeff.) | $W/(m^2K)$ | 30 |
| $\alpha_{TM}$ (tube-thermal mass h.tr.coeff.) | $W/(m^2K)$ | 0 |
| $f_{k^s}$ (graphite-AC thermal cond. ratio) | - | 100 |

**Table 9.3:** Pellets model parametrisation for the analysis.

| Initial state | | 0 bar, 77 K | | 0 bar, 300 K | |
|---|---|---|---|---|---|
| Final state | | 30 bar, 77 K | | 30 bar, 77 K | |
| Description | Unit | Vessel total (per kg $H_2$ added) | | Vessel total (per kg $H_2$ added) | |
| $H_2$ addition | [g] | 5000 (1000) | | 5000 (1000) | |
| Energy removal | [MJ] | 10.0 (2) | | 28.8 (5.8) | |
| % solid | [%] | 0 (-) | | 65.1 (-) | |
| $LN_2$ equiv. | [l ] | 62.5 (12.5) | | 179.3 (35.8) | |
| | | per kg adsorbent | per liter (adsorb. vol.) | per kg adsorbent | per liter (adsorb. vol.) |
| $H_2$ addition | [g] | 45.6 (4.6%wt) | 31.0 | 45.6 (4.6%wt) | 31.0 |

$*$: See table 6.2 for explanation of the quantities given.

**Table 9.4:** Cooling requirement for filling the adsorption vessel of table 9.3. The state of the entering gas is 30 bar and 77 K.

While filling with a constant mass flow fate, pressure inside the vessel will increase and at the moment when the desired storage pressure is achieved, feed mass flow rate must be reduced in order to avoid overpressures that the vessel can't withstand. From this point on, the feed rate is dictated by the ability of the cooling system to remove the energy released by adsorption from the vessel in order to increase its storage performance by reducing its temperature. Vessel cooling is done with an internal $LN_2$ cooling system such as the one used for the experimental adsorption vessel in chapter 8. In this case, cooling performance depends on the heat conduction properties of the bed. Results obtained in the present study for this configuration suggest that it is not high enough for reasonable filling times to be achieved.

*Strategy II* consists of connecting the vessel to a recirculation system [69], such as the one depicted in figure 6.5. In this case, the filling process starts by pressurizing the recirculation system with hydrogen coming from the feeding line. When the storage pressure is achieved, the compressor starts to recirculate gas, so as to extract relatively hot gas from the vessel, cool it down at the heat exchanger and introduce it back into the vessel, thus using the hydrogen itself as the vessel cooling fluid. Thereby, as hydrogen is accumulated in the vessel, additional hydrogen is supplied to the circuit from the feeding line in order to maintain the pressure at the required level. In this filling system, the pressure reducer between recirculation system and feeding line as well as the compressor can be operated in a way so that a constant mass flow rate is always observed at the vessel inlet. This is the case considered here. In addition, neither mass accumulation in nor thermal mass effects of the recirculation system connecting lines or the heat exchanger are considered.

The following sections present several vessel filling simulations using both strategies. In the case of strategy II, different cooling fluids at the heat exchanger are also investigated. A combination of strategies I and II is also included. In the text and figures, the value of the feed mass flow rate will be given indirectly by the quantity "isothermal filling duration", $t_{isoth}$, which represents the time necessary to fill the vessel with the mass flow rate in question under isothermal conditions. For instance, since 5 kg of $H_2$ has to be introduced into the vessel in order to achieve the final conditions, an isothermal

filling duration of 3 min gives a mass flow rate of 5 kg / 3 min = 27.78 g/s.

### 9.2.1 Filling Strategy I With Internal $LN_2$ Cooling System

#### 9.2.1.1 Adsorption Bed

Figure 9.1 shows temperature contour plots at various times for a filling process with an isothermal filling duration of 3 min. In addition, figures 9.3 and 9.4 show axial and radial temperature profiles, and figure 9.2 shows the time dependent behaviour of volume-averaged quantities. The figures show that, as hydrogen is introduced into the initially evacuated vessel, a considerable temperature increase due to adsorption effects can be seen in the region already reached by the gas. As time advances, this effect propagates until the whole tube is affected. Near the inlet, as the adsorption energy release rate diminishes and is not high enough anymore to heat the entering cold gas, a locally temperature reduction can be seen. Temperature gradients appearing between the bed and wall cause heat transfer towards the wall, however, the $LN_2$ in contact on its external surface impedes a notable temperature increase.

The time-course of the average bed pressure ($\overline{P}_{bed}$) can be seen in figure 9.2. Although relatively high pressure gradients occur at the very beginning, they disappear shortly after and the curve represents the pressure inside the vessel. The storage pressure of 30 bar is reached after about 1:25 min (henceforth, this time is identified as $t_{real,P_{st}}$), approximately half of the isothermal filling time ($t_{isoth}$ = 3 min). At this point, the bed temperature on the axis has increased more than 120 K, whereas, at the wall, only small changes can be seen (see also figure 9.4). This gives an average bed temperature increase ($\Delta\overline{T}_{bed}$) of about 66 K. Average wall temperature increase ($\Delta\overline{T}_{wall}$) does not exceed 6 K.

Once the storage pressure has been reached, the feed mass flow rate must be reduced. This can be seen by the kink of the specific stored mass ($\Delta m_{real}$) curve at 1:25 min. From this point on, the increase of $\Delta m_{real}$ depends on the decrease of $\overline{T}_{bed}$, which is attained by cooling. Since in this concept the cooling performance strongly depends on the effective bed thermal conductivity, which is

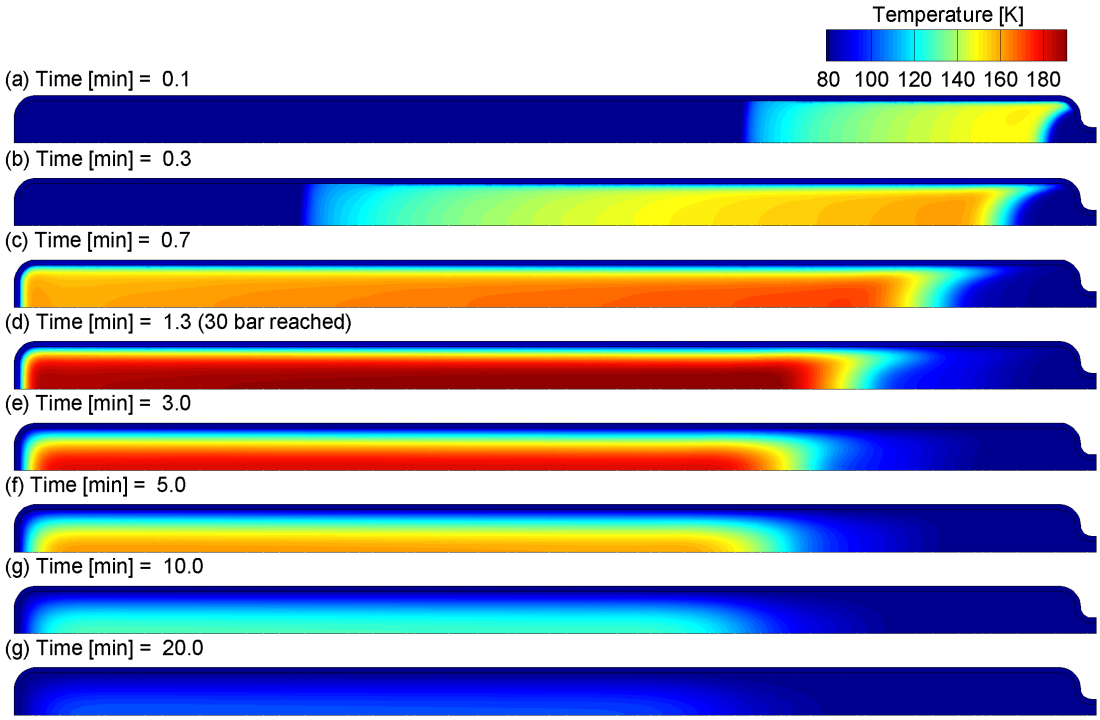


**Figure 9.1:** Temperature contour plots at various times for a filling process with an isothermal filling duration of 3 min.

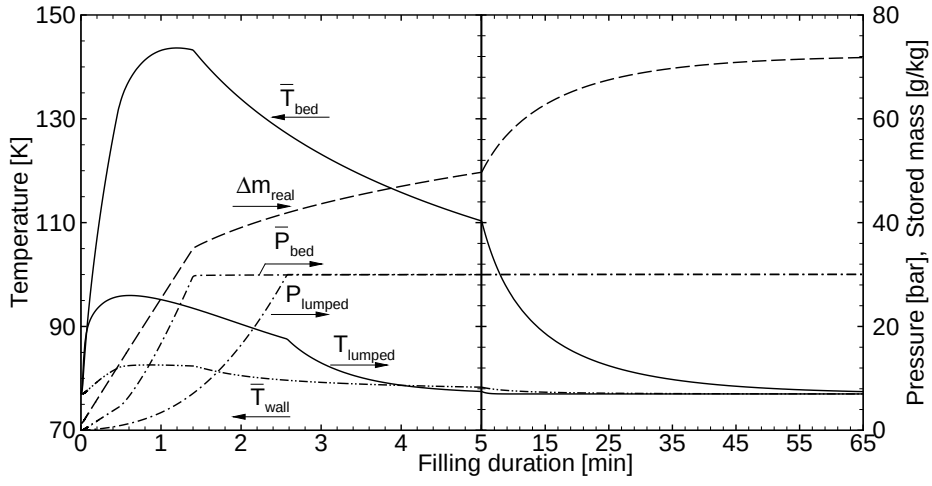


**Figure 9.2:** Time dependent behaviour of average quantities for the filling shown in figure 9.1. The kink of the curves at 5 min is only due to the axis scale change.

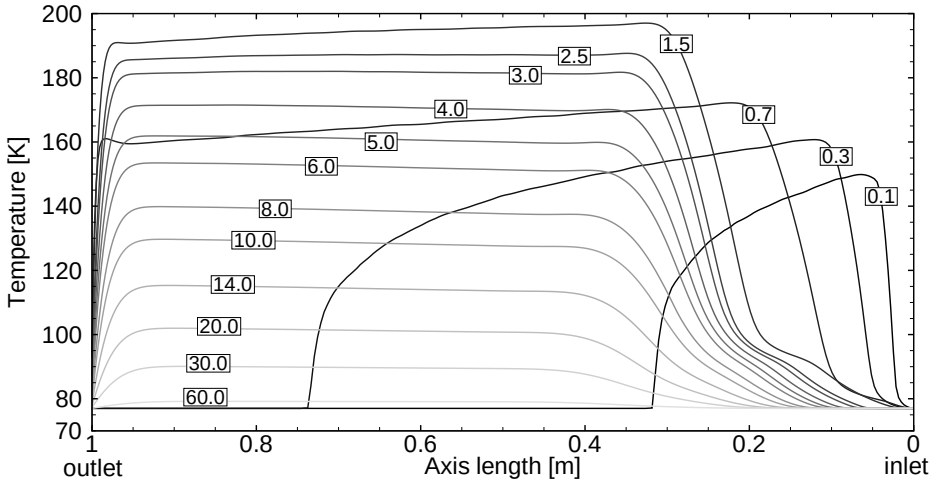


**Figure 9.3:** Axial temperature profiles for the filling shown in figure 9.1. The time values are expressed in minutes over each curve.

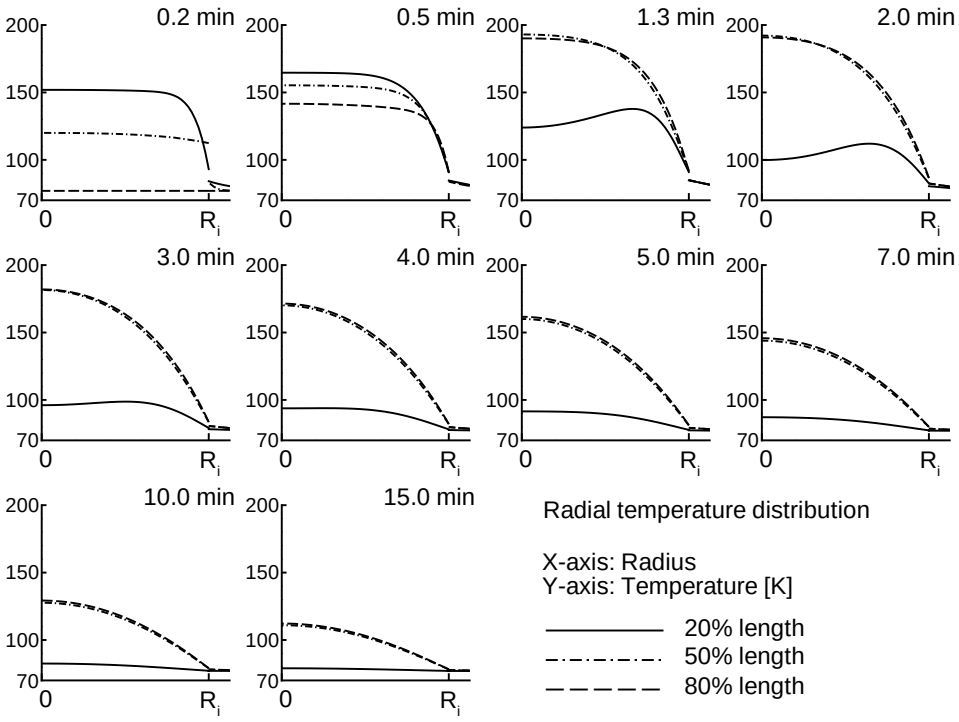


**Figure 9.4:** Radial temperature profiles at three positions along the tube axis length for the filling shown in figure 9.1. 0% length is the tube inlet. In the X-axis, positions from 0 to $R_i$ are within the bed, positions larger than $R_i$ are within the tube wall.

very low, long times are necessary to cool the vessel down back to 77 K. In this simulation, more than one hour is necessary.

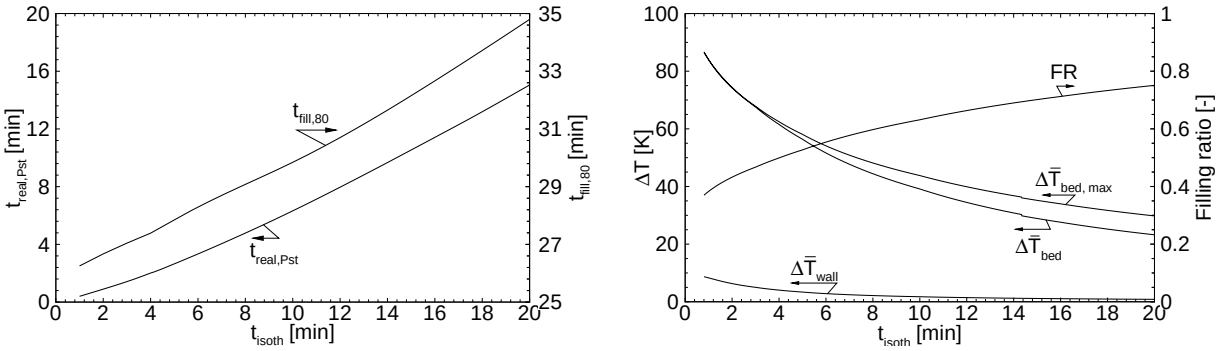


**Figure 9.5:** Variation of bed and wall temperature increases (values at $t_{real,P_{st}}$) and characteristic filling times as a function of the isothermal filling duration. Results from the adsorption bed model.

Figure 9.2 also shows the time-course of pressure and temperature obtained with a lumped model for this process. The lumped model shows a much lower temperature increase and a much shorter filling duration. The reason for this is that the lumped model completely neglects thermal conduction resistances within the system, the main bottle-neck of this configuration, so that the cooling system can remove energy from the system more efficiently. Thus, the use of the lumped model for this kind of process does not provide reliable results.

A series of simulations were carried out to determine the effect of isothermal filling duration (or feed mass flow rate) on the quantities $t_{real,P_{st}}$, $\Delta\overline{T}_{bed}$ and $\Delta\overline{T}_{wall}$. In addition, two other quantities are shown: the filling ratio FR, which is the ratio of the specific stored mass at $t_{real,P_{st}}$ to the final specific stored mass; and the total filling time $t_{fill,80}$, which is the time at which the total energy of the vessel is the same of that of the same vessel with the same gas amount but in equilibrium at 80 K. This means that, if the filling process would be stopped at $t_{fill,80}$, the $LN_2$ instantaneously completely removed from the system and the vessel isolated from the environment, its temperature would be exactly 80 K after a long time, i.e., when this virtual closed adiabatic system reaches equilibrium. The results are depicted in figure 9.5a-b. With these values, it is possible to have an idea how figure 9.2 would look for other $t_{isoth}$'s because the

qualitative behaviour of the curves is very similar. Figure 9.5a shows that, for $t_{isoth}$=0 (the fastest vessel pressurization possible), by extrapolation, the total filling time $t_{fill,80}$ still exceeds 30 min, a result of the very low bed thermal conductivity and the high amount of energy to be transferred (compare table 9.2). Figure 9.5b shows that $\Delta\overline{T}_{bed}$ decreases as the mass flow rate decreases and goes through a maximum before the vessel has reached the storage pressure for lower mass flow rates (higher $t_{isoth}$). Relative to the bed, the tube wall shows very low temperature changes.

The results presented in this section show that a bed thermal conductivity improvement would lead to shorter filling times. This can be accomplished by mixing the carbon powder with a highly thermal conductive material. However, this technique implicates an reduction of the storage capacity since part of the carbon bed is replaced by a non-adsorbing material. Moreover, this technique is highly dependent on the number of new contact points created between particles [51].

Another interesting technique, widely used in high-pressure gas storage systems at room temperature, is to fill the vessel to a pressure higher than the design pressure [3]. This is done because filling a vessel with 300 K $CH_2$ results in a 433 K $CH_2$ temperature immediately after filling. The increase in temperature reduces the amount of gas that can be stored at a given pressure, so that, to avoid losses in storage capacity, pressure vessels are often filled to higher pressures than the design pressure. The pressure then drops as heat is transferred to the environment and/or as gas is extracted from the vessel. For an adsorption vessel, this would require very high pressures compared to the design pressure, as depicted in figure 9.6, which shows the results of the same simulations presented above but with the difference that the pressure is not limited to the design pressure and the mass flow rate does not have to be reduced. Filling stops when the desired mass has been introduced into the vessel. The figure shows the values at the end of the filling process. For fast filling, the resulting pressures are at least four times higher than the design pressure. For comparison, pressure vessels storing compressed gas at room temperature require a pressure about 10% higher than the design pressure [3]. In addition, this technique applied to adsorption vessels would require that

roughly 60 liters $LN_2$ (table 6.2) be available in the vessel internal cooling system in order to drop the pressure afterwards. Thus, the vessel overdimensioning to withstand high pressures together with the extra volume to accommodate large amounts of $LN_2$ result in a much heavier and bigger vessel, a crucial disadvantage.

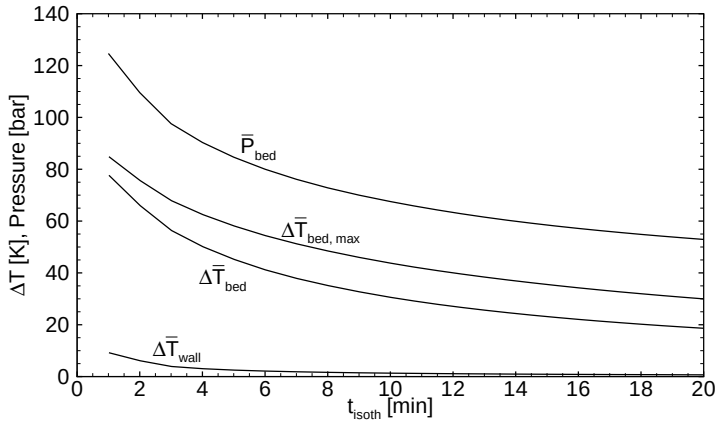


**Figure 9.6:** Final pressure and increase of bed and wall average temperatures as a function of the isothermal filling duration for filling without a pressure design limit.

#### 9.2.1.2 Pellets

The analysis carried out in the previous section was also made with the pellets model. Figure 9.7 shows contour plots at various times during vessel filling with an isothermal filling duration of 2 min. The pellets have a high resistance to flow so that it is necessary to facilitate gas motion in the vessel tubes by means of channels and slits, which in addition increase the surface area between adsorbent and bulk gas volume and thus reduce the diffusional path for the molecules to reach all parts of the adsorbent volume. Since flow in the bulk gas volume (channels and slits) is much faster than mass transport in the adsorbent, a nearly homogeneous pressure increase in the bulk gas volume along the tube is observed during filling. In consequence, the pellets have then a very similar pressure distribution as time advances because pressure conditions on their external surface are homogeneous. Concerning the tem-

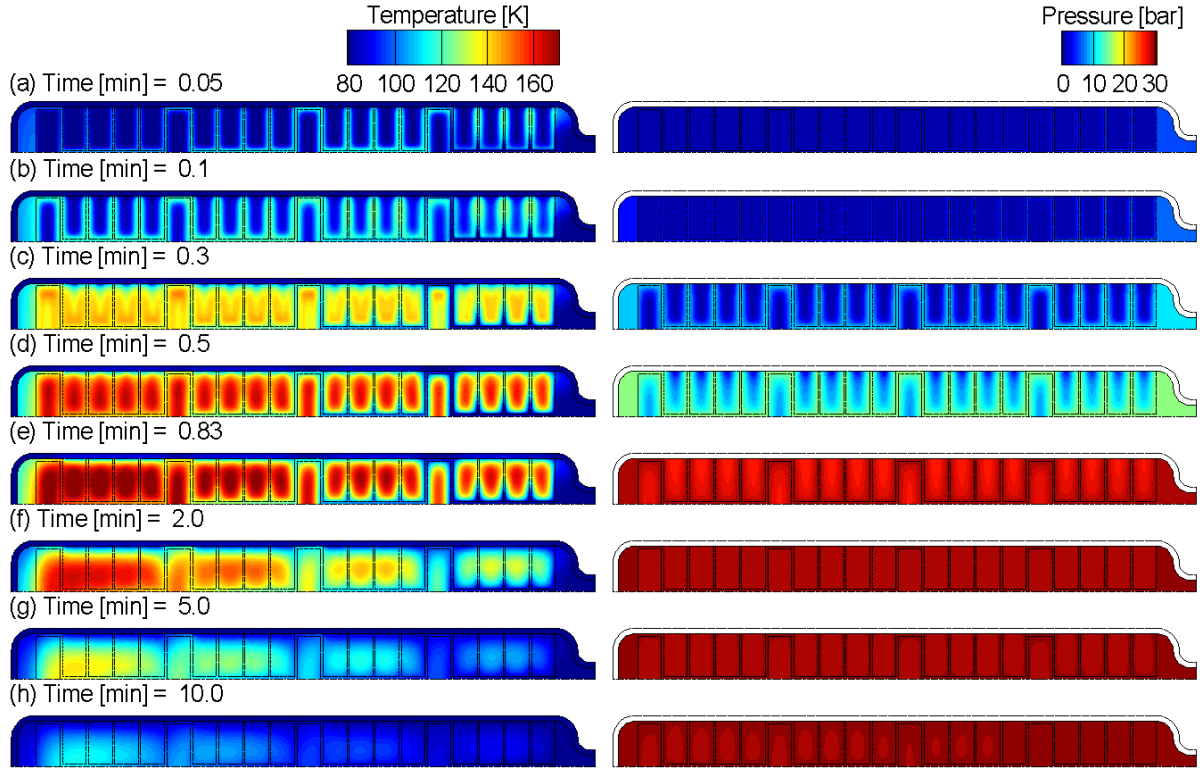


**Figure 9.7:** Pressure and temperature contour plots at various times for a filling process with an isothermal filling duration of 2 min.

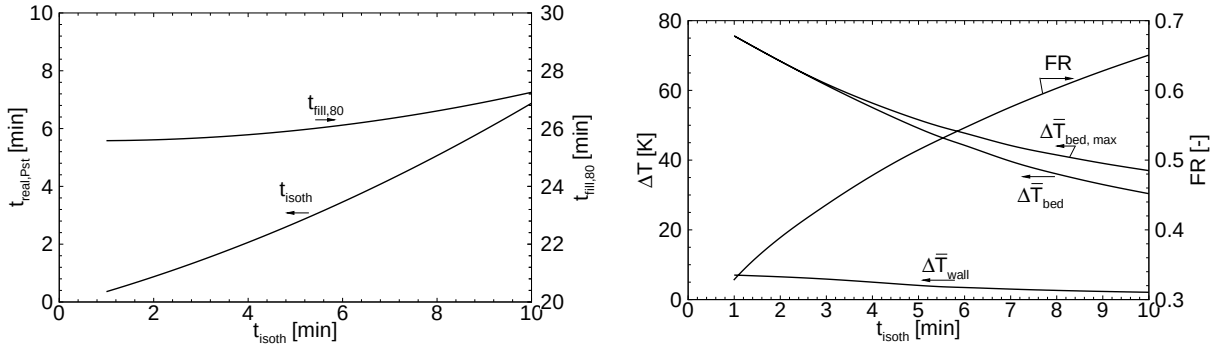


**Figure 9.8:** Variation of bed and wall temperature increases (values at $t_{real,P_{st}}$) and characteristic filling times as a function of the isothermal filling duration. Results from the pellets model.

perature, pellets near the inlet are in average somewhat colder since cold gas flows around them.

The time progression of average quantities in the vessel with pellets is qualitatively very similar to the ones obtained by the simulations with the adsorption bed vessel presented in the previous section as, for instance, shown in figure 9.2. The variation of the average temperature increase of wall and pellets as well as the characteristic times for the case of pellets is shown in figure 9.8. As it can be seen, the results are very similar to the bed case. Notable is, however, the shorter filling times. This is due to the fact that the pellets have a higher effective thermal conductivity, thus dissipating the energy release due to adsorption faster than the adsorption bed. A prerequisite for this better dissipation is a good contact between pellets and tube wall.

### 9.2.2 Filling Strategy II: Recirculation System

In this section, the recirculation system is investigated as a technique for filling adsorption storage vessels using the adsorbate itself as the energy carrier to remove energy from the vessel [69]. In this configuration, no internal $LN_2$ cooling system exists and the tubes are treated as adiabatic entities.

#### 9.2.2.1 Adsorption Bed

Figure 9.9 shows temperature contour plots at various times during simulation of the filling process with a isothermal filling duration of 3 min. Again, as stated before, the entering gas is adsorbed and a considerable temperature increase can be seen in the region already reached by it. As time advances, the temperature continues to increase due to both adsorption and gas compression. In the region near the inlet, the low enthalpy of the entering gas decreases the temperature after a short time.

At the time at which the pressure at the outlet side exceeds the storage pressure, the outlet valve opens allowing gas outflow towards the compressor inlet. This is in contrast to strategy I, since here the inlet mass flow rate is not re-

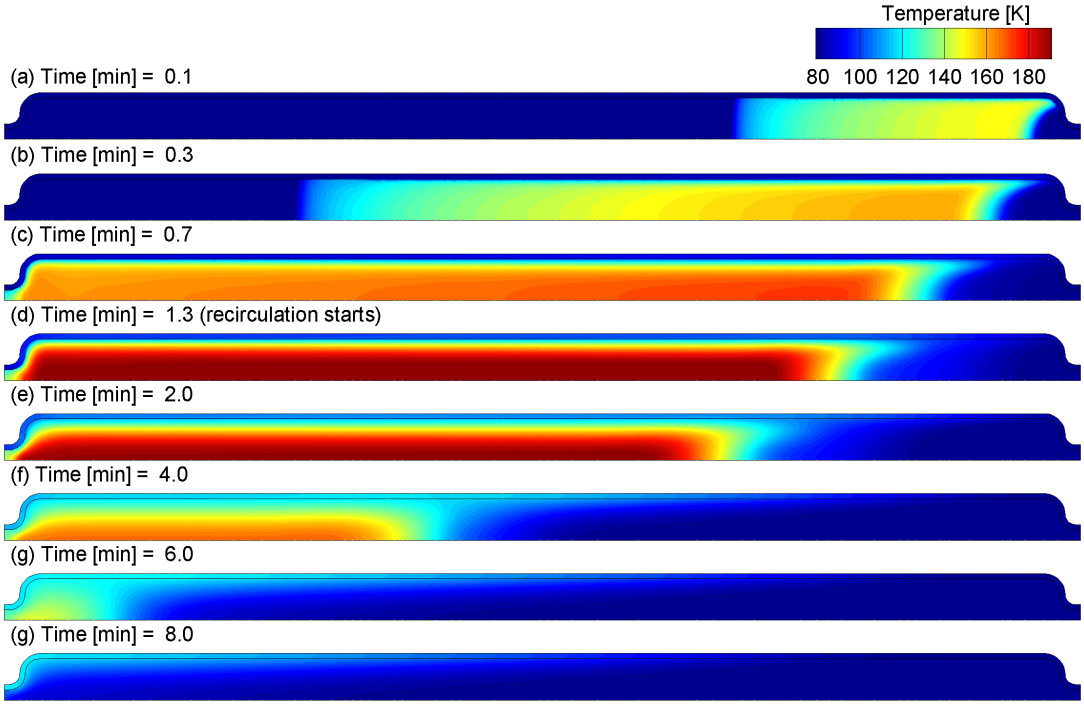


**Figure 9.9:** Temperature contour plots at various times for a filling process with a recirculation system. The isothermal filling duration is 3 min.

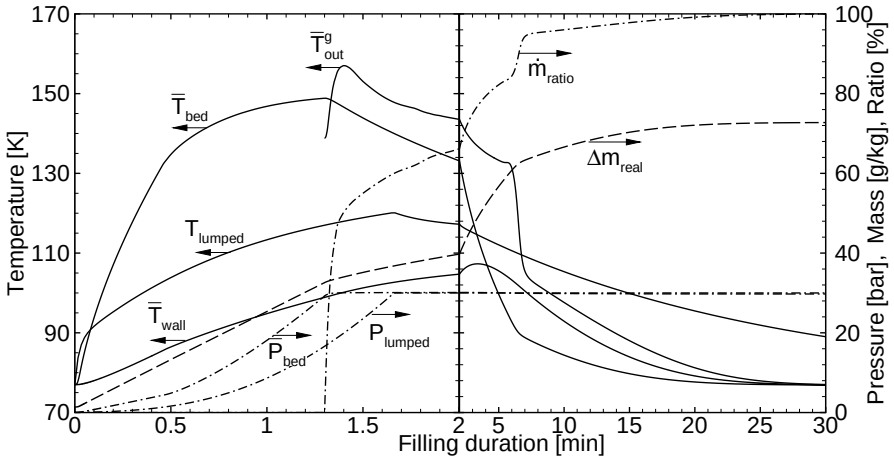


**Figure 9.10:** Time dependent behaviour of average quantities for the filling shown in figure 9.9. The kink of the curves at 2 min is only due to the axis scale change.

duced but outflow is allowed to relieve pressure. The outflowing gas is cooled in the external heat exchanger and introduced back into the vessel. Vessel cooling is thus accomplished by introducing cold gas and extracting comparatively hot gas. The contour plots show how the cold gas cooling effect advances towards the outlet side as time passes by. As a complement to the contour plots, figures 9.11 and 9.12 show axial and radial temperature profiles at various times as well.

Figure 9.10 shows the time devolution of average quantities during the process. From the average pressure (curve $\overline{P}_{bed}$), it can be seen that the storage pressure is achieved after 1:18 min. Up to this time, the average bed temperature $\overline{T}_{bed}$ increases, and from this time on, it decreases. The wall is heated by the bed through heat transfer during the first 5 minutes, time at which their average temperatures cross and the net heat transfer changes direction. Wall temperature increases much more than in strategy I, because in this case no $LN_2$ cooling exists.

Once the storage pressure is achieved, outflow starts. This is represented by the curve $\dot{m}_{ratio}$, which is defined as the ratio of the outflow to the inflow mass flow rate in percent. The inflow rate is constant throughout the process. As long as the final mass to be stored has not been achieved, i.e., the final temperature has not been reached, the outflow rate is lower than the inflow rate, whereas the difference is the instantaneous rate of increase of the stored mass in the vessel. The stored mass is given by curve $\Delta m_{real}$.

The outlet gas leaves the vessel with an average temperature given by the curve $\overline{T}^{g}_{out}$. The higher this temperature, the higher is the cooling effect because the enthalpy loss due to outflow is higher. The lower this temperature, the longer it takes to achieve the final temperature. That's why the temperature curves approach 77 K asymptotically.

Lumped model results are also depicted in figure 9.10. They are not in good agreement with that of the 2D model because the lumped model does not provide a spatial temperature distribution but rather only an average temperature, so that the enthalpy difference between outflow and inflow during recirculation is lower, and so is the cooling effect. Thus, lumped model results

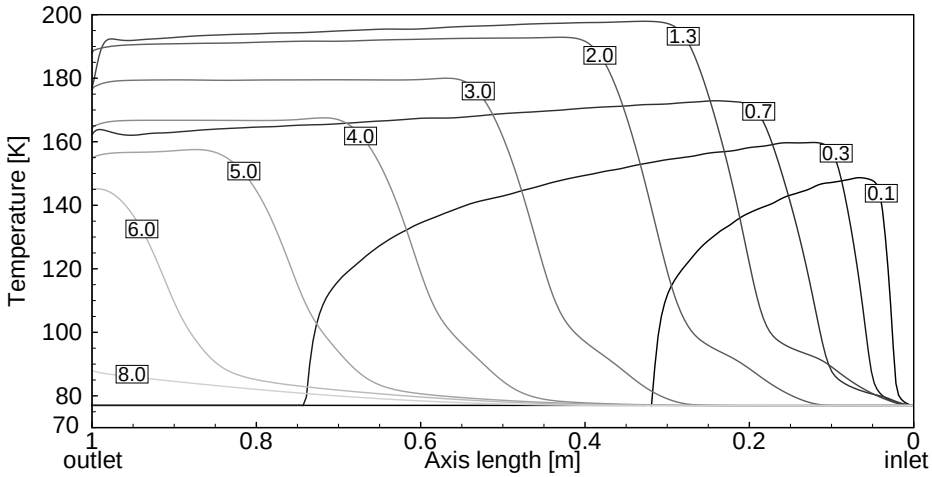


**Figure 9.11:** Axial temperature profiles for the filling shown in figure 9.9. The time values are expressed in minutes over each curve.

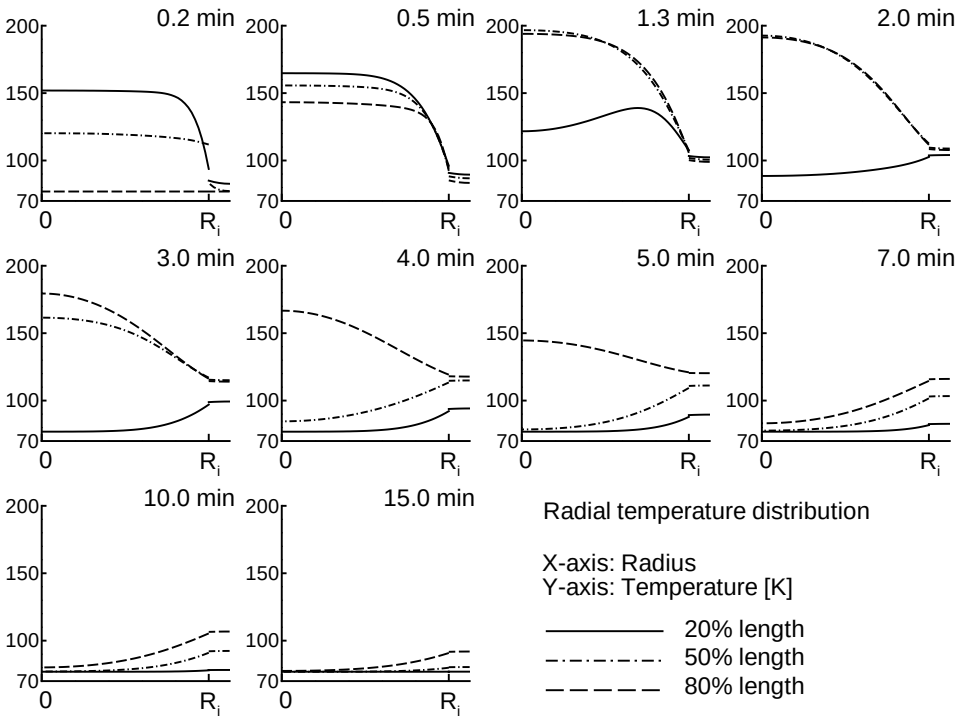


**Figure 9.12:** Radial temperature profiles at three positions along the tube axis length for the filling shown in figure 9.9. 0% length is the tube inlet. In the X-axis, positions from 0 to $R_i$ are within the bed, positions larger than $R_i$ are within the tube wall.

exhibit longer filling times and are not reliable for this kind of process.

Figure 9.10 also shows that for the given mass flow rate, the process lasts about 30 minutes; the value of $t_{fill,80}$ is, however, 20 min. The increase of the bed and wall average temperature at $t_{real,P_{st}}$ are 71 and 22 K, respectively. The values for other mass flow rates are shown in figure 9.13. As it can be seen, the real

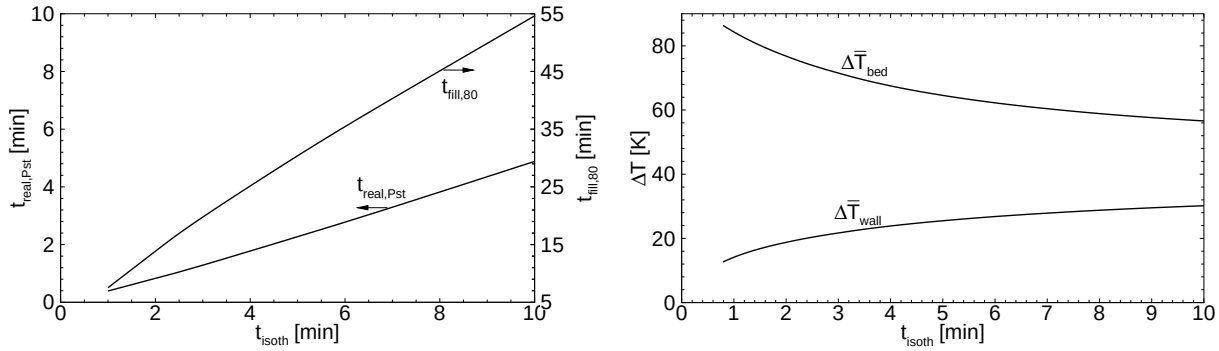


(a) (b)

**Figure 9.13:** Variation of bed and wall temperature increases (values at $t_{real,P_{st}}$) and characteristic filling times as a function of the isothermal filling duration. Results for the recirculation system.

time to achieve the storage pressure $t_{real,P_{st}}$ is roughly half of the isothermal filling duration $t_{isoth}$. The average temperature increase of the bed and wall at $t_{real,P_{st}}$ decreases and increases, respectively, as $t_{isoth}$ increases. This is because there is more time for heat transfer from the bed to the wall as $t_{isoth}$ increases. The filling time (represented, for instance, by $t_{fill,80}$) approaches zero as $t_{isoth}$ goes to zero (infinite mass flow rate) and shows a linear-like behaviour. Thus, it can be concluded that any desired filling time might be attained with the recirculation system, as long as the external components, such as the compressor and heat exchanger, are capable of satisfying the requirements, i.e., to maintain a certain mass flow rate in the system and to perform the necessary cooling. It must be noted, however, that the model assumes local equilibrium between bed fluid and particles and neglects intraparticle diffusion as well. These transport processes must be included when investigating high mass flow rates in the recirculation system.

The influence of the external heat exchanger cooling fluid can be taken

into account by considering different hydrogen temperatures at the heat exchanger outlet, i.e., vessel inlet temperature. In the analysis, two cases are considered: 60 K and 45 K. Figures 9.14-9.19 show the average quantities of several simulations: isothermal filling durations of 1 min and 3 min for the cases of heat exchanger outlet gas temperatures of 77 K, 60 K and 45 K. The symbols in the figures show the time $t_{fill,80}$, i.e., time at which, once the filling is stopped, the equilibrium temperature of the vessel would be 80 K. The curves for the 77 K-recirculation case has already been discussed above in the text, in the following, the other temperature cases are discussed.

Qualitatively, the behaviour of the averages curves is similar whatever is the vessel inlet gas temperature. In the cooling phase, though, temperature curves approach different levels. An interesting feature of the process while feeding the vessel with gas at a lower temperature than the desired temperature is that a supercooled region is generated at the inlet and advances towards the outlet as time passes by. Due to the fact that the storage capacity of the adsorbent is not a linear function of temperature, the supercooled region can store much more hydrogen than the storage loss due to warmer regions in the vessel. As a consequence, as the supercooled region becomes bigger, the pressure in the vessel has to be decreased in order not to exceed the final storage mass. This effect can be seen in figures 9.16-9.19. When this point is reached, it is not possible to stop the recirculation filling because the vessel possesses more energy than the same vessel with the same total amount of gas but at equilibrium at a temperature of, for instance, 80 K. This means that stopping the filling at that point would lead to both higher final pressure and temperature when the vessel reaches thermodynamical equilibrium. In addition, the tube wall would further increase the final bed temperature because it is warmer than the bed. Thus, the recirculation has to continue and the average pressure permanently reduced until the total energy of the vessel is at least as low as the total energy of the same vessel at equilibrium at desired final conditions. In this way, it is ensured that the final temperature will be at most equal to the desired storage temperature when the vessel achieves equilibrium. The time points at which the recirculation could be stopped are given by the square symbols in the figures. They correspond to a final temperature of 80 K.

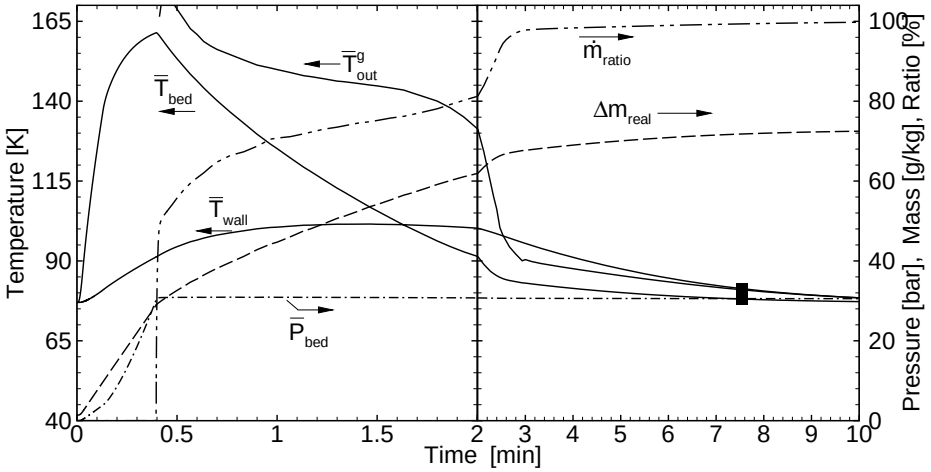


**Figure 9.14:** Time-course of average quantities during filling with a recirculation system. Heat exchanger gas outlet temperature: 77 K. Isothermal filling duration: 1 min.

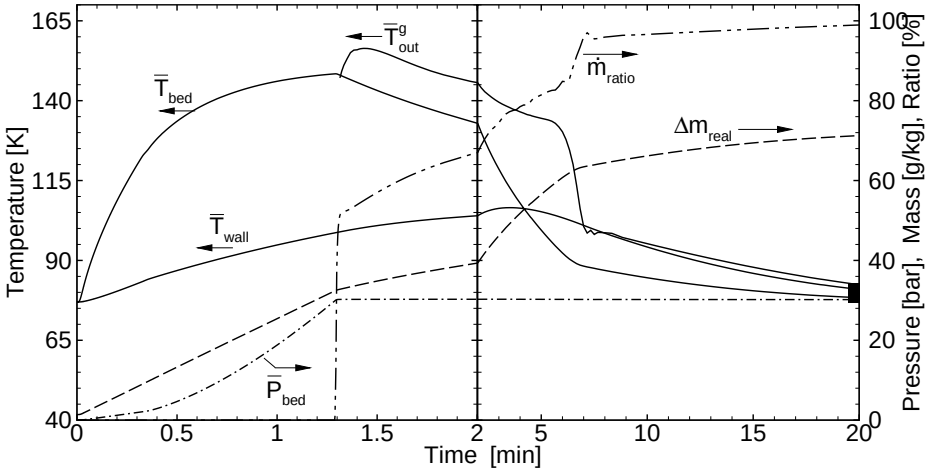


**Figure 9.15:** Time-course of average quantities during filling with a recirculation system. Heat exchanger gas outlet temperature: 77 K. Isothermal filling duration: 3 min.

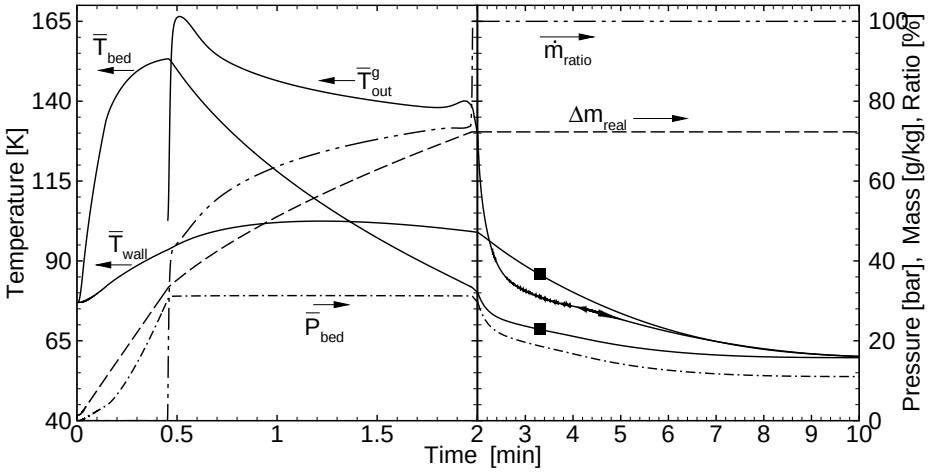


**Figure 9.16:** Time-course of average quantities during filling with a recirculation system. Heat exchanger gas outlet temperature: 60 K. Isothermal filling duration: 1 min.

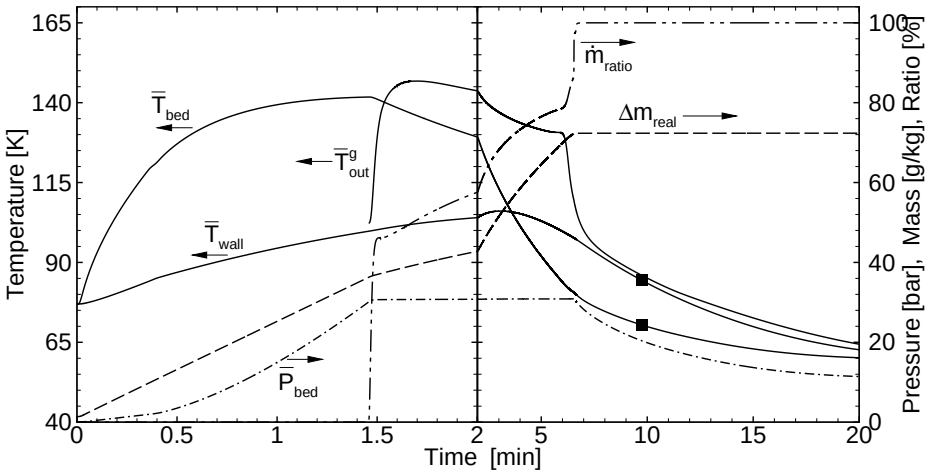


**Figure 9.17:** Time-course of average quantities during filling with a recirculation system. Heat exchanger gas outlet temperature: 60 K. Isothermal filling duration: 3 min.

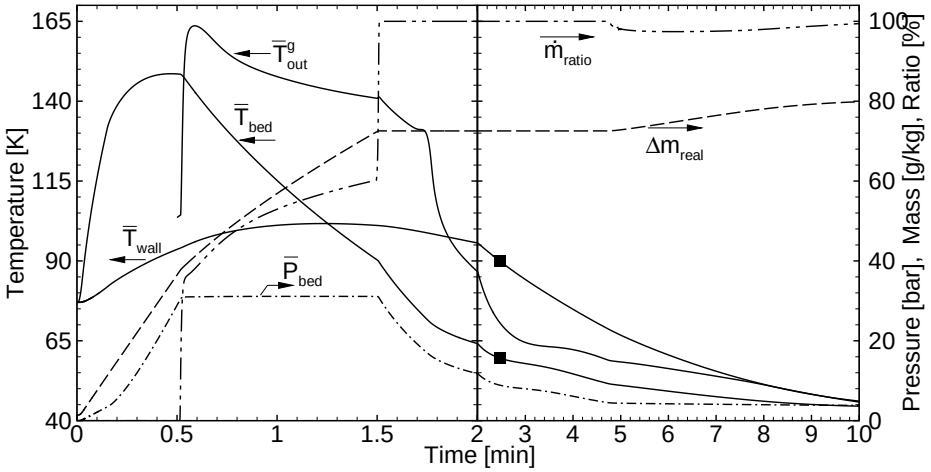


**Figure 9.18:** Time-course of average quantities during filling with a recirculation system. Heat exchanger gas outlet temperature: 45 K. Isothermal filling duration: 1 min.

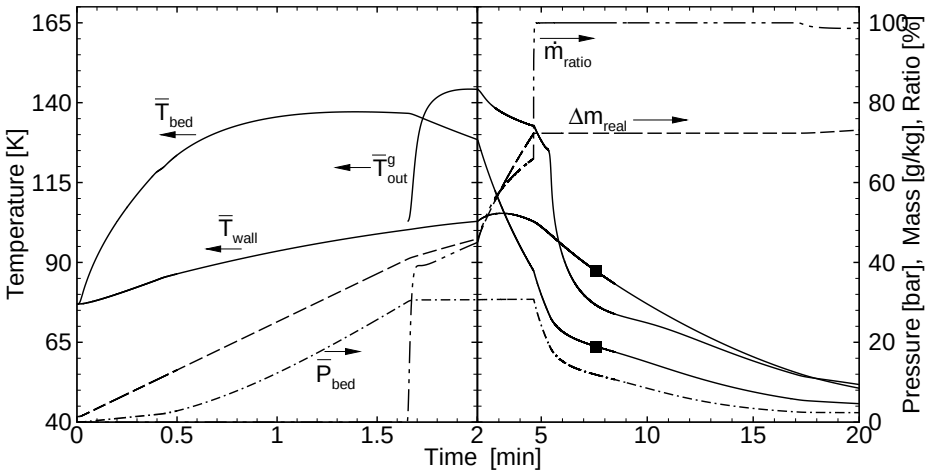


**Figure 9.19:** Time-course of average quantities during filling with a recirculation system. Heat exchanger gas outlet temperature: 45 K. Isothermal filling duration: 3 min.

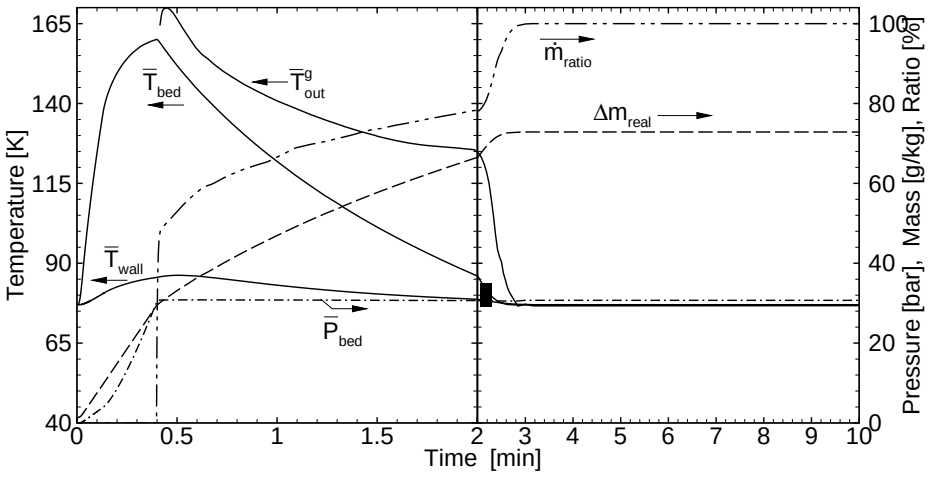


**Figure 9.20:** Time-course of average quantities during filling with a recirculation system and simultaneous vessel internal $LN_2$ cooling. Heat exchanger gas outlet temperature: 77 K. Isothermal filling duration: 1 min.

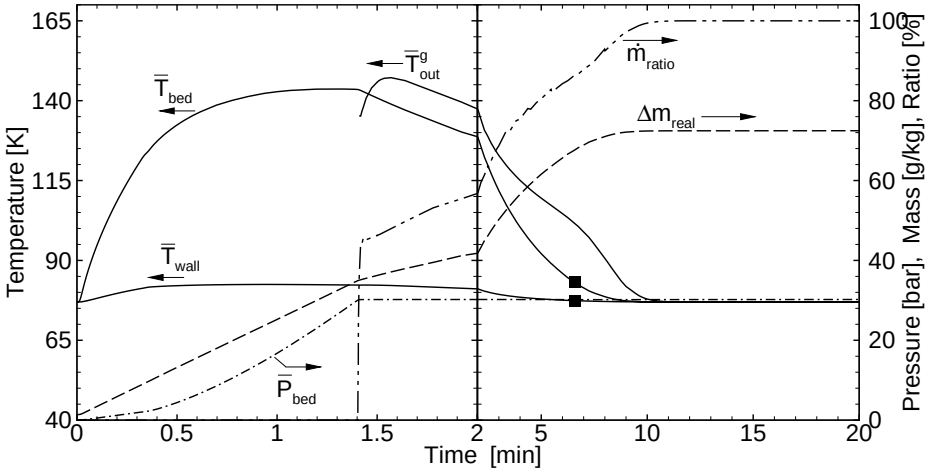


**Figure 9.21:** Time-course of average quantities during filling with a recirculation system and simultaneous vessel internal $LN_2$ cooling. Heat exchanger gas outlet temperature: 77 K. Isothermal filling duration: 3 min.

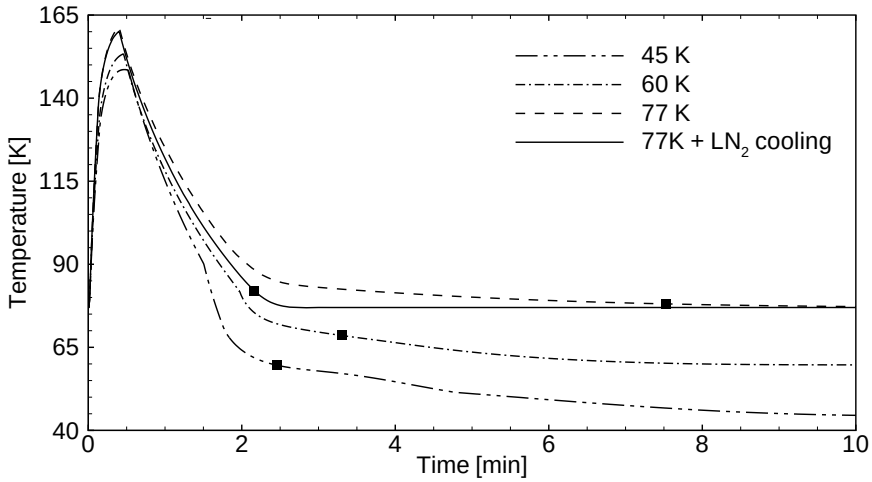


**Figure 9.22:** Average bed temperature during filling with a recirculation system for different cooling performances and configurations. The temperature represents the vessel inlet gas temperature. Isothermal filling duration is 1 min.

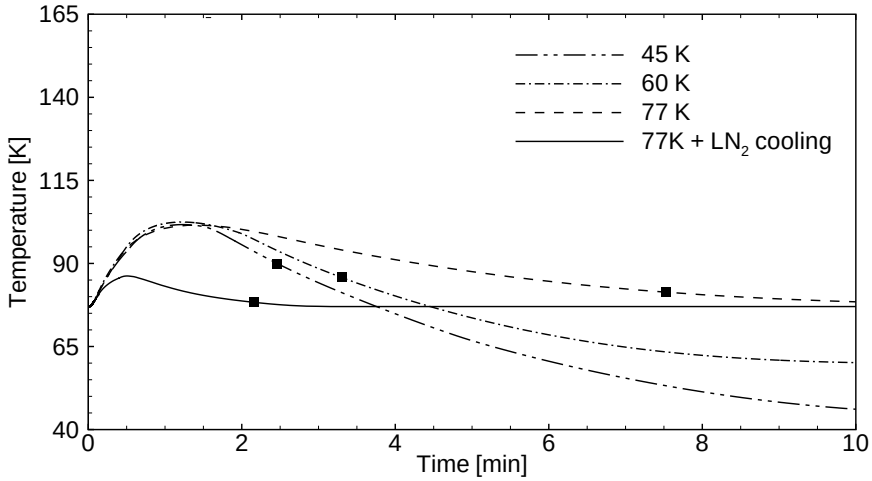


**Figure 9.23:** Average wall temperature corresponding to figure 9.22.

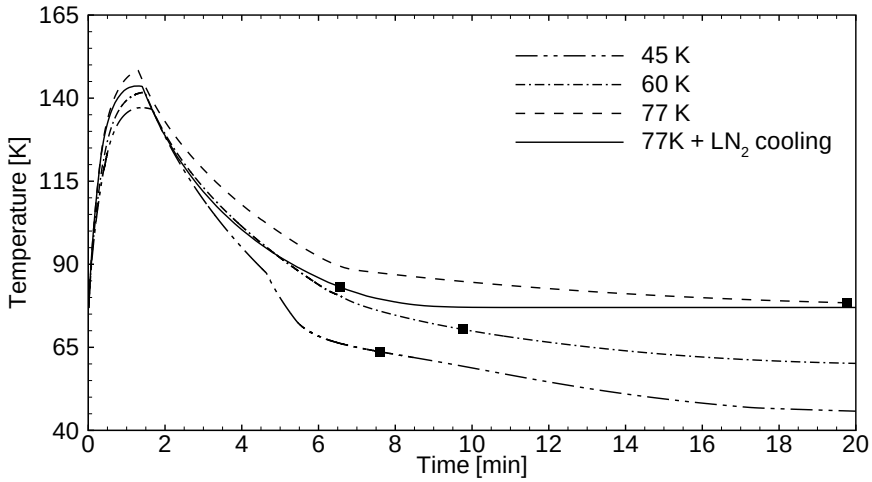


**Figure 9.24:** Average bed temperature during filling with a recirculation system for different cooling performances and configurations. The temperature represents the vessel inlet gas temperature. Isothermal filling duration is 3 min.

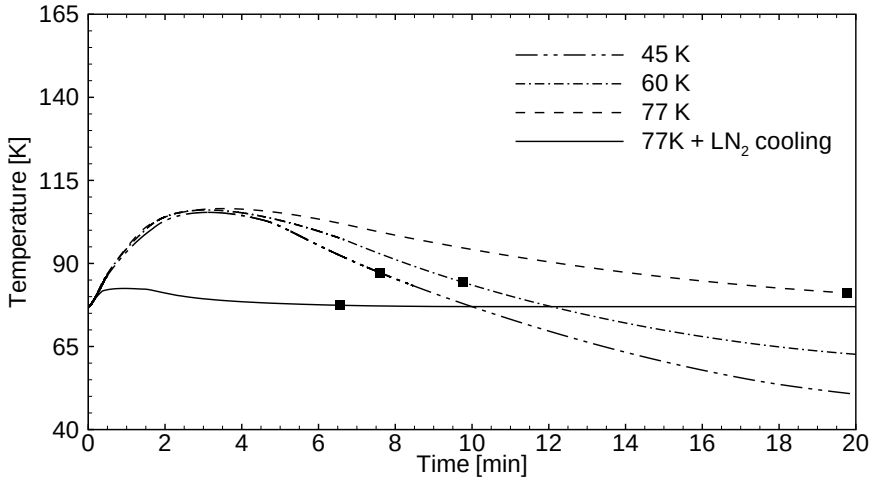


**Figure 9.25:** Average wall temperature corresponding to figure 9.24.

For the 60 K case, the average pressure must be reduced to about 12 bar as the vessel temperature approaches 60 K. For the 45 K case, in contrast, the average pressure must be reduced to much lower pressures, in the order of 1 bar. But, since there must be a pressure gradient between vessel inlet and outlet to guarantee hydrodynamic flow through the bed, the outlet pressure tends to go to zero as the average bed temperature approaches 45 K. In the simulations, however, a minimum pressure of 1 bar was allowed. That's why the stored mass $\Delta m_{real}$ increases after a period in which it was held constant by decreasing the pressure, as shown in figures 9.18-9.19. When 1 bar is reached at the vessel outlet, the pressure reduction cannot be continued and this leads to an increase of the storage capacity as the temperature further decreases.

Upon analyzing figures 9.14-9.19, it can be concluded that the wall temperature increase in the initial phase considerably prolongs the filling time because it has to be cooled down in the final phase. In addition, since the temperature gradients between bed and wall in the initial phase are higher than that in the final phase (figure 9.12), the wall cooling takes longer than the wall heating. Wall heating can be avoided with a vessel internal $LN_2$ cooling system. The simultaneous use of a vessel internal $LN_2$ cooling system and recirculation optimizes the filling process because, on the one hand, wall heating is minimized by the $LN_2$ and, on the other hand, the recirculation cools down the bed efficiently. Figures 9.20-9.21 show two filling process with this concept for isothermal filling durations of 1 min and 3 min, respectively. The wall temperature curves show a minimal increase during the process.

Figures 9.22 and 9.23 compare the average bed and wall temperatures, respectively, for the recirculation simulations with $t_{isoth}$ = 1 min. Figures 9.24 and 9.25 show the comparison for $t_{isoth}$ = 3 min. The figures show that, during the first minutes of the process, bed and wall temperatures behave qualitative very similar. Although the maximum value reached by the bed temperature decreases as the inlet temperature decreases, the wall temperature shows almost no difference. Solely the process with simultaneous $LN_2$ cooling shows a very low wall temperature increase compared to the others. The shortest filling times, given by the symbols, are obtained with the recirculation-$LN_2$ cooling configuration. The disadvantage due to wall heating in the configurations with

$LN_2$ cooling can be indirectly seen in the bed temperature. It is necessary to cool it down to temperatures lower than the desired final temperature in order to account for posterior heat transfer with the wall as the vessel goes to equilibrium. Therefore, the utilization of cooling fluids other than $LN_2$ or even the utilization of liquid hydrogen in the recirculation system does not make the process more efficient. Moreover, this would considerably increase the operation costs as well as make the cooling facility much more complex. Handling of liquid nitrogen is much easier than that of liquid hydrogen or, for instance, liquid helium [70], so that it is worth to restrict the cooling by means of $LN_2$.

#### 9.2.2.2 Pellets

This section addresses the filling of the adsorption vessel containing pellets with a recirculation system. As stated before, channels and slits between pellets must be built in such a configuration in order to facilitate gas flow through the tube. If the tube cross-section is totally blocked by a pellet, the flow resistance is so high that big pressure gradients are needed to guarantee gas motion through the pellets and the operation of a recirculation system turns out to be difficult.

Since flow through the vessel tubes does not necessarily go through the pellets but rather around them through the channels and slits, pellets positioning as well as channels configuration are decisive for filling characteristics. In the analysis, two configurations are considered: *case 1*, which consists of a stack of center-perforated pellets where one in five pellets is not center-perforated (same geometry as in chapter 8); and *case 2*, which consists of a stack of successive center-perforated and non-center-perforated pellets.

Figure 9.26 shows temperature contour plots at various times for a filling process with an isothermal filling duration of 3 min using the recirculation system for both geometric cases. In addition, figure 9.27 shows the time dependent behaviour of volume-averaged quantities. The contour plots show that the interior of the pellets are warmer than their external surfaces, by which the channels and slits are formed, so that heat transfer must happen from the interior to the external surface of the pellets before it can be removed from the

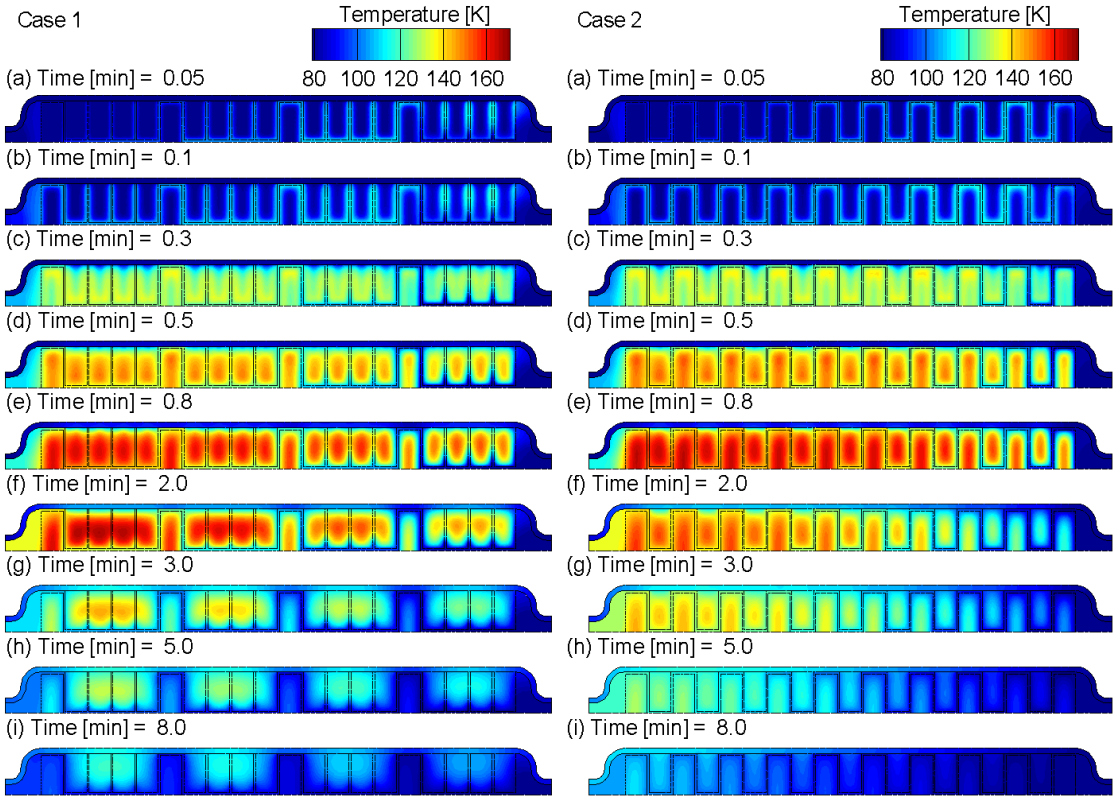


**Figure 9.26:** Temperature contour plots at various times for a filling process with an isothermal filling duration of 3 min.

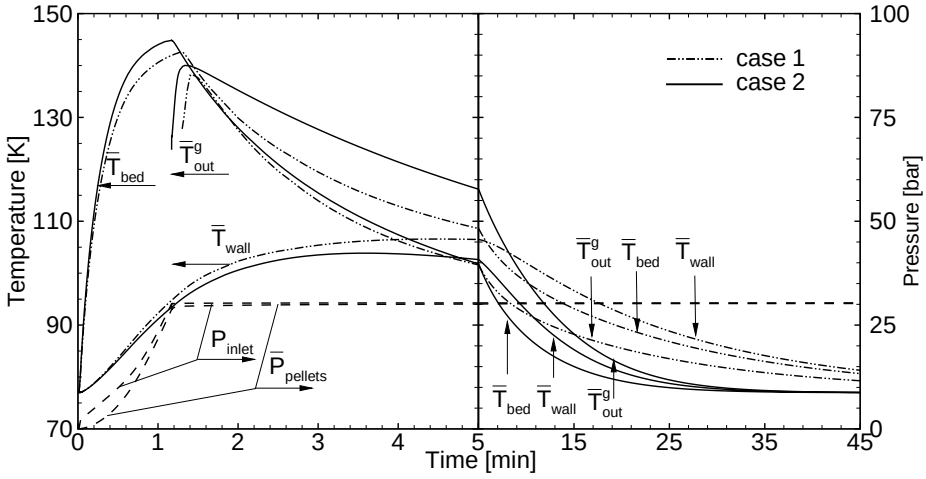


**Figure 9.27:** Time dependent behaviour of average quantities for the filling shown in figure 9.1. The bend of the curves at 5 min is only due to the axis scale change.

vessel through the recirculating flow. Cooling characteristics of a vessel with pellets through recirculation still depends on the heat conduction properties of the adsorbent because of this internal heat conduction process. Therefore, it is important that the channels are as long as possible in order to increase both the heat transfer area and the time of stay of the gas flowing in the vessel. Upon analyzing figure 9.27, it can be seen that, in case 1, the temperature of the gas leaving the vessel is always lower than the average temperature of the pellets and wall, whereas, in case 2, the outlet temperature is always higher. This confirms the less efficient cooling effect through recirculation in case 1 because the recirculating gas covers relatively long distances flowing on the tube axis and does not optimally cool down peripheric regions, which are mainly cooled through heat conduction. In case 2, although the interior of the pellets are also cooled through conduction, the conduction lengths are shorter. Moreover, the longer length of the channels allows for better heat transfer to the recirculating flow.

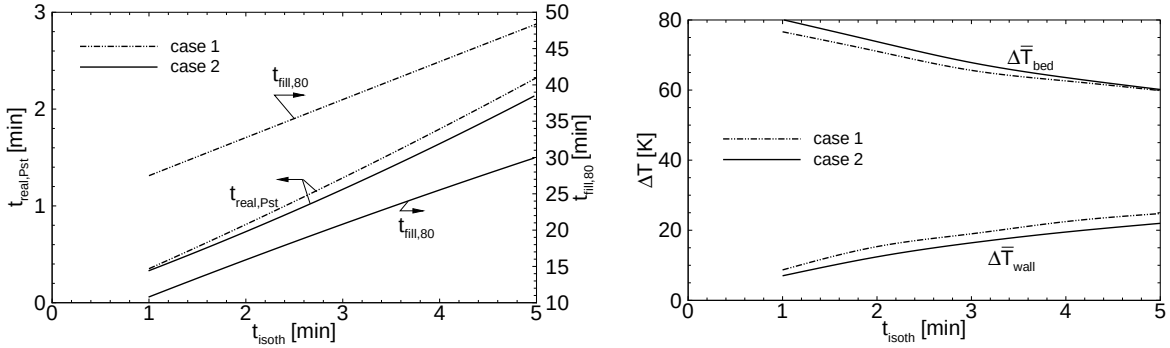


**Figure 9.28:** Variation of bed and wall temperature increases (values at $t_{real,P_{st}}$) and characteristic filling times as a function of the isothermal filling duration. Results for the recirculation system.

A series of simulations gives the variation of the characteristic filling times and the average temperature of pellets and wall as a function of the mass flow rate. Results are depicted in figure 9.28 for both geometry cases. Qualitative dependences are similar to the adsorption bed vessel. Interesting is the difference on filling times between both cases. In case 1, filling lasts approx. 20 min longer due to unfavourable pellets positioning.

## 9.3 Discharge

Discharge processes were extensively analysed in chapter 6 by means of a lumped model. The analysis was restricted to long processes (low extraction rates), for which conditions of homogeneous temperature within the vessel insulation can be assumed. In this section, discharge is analysed with the 2D model by considering both long and short processes. It will be shown that the assumption of temperature homogeneity is well satisfied in the case of long discharges. The analysis is restricted to the adsorption bed configuration.

Filling processes analysed in the previous sections were considered to be adiabatic. Discharge processes, however, due to longer durations, will include heat transfer with the environment. The boundary conditions on the external surface of the tube wall are the same as the ones used in the analysis with the lumped model and are given in table 6.1. In addition, discharge will be considered to be processes of gas extraction from the vessel at a constant mass flow rate. The mass flow rate is given indirectly by the isothermal discharge duration $t_{isoth}$, which is the time necessary to unload the vessel from the storage pressure ($P_{st}$=30 bar) to the depletion pressure ($P_d$=1 bar) isothermally.

Figure 9.29 shows temperature contour plots at various times during a discharge process with $t_{isoth}$=4h, and figure 9.30 shows the average quantities within the vessel as a function of time. As it can be seen, both average bed and wall temperatures as well as the pressure within the vessel decrease as time passes by. After about 120 min, the pressure already reaches the depletion pressure, so that, from this point on, gas supply at the same rate cannot be maintained anymore. The time at which the depletion pressure is reached in the real discharge process is denominated as $t_{real,Pd}$ and it is half of the isothermal discharge duration in this case. At $t_{real,Pd}$, the average bed temperature $\overline{T}_{bed}$ has decreased approximately 21 K ($\Delta\overline{T}_{bed}$ = 17 K), whereas the average wall temperature $\overline{T}_{wall}$ has decreased approximately 17 K ($\Delta\overline{T}_{wall}$ = 17 K). Radial temperature distribution at three axial positions is shown for various times in figure 9.31. Lower temperatures are observed on the axis, whereas, on the wall, due to its thermal mass, bed temperature is somewhat higher. Temperature decrease causes an increase of the residual gas at the depletion

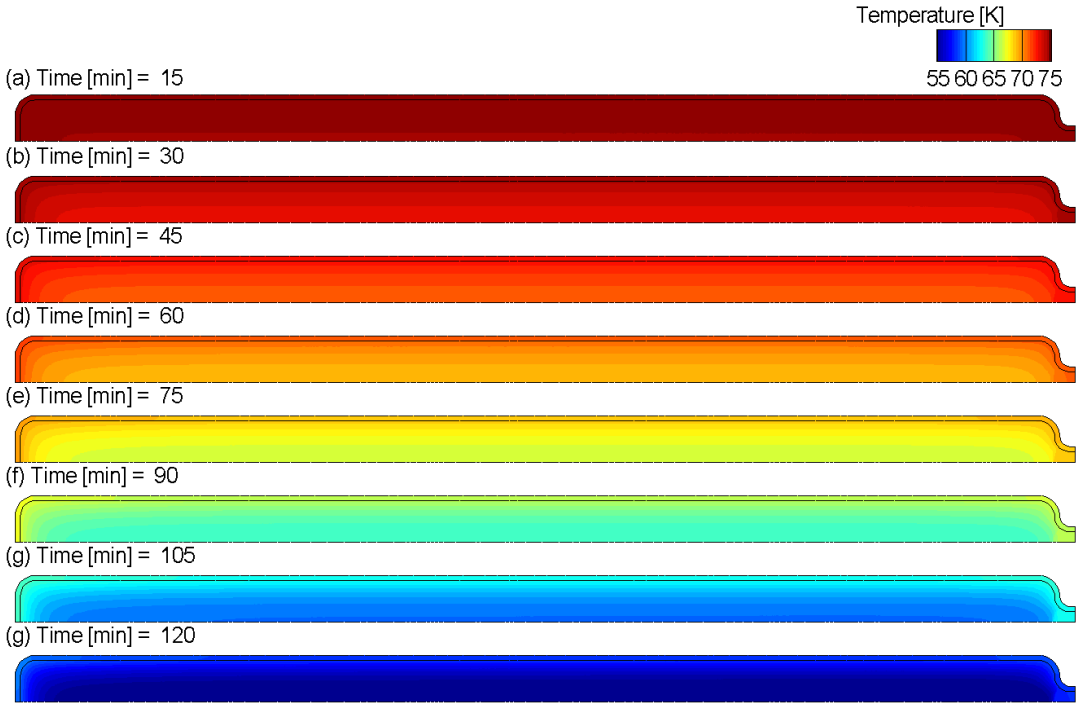


**Figure 9.29:** Temperature contour plots at various times for a discharge process with constant mass flow rate. The isothermal discharge duration is 4 hours.

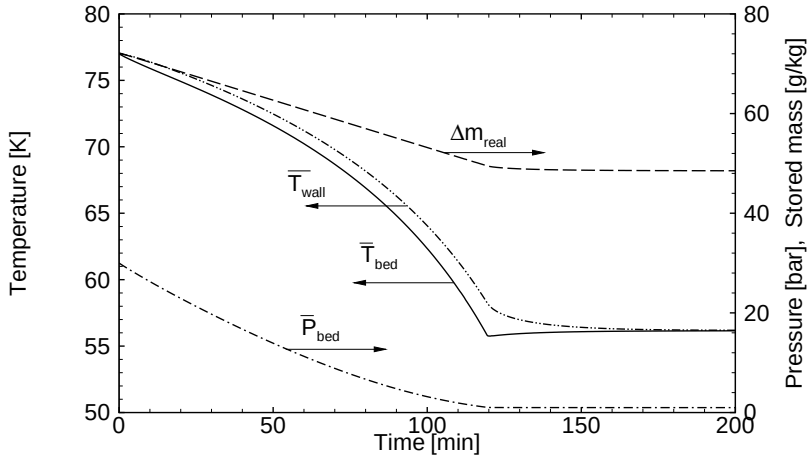


**Figure 9.30:** Time dependent behaviour of average quantities for the discharge shown in figure 9.29.

.

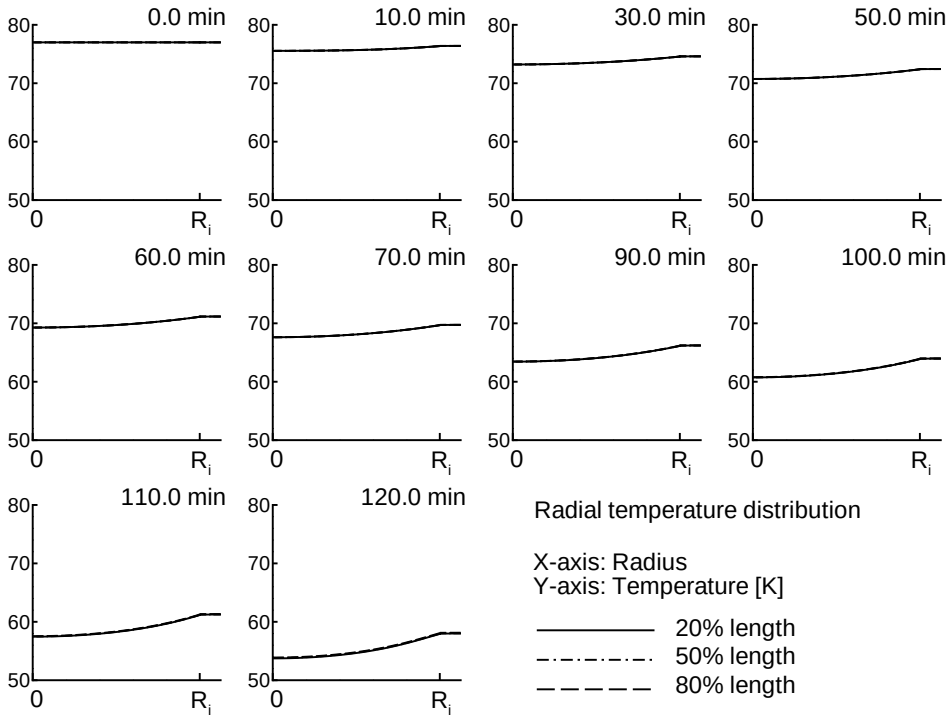


**Figure 9.31:** Radial temperature profiles at three positions along the tube axis length for the discharge shown in figure 9.29. 0% length is the tube outlet. In the X-axis, positions from 0 to $R_i$ are within the bed, positions larger than $R_i$ are within the tube wall. No difference is seen between axial positions.

pressure because it increases the storage capacity of the adsorbent, thus decreasing the amount of gas that can be extracted from the vessel. That's why the depletion pressure is reached earlier than in the case of isothermal discharge ($t_{real,Pd}$<$t_{isoth}$). The amount of hydrogen delivered was about 50% of the amount that would be delivered during an isothermal process. This quantity is the capacity ratio CR, which is defined as the ratio of gas delivered by discharging from the storage to the depletion pressure and the amount obtained from discharging isothermally between the same two pressures.

A series of simulations were carried out to determine the effect of the extraction mass flow rate (by means of $t_{isoth}$) on the average bed and wall temperatures and the capacity ratio. The results are depicted in figure 9.32, which shows that, the higher the mass flow rate (shorter $t_{isoth}$), the higher is the av-

erage bed temperature decrease and the lower is the average wall temperature decrease, because the shorter is time for heat transfer between bed and wall during the process. As $t_{isoth}$ increases, their curves approximates and for $t_{isoth}$>20 h, only a small difference can be seen between bed and wall temperature decreases. This verifies the temperature homogeneity assumption for long discharges. Figure 9.32 also shows the temperature decrease ($\Delta T_{lumped}$) obtained with a lumped model representing the adsorption vessel in question. It can be seen that, for long discharges, the results of both models are the same. As to the capacity ratio, the figure shows that it increases for longer processes, because bed temperature is higher.

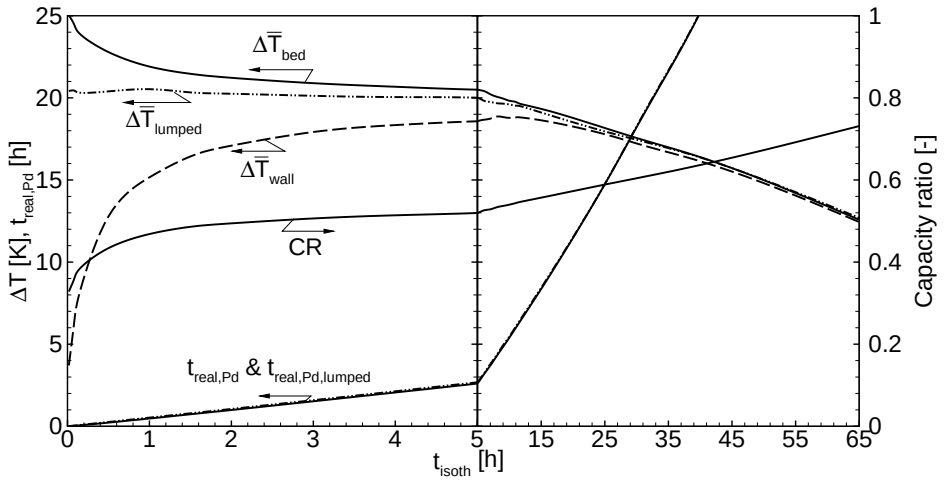


**Figure 9.32:** Variation of bed and wall temperature decreases (values at $t_{real,P_d}$) and characteristic discharge times as a function of the isothermal discharge duration.

# 10 Summary

Hydrogen storage is of key importance for the establishment of a hydrogen economy. Within the scope of this work, hydrogen storage by adsorption on activated carbon at cryogenic temperatures has been analysed. The work has been mainly concerned with storage systems for mobile applications such as hydrogen-powered vehicles. Adsorption is one of the current technologies being analysed for hydrogen storage among gas compression, hydrogen liquefaction and absorption in hydrides.

A fundamental information regarding adsorption systems and processes is represented by the adsorption isotherms. These provide the storage capacity of the adsorbent at a constant temperature as a function of pressure. In this work, the adsorption isotherms have been modelled by the Ono-Kondo lattice theory and the resulting model equations have been parametrised with experimental data of adsorption equilibrium over wide ranges of pressure and temperature. Good agreement between experimental and modelled isotherms has been obtained. With the principles of solution thermodynamics, the adsorption system could be completely described thermodynamically. The thermodynamic functions obtained with this approach are relatively simple and valid for all conditions of pressure and temperature. With them, mass and energy balances could be easily performed.

Basically, this thesis can be divided in two parts: the first part addresses macroscopic balances, whereas the second part deals with microscopic balances. In the first part, an extensive analysis by means of a lumped model has been carried out in order to attain a global assessment and a overall view of the requirements of the system. The analysis has been enriched by including a comparison with other storage technologies – a low-pressure liquid hydrogen vessel and a high-pressure cryogenic vessel filled with either liquid hydrogen or cryogenic compressed hydrogen at 80 K – under the same operating condi-

tions. The analysis has been concerned, for instance, with hydrogen venting losses during vessel operation, inactivity (dormancy) and filling. Particularly for adsorption vessels, the analysis has also presented the thermal management requirements on operating an adsorption vessel, such as the total cooling performance during filling for several initial conditions as well as the total supply of energy during discharge for several operating conditions.

In the second part of this thesis, a more elaborated model of an adsorption vessel obtained by performing microscopic balances has been presented. The model divides the vessel in different domains: adsorbent, bulk gas volumes, vessel wall and environment. Adsorbent volumes may be configured so as to represent an adsorption bed composed of fine grain powder or a pellet – compressed powder shaped into a larger discrete object. The functionality of the model has been shown by comparing simulations results with dynamic experimental data. Good agreement has been obtained, both qualitative and quantitative. The model has also contributed to a better understanding and visualization of filling and discharge processes and might be utilized, for instance, as a tool for system design, process development and optimization.

Adsorption systems for hydrogen storage have been proven to be feasible. However, the storage capabilities of such a system are far from the requirements for viable onboard hydrogen storage. This is also the case for other storage technologies currently being developed such as gas compression, liquefaction and hydrides. Simple, incremental improvements in these technologies do not seem to allow the technologies to meet the rigorous storage requirements. Adsorption systems, in addition, have several other characteristics that might hinder their application.

Adsorption systems require cryogenic temperatures (77 K-100 K) in order to achieve considerable storage capacity. It follows that the system, in spite of superinsulation, is subject to heat leakage losses. The results of the present study have shown that these losses can achieve about 25% of the vessel storage capacity in the case of two weeks of inactivity if the vessel is initially full.

Adsorption systems also require thermal management during operation. In discharge processes, the system must be heated up in order to facilitate hydro-

gen desorption. Without energy supply, the operation time of a vehicle with a full tank can in some cases be only 10-20% of that with heat management. This is a consequence of the increasing residual amount of hydrogen at the depletion pressure as the system temperature drops. It has been shown that the system has to be gradually heated up as hydrogen is extracted so as to achieve a final temperature of around 150 K. At this temperature only a irrelevant amount of gas remains in the tank at the depletion pressure. In practical systems waste heat from the fuel cell or combustion engine should be utilised for this purpose.

In charge processes, adsorption systems have to be cooled down. Rapid charging under conditions in which the heat of adsorption is not efficiently dissipated can results in up to 70% storage capacity loss. Providing cooling, the cooling power for filling a tank with a storage capacity of 5 kg of hydrogen und pratical conditions is equivalent to the evaporation heat of about 85 liters of liquid nitrogen. Moreover, this has to be provided during filling time, which is expected from consumers to be shorter than 3 minutes.

The cooling strategy adopted is crucial for the achievement of short filling times during charge processes. Cooling concepts in which the heat dissipation rate depends on the heat conduction properties of the adsorbent have filling times that are hardly shorter than 20 minutes. In contrast, the results have shown that the proposed recirculation system in which the hydrogen itself is used as the vessel cooling fluid is more suitable to attain short filling times. In this concept, hydrogen is introduced into the storage vessel and the system heats up, any non-adsorbed relatively hot gas is recirculated back into the refrigeration unit, cooled and introduced again into the vessel. This is continuously done until the desired storage conditions are achieved. The attained filling times have been found to vary approximately hyperbolically with the applied recirculation mass flow rate so that any filling time should theoretically be possible; it depends only on the power of the recirculation system. In discharge processes, heating strategy do not play an important role because, in the worst case, extraction will last some hours so that there is enough time for heat conduction within the system.

The big advantage of adsorption system is the low operating pressure, which

makes it particularly suitable for scenarios in which filling stations have on-site hydrogen production. Since current electrolysers outputs hydrogen at pressures of about 60-100 bar, no in-between gas compression (at least not over high pressure ratio) would be required. However, in order to operate with adsorption systems, these filling stations would have to be equipped with robust liquid nitrogen refrigeration systems and recirculation systems. This study has estimated that a primary energy quantity equivalent to roughly 10 kg of hydrogen (65% production, 25% cooling, 10% others) might be necessary for producing and storing 5 kg of hydrogen into an adsorption system. This certainly represents high energy expenses and high operation costs.

Adsorption and compressed gas storage systems are comparable in terms of energy intensity, storage capacities, system volume and weight. However, $CH_2$ systems do not require thermal management during operation. Hence, from an operational point-of-view, $CH_2$ systems are more convenient. Liquid hydrogen and hydride storage systems yield higher volumetric capacities, what is of particular importance for mobile applications. However, these systems are very energy intensive. Based on these statements, compressed gas systems seem to be the most satisfactory near term storage technology when operation and energy intensity factors are considered. In this case, driving range reductions of about 50% are to be expected for hydrogen-powered vehicles due to volumetric constrains. Promising utilisations of adsorption systems are limited to very special applications.

# A Appendix

## A.1 Euler's Theorem [21]

The energetic fundamental relation of a system may be expressed as

$$U = U(S,\ V,\ N_1,\ ...,\ N_C), \tag{A.1}$$

and its first derivation is

$$dU = \left[\frac{\partial U}{\partial S}\right]_{V,N_1,...,N_C} dS + \left[\frac{\partial U}{\partial V}\right]_{S,N_1,...,N_C} dV + \sum_{j=1}^{C} \left[\frac{\partial U}{\partial N_j}\right]_{S,V,N_{c=1..C,c\neq j}} dN_j\,. \tag{A.2}$$

The various partial derivatives in the foregoing equation are the intensive parameters and the following notation is conventional:

$$\left[\frac{\partial U}{\partial S}\right]_{V,N_1,...,N_C} \equiv T, \text{ the temperature,} \tag{A.3}$$

$$-\left[\frac{\partial U}{\partial V}\right]_{S,N_1,...,N_C} \equiv P, \text{ the pressure,} \tag{A.4}$$

$$\left[\frac{\partial U}{\partial N_j}\right]_{S,V,...,N_k,...} \equiv \mu_j, \text{ the chemical potential of } j\text{th component}. \tag{A.5}$$

The homogeneous first-order property of the fundamental relation permits that equation to be written in a particularly convenient form, called the Euler form. From the definition of the homogeneous first-order property it follows that, for any $\lambda$

$$U(\lambda\, S,\ \lambda\, V,\ \lambda\, N_1,\ ...,\ \lambda\, N_C) = \lambda\, U(S,\ V,\ N_1,\ ...,\ N_C)\,. \tag{A.6}$$

Differentiating it with respect to $\lambda$

$$\sum_{X_k=S,V,N_1,...,N_C} \frac{\partial U(...,\lambda X_k,...)}{\partial(\lambda X_k)} \frac{\partial(\lambda X_k)}{\partial \lambda} = U(S,\ V,\ N_1,\ ...,\ N_C)\,, \tag{A.7}$$

or

$$\sum_{X_k=S,V,N_1,...,N_C} \frac{\partial U\,(...,\lambda X_k,...)}{\partial\,(\lambda X_k)}\,X_k = U(\,S,\,V,\,N_1,\,...,\,N_C)\,. \tag{A.8}$$

Equation A.8 is true for any $\lambda$ and in particular for $\lambda = 1$, in which case it takes the form

$$\sum_{X_k=S,V,N_1,...,N_C} \frac{\partial U\,(...,X_k,...)}{\partial X_k}\,X_k = U(\,S,\,V,\,N_1,\,...,\,N_C)\,. \tag{A.9}$$

Inserting the intensive parameters defined by equations A.3-A.5 into equation A.9, it follows that

$$U = TS - PV + \mu_1 N_1 + ... + \mu_C N_C\,. \tag{A.10}$$

# List of Figures

# List of Tables

# List of symbols

## Latin letters

| | | |
|---|---|---|
| $A$ | [$m^2$] | Area |
| $A$ | [kg/kg] | Model parameter |
| $B_{AS}$ | [$m^3$/kg] | Second virial coefficient |
| $B_0$ | [m] | Porous medium structural paramater |
| $C$ | [variable] | Model pre-factor, model parameter |
| $c_p$ | [J/(kg K)] | Constant-pressure specific heat |
| $C$ | [-] | Number of gas components |
| $C$ | [variable] | Model pre-factor, model parameter |
| $D$ | [m] | Thickness of the interfacial layer |
| $D$ | [kg] | Delivery |
| $D$ | [m/s] | Diffusion coefficient |
| $D_p$ | [m] | Particle diameter |
| $E$ | [J] | Total energy |
| $E$ | [J] | Interaction energy of adsorbate-adsorbate molecules |
| $E_a$ | [J] | Interaction energy of adsorbate molecule and adsorbent surface |
| $E_s$ | [J/mol] | Activation energy of hopping, energy barrier between adsorption sites |
| $f$ | [Pa] | Fugacity |
| $F$ | [J] | Helmholtz free energy |
| $F$ | [J/kg] | Helmholtz free energy per unit mass of adsorbent |
| $\vec{F}$ | [N], [$N/m^3$] | External force on fluid |
| $g$ | [J/kg] | Specific Gibbs free energy |

| | | |
|---|---|---|
| $G$ | [J] | Gibbs free energy |
| $G$ | [J/kg] | Gibbs free energy per unit mass of adsorbent |
| $\Delta G$ | [J/kg] | Gibbs free energy integral function |
| $h$ | [J/kg] | Specific enthalpy |
| $H$ | [J] | Enthalpy |
| $H$ | [J/kg] | Enthalpy per unit mass of adsorbent |
| $\Delta H$ | [J/kg] | Enthalpy integral function |
| $\vec{J}$ | [kg/(m$^2$ s)] | Mass flux vector |
| $k$ | [J/K] | Boltzmann's constant |
| $k$ | [J/(m K)] | Thermal conductivity |
| $K_0$ | [m] | Porous medium structural paramater |
| $m$ | [kg] | Mass |
| $\dot{m}$ | [kg/s] | Mass flow rate |
| $M$ | [kg/mol] | Molecular weight |
| $n$ | [kg] | Amount |
| | [kg/kg] | Amount per unit mass of adsorbent |
| $N$ | [-] | Number of layers |
| $P$ | [Pa] | Pressure |
| $P^o$ | [Pa] | Reference pressure |
| $\dot{Q}$ | [W] | Heat transfer rate |
| $\vec{\mathbf{r}}$ | [m] | Position vector |
| $\overline{r}_p$ | [m] | Mean pore size |
| $R$ | [J/(kg K)] | Universal gas constant |
| | [J/(mol K)] | |
| $R_p$ | [m] | Particle radius |
| $s$ | [J/(kg K)] | Specific entropy |
| $S$ | [J/(K)] | Entropy |
| | [J/(kg K)] | Entropy per unit mass of adsorbent |
| $\Delta S$ | [J/(kg K)] | Entropy integral function |
| $t_{isoth}$ | [s] | Isothermal filling duration |
| $T$ | [K] | Temperature |
| $T_\infty$ | [K] | External fluid temperature |
| $u$ | [J/kg] | Specific internal energy |
| $U$ | [J] | Internal energy, potential energy function (chapter 2) |

| | | |
|---|---|---|
| | [J/kg] | Internal energy per unit mass of adsorbent |
| $V$ | [m$^3$] | Volume |
| $\vec{v}$ | [m/s] | Velocity |
| $x$ | [-] | Site fraction (Ono-Kondo model) |
| $x$ | [-] | Quality |
| $x$, $y$, $z$ | [m] | Cartesian coordinates |
| $y$ | [-] | Mass fraction, molar fraction |
| $\dot{W}$ | [W] | Mechanical work rate |
| $z_0$, $z_1$, $z_2$ | [-] | Lattice coordination numbers |

## Greek Letters

| | | |
|---|---|---|
| $\alpha$ | [W/(m$^2$ K)] | Heat transfer coefficient |
| $\varepsilon$ | [-] | Porosity |
| $\varepsilon_{\text{void}}$ | [-] | Total porosity of the medium (adsorbent) |
| $\lambda$ | [m] | Mean free path |
| $\mu$ | [J/kg] | Chemical potential |
| $\mu$ | [kg/(m s)] | Viscosity |
| $\rho$ | [kg/m$^3$] | Density |
| $\tau$ | [Pa] | Stress tensor |
| $\tau$ | [-] | Tortuosity factor |
| $\upsilon$ | [m$^3$/kg] | Specific volume |
| $\Phi$ | [J] | Surface potential |
| | [J/kg] | Surface potential per unit mass of adsorbent |
| $\Psi$ | [-] | Error function |

## Subscripts

| | |
|---|---|
| $b$ | Bulk gas |
| $b$ | Adsorption bed |

| | |
|---|---|
| *cap* | Capillary |
| *CV* | Control volume |
| *d* | Depletion |
| *eff* | Effective |
| *esk* | Skeleton |
| *final* | Final conditions |
| *i* | Gas component |
| *i* | Layer index (Ono-Kondo Model) |
| *in* | Flow properties at inlet |
| *initial* | Initial conditions |
| *ins* | Insulation |
| *K* | Knudsen |
| *ma* | Macropore |
| *mc* | Maximum capacity |
| *mi* | Micropore |
| *out* | Flow properties at outlet |
| *ref* | Property at the reference state |
| *st* | Pure standard state |
| *S* | Solid |
| *S* | Surface |
| *st* | Storage |
| *TM* | Thermal mass |
| *TW* | Pressure tube wall |
| *V* | Viscous |

## Superscripts

| | |
|---|---|
| *a* | Absolute amount |
| *comp* | Compression functions |
| *e* | Excess adsorbed phase |
| *exp* | Experiments |
| *f* | Fluid phase |

| | |
|---|---|
| $g$ | Gas phase |
| $imm$ | Immersion functions |
| $l$ | Liquid phase |
| $mod$ | Model |
| $o$ | Reference state |
| $o$ | Property at the ideal-gas reference state at $T$ and $P^o$ |
| $R$ | Residual properties |
| $s$ | Solid phase, adsorbent |
| $w$ | Vessel wall |
| $*$ | Property in vacuo |

## Abbreviations

| | |
|---|---|
| $AH_2$ | Adsorptive storage, hydrogen adsorption storage systems |
| $CH_2$ | Compression storage, compressed gas storage systems for hydrogen |
| HTH | High-temperature hydrides |
| $LH_2$ | Liquefaction storage, liquid hydrogen storage systems |
| $LN_2$ | Liquid nitrogen, liquid nitrogen refrigeration |
| LTH | Low-temperature hydrides |

# Bibliography


[1] Fuel Cells 2000. www.fuelcells.org.

[2] S. M. Aceves, G. D. Berry, J. Martinez-Frias, and F. Espinosa-Loza. Vehicular storage of hydrogen in insulated pressure vessels. *Int. J. Hydrogen Energy*, 31 (15):2274–2283, 2006.

[3] S. M. Aceves, G. D. Berry, and G. D. Rambach. Insulated pressure vessels for hydrogen storage on vehicles. *Int. J. Hydrogen Energy*, 23(7):583–591, 1998.

[4] M. Altmann, P. Schmidt, R. Wurster, M. Zerta, and W. Zittel. Potential for hydrogen as a fuel for transport in the long term (2020 - 2030), http://www.lbst.de/publications/studies__d/2004/LBST-study-IPTS_2004_eur21090en.pdf. Technical report, Institute for Prospective Technological Studies, 2004.

[5] G. L. Aranovich and M. D. Donohue. Adsorption isotherms for microporous adsorbents. *Carbon*, 33(10):1369–1375, 1995.

[6] G. L. Aranovich and M. D. Donohue. Adsorption of supercritical fluids. *J. Colloid Interface Sci.*, 180:537–541, 1996.

[7] L. E. Arri and D. Yee. Modeling coalbed methane production with binary gas sorption. *presented at the SPE Rocky Mountain Regional Meeting, Casper, Wyoming, May 18-21*, 1992.

[8] S. K. Bhatia and A. L. Myers. Optimum conditions for adsorptive storage. *Langmuir*, 22:1688–1700, 2006.

[9] S. K. Bhatia and D. Nicholson. Transport of simple fluids in nanopores: Theory and simulation. *AIChE J.*, 52(1):29–38, 2006.

[10] S. Biloe, V. Goetz, and S. Mauran. Dynamic discharge and performance of a new adsorbent for natural gas storage. *AIChE J.*, 47(12):2819–2830, 2001.

[11] R. B. Bird, W. E. Stewart, and E. N. Lightfoot. *Transport Phenomena*. John Wiley and Sons, New York, 2002.

[12] BMW. `http://en.wikipedia.org/wiki/BMW_Hydrogen_7`.

[13] P. Bénard and R. Chahine. Modeling of high-pressure adsorption isotherms above the critical temperature on microporous adsorbents: Application to methane. *Langmuir*, 13(001):808–813, 1997.

[14] P. Bénard and R. Chahine. Determination of the adsorption isotherms of hydrogen an activated carbons above the critical temperature of the adsorbate over wide temperature and pressure ranges. *Langmuir*, 17(003):1950–1955, 2001.

[15] P. Bénard, R. Chahine, P. A. Chandonia, D. Cossement, G. Dorval-Douville, L. Lafi, P. Lachance, R. Paggiaro, and E. Poirier. Comparison on hydrogen adsorption on nanoporous materials. *J. Alloys Compd.*, Article in Press, 2006.

[16] Pierre Bénard and Richard Chahine. Modeling of adsorption storage of hydrogen on activated carbons. *Int. J. Hydrogen Energy*, 26(002):849–855, 2001.

[17] U. Bossel. Does a hydrogen economy make sense? *Proceedings of the IEEE*, 94 (10), 2006.

[18] U. Bossel, B. Eliasson, and G. Taylor. The future of the hydrogen economy: Bright or bleak? *www.efcf.com/reports*, 2005.

[19] U. Bunger and G. Owren. Development potentials for small mobile storage tanks with vacuum powder insulation. In *11th World Hydrogen Energy Conference, Stuttgart, Germany.*, 1996.

[20] Vasilis N. Burganos and Stratis V. Sotirchos. Knudsen diffusion in parallel multidimensional or randomly oriented capillary structures. *Chem. Eng. Sci.*, 44 (11):2451–2462, 1989.

[21] H. B. Callen. *Thermodynamics and an Introduction to Thermostatistics*. John Willey and Sons, New York, 1985.

[22] R. Chahine and T. K. Bose. Low-pressure adsorption storage of hydrogen. *Int. J. Hydrogen Energy*, 19(002):161–164, 1994.

[23] P. Chen, X. Wu, J. Lin, and K. L. Tan. High h2 uptake by alkali-doped carbon nanotubes under ambient pressure and moderate temperatures. *Science*, 285:91–93, 1999.

[24] A. Clark. *The Theory of Adsorption and Catalysis*. Academic Press, New York and London, 1970.

[25] R. E. Cunningham and R. J. J. Williams. *Diffusion in Gases and Porous Media*. Plenum Press - New York and London, 1980.

[26] H. W. Davidson and B. M. Turk. The flow of gases through packed beds of colloidal carbon blacks. *Br. J. Appl. Phys.*, 5:55–60, 1954.

[27] R. K. Dixon. Advancing towards a hydrogen energy economy: Status, opportunities and barriers. *Mitigation and Adaptation Strategies for Global Change*, 12(3):325–341, 2007.

[28] D. D. Do. *Adsorption Analysis: Equilibria and Kinetics*. ICP, London, 1998.

[29] DOE. `http://www1.eere.energy.gov/hydrogenandfuelcells/storage/index.html`.

[30] M. Gardiner and A. Burke. Hydrogen storage options: Technologies and comparisons for light-duty vehicle applications. Technical report, Institute of Transportation Studies, 2005.

[31] M. R. Gardiner and K. Bradley. A comparison of hydrogen storage technologies: Compressed hydrogen gas, liquid hydrogen and activated carbon. In *14th Annual U.S. Hydrogen Conference*, 2003.

[32] K. A. M. Gasem and R. L. Robinson-Jr. Sequestering carbon dioxide in coalbeds. Technical report, Oklahoma State University, 2002.

[33] J. W. Gibbs. *Collected Works of J. W. Gibbs*. Longmans and Green, New York, 1928.

[34] GM, LBST, bp, ExxonMobil, Shell, and TotalFinaElf. Well-to-wheel analysis of energy use and greenhouse gas emissions of advanced fuel/vehicle systems - a european study. Technical report, GM, LBST, bp, ExxonMobil, Shell, TotalFinaElf, 2002.

[35] S. J. Gregg and K. S. W. Sing. *Adsorption, Surface Area and Porosity*. Academic Press, London and New York, 1967.

[36] S. Gumma and O. Talu. Gibbs dividing surface and helium adsorption. *Adsorption*, 9:17–28, 2003.

[37] T. Hocker, G. L. Aranovich, and M. D. Donohue. Monolayer adsorption for the subcritical lattice gas and partially miscible binary mixture. *J. Colloid Interface Sci.*, 211:61–80, 1999.

[38] K. H. H. Huebner, D. L. Dewhirst, D. E. Smith, and T. G. Byrom. *Finite Element Method*. John Wiley and Sons, New York, 2001.

[39] F. P. Incropera and D. P. de Witt. *Fundamentals of Heat and Mass Transfer*. John Wiley, 1992.

[40] B. D. James, G. N. Lomax, C. E. Thomas, and I. F. Kuhn. *Comparison of Onboard Hydrogen Storage for Fuel Cell Vehicles*. Directed Technologies Report DE-AC02-94CE50389, prepared for Ford Motor Company, 1996.

[41] V. N. Kaliakin. *Introduction to Approximate Solutions Techniques, Numerical Modeling, and Finite Element Methods*. Marcel Dekker, Inc., New York, 2001.

[42] M. Kaviany. *Principles of Heat Transfer in Porous Media*. Springer Verlag, 1995.

[43] K. Malek and M.-O. Coppens. Knudsen self- and fickian diffusion in rough nanoporous media. *Journal of Chemical Physics*, 119(5):2801–2811, 2003.

[44] E. A. Mason and A. P. Malinauskas. *Gas Transport in Porous Media - The Dusty-Gas Model*. Elsevier, Amsterdam, 1983.

[45] K. R. Matranga, A. L. Myers, and E. D. Glandt. Storage of natural gas by adsorption on activated carbon. *Chem. Eng. Sci.*, 47:1569, 1992.

[46] H. Matsuda and M. Nagami. Study of large hydrogen liquefaction process - `http://www.enaa.or.jp/WE-NET/ronbun/1997/e5/sanso1997.html`. 1997.

[47] J. W. McBain. Theories of occlusion and the sorption of iodine by carbon. *Trans. Faraday Soc.*, 14:202, 1919.

[48] F. Michl. Cryoadsorptive hydrogen storage. Technical report, FutureCarbon GmbH (Internal communication), 2006.

[49] Yu. Ya. Milenko, R. M. Sibileva, and M. A. Strhemechny. Natural ortho-para conversion rate in liquid and gaseous hydrogen. *J. Low Temp. Phys.*, 107 (1-2):77–92, 1997.

[50] J. P. B. Mota, A. E. Rodrigues, E. Saatdjian, and D. Tondeur. Charge dynamics of a methane adsorption storage system: Intraparticle diffusional effects. *Adsorption*, 3(2):117–125, 1997.

[51] J. P. B. Mota, A. E. Rodrigues, E. Saatdjian, and D. Tondeur. Dynamics of natural gas adsorption storage system employing activated carbon. *Carbon*, 35(9):1259–1270, 1997.

[52] J. P. B. Mota, E. Saatdjian, D. Tondeur, and A. E. Rodrigues. A simulation model of a high-capacity methane adsorptive storage system. *Adsorption*, 1(1):17–27, 1995.

[53] A. L. Myers. Thermodynamics of adsorption in porous materials. *AIChE Journal*, 48(1):145–160, 2002.

[54] A. L. Myers and P. A. Monson. Adsorption in porous materials at high pressure: Theory and experiment. *Langmuir*, 18(26):10261–10273, 2002.

[55] A.L. Myers. *Chemical Thermodynamics for Industry*, volume Chapter 21. Ed. T.M. Letcher, Royal Society of Chemistry, Cambridge, UK, 2004.

[56] J.A. Nelder and R. Mead. A simplex method for function minimization. *Computer J.*, 7:308–313, 1965.

[57] D. Nicholson and N. G. Parsonage. *Computer Simulation and the Statistical Mechanics of Adsorption*. Academic Press, London, 1982.

[58] A. Niedzwiecki. Technical report, Quantum Technologies - US DOE Hydrogen Vision Meeting - IEA HIA Task 17, 2001.

[59] S. Ono and S. Kondo. *Molecular Theory of Surface Tension in Liquids*. Springer-Verlag, 1960.

[60] Ovonic. `http://www.ovonic-hydrogen.com/pdfs/ovonic_metal_hydride_fuel_storage_system.pdf`.

[61] S. V. Patankar. *Numerical Heat Transfer and Fluid Flow*. Hemisphere Publ. Co., 1980.

[62] M. J. Prakash, M. Prasad, and K. Srinivasan. Modeling of thermal conductivity of charcoal-nitrogen adsorption beds. *Carbon*, 38:907–913, 2000.

[63] J. S. Rowlinson and B. Widom. *Molecular Theory of Cappilarity*. Clarendon Press, 1982.

[64] W. Rudzinski and D. W. Everett. *Adsorption of Gases on Heterogeneous Surfaces*. Academic Press, London and New York, 1992.

[65] D. M. Ruthven. *Principles of Adsorption and Adsorption Processes*. Wiley, New York, 1984.

[66] P. M. Satya Sai and K. Krishnaiah. Development of the pore-size distribution in activated carbon produced from coconut shell char in a fluidized-bed reactor. *Ind. Eng. Chem. Res.*, 44:51–60, 2005.

[67] Giselle Sandí. Hydrogen storage and its limitations. *The Electrochemical Society - Interface*, pages 40–44, 2004.

[68] L. Schlapbach and A. Züttel. Hydrogen storage materials for mobile applications. *Nature, Insight Review Articles*, 414, 2001.

[69] W. Schütz, F. Michl, W. Polifke, and R. Paggiaro. *Storage System for Storing a Medium and Method for Loading a Storage System with a Storage Medium and Emptying the Same Therefrom.* Patent (WO/2005/044454) - http://www.wipo.int/pctdb/en/wo.jsp?wo=2005044454, 2005.

[70] R. B. Scott. *Cryogenic Engineering.* Van Nostrand Company, 1967.

[71] Carlos Sereno and Alírio Rodrigues. Can steady-state momentum equations be used in modelling pressurization od adsorption beds? *Gas Separation & Purification*, 7(3):167–174, 1993.

[72] S. Sircar. Excess properties and thermodynamics of multicomponent gas adsorption. *J. Chem. Soc., Faraday Trans. 1*, 81(1):1527–1540, 1985.

[73] S. Sircar. Gibbsian surface excess for gas adsorption-revisited. *Ind. Eng. Chem. Res.*, 38:3670–3682, 1999.

[74] Karl J. Sladek, Edwin R. Gilliand, and Raymond F. Baddour. Diffusion on surfaces ll. correlation of diffusivities of physically and chemically adsorbed species. *Ind. Eng. Chem. Fundam.*, 13 (2):100–105, 1974.

[75] J. M. Smith and H. C. Van-Ness. *Introduction to Chemical Engineering Thermodynamics.* McGraw-Hill, New York, 1959.

[76] W. A. Steele. *The interaction of gases with solid surfaces.* Pergamon Press, 1974.

[77] M. Suzuki. *Adsorption Engineering.* Kodansha and Elsevier, Tokyo-Amsterdam, 1990.

[78] O. Talu and A. L. Myers. Rigorous thermodynamic treatment of gas adorption. *AIChE J.*, 34:1887–1893, 1988.

[79] Y. S. Touloukian and C. Y. Ho. *Thermophysical properties of matter - The TPRC Data Series - A Comprehensive Compilation of Data.* New York, IFI/Plenum, 1970-[79].

[80] R. von Helmont and U. Eberle. Fuel cell vehicles: Status 2007. *J. Power Sources*, 165:833–843, 2007.

[81] N. Wakao and S. Kaguei. *Heat and Mass Transfer in Packed Beds.* Gordon and Breach Science Publishers, 1982.

[82] W. Weindorf, U. Bünger, and J. Schindler. Comments on the paper by baldur eliasson and ulf bossel - the future of the hydrogen economy: Bright or bleak? - `http://www.hyweb.de/News/LBST_Comments-on-Eliasson-Bossel-Papers_July2003_protected.pdf`. 2003.

[83] H. William. *Numerical recipes in C, C++.* Cambridge Univ. Press, 2002.

[84] C.J. Winter and J. Nitsch, editors. *Hydrogen As An Energy Carrier.* Springer-Verlag, 1988.

[85] Conversations with BMW co-workers during the progress of the diploma thesis by Vitus Zimmermann: Untersuchungen am Fluessigluft-System zur Standzeitverlängerung von Fluessigwasserstoffspeichern fuer automobile Anwendungen am Beispiel CooLH2.

[86] G. Van Wylen, R. Sonntag, and C. Borgnakke. *Fundamentals of Classical Thermodynamics.* John Wiley, 1994.

[87] J. L. Xia, B. L. Smith, and G. Yadigaroglu. A simplified model for depressurization of gas-filled pressure vessels. *Int. Comm. Heat Mass Transfer*, 20:653–664, 1993.

[88] D. M. Young and A. D. Crowell. *Physical Adsorption of Gases.* Butterworths and Co., London, 1962.

[89] B. A. Younglove. Thermophysical properties of fluids. i. argon, ethylene, parahydrogen, nitrogen, nitrogen trifluoride and oxygen. *J. Phys. Chem. Ref. Data*, 11:1–11, 1982.

[90] J. M. Zalc, S. C. Reyes, and E. Iglesia. Monte-carlo simulations of surface and gas phase diffusion in complex porous structures. *Chem. Eng. Sci.*, 58:4605–4617, 2003.

[91] Z. Zhou, B. Smith, and G. Yadigaroglu. A mathematical model and its analytical solution for slow depressurization of a gas-filled vessel. *J. Eng. Math.*, 31:43–57, 1997.

[92] A. Züttel. Hydrogen storage and distribution systems. *Mitigation and Adaptation Strategies for Global Change*, 12(3):343–365, 2007.